Department of Mechanical Engineering
University College London

A study of fuel spray structure and its relationship to emissions and performance of a gasoline direct injection engine

Submitted for the Degree of Doctor of Philosophy

Shane T.C. O' Donoghue

2002

The author declares that all work within this thesis is his own, unless stated otherwise.

Signed: S.T.C. O' Donoghue

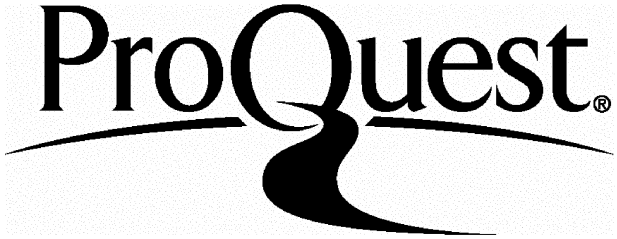

Abstract

The research reported in this thesis is one of three linked investigations aimed at improving the understanding of the flow and fuel/air mixing processes that occur within direct injection gasoline engines through the application of both experimentation and modelling techniques. The components of work covered by this thesis are an investigation into the structure of fuel sprays from four different high-pressure swirl injectors, and a subsequent investigation of how two of them perform in a single-cylinder direct injection gasoline engine.

The fuel injectors were initially tested on a rig in the UCL fuel systems test facility. Two different experiments were carried out to obtain a significant amount of information about each of the injectors' sprays under various conditions. High-speed photography using a copper vapour laser for illumination was employed to capture details of the spray structures, as well as penetration rates and cone angles. In a separate series of tests, droplet sizes were obtained using a Malvern particle sizer. A tomographic technique was developed in an attempt to deconvolve the spray structure.

A statistical design of experiment approach was used because of the large number of variables to be investigated during the engine testing. Two designs of injectors were tested in two positions for two different fuel pressures. For each arrangement, a Central Composite Rotatable Design of experiment was employed for four variables at five levels. The variables were inlet valve timing, fuel injection timing, ignition timing and air/fuel ratio. The results of these tests were modelled by regression analysis using quadratic functions, which included the possibility of interactions between pairs of variables.

The measured engine responses were unburnt hydrocarbons (HC) emissions, oxides of nitrogen emissions (NOx), brake specific fuel consumption (BSFC) and exhaust gas temperature. The results from the engine and injector testing suggest that there is a strong, yet complex interaction between the fuel spray structure and the engine performance.

To my parents

Acknowledgements

I would not be writing this thesis if it was not for the determined supervision of Chris Nightingale. For that and more, I am eternally grateful to him.

I would also like to thank those at Jaguar Cars responsible for this project, in particular Steve Richardson and Xiang Dong Chen for supplying information and components to make the project happen.

The UCL technical staff were largely responsible for the timely completion of engine and injector testing, thanks to their experience and understanding. In addition, the members of the IC engine research group provided an interesting environment in which to complete my work, in particular Paul Williams for his additional support.

Financially, I would like to express thanks to the Engineering and Physical Sciences Research Council and Jaguar Cars for providing support throughout the project.

Last, but certainly not least, I would like to thank my kind friends and family, and my partner Kerry, for always supporting me and my decisions in life.

Table of Contents

List of Figures

Chapter 1

Chapter 2

Chapter 3

Nomenclature

Abbreviations

aBDC	After bottom dead centre
aSOI	After start of injection
aTDC	After top dead centre
BDC	Bottom dead centre
BMEP	Brake mean effective pressure
BSFC	Brake specific fuel consumption
BTDC	Before top dead centre
bTDC	Before top dead centre
C_3H_8	Propane
CA	Crank angle
CCRD	Central composite rotatable design
CFD	Computational fluid dynamics
CI	Compression ignition
CO	Carbon monoxide
CO_2	Carbon dioxide
COV of IMEP	Coefficient of variation of indicated mean effective pressure
DDM	Discrete droplet model
DI	Direct injection
DMI	Direct mixture injection
FMEP	Frictional mean effective pressure
EGR	Exhaust gas recirculation
GDI	Gasoline direct injection
GFS	Gerris flow solver
H_2	Hydrogen
H_2O	Water
HC	Hydrocarbons
HCCI	Homogeneous charge compression ignition
He	Helium
HT	High tension
IC	Internal combustion
IMEP	Indicated mean effective pressure
ISFC	Indicated specific fuel consumption
IVO	Inlet valve opening
lds	Liquid droplet sprays
LDV	Laser Doppler velocimetry
LE	Leading edge
LIF	Laser induced fluorescence
MBT	Maximum brake torque
MEP	Mean effective pressure
mil	Metal particles in liquid
MPI	Multi-point injection
MS	Main spray
N_2	Nitrogen
NCP	New combustion process
NO	Nitric oxide
NOx	Oxides of nitrogen
PC	Personal computer
PCI	Peripheral component interconnect
PDA	Phase Doppler anemometry
PFI	Port fuel injection
pia	Particles in air
pil	Particles in liquid

PLIF	Planar laser induced fluorescence
ppm	Parts per million
SCV	Swirl control valve
SI	Spark ignition
SMD	Sauter mean diameter
SOI	Start of injection
TDC	Top dead centre
THC	Total hydrocarbons
UHC	Unburned hydrocarbons
VCO	Valve covering orifice
vppm	Volumetric parts per million
VOF	Volume of fluid
VVA	Variable valve actuation
WOT	Wide open throttle
WWMP	World-wide mapping point

Symbols

γ	Ratio of specific heats
η_f	Fuel conversion efficiency
$\eta_{f,b}$	Brake fuel conversion efficiency
$\eta_{f,ig}$	Gross indicated fuel conversion efficiency
η_{th}	Thermal efficiency
η_v	Volumetric efficiency
θ	Angle of cone spray
ν	Volume
c_p	Specific heat at constant pressure
c_v	Specific heat at constant volume
h	Thickness of fuel sheet
L/D	The length of the final (parallel sided) exit orifice passage, divided by the diameter of that exit orifice, for a fuel injector
P	Pressure
P_{atm}	Atmospheric pressure
r	Compression ratio

Chapter 1

A LITERATURE SURVEY

1 - A literature survey

1.1 The reasons for using Gasoline Direct-Injection (GDI)

The world's car manufacturers face a stiff challenge. Today's consumer demands a vehicle that delivers superb fuel economy and performance while being very responsive to drive. The marketplace is not the only force driving the car companies. World governments are introducing ever-tightening emissions legislation. The most recent is the likely introduction of legislated values of carbon dioxide (CO_2). The only method of reducing the emission of CO_2 is the reduction of every car's fuel consumption [Mitsubishi Website, 2000].

Research into new technologies is a continuing process to keep up with these demands. In recent years several significant steps were made. Fuel injection replaced the carburettor, improving control of engine operating parameters such as air/fuel ratio in order to reduce emissions. The introduction of unleaded fuel and catalytic convertors greatly aided the reduction in exhaust emissions. More recently, engineers have been experimenting with technologies such as variable-valve actuation (VVA) and cylinder de-activation. It could be argued that the spark-ignition (SI) internal combustion engine is near the end of its development cycle. However, another technology has emerged which promises to keep the SI engine in wide-scale use, and to improve its fuel economy so that it is close to that of the diesel engine.

Gasoline direct-injection (GDI) is not a new idea, dating from the early part of the 20th century. An impetus was given to the development of the injection of gasoline during World War 2 by the requirement of aircraft fuel systems to be able to operate over a range of altitudes with the chance of experiencing quite high 'g' forces. Later versions of the Rolls-Royce Merlin engine used a port injection system, but Daimler-Benz developed a full GDI system [Banks, 1950]. There were spasmodic attempts to apply GDI to automotive engines after the war, two attempts being at opposite ends of the spectrum. Norbye [1988] described the application of GDI to a small two-stroke engine to try to reduce the poor fuel consumption of the base engine, while the 1954 Mercedes-Benz 300SL sportscar [Scherenberg, 1955] applied GDI to obtain a gain in performance.

However, it was port fuel injection that became the predominant method of obtaining performance gains from the 1960s onwards. Arguably, the first modern generation GDI engine was produced by Ford [Simko *et al*, 1972], but it was not put into production for several reasons, even though stable stratified combustion was attained. The reasons centred on the narrow-spacing configuration, where the spark plug was situated near the injector in the combustion chamber and were as follows:

- Increased hydrocarbon emissions due to incomplete combustion
- Spark plug wetting leading to soot formation
- Poor performance and restricted range of possible modes of operation due to the limitations in electronic control systems at that time

For these reasons, and others such as injector durability and carbonisation of gasoline, GDI engines did not make any impression on the market until the 1990s, when the pressure for greater fuel economy led to the required technical progress being made.

Mitsubishi launched a mass-production GDI vehicle in 1996. This launch convinced many of the world's car makers that the future of the SI engine lay with GDI technology. Several other manufacturers have reached a stage at which they are already manufacturing, or about to manufacture, their own GDI engine [Ford: Schamel *et al*, 2000, Nissan: Takagi *et al*, 1998, Renault: Jost, 2000, Toyota: Tomoda *et al*, 1997]. Mitsubishi alone has declared [Mitsubishi Website, 2000] that it intends to replace all of its gasoline-powered models with GDI-powered versions by 2010.

There are several potentially very good reasons why an engine injecting its fuel directly into the combustion chamber is more desirable than one that mixes the fuel with air before drawing it into the cylinder. The latter part of the previous sentence hints at the first - engine throttling. This is the process by which traditional SI engines vary their output to match their load. As the driver presses the accelerator pedal a throttle plate opens to increase the area for the fuel-air mixture to flow. Unfortunately, at low loads, the pressure difference across the throttle is quite high, reducing the part-load efficiency of the engine due to increased pumping losses. The GDI engine has the potential to eliminate throttling completely.

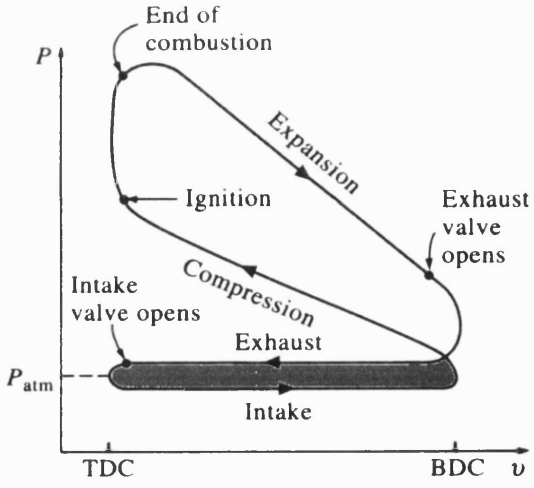

Figure 1.1 - Pressure-volume diagram for a four-stroke SI engine [Adapted from Cengal/Boles, 1994].

A pressure-volume diagram representing an SI engine with port fuel injection (PFI) at part-load is shown in figure 1.1. The shaded area under the curve represents the pumping losses of the engine due to throttling. The shaded area of negative work effectively acts to reduce the overall work output by partially neutralising the positive work output of the compression/expansion part of the cycle. This is obviously an inefficient way to control work output. The alternative approach of simply reducing the fuel burnt per cycle will not work with the standard SI engine due to the limited range of air/fuel ratios over which combustion can be sustained. Stratification of charge is a possible way of maintaining combustion over a wide range of air/fuel ratios.

Since the 1920s [Heywood 1988], stratification in an SI engine has been acknowledged as a source of great potential benefit, combining the full-load performance of the SI engine with the part-load economy of a compression ignition (CI) engine by eliminating the need for throttling. Stratification is extremely difficult to achieve with PFI due to the long period that elapses between the injection of fuel in the inlet port and the initiation of combustion. There have been a number of attempts [Ando *et al*, 1991, Takemura *et al*, 1991, Kiyota *et al*, 1992, Ohm *et al*, 1993, Queenan *et al*, 1997] to achieve stratification with PFI, but it has not proved possible to totally eliminate the throttle. GDI offers the chance of short mixing times if the fuel is injected late in the compression stroke, hence making stratified charge operation far more feasible. The concept of stratified charge is based on establishing an ignitable air/fuel mixture around the spark plug, at the time of sparking, while having a very lean mixture elsewhere. This way, combustion can be maintained even though the overall air/fuel ratio is as high as 40:1 [Kume *et al*, 1996].

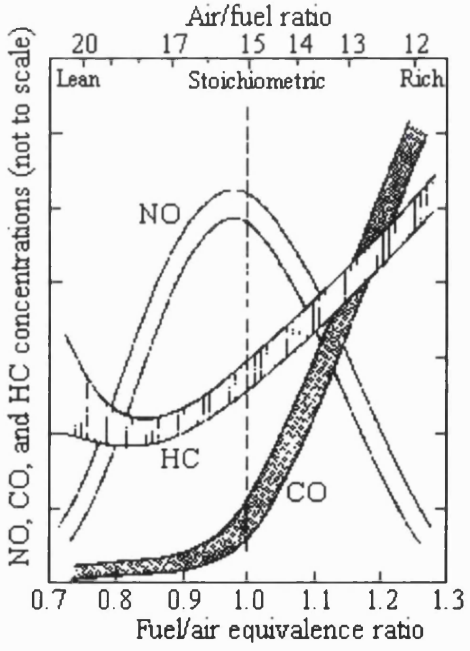

Figure 1.2 - Variation of pollutant concentrations in an SI engine with fuel/air equivalence ratio [Adapted from Heywood, 1988].

The reduction of fuel consumption has a direct impact on the emissions. The less fuel and air being used, the lower the volume of pollutants produced. Operating with a mixture lean of stoichiometric also has the effect of reducing the output of each of the pollutants shown in figure 1.2. The fuel economy (and hence overall emissions) of a GDI engine is further improved over the PFI engine at start-up. In a PFI engine, when the walls of the inlet port are still cool, fuel gathers in 'puddles'. This is known as 'wall-wetting' and is a significant source of emission of unburned hydrocarbons (UHC). As the fuel is injected directly in a GDI engine, this source of emissions is eliminated, although wetting of the cylinder surfaces themselves can still be a problem.

Stratified charge GDI engines are returned to homogeneous operation at full load conditions [Harada *et al*, 1997, Iwamoto *et al*, 1997] in order to achieve a comparable specific power output to a homogeneous charge engine. In fact, there is the potential for increased power [Anderson *et al*, 1996]. As the fuel is injected (as a fine spray) directly into the cylinder it vaporises quickly into the airflow. This causes the air to cool and contract. More air may now be drawn into the cylinder than would otherwise have been possible, improving the volumetric efficiency, η_V, according to equation 1.1 below [Stone, 1999].

$$\eta_V = \frac{\text{volume of 'ambient' density air inhaled per cylinder per cycle}}{\text{cylinder swept volume}} \qquad \textbf{(1.1)}$$

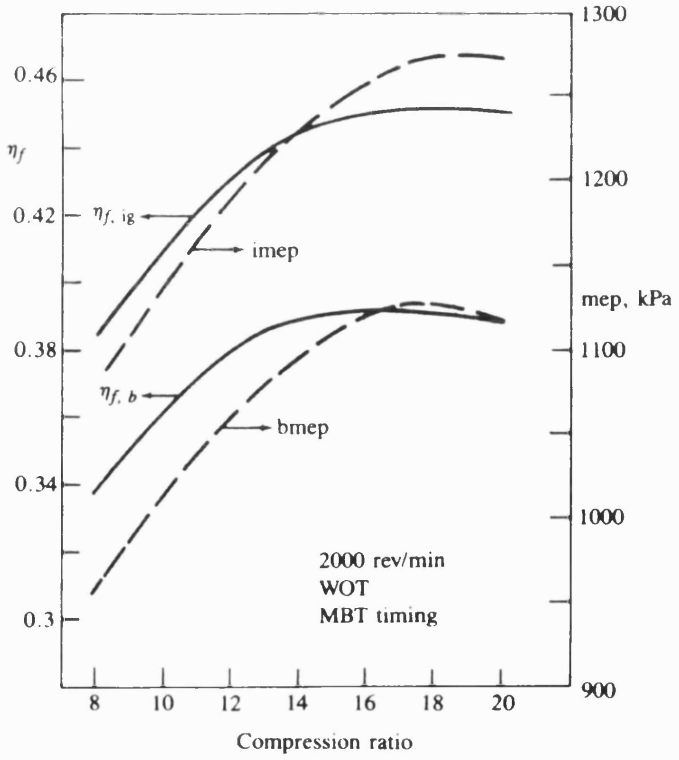

Figure 1.3 - Effect of compression ratio on IMEP and fuel conversion efficiency [Heywood, 1988].

The cooling of the air also reduces the tendency for the engine to knock. Knocking is defined as spontaneous ignition of the air-fuel mixture before sparking. It causes a sharp pressure rise within the cylinder and is audible to the driver. It is undesirable as it can cause long-term damage to an engine. In a PFI engine the compression ratio is limited by the onset of knock. Indeed, modern PFI engines now utilise a knock sensor on the crankcase to aid the control of the air-fuel mixture. GDI allows a higher compression ratio due to the charge-cooling effect [Anderson *et al*, 1996]. According to Heywood [1988], an engine's fuel conversion efficiency (η_f) increases by approximately 3 percent per unit increase of compression ratio. The engine's power output increases by the same amount. Figure 1.3 illustrates the effect of compression ratio on indicated mean effective pressure (IMEP) and fuel conversion efficiency, η_f, of an eight-cylinder SI engine at 2000rpm and wide-open throttle (WOT). Figure 1.4 below illustrates Mitsubishi's claim of increased power due to GDI.

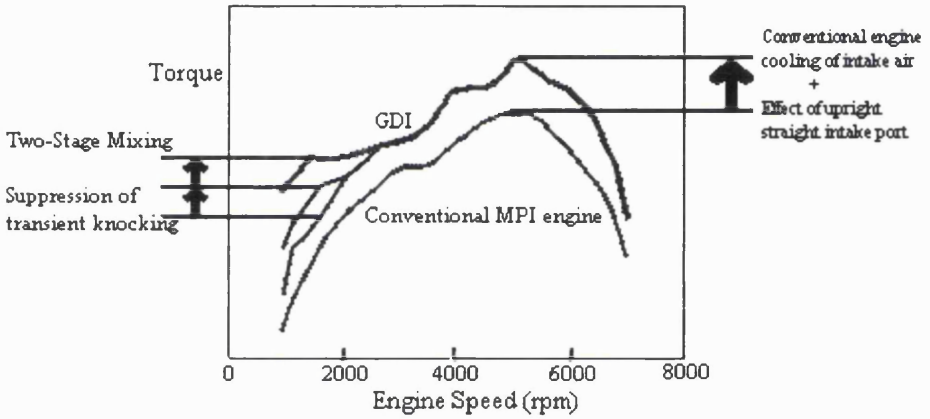

Figure 1.4 - Mitsubishi's claims for increased power due to GDI technology [Adapted from Mitsubishi Website, 2000].

In Europe, unleaded gasoline is relatively high in sulphur content. This would contribute to catalytic convertor poisoning in a GDI engine operating at the ultra-lean air-fuel mixtures attainable with stratified combustion. To combat that, but still capitalise on the inherent advantages of the GDI concept, a number of engines have been designed to operate with a homogeneous charge [Anderson *et al*, 1996, Andrews, 1998, Webster, 1998]. Homogeneous charge engines can operate lean, but not to the same level as a stratified charge engine. Toyota claims to have operated their lean burn engine to 25:1 [Inoue *et al*, 1993]. However, lean burn catalysts are particularly susceptible to sulphur poisoning from sulphur-rich European gasoline. Renault use exhaust gas re-circulation (EGR) as the dilutent rather than air, so that a conventional three-way catalyst can be used. Most of the same advantages accrue when EGR is used rather than air.

Homogeneous charge lean burn engines will show some gain in efficiency through the reduction of pumping losses, although the improvement will not be as great as with stratified charge. These advantages are based on efficiency gains. There will also be a gain in efficiency due to the 'γ effect', and reduced heat losses [Cengal *et al*, 1994]. The specific heat ratio, γ (c_p/c_v), has a direct effect on the thermal efficiency:

$$\eta_{th} = 1 - r^{(1-\gamma)} \quad \textbf{(Otto cycle efficiency formula)}$$

An increase in the specific heat ratio raises the thermal efficiency of the engine. The specific heat ratio is higher under lean operation. The reduced heat losses come about because the specific heat of exhaust gases is relatively high, such that they act as a thermal sink and reduce the peak combustion temperature.

When compared with complicated engine designs such as Mitsubishi's stratified charge engine, there will be a gain in volumetric efficiency due to fewer compromises having to be made in port shape and piston profile to set up the pronounced reverse tumble motion. Homogeneous GDI engines can also make full use of the charge cooling and increased compression ratio effects discussed earlier. Although homogeneous charge GDI engines have their merits, it is likely that some manufacturers will adopt this method only as their first-generation GDI design before moving to stratified charge. Homogeneous units are inherently simpler to develop, as it is easier to ensure mixing of fuel and air than to try to keep the two gas streams apart.

In summary, GDI engines have the potential to reduce the average fuel consumption across the globe (if made in sufficient numbers), hence reducing the emission of pollutants such as CO_2. At the same time, the vehicles powered by GDI engines should live up to the driver's performance, comfort and driveability expectations.

1.2 The current state of GDI development

It was mentioned previously that many car manufacturers either have a GDI engine in production or on the way to market. The execution and technology of each differs significantly. In this section, current research and development in GDI technology is reviewed.

In the years between the mid-nineteen sixties to the mid-nineteen eighties, the possibility of a stratified-charge GDI engine was thoroughly researched [Bishop *et al*, 1968, Mitchell *et al* 1968 & 1972, Simko *et al*, 1972, Haslett *et al*, 1976, Wood, 1978, Scusssel *et al*, 1978, Witze, 1980, Lorusso *et al*, 1984]. One of the conclusions at the time was that the degree of control required was not feasible. However, the technology now exists for computer control to be practical. The computer is small enough to fit in a corner of the engine bay, not the whole luggage bay. This

alone will not give the improvements required in fuel consumption and emissions control. The area of greatest challenge is the establishment of an appropriate air flow field within the cylinder prior to combustion, together with a fuel spray introduced in such a way as to promote the type of combustion required, that is to say either stratified or homogeneous. Therefore, the fuel injection system is currently one of the most active areas of research in GDI.

To achieve projected fuel savings, a GDI fuel injection system must match the airflow field produced by an engine's combustion chamber design. The required air-fuel mixture must be produced by this interaction over the operating range of the engine, at the correct time and place within the cylinder. According to Kume *et al* [1996], a well-atomised, and repeatable spray is required, especially when operating in stratified mode. Mitsubishi's GDI system has the ability to operate in two distinct modes. As yet, part-load operation still requires a degree of throttling. However, the fuel system is capable of injecting late into the cylinder. Mitsubishi have used a combination of upright intake ports and a bowl-shaped cavity in the piston to bring a rich air-fuel mixture to the spark plug at the correct time, as shown in figure 1.5. Mitsubishi brought this design to the market in 1996 [Mitsubishi Website, 2000], and thereby won the accolade of being the first manufacturer to mass-produce a GDI engine capable of satisfying today's tight emissions legislation.

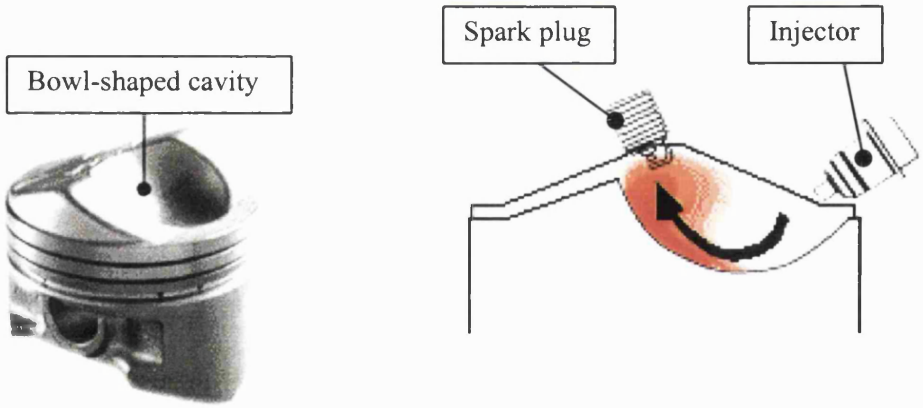

Figure 1.5 - Mitsubishi's bowl-shaped piston cavity [Adapted from Mitsubishi web site, 2000].

Iwamoto *et al* [1997] describe the strategies of the Mitsubishi GDI engine in detail. In late-injection (stratified-charge) mode, the fuel is injected at the rising piston surface. As the fuel impinges on the hot piston crown, the fuel vaporises. This vapour is then entrained into the bulk air motion towards the spark plug. The reverse tumble, created by the upright intake ports (see figure 1.6) is maintained by the 'ramp' effect of the piston cavity. This ordered motion directs the rich fuel-air mixture towards the spark plug at the time of ignition, enabling combustion to occur with an air-fuel ratio exceeding 40:1 [Kume *et al*, 1996]. However, it has been shown that

the production engine operates in this mode for a small proportion of its operating range, limiting the advantages to idling and light load settings [Wirth *et al*, 1998].

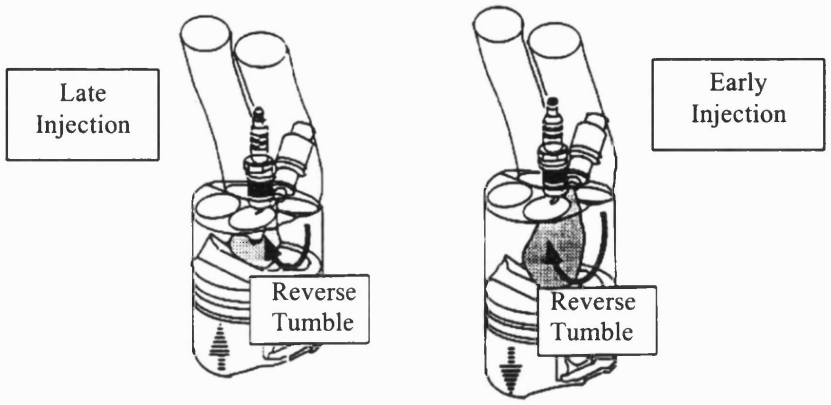

Figure 1.6 - Upright intake ports promote reverse tumble [Adapted from Kume *et al*, 1996].

Homogeneous operation is achieved with the Mitsubishi GDI engine by changing the injection timing to occur early in the induction stroke. The fuel does not hit the piston in this mode. Instead, it mixes with the air to form a homogeneous mixture throughout the cylinder. In this mode, the Mitsubishi engine behaves similarly to a PFI engine, but with the added advantage of charge cooling. Therefore, the engine has an increased volumetric efficiency, and the potential to run with a higher compression ratio, leading to increased power and torque.

Ricardo has also developed a GDI engine based on upright intake ports and a bowl-shaped cavity in the piston [Jackson *et al*, 1996]. The Ricardo engine appears to be a 'mirror-image' of the Mitsubishi engine as shown in figure 1.7, with the inlet and exhaust sides of the engine changed around. This inversion in the schematic drawing of the engine has probably been applied to make the design look different from Mitsubishi's pioneering engine. The inlet ports are similarly shaped, as is the piston crown [Jackson *et al*, 1997].

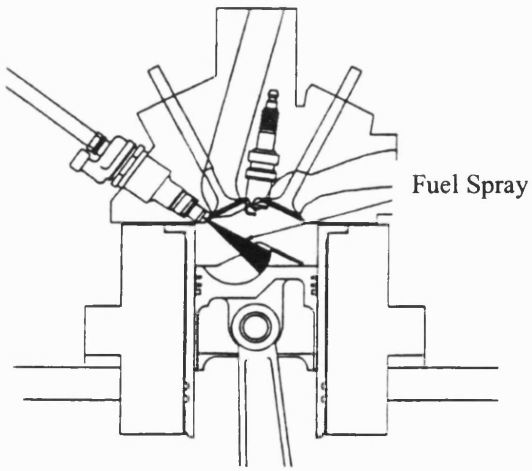

Figure 1.7 - Ricardo top entry GDI engine [Adapted from Jackson *et al*, 1997].

Toyota's production GDI engine utilises a 12 MPa fuel supply [Harada *et al*, 1997]. This engine uses the same concepts as Mitsubishi: a shaped piston crown and enhanced bulk air motion coupled with an advanced electromagnetic fuel injector. However, Toyota rely on swirl as opposed to tumble, promoted by closing one port using a swirl control valve (SCV), so that flow is directed through the second port which is helical-shaped. The cavity in the piston acts as the combustion chamber. This system is represented schematically in figure 1.8.

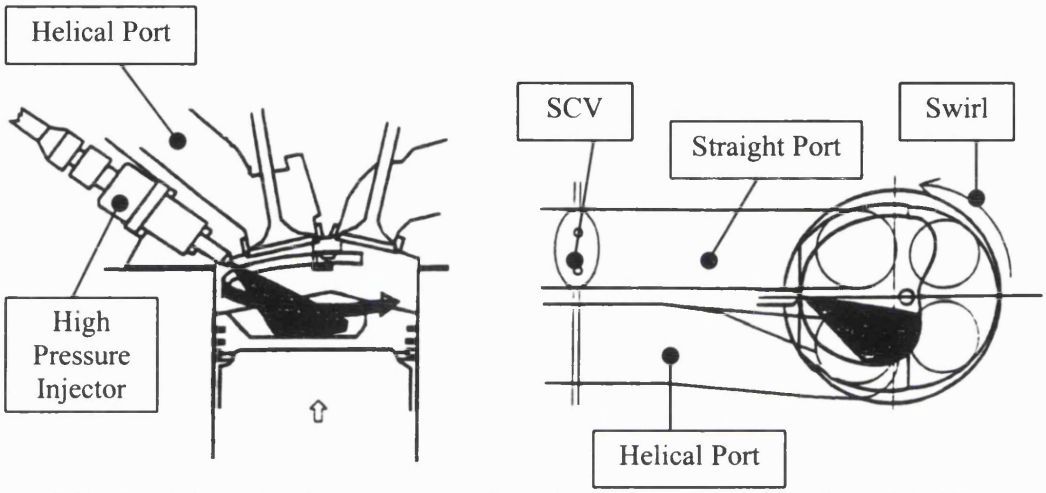

Figure 1.8 - Toyota's combustion chamber configuration [Adapted from Harada *et al*, 1997].

Toyota utilises a three-stage strategy to release the potential of the GDI concept. Late injection and early injection follow the same pattern as described with the Mitsubishi system. The Toyota engine can also operate with two-stage injection. In this mode, the fuel is injected during both intake and compression strokes. Toyota claim that this smoothes the transition between ultra-lean operation (stratified) and stoichiometric (homogeneous). The three modes are illustrated in figure 1.9.

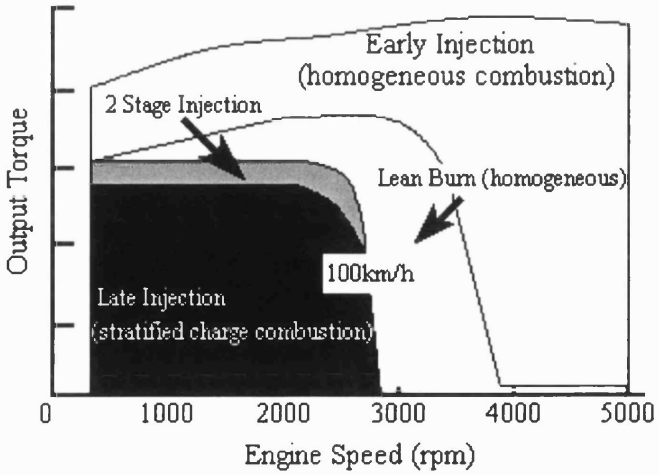

Figure 1.9 - Toyota's 3-mode combustion strategy [Adapted from Harada *et al*, 1997].

More recently, Toyota have developed a new approach based around a fan-shaped spray formed by a slit nozzle [Koike *et al*, 2000]. The fan-spray and a shell-shaped piston cavity produce a stratified mixture, but a distinct air motion such as tumble or swirl is not necessary although it may be desirable. This reduces packaging constraints and allows the inlet ports to be optimised for increased power. Toyota claim [Kanda *et al*, 2000] that this new combustion process (NCP) allows a wider range of stratified combustion operation and excellent homogeneous operation, without the need for a complicated inlet port. The NCP is shown in figure 1.10 along with a photograph of the fan-spray. The exit hole is very thin (0.16 mm) and arch-shaped, producing a highly atomised spray in the shape of a fan.

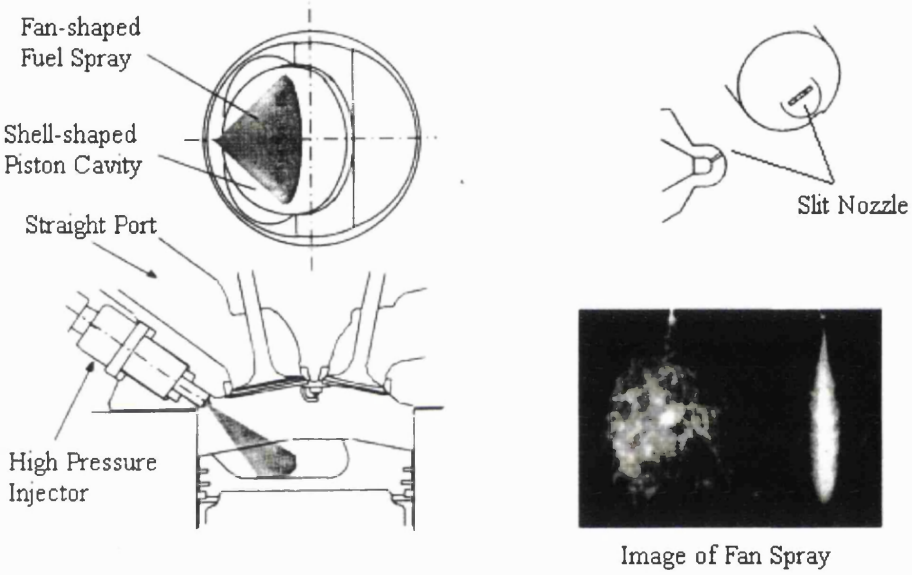

Figure 1.10 - Illustration of Toyota NCP system and image of fan spray (2 views: from the front and the side) [Kanda *et al*, 2000, Koike *et al*, 2000].

Yamaguchi (2000) describes the operation of this new system applied to a 3.0-litre six-cylinder production engine. The GDI engine is designated as the 2JZ-FSE, and is compared directly to the 2JZ-GE, a port-injection engine with the same cylinder dimensions. Quoted power and torque figures are identical, but the GDI version produces the peak figures at lower engine speeds, reducing engine wear and increasing passenger comfort. The compression ratio of the 2JZ-FSE is 11.3:1 compared to 10.5:1 for the PFI unit, which should bring a fuel conversion efficiency gain of nearly 3% according to Heywood [1988]. Toyota claim a 21% fuel-economy improvement over the Japanese urban cycle, due to the combination of advantages offered by the GDI system.

Toyota's first production GDI engine (with helical ports) operated as lean as 50:1 when in stratified-charge mode. However, there was a limited range of engine speeds and loads at which

this engine was capable of sustaining stratified-charge operation. The latest concept has improved on this by allowing stratified-charge operation to occur up to approximately 75 mph. The new 2JZ-FSE operates with air/fuel ratios between 20:1 and 40:1 for the lean-burn mode. The complicated helical ports required for the first engine are no longer needed. The new engine has two straight ports. One is fitted with the SCV as before. At light loads and low speeds this valve closes fully. This has the effect of increasing the flow rate through the other port and promoting axial swirl within the combustion chamber. At high engine speeds and loads, this valve is fully open. There is a weak stratified charge mode in between, which ensures a smooth transition between the two extremes.

AVL introduced a radical approach to GDI mixture preparation with their Direct Mixture Injection (DMI) concept [Fraidl *et al*, 1996]. The DMI concept utilises the advantages of air-assisted injection and pre-evaporation of the fuel without the need for an external pressurised air supply. Figure 1.11 illustrates the main components in the DMI injector.

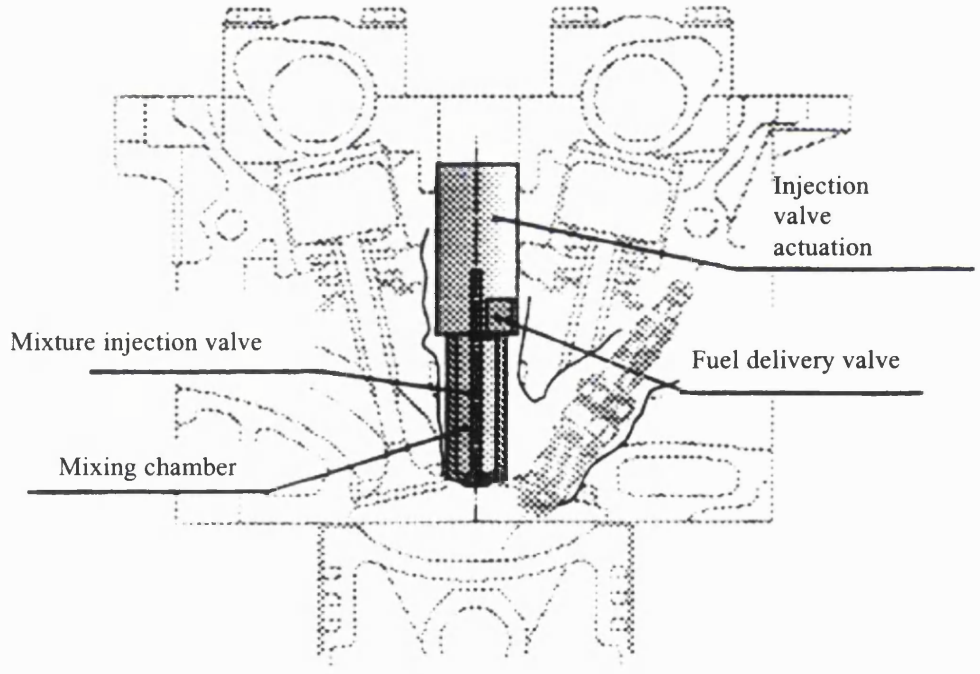

Figure 1.11 - AVL's DMI injector installed centrally [Adapted from Fraidl *et al*, 1996].

The DMI injector utilises charge from the preceding engine cycle to produce the mixture injection pressure. The DMI valve is opened when there is a greater pre-chamber pressure than combustion chamber pressure during the late part of the induction stroke and the early part of the compression stroke. The fuel-air mixture then flows into the combustion chamber until the pressures equalise. The flow is reversed as the combustion chamber pressure rises during the compression stroke. Pressurised gas flows back into the pre-chamber for use in the next cycle.

The DMI valve closes to avoid combustion in the pre-chamber. As soon as the valve is closed, fuel is injected into the pre-chamber to evaporate before the opening of the DMI valve. The timings of the engine cycle at part and full load are provided in figure 1.12.

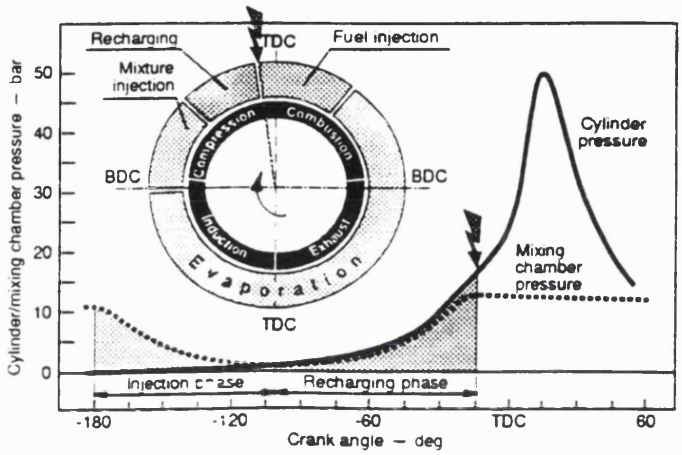

Full-load timing diagram

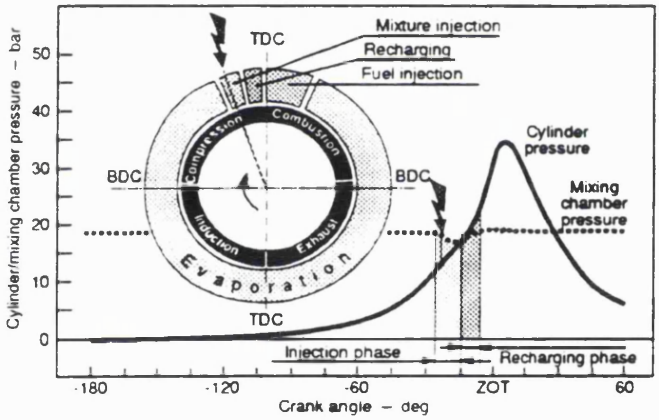

Part-load timing diagram

Figure 1.12 - AVL's DMI timing diagrams [Adapted from Fraidl *et al*, 1996].

Fraidl *et al* (1996) claim that unthrottled operation is possible with certain late injection timings. The fuel itself need only be injected into the pre-chamber at a pressure just above that of the chamber, because atomisation during the injection event is not required. The time available for evaporation is up to 20 times as long as is achieved with conventional GDI systems using a late injection strategy.

Mixture stratification is improved with the DMI system because the penetration velocities are significantly reduced. This is due to the relatively low-pressure difference driving the entering charge. The mixture enters with the fuel in its vapour form, which also serves to reduce the

penetration. The shape of the resultant spray can be tailored to suit an engine strategy by altering the valve and valve seat geometry.

The DMI engine runs in homogeneous mode at high speeds or under heavy loads. The pressure difference between the pre-chamber and the cylinder is increased in this mode, transforming the spray into a wide hollow cone, spreading the fuel-air mixture around the combustion chamber for homogeneous combustion. A high-velocity airflow field is not required which means that less complicated combustion chamber and inlet port designs are possible.

The DMI concept has not reached production to date, however, as there appear to be many disadvantages associated with the concept. Packaging the DMI injector in a four-valve combustion chamber will reduce the effective valve area, constricting the engine's breathing. This need for space also restricts the design of the camshaft spacing, etc. AVL claim that UHC emissions are reduced at idle by nearly 50% by the use of DMI, but do not mention cold-starts. It is thought that fuel could remain in the pre-chamber on engine turn-off, leading to increased UHC emissions when the engine is next started. It is also thought that there will be some loss of efficiency due to the extra pumping work required between the cylinder and the pre-chamber while running in the homogeneous mode. Finally, as with all engines operating with a lean mixture, suitable exhaust after-treatment has yet to be satisfactorily developed.

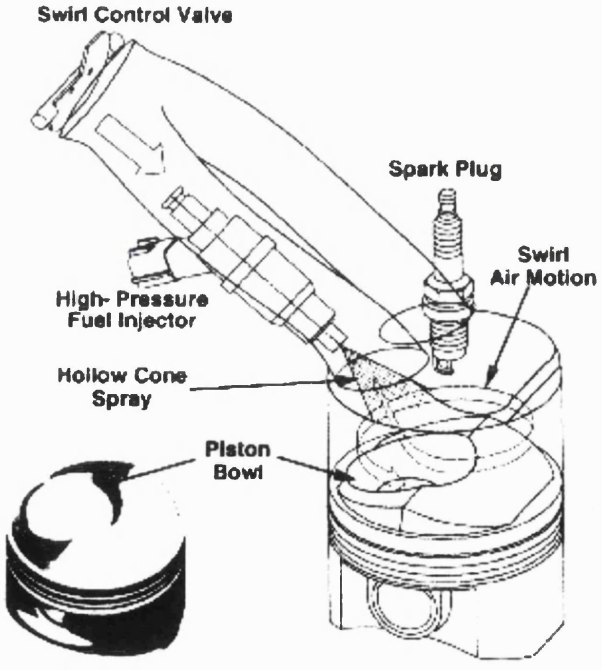

Figure 1.13 - Layout of Nissan's GDI system [Takagi *et al*, 1998].

Renault became the first European car manufacturer to offer a GDI engine on the market in 1999 [Jost, 2000]. Renault's aims were to reduce overall fuel consumption without increasing

the emission of harmful pollutants. A fuel economy improvement of 20% is claimed. A high EGR ratio is employed to produce fewer oxides of nitrogen (NOx) emissions. However, this engine does not operate with a stratified charge at any time and so the 20% improvement in fuel economy would seem to be rather optimistic, though the increased EGR would reduce the amount of throttling necessary.

Nissan also have produced a direct injection SI engine [Takagi *et al*, 1998]. Fuel consumption is claimed to have been reduced by more than 20%, with power output increased by 10% and a reduction in cold start UHC production of 30%. Nissan have achieved this by use of straight intake ports (increasing volumetric efficiency for high power) and a swirl control valve similar in concept to Toyota's GDI system. Nissan also employ a piston cavity to control the positioning of the charge. A schematic of this engine is shown in figure 1.13.

This layout enables the Nissan engine to operate with a homogeneous charge at high speed and heavy loads with a small loss in volumetric efficiency (due to the piston cavity). The swirl control valve and the piston cavity enable the engine to operate with a stratified charge at light loads, improving the fuel consumption by operating as lean as 40:1. Nissan do acknowledge, however, that the engine-out NOx and HC emissions are quite high, which will require more sophisticated after-treatment in the exhaust, or the addition of EGR to the engine. This engine would not be suitable for use with European gasoline which is high in sulphur content.

Iwamoto *et al* [1997] attribute the recent success of Mitsubishi's GDI engine in part to developments in the design of the electromagnetic swirl injector. Zhao *et al* [1997] state that the GDI injector may be the most critical component in determining the success of the GDI combustion system. The requirements for the GDI injector substantially exceed those of a normal PFI injector, and hence add to the cost of the overall system. Some of the criteria are:

- Increased level of fuel atomisation
- Expanded operating range
- Resistance to deposit formation
- Resilience to elevated cylinder temperatures and pressures
- Stable operation over a range of cylinder pressures

In summary, the injector should be capable of injecting an accurately measured fuel quantity in a highly atomised spray structure, which is stable and repeatable. According to Dodge [1996], the Sauter mean diameter (SMD) of the drop-size distributions should be approximately 15 μm

or smaller if the fuel is to have evaporated before sparking. The design of the injector itself plays a major part in determining droplet size, as does the fuel-line pressure.

With PFI engines, operation is possible with relatively low fuel pressures, as the spray is very often impacted on hot port and valve surfaces from where it evaporates. A GDI engine usually requires small droplets so that evaporation occurs before impaction, at least at some of the operating conditions. Mitsubishi's engine utilises a fuel pressure of 5.5 MPa, while Jackson *et al* [1996] describe a similar engine which operates within a range of 5 - 10 MPa. Lower fuel pressures are not likely to be possible due to a number of reasons. The first, and most significant, is the requirement for good fuel atomisation. Even if fine atomisation were possible at lower pressures, metering errors would occur due to the variation of metering pressure differential caused by rapid changes in cylinder pressure. However, it is not practical to have very high pressures either, as pump wear becomes a problem. Currently, some diesel fuel systems operate at pressures up to 200 MPa [Kimberley, 1999]. However, this is aided by the lubrication properties of diesel. Gasoline does not have this lubricity. Therefore a higher-pressure system will be, at best, more expensive to design and produce. At worst, impractical.

1.3 An investigation into the structure of GDI fuel sprays

It has become apparent that the success of the GDI engine depends heavily on the characteristics of the fuel spray. Modern tools have enabled the researcher to examine closely the structure of these sprays. This, in turn, leads to precise control of the spray position, direction and content. The contribution of the GDI fuel injector becomes more important as manufacturers strive to optimise the stratified-charge gasoline engine. In this section, previous work on fuel sprays for GDI engines will be reviewed in detail.

In the years since Mitsubishi launched their first GDI engine on the market, a significant amount of research has been carried out specifically on the spray of fuel from GDI injectors. This research can be divided into two categories: modelling and experimental work. The former requires the use of sophisticated software and a significant amount of experimental data before it may become an acceptable method of prediction. The latter requires more resources than a fully developed model, and yet it provides data that is required to develop a successful model. Different models have to be used for different designs of injector, each requiring experimental data. To date, there is no single fuel spray model that has the ability to characterise every fuel spray.

1.3.1 Modelling of fuel sprays

Models of varying complexity have been employed to try to predict fuel spray behaviour. The simplest models use single component fuels in their prediction of evaporation. This technique simplifies the calculations, but fails to predict the complex volatility characteristics of gasoline. Simpler models require information on droplet diameters and velocities exiting the injector nozzle. The nozzle geometry is rarely included.

Yamauchi *et al* [1998] employed these techniques to predict fuel spray development from a high-pressure swirl injector in a Subaru GDI research engine. The single-component fuel used was octane. The CFD software employed was KIVA, and the Discrete Droplet Model (DDM) was utilised. Han et al [1997] explained the basic idea of this modelling technique - illustrated in figure 1.14.

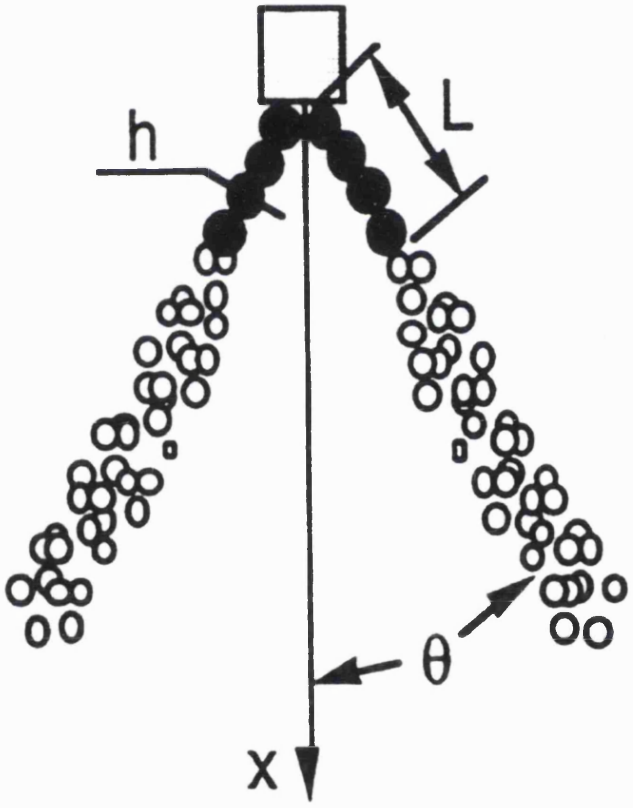

Figure 1.14 - Sheet disintegration according to the DDM technique [adapted from Han *et al*, 1997].

Instead of modelling the complex interior of the nozzle, it is assumed that the spray consists of a conical liquid sheet with a given length and thickness. The angle of the spray is determined by the injector geometry. The liquid sheet is not assumed to be intact however. It is divided up into discrete packets of droplets, each packet with a characteristic size. These packets are given a thickness equal to that of the sheet. The packets are assumed to experience negligible drag

force. Once beyond the break-up stage, these discrete packets must be divided up into actual droplets. Figure 1.15 illustrates the break-up of these parcels and the swirl angle assigned to them.

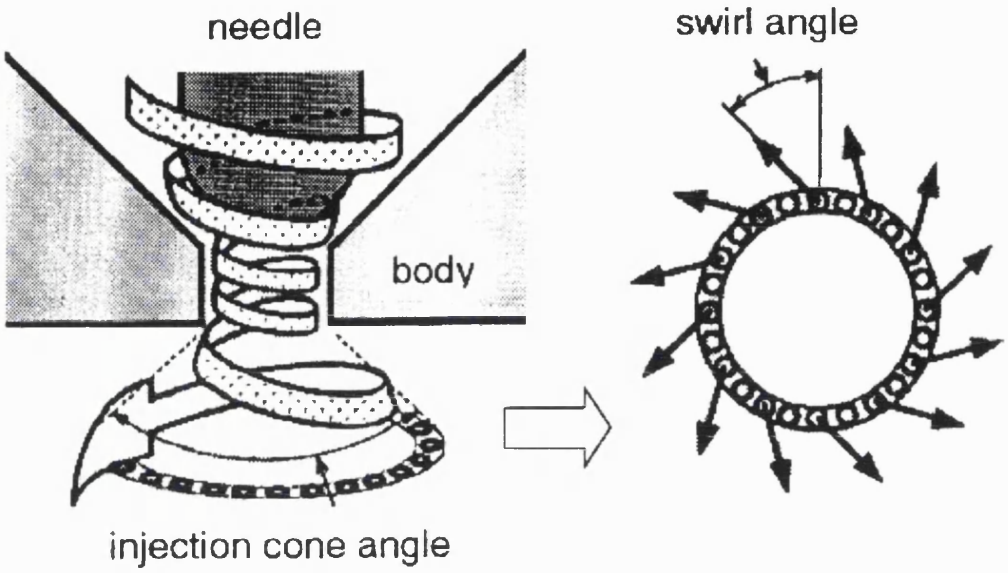

Figure 1.15 - Schematic of a high-pressure swirl nozzle outlet and the treatment of the injection of droplet parcels in calculation [Yamauchi *et al*, 1996].

To simplify the model further, Yamauchi *et al* assumed that the droplet parcels were injected at a position downstream of the injector nozzle, with a swirl velocity component. This simplification was made to eliminate the need for modelling the complex break-up of the liquid sheet after exiting the nozzle. The experimental data was taken from an engine using gasoline as its fuel. The calculated distribution of the droplet parcels at 0.8 ms after start of injection is shown in figure 1.16.

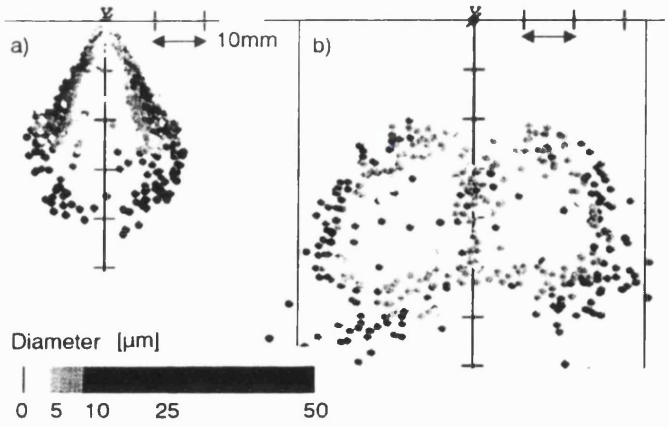

Figure 1.16 - Calculated droplet parcel distribution a) at 0.8 ms after start of injection, b) at 2.6 ms after start of injection [adapted from Yamauchi *et al*, 1998].

Other researchers to use this approach were Han *et al* [1997], Selim *et al* [1997], Suh *et al* [1999] and Fan *et al* [1999]. The advantage of this type of model is its relative simplicity. However, every nozzle will produce different droplet diameters and velocities, each requiring experimental data before the model can be run. In recent years, this technique has been refined with multi-component fuel models as the effects of the different boiling points of the various components in gasoline are now thought to be very significant in spray formation. Modelling the initial atomisation as the fuel exits the nozzle is another obvious area for modellers to address.

Ambient conditions play a significant part in the atomisation of multi-component fuels [Shelby *et al*, 1998]. Data input is similar to the single-component fuel model, but extra care must be taken with regards to the ambient temperatures and pressures. This adds complication to the model, but increases its prediction accuracy. Zeng *et al* [2000] approached the problem of modelling a multi-component fuel. The test fuel had four components. Its distillation curve was similar to that of a California Phase 2 gasoline, and consisted of 15% iso-pentane, 20% hexane, 45% iso-octane and 20% decane by mass. The disintegration of the liquid sheet of fuel exiting the injector was also modelled using the technique developed by Han *et al* [1997]. This new model took into account internal circulation within the droplets, leading to preferential vaporisation of the more volatile components and droplet surface regression due to vaporisation. Results for single and multi-component fuels were compared. It was found that the improved modelling of the fuel's volatility influences several important spray characteristics: penetration and global vaporisation being the most significant. Senda *et al* [1994 & 2000] also investigated multi-component fuels.

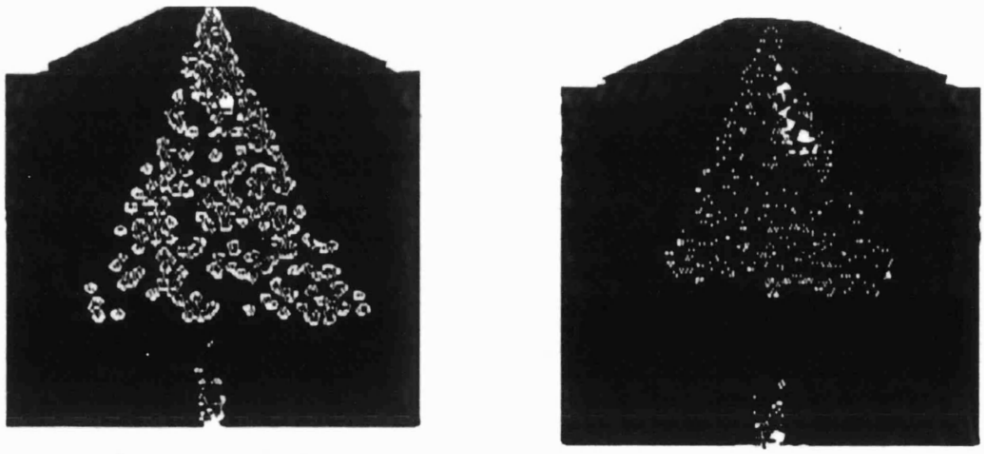

single component

multi-component

Figure 1.17 - Plot of equivalence ratio distribution (light intensity) and droplet position at 490° CA [Adapted from Zeng *et al*, 2000].

'Flash boiling' is a known phenomenon of multi-component fuel sprays [VanDerWege *et al*, 1998]. Flash boiling (or 'disruptive evaporation') is the phenomenon that occurs when the vapour pressure of one or more components of the fuel exceeds the local atmospheric pressure. It tends to cause a sudden disruption of the spray. Experiments have shown that this behaviour is only to be found when using a fuel containing high volatility components [VanDerWege *et al*, 2000]. It can be deduced that it should be a requirement for any comprehensive multi-component fuel model to have the ability to predict the changes in the spray structure due to these fuel volatility effects.

However, in recent years this phenomenon has not been included in model development, although quite early research suggests that it may be possible to simulate the effect of flash boiling. Brown *et al* [1962] were one of the first to acknowledge the effect of flash boiling on spray disintegration. Testing was carried out using sprays from water and Freon-11 jets to investigate the disruptive effects of flashing. Lienhard *et al* [1970] expanded on this work by developing expressions for spray break up due to flashing and aerodynamic forces. A distribution function for break-up length was predicted. As with Brown *et al*, gasoline was not used. Water and liquid nitrogen were used in free orifice jets. It was concluded that the break up was difficult to describe mathematically. For water, an equation was derived, but it depended on a random variable. The variability, in turn, depended on an equation derived from the histogram of experimental results. Due to the limitations of the authors' apparatus, break-up was almost impossible to predict with liquid nitrogen.

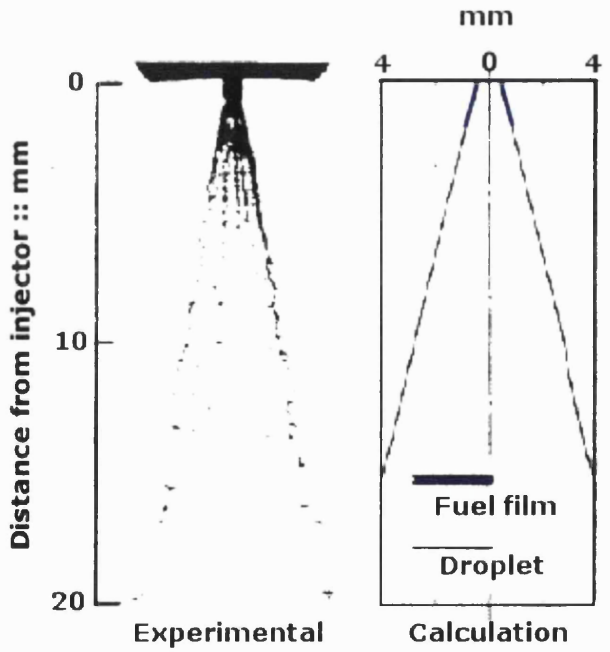

Figure 1.18 - Comparison between experimental and calculated spray shapes [Adapted from Senda *et al*, 1994].

A more detailed study was conducted by Oza *et al* [1983] based around the use of direct-injection into a constant volume vessel filled with nitrogen. Three fuels were used (propane, methanol and Indolene clear) and three different injectors (a modern electromagnetic injector with a needle valve, a pencil injector and a diesel injector with a poppet valve). Photographs were taken of the resultant sprays for subsequent analysis. Flash boiling was induced by heating the fuel and the injector bodies and reducing the atmospheric pressure. It was found that there are two distinct flash-boiling regimes: internal and external. Internal flashing occurs within the injector nozzle and causes liquid-sheet break up before the spray is formed. External flashing occurs after injection, and serves to shatter the initially intact liquid jet of fuel. This causes an increase in the spray-cone angle and a reduction in droplet size. However, at the high pressures demanded to produce a suitable pressure ratio (the ratio between fuel pressure and cylinder pressure) for acceptable atomisation, bubble growth may be retarded and disappear altogether.

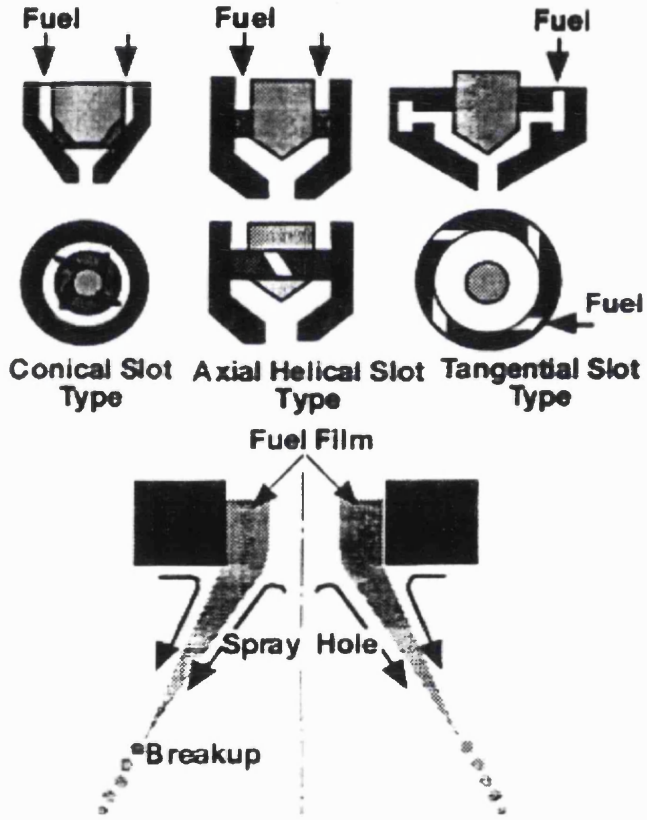

Figure 1.19 - The basic principle of the swirl nozzle [Iwamoto *et al*, 1997].

Senda *et al* [1994] attempted to model the atomisation process with a flash boiling spray and compared their results with experimental values. The engine under investigation had port fuel injection. With regards to spray shape and penetration, their predictions were accurate, but the estimation of characteristics of a flash boiling spray was dependent upon the experimental results to a certain degree. Figure 1.18 shows the difference between experimental and model results for injection, where the atmospheric pressure was 8 kPa and the fuel was n-Hexane. This

relatively low cylinder pressure is required to induce flash boiling in n-Hexane. This would not be the case within the cylinder of a GDI engine operating with gasoline.

Several researchers have extended their models to predict how fuel will leave the injector, given the nozzle geometry. These models utilise a fine mesh describing the injector nozzle shape and are capable of predicting the fuel droplet sizes and velocities on exit from the injector. To date, most of these models concentrate on the swirl-type nozzles, the basic principle of which is shown in figure 1.19.

Afzal *et al* [1999] investigated the effects of internal geometry on spray formation with multi-hole diesel injectors. The study consisted of an experiment with enlarged transparent models and a parallel Computational Fluid Dynamics (CFD) analysis. The fine mesh, built inside the nozzle geometry is shown in figure 1.20.

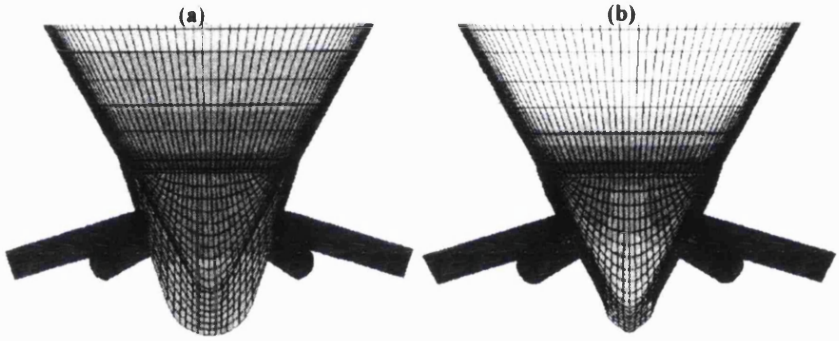

Figure 1.20 - Numerical grid for conical sac (a) and valve covering orifice (VCO) nozzles (b) [Adapted from Afzal *et al*, 1999].

The work mainly concentrated on predicting when cavitation would be present as this has a great effect on the final form of the spray. The findings were that there are two identifiable types of cavitation: conventional hole cavitation and a vortex cavitation formed inside the sac volume. The latter was found to induce hole-to-hole variation. The predicted velocity flow field and turbulent kinetic energy distributions inside the injection hole are illustrated in figure 1.21.

Abo-Serie *et al* [2000] expanded on the work of Afzal *et al* [1999] by applying the theory specifically to GDI injector sprays. The model developed is a sophisticated one. It is based on a two-phase extension of the GFS CFD code. This allowed the tracking of liquid-gas surfaces using the volume of fluid (VOF) methodology. According to the published paper the model solves the full Navier-Stokes equations describing the motion of the moving fluids.

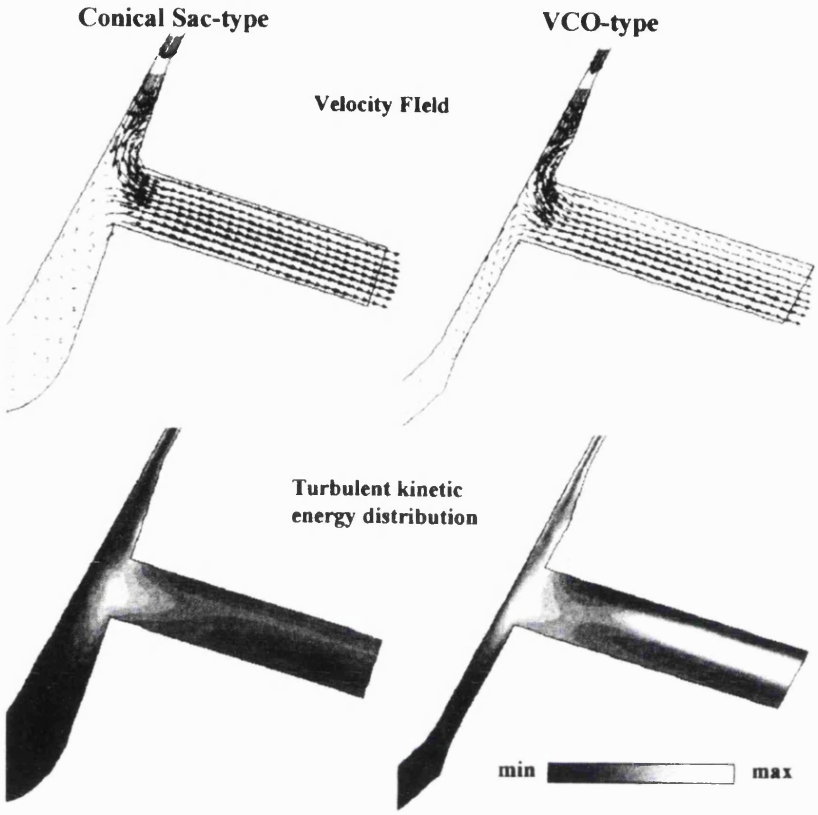

Figure 1.21 - Predicted velocity flow field and turbulent kinetic energy distributions inside the injection hole [Adapted from Afzal *et al*, 1999].

The first step of the calculation resulted in predictions for the behaviour of the pressure wave dynamics within the fuel system itself, with four injectors attached to a common-rail system. The computed results showed considerable fluctuations in the injection pressure. The formation of a liquid sheet within the injector nozzle was then predicted and this two-phase calculation was extended outside the nozzle in order to determine the spray cone angle. The latter was calculated as a function of the swirling motion and the geometry of the nozzle. The authors state that the predictions from the model are to be compared with experimental values in a future study.

It is obvious that a good working model would decrease the development time of a GDI engine. For instance, Miyajima *et al* [2000] developed a model to predict the spray shape from a newly designed nozzle. The model was not a complicated one. CFD using the finite volume method was employed, with an unstructured mesh. The fuel velocity was the inlet condition and the outlet condition was that the fuel velocity and fuel pressure gradients were set to zero. As can be seen in figure 1.22, the only internal geometry modelled was the cross-section of the outlet. The type of fuel modelled was not stated, but in the accompanying experiment, a low aromatic white spirit was used as the fuel. The modelling approach enabled predictions to be made of changes

in the spray resulting from alterations to the nozzle design, without the need for any further experimentation. However, it is likely that experimental work will always be required, if only to validate new models.

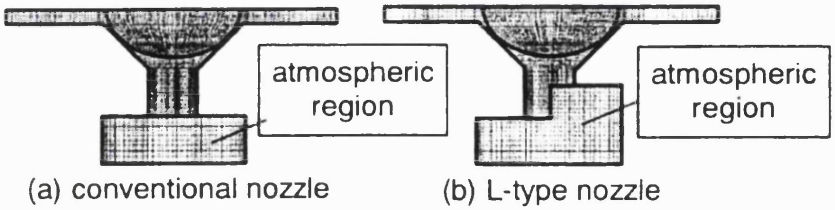

Figure 1.22 - Computational mesh used by Miyajima *et al* [2000].

1.3.2 Fuel spray experiments

Experimental work on GDI fuel sprays has been performed extensively over the past decade. Some fundamental work has been carried out using test rigs rather than firing engines. This is simpler from the experimental point of view, and it also helps building up an understanding by concentrating on certain aspects. In a laboratory, ideal conditions are produced so that fuel injectors may be tested without the complications of real-engine conditions. This type of testing allows an understanding to be obtained of the relative effects of fuel pressure, ambient conditions, fuel volatility, etc. The complexity of rig experiments has increased as researchers strive to gain more understanding.

Experimental work can be divided into qualitative and quantitative measurements. Visualisation techniques are used in qualitative work, such as Mie-scattering or Laser Induced Fluorescence (LIF), where the results are in the form of images. Mie-scattering reveals the pattern of the liquid fuel spray, while the application of LIF extends the visualisation to cover fuel vapour. In principle, LIF can be calibrated to indicate actual air-fuel ratios, but its sensitivity to temperature and quenching effects means that any quantitative data has to be treated with great caution. The development of an engine is aided by optimising injector spray characteristics, such as penetration rate and spray angle. Quantitative experiments, such as Phase Doppler Anemometry (PDA) or Laser Diffraction, result in numerical data, which can be used as a guide to develop the engine further, or for the purposes of producing a CFD model. PDA gives measurements of droplet diameter and velocity, while laser diffraction is limited to the measurement of droplet size distribution. Laser diffraction is restricted to test rig applications, as it is virtually impossible to apply to the cylinder of a firing IC engine.

Investigations of fuel sprays began by spraying into quiescent air at ambient temperature and atmospheric pressure. These tests replicate the pressure inside a cylinder under early injection strategies, when the air pressure is close to atmospheric [Parrish *et al*, 1997]. The effects of fuel

pressure can be investigated in this way. In general, it is found that, as injection pressure is increased, the volume of fuel in the initial slug of fuel increases, as does the penetration. Figure 1.23 illustrates this. This slug at the start of injection does contain a high density of fuel, which is undesirable from the point of view of subsequent evaporation. However, it represents a very small proportion of the overall spray volume on a well-designed injector.

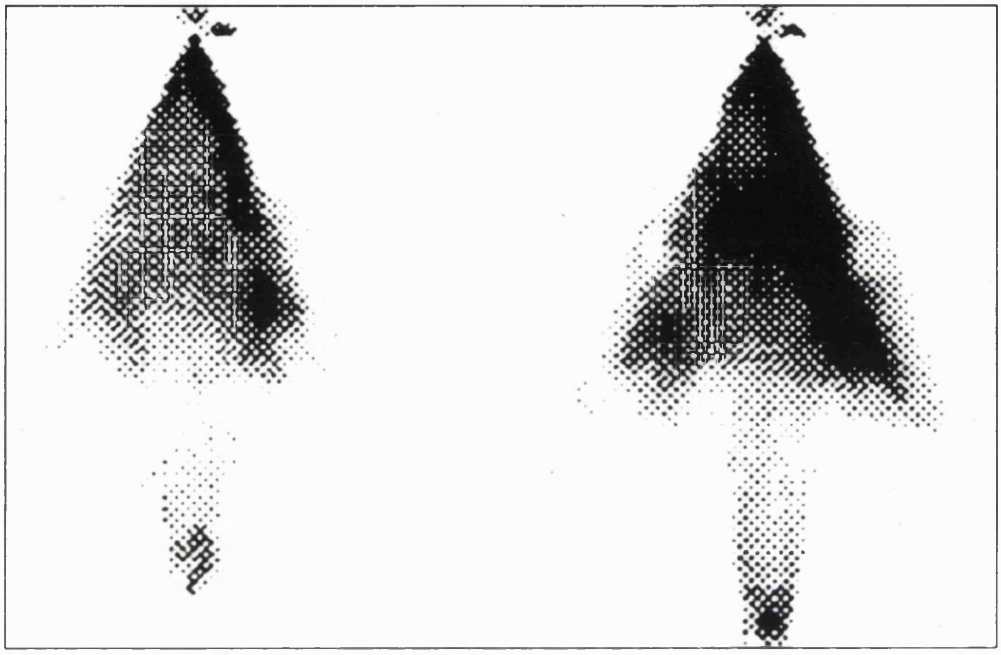

(a) (b)

Figure 1.23 - Illustration of slug growth with fuel pressure - (a) Fuel pressure 4.83 MPa. (b) Fuel pressure 6.21 MPa [Adapted from Parrish *et al*, 1997].

Atomisation improves at higher fuel pressures. Spray cone angle is found to be relatively independent of injection pressure, but the formation of counter-rotating vortices on the periphery of the leading edge of the spray is more prominent, and forms earlier with a higher fuel injection pressure [Arcoumanis *et al*, 1999, Shelby *et al*, 1998] as shown in figure 1.24.

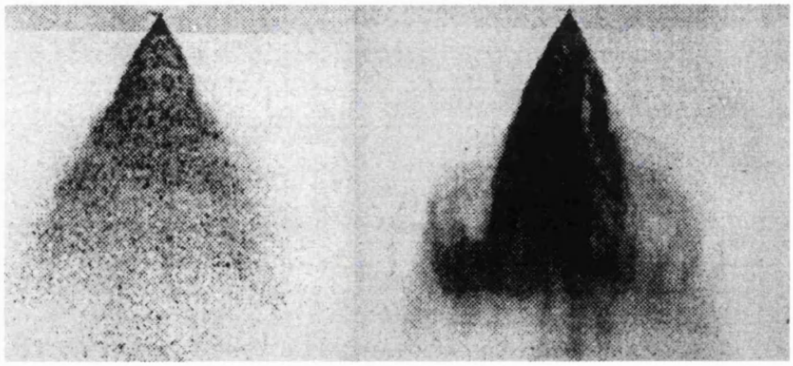

(a) (b)

Figure 1.24 - The formation of counter-rotating vortices increases with fuel pressure - (a) Fuel pressure 2 MPa. (b) Fuel pressure 10 MPa [Adapted from Arcoumanis *et al*, 1999].

Variations in ambient conditions are found to have considerable influence on spray characteristics. Naitoh *et al* [1996] found that both the initial spray cone angle and the spray penetration decrease with an increase in the ambient pressure. These changes are evident in figure 1.25. The mean droplet size was also found to increase with an increase in ambient pressure. Changing the ambient pressure is achieved by using a pressure chamber or a vessel into which the injector sprays [Meyer *et al*, 1997]. The pressure may then be increased with an inert gas or decreased using a vacuum pump [Miyajima *et al*, 2000].

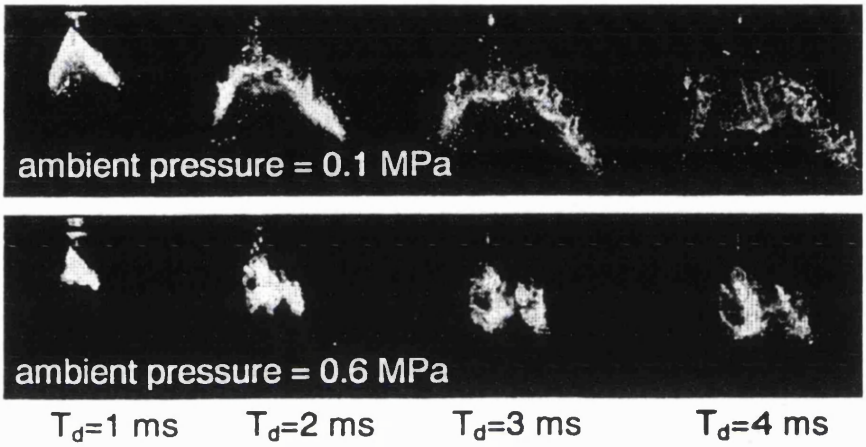

Figure 1.25 - Penetration reduces with an increase in ambient pressure [Adapted from Miyajima *et al*, 2000].

Single-component fuels are often used [Pontoppidan *et al*, 1997] instead of gasoline. The more common are hexane, heptane and iso-octane. These three have thermophysical properties similar to gasoline, such as the dynamic viscosity, density, thermal conductivity and surface tension [Fardad *et al*, 1999]. Recently, the effects of the temperature of the injector body and the fuel have also been investigated with the aim of understanding the volatility effects of multi-component fuels [VanDerWege *et al*, 1998]. The major difference between rig tests and engine tests is that rig tests do not replicate the interaction between the fuel spray and the airflow within an engine's cylinder [Iwamoto *et al*, 1997].

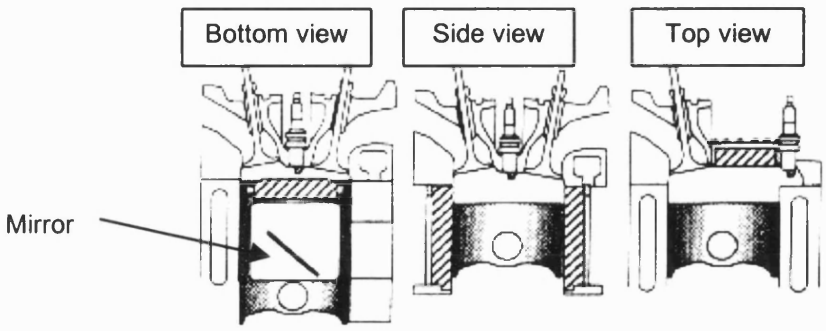

Figure 1.26 - The three conventional types of optical engine [Adapted from Kano *et al*, 1998].

The next logical stage of complexity is testing with a firing engine. The same experiments may be carried out as with rig tests if an optical engine is used. There are three types of optical engine generally used: bottom view, side view, and top view [Kano *et al*, 1998]. These are illustrated in figure 1.26.

In the bottom view method both the piston and the engine block are extended. This is to accommodate a mirror in the piston angled at 45°, which enables the combustion chamber to be observed in association with a transparent piston crown and a source of illumination. Bowditch [1961] devised this system so that no modifications are required of the combustion chamber. Unfortunately, the increased use of bowl-cavity pistons in GDI engines restricts the application of this method. The side view method relies on either a transparent (usually quartz or sapphire) cylinder or a cylindrical window flush with the cylinder. The latter is claimed to be easier to seal and is less complicated to manufacture [Davy, 2000]. The top view method requires an observation window in the top of the combustion chamber. This is rarely used on current research engines, as most modern engines have a four-valve pent-roof configuration.

With all of the above, the usual practice is to introduce illumination to the combustion chamber and to record the images for subsequent analysis. Mie-scattering and LIF are the techniques usually employed. In this way, each of the experiments performed in the rig tests can be carried out, with the added effect of the airflow within the cylinder, to build an accurate picture/model of the changes within a GDI fuel spray, and the factors that affect those changes. The main parameters under investigation to date are:

- Fuel pressure
- Fuel volatility
- Fuel temperature
- Ambient pressure
- Bulk air motion

The spray characteristics being examined are generally:

- Droplet size
- Spray angle
- Penetration

To date, not many researchers have examined all of these factors. As it is relatively easy to vary the fuel injection pressure, this has been thoroughly investigated, both qualitatively and quantitatively. Images of a GDI spray do not appear significantly different in shape with a change in fuel pressure [Moriyoshi *et al*, 1998], but reducing the fuel pressure has an adverse effect on the atomisation of the spray. This means that the droplets will be larger, leading to

slower atomisation within an engine. This, in turn, is likely to lead to higher emissions of pollutants, a higher coefficient of variation of IMEP and lower power output, as indicated in figure 1.27. Slower evaporation also reduces the range of injection timing available to an engine designer. In general, penetration is increased at higher fuel pressures [Miyajima *et al*, 2000].

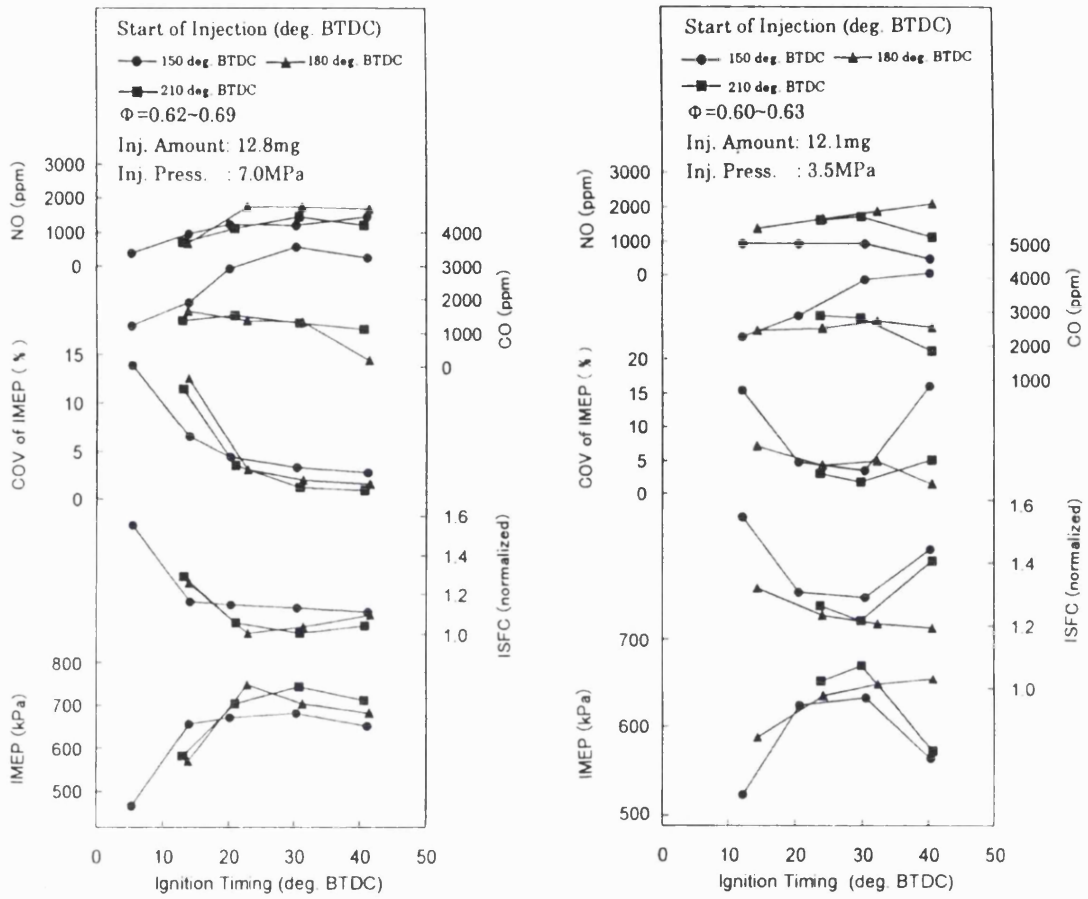

Figure 1.27 - Comparison of emissions and power output at different fuel injection pressures [Adapted from Moriyoshi *et al*, 1998].

Fuel volatility was not considered a significant factor in gasoline direct injection spray research until recently [VanDerWege *et al*, 1998]. Using planar laser-induced fluorescence (PLIF), VanDerWege *et al* [2000] investigated the effects of fuel volatility and operating conditions on fuel sprays. As mentioned earlier, flash boiling of the lighter fractions of the fuel disrupts the fuel spray. If evaporation in the core of the spray is fast enough then the overall spray width reduces, due to the production of a vapour core along the axis of the spray, caused by an increase in fuel temperature and a decrease in ambient density. This phenomenon is shown in figure 1.28, where the bottom row of pictures illustrates how the spray changes from its normal form (top row) when flash boiling is present.

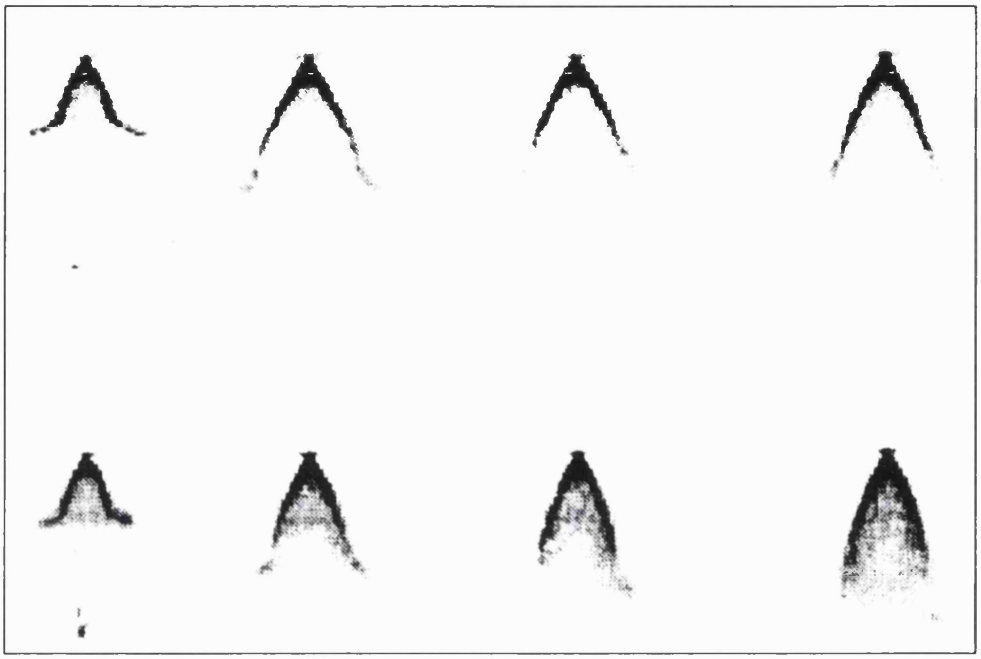

Figure 1.28 - VanDerWege *et al* [2000] illustrated the effects of evaporation in the core of the spray.

The flash boiling also affected the penetration of the spray. Higher volatility components of the fuel were found to penetrate faster (surprisingly). It is thought that this was due to the rapid evaporation of the light ends, which then become entrained towards the centre of the spray and followed the air motion created by the initial slug of fuel. The flash boiling (caused by volatility effects) also served to reduce the size of the fuel droplets, improving atomisation.

Davy *et al* [2000] investigated the effects of flash boiling on mixture formation as well as the change in spray structure at different temperatures. At low temperatures, the spray appeared to be a hollow cone. As the fuel temperature was increased, the spray became filled and eventually the angle of the spray reduced. It was also noted that at the lower temperatures, individual fuel droplets were visible, but the spray appeared more 'misty' with elevated temperatures. This suggested a reduction in the size of the fuel droplets. A comparison was made between gasoline (multi-component) and two other fuels (iso-octane and a blend of pentane, iso-octane and n-nonane) to assess the effect. The single-component fuel did not undergo these changes, which were attributed to flash boiling. It was therefore assumed that the rapid evaporation of the light ends of gasoline was responsible for the onset of flash boiling.

The ambient pressure into which the injection of fuel is occurring has a significant effect on the resultant spray. Drag force acting on the fuel increases as the density of the air increases. The spray narrows as the ambient pressure increases, forming a more solid cone [Shelby *et al*, 1998]. Conversely, a decreased pressure (i.e. below ambient) opens up the spray. Penetration is

increased with a reduced ambient pressure due to the reduced drag between the air and the droplets.

Several researchers have investigated the effects of bulk air motion on fuel spray formation. The usual method is to motor an engine without spark, but with the fuel injector spraying and then to use Laser Doppler Velocimetry (LDV) to measure the in-cylinder velocities. It is generally observed that the shape of the fuel spray is significantly distorted by the intake airflow. This effect becomes more pronounced with increasing engine speed [Stanglmaier *et al*, 1998]. Other researchers on this subject include Himes *et al* [1999] and Moriyoshi *et al* [1998].

Himes *et al* made velocity measurements in a motored engine in the vicinity of the fuel spray. To simplify the test the spray was not present. Three operating conditions were investigated: low load and speed, medium load and speed and high load with a medium speed. The swirl motion was found to change direction from anti-clockwise during the low load case to clockwise under high load. It was also shown that the air motion in the cylinder would cause a movement of the spray towards the region between the intake valves.

Moriyoshi *et al* evaluated a GDI system with enhanced air motion. Combining a strong swirl flow with a cavity in the piston created the enhanced motion. A complicated inlet design was utilised to create the swirling motion. One inlet port was helical and the other straight, but incorporating a swirl control valve (SCV). It was found that the fuel would be conserved at the centre of the swirling motion (in the piston cavity), but nearing TDC the combination of swirl and squish carries the rich mixture toward the spark plug. Stable combustion was achieved and it was stated that engine load control was easier than other GDI systems as it was proportional to the amount of fuel injected. However, oxides of nitrogen pollution were worse than other lean burn systems. This was claimed to be due to the charge stratification, extending to almost stoichiometric in the combustion chamber. At the high load case, the increased swirl intensity was detrimental to the engine performance. This can be offset by strict control of the swirl.

1.4 The way forward

It is apparent that the GDI engine offers many advantages, but not all of them have yet been fully realised. The crux of the total success of this type of engine is the fuel spray and its interaction with an appropriate air motion within the cylinder. Researchers are making progress towards developing modelling tools that will allow GDI engines to reach their full potential. The review of the literature has suggested that all of the following features will have to be modelled if accurate predictions are to be obtained of a GDI spray:

- The internal geometry of the injector - particularly how it affects cavitation,
- The initial fuel slug - particularly how it influences subsequent air motion in the centre of the spray,
- The atomisation processes as the fuel leaves the injector,
- The evaporation characteristics of realistic multi-component fuels,
- The prediction of whether or not flash boiling will occur and, if it does, what its effects will be,
- The prediction of realistic penetration rates that, in turn, are dependent on the adoption of suitable drag coefficients for the droplets combined with realistic modelling of the air motion surrounding the spray.

There is still much work to be performed before these requirements are met. It is apparent that there is relatively limited experimental data available which researchers can apply to help develop their models. Individual experimental investigations have tended to be restricted to one type of injector and a limited number of variables (e.g. effects of fuel and ambient pressures). It has not been clear which of the effects observed were dependent on the particular design of injector used and which were typical of swirl-type injectors in general. The first part of this thesis will be devoted to describing how a comprehensive set of experiments was performed with different types of injector, tested using a relatively large number of variables (fuel pressure, fuel temperature, ambient pressure and fuel type). It was hoped that these results would allow a better understanding to be developed of the influence of injector design and the effects of the variables and any interactions. The results are being utilised by the other two PhD in the group of three. One student is able to validate his spray models with the information, while the second student is finding the results useful to understand the modifying effects of airflow on fuel sprays that he observed in a firing engine.

The second part will address another important area, namely how changes in injector spray affect engine performance, particularly the emissions characteristics. The point being that improvements in spray modelling can only be fully effective if linked with a better understanding of how fuel preparation influences engine performance. An area of particular interest will be the influence of valve timing. Variable Valve Timing is being used quite widely on PFI engines and some of the benefits are applicable to GDI engines too. However, complex interactions occur between GDI fuel sprays and air flows at different inlet valve timings and a greater understanding is required of their effects. The results obtained by the PhD student working with the optical version of the engine will be used to explain some of the results.

The work is based on a GDI cylinder head designed to produce a homogeneous charge (as opposed to stratified charge). The cylinder head was chosen for reasons of availability. It was versatile in that it could accommodate a GDI injector in either a central or a side-mounted position.

Chapter 2

GDI FUEL INJECTOR SPRAY CHARACTERISTICS

2 - GDI fuel injector spray characteristics

2.1 Introduction

The purpose of the testing described in this chapter was to provide more comprehensive data than hitherto available in the literature on the differences in sprays between four types of swirl-type injectors designed for use in direct injection gasoline engines. The injectors were to be tested over a wide range of variables on a test rig to simulate as far as possible the conditions experienced on a running engine. The test results were to benefit the three students working on the GDI engine project in the following ways:

(i) Provision of penetration rates, droplet sizes and spray angles for the student working with CFD programs to validate his models.

(ii) Provision of images for the student working with the optical engine to compare his results with those obtained in quiescent air on a test rig. The comparison was to give insights as to the influence of airflows on spray formation and dispersion.

(iii) Provision of data for the author to help him understand the emissions results that he subsequently obtained on the Hydra test bed engine.

2.2 Description of test equipment

2.2.1 Spray imaging

The first part of the testing centred on photography of the fuel sprays using a high-speed drum camera. A copper-vapour laser provided the required illumination. The basic layout of the test rig is illustrated in figure 2.1. Note that to produce a relatively thin light sheet (less than 2.0 mm thick), the laser beam was first passed through an Oxford Lasers designed light-sheet box, which contained a series of optical lens and mirrors. A copper-vapour laser was used as it provided the combination of high-energy pulses (up to 2.0 mJ), short pulse duration (10-30 ns), and a rapid repetition rate.

The laser frequency was set at 10 kHz for the duration of the testing, resulting in photographs of the fuel spray 0.1 ms apart. The pulsewidth of injection was set at 4 ms, enabling the drum camera to capture a complete pulse on one 1.0 m length of film while operating at a rotational speed of approximately 180 rev/second. The camera shutter was set to open for the duration of injection, but the film was only exposed while the laser was pulsing, resulting in two pictures per frame (frame size: 35 mm). The orientation of the light sheet was altered according to requirements.

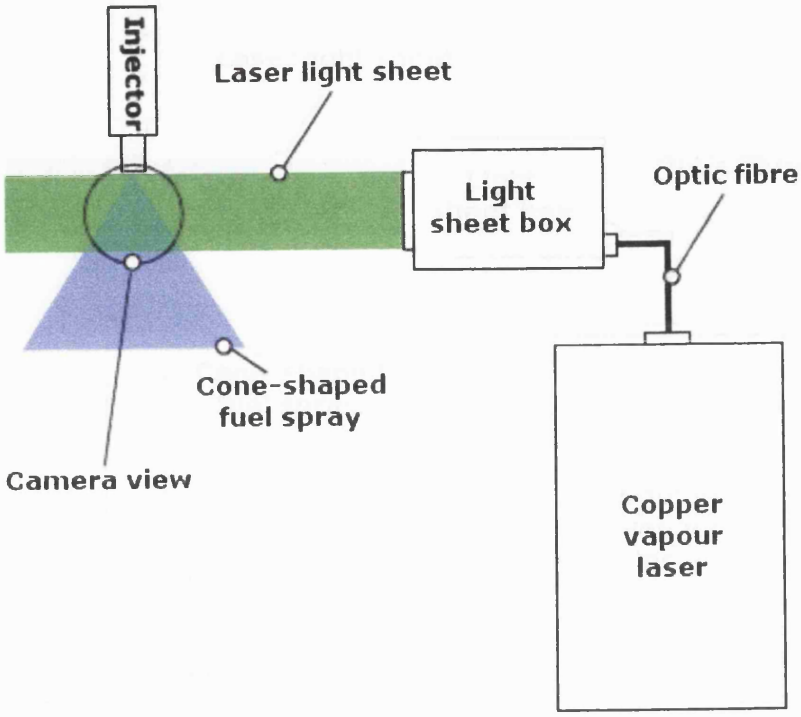

Figure 2.1 - Schematic of test rig for spray imaging.

2.2.2 Particle sizing

A Malvern 2600 series particle sizer was employed to measure the size of the fuel droplets. This instrument is based on a class 3a Helium-Neon laser, fitted with a beam expander to produce a 9 mm diameter beam. When the beam encounters a spray of small drops, light is diffracted according to Fraunhofer Diffraction Theory. The diffracted light is collected and focussed by a Fourier-Transform lens onto a series of 31 half-annular light-sensitive rings. Thus, the pattern of diffracted light is recorded, and subsequently transformed by mathematical analysis into a droplet size distribution. The software calculates a series of mean diameters, the most relevant one for this investigation being Sauter Mean Diameter.

Data was collected over a number of consecutive spray sequences, the readings being recorded at the same point in each spray sequence by the use of the Malvern Spray Synchroniser. The sampling time for each reading was approximately 10 μs. Readings were taken over 100 spray pulses. The experience of Williams [1994] was that more representative results are obtained by averaging over this number of pulses.

The Malvern Spray Synchroniser, in series with the injector's drive circuit, controlled pulsing of the injector in this instance. An extraction system for the fuel vapour was employed throughout the testing. A schematic of the apparatus is provided in figure 2.2.

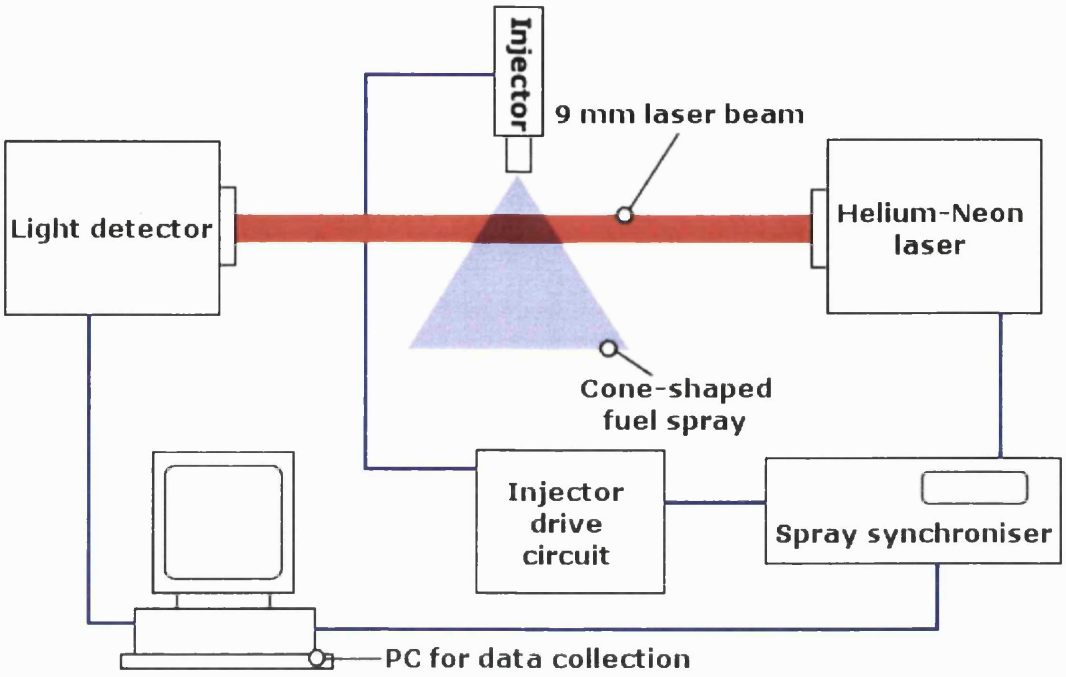

Figure 2.2 - Schematic of test rig for particle sizing.

2.2.3 The fuel injectors

In total, four different types of gasoline direct-injection (GDI) injectors were tested. The injectors most often considered for use in GDI engines are the high-pressure swirl variety. As the name suggests, the internal design of the injector sets up a swirling motion of the fuel spray on exit from the injector tip, as illustrated in figure 2.3.

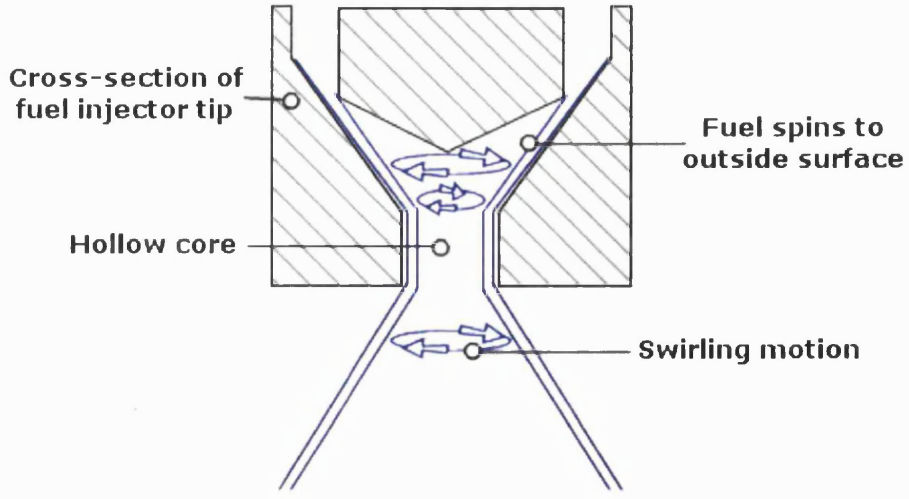

Figure 2.3 - A high-pressure swirl injector.

All injectors under test were of this description, but their characteristics varied as follows. Note that the L/D ratio represents the orifice length-to-diameter ratio in the summary tables.

Injector A

Injector A was a production unit taken from a current GDI engine. The Ford Motor Company supplied the injector and drive circuit for the test injector. The injector was of relatively early design and therefore utilised a relatively low fuel pressure (55 bar) in comparison to later designs. It was still described as a high-pressure swirl injector.

Nozzle type	Swirl device upstream of an open nozzle
Measured outlet diameter(*)	915 μm
Estimated L/D ratio for outlet orifice(**)	< 1
Manufacturer's nominal offset angle	None
Manufacturer's nominal fuel pressure	55 bar
Manufacturer's nominal spray cone angle	60 degrees
Manufacturer's nominal flow rate	Not known
Fuel pressure for testing	55 bar

Figure 2.4 - Summary of injector A properties.

* Measured by photographing the nozzle through a microscope lens at a known magnification.

** This is a best estimate, obtained from a combination of examination with a microscope, measurement and knowledge of the nozzle though other literature.

Injector B

Injector B differed from the others in that it sprayed at an angle (20°) to the injector's axis (figure 2.6). It too was classified as a high-pressure swirl injector. It was designed to be used with 120 bar fuel supply pressure. All necessary hardware for testing injector B was provided by Jaguar Cars.

Nozzle type	Swirl device upstream of an offset nozzle
Measured outlet diameter(**)	< 500 μm
Estimated L/D ratio for outlet orifice(**)	> 1
Manufacturer's nominal offset angle	20 degrees
Manufacturer's nominal fuel pressure	120 bar
Manufacturer's nominal spray cone angle	37 degrees
Manufacturer's nominal flow rate	11.0 cm^3/s
Fuel pressure for testing	120 bar

Figure 2.5 - Summary of injector B properties.

** This is a best estimate, obtained from a combination of examination with a microscope, measurement and knowledge of the nozzle though other literature.

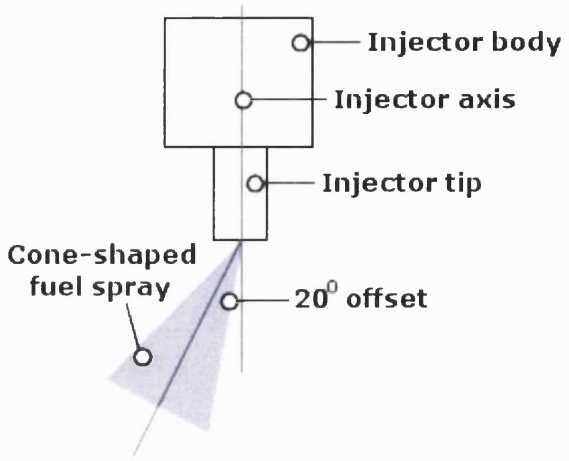

Figure 2.6 - The angle of injection for injector B.

Injector C

The nominal spray angle of injector C was 60°. The spray angle was the only major difference between injector C and injector D. Jaguar Cars supplied both injectors and their drive circuits. Its manufacturer suggested three possible operating fuel pressures for this injector: 20, 50 and 100 bar. Testing was conducted at both 20 and 100 bar. It is likely that the 20 bar pressure would only be used for starting and early running.

Nozzle type	**Swirl device upstream of an open nozzle**
Measured outlet diameter(*)	450 μm
Estimated L/D ratio for outlet orifice(*)	0.467
Manufacturer's nominal offset angle	None
Manufacturer's nominal fuel pressure	20, 50, 100 bar
Manufacturer's nominal spray cone angle	60 degrees
Manufacturer's nominal flow rate	12.5 cm^3/s
Fuel pressure for testing	20, 100 bar

Figure 2.7 - Summary of injector C properties.

* Measured by photographing the nozzle through a microscope lens at a known magnification.

Injector D

Injector D was of the same basic design from the same manufacturer as injector C, but differed in that its spray angle was 90° as opposed to 60°. Both injectors were described as high-pressure swirl injectors.

Nozzle type	Swirl device upstream of an open nozzle
Measured outlet diameter(**)	≈ 800 μm
Estimated L/D ratio for outlet orifice(**)	< 0.5
Manufacturer's nominal offset angle	None
Manufacturer's nominal fuel pressure	20, 50, 100 bar
Manufacturer's nominal spray cone angle	90 degrees
Manufacturer's nominal flow rate	12.5 cm^3/s
Fuel pressure for testing	20, 100 bar

Figure 2.8 - Summary of injector D properties.

** This is a best estimate, obtained from a combination of examination with a microscope, measurement and knowledge of the nozzle though other literature.

2.3 Discussion of results

2.3.1 Spray imaging

Fuel was injected into quiescent air for all tests. Most tests were performed with the injectors spraying into the open atmosphere, but some testing took place with the injector under test spraying into a partially evacuated chamber at a pressure of 0.5 bar absolute. A mounting block was designed with water passages such that it was possible to vary the temperature of the injector body over the range from ambient up to 80°C. Heating was applied by pumping hot water through the mounting block of the injector. A thermocouple was attached to the injector body to measure its temperature. Regular unleaded gasoline was used for the tests, with some tests repeated using iso-octane as a control fuel. The method of supplying fuel at pressure was that of using a combination of pneumatic and hydraulic cylinders. This was first applied on a previous project [Salters, 1996], and then re-designed by the author for this project to give the potential of higher delivery pressures (up to 150 bar). It should be noted that there was no additional heating of the fuel with this arrangement caused by the fuel being passed through an electrically-driven pump. Figure 2.9 shows a schematic diagram of this arrangement.

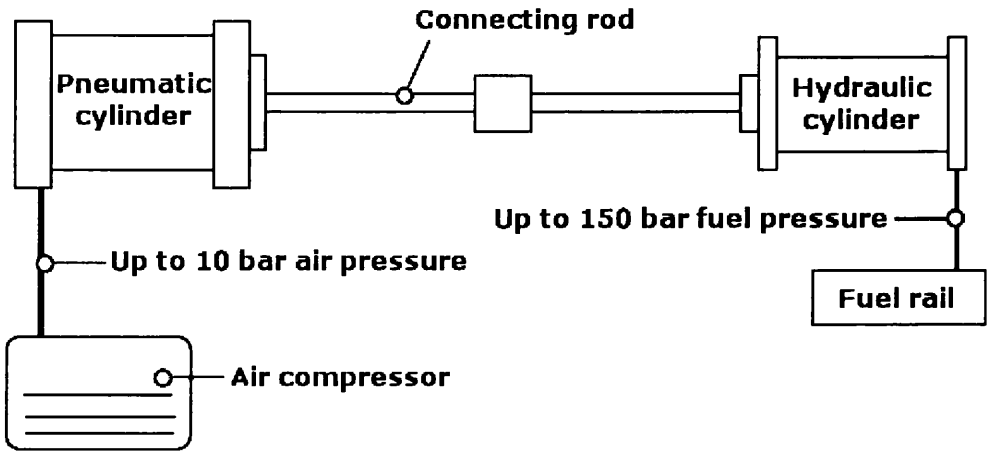

Figure 2.9 - Fuel system.

The orientation of the camera could be changed from the basic arrangement where the light sheet intercepted the spray parallel to the injector axis to obtain a side view (figure 2.1) or at right angles to it to obtain an end-on photograph. This is illustrated in figure 2.10. Note that the light sheet appears as a thin line in this plane. Additionally, it was at times necessary to mount the light sheet box underneath the injector, with the light sheet approaching the injector along its axis. This is illustrated in figure 2.17.

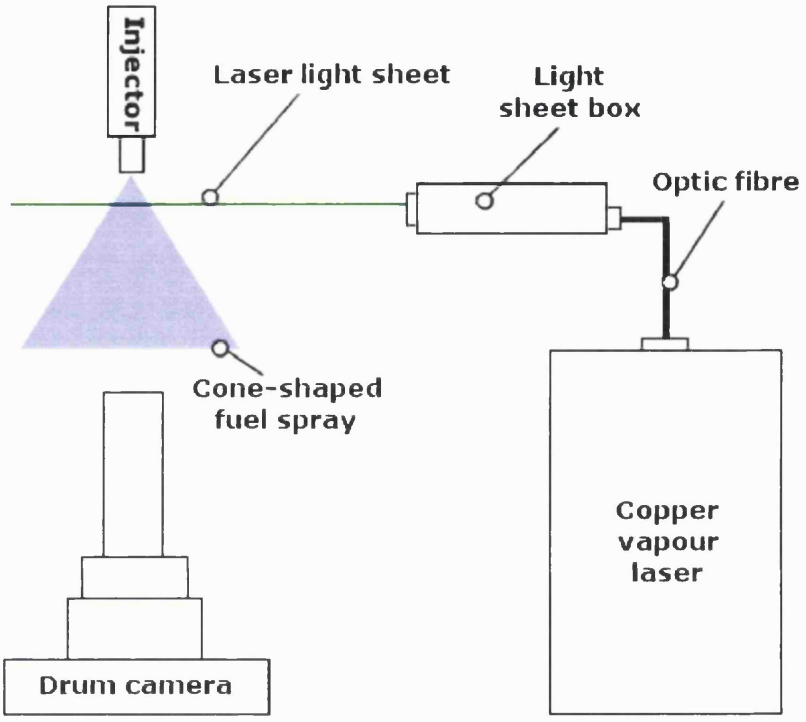

Figure 2.10 - Orientation of light sheet for end-on photographs.

The resolution of the high-speed photography was such that a detailed visual analysis of each picture was possible. The areas under investigation were:

- Cone structure: hollow or filled?
- Formation of curl-up vortices
- Penetration rates
- Cone spray angle
- Presence of swirling motion

These characteristics will be examined in turn for each injector in the following sections.

2.3.2 Cone structure: hollow or filled?

There has been discussion in published work [Zhao *et al*, 1997] as to whether or not it is possible to have a completely hollow cone structure. Figure 2.11 illustrates the initial formation of a hollow cone in a high-pressure swirl injector. Current understanding is that fuel emerges from the injector in

the form of a cone, which then breaks up into droplets at a short distance from the injector tip. There is a low-pressure area formed in the centre of the cone by the high-velocity spray as it entrains surrounding air. This will serve to suck inward droplets formed from the disintegrating surface of the conical sheet of fuel. The extent to which the cone will fill will be dependent on a number of factors including droplet size. The break-up of the spray may be enhanced if 'flash boiling' occurs. Flash boiling is the phenomenon that takes place when the vapour pressure of one or more components of the fuel exceeds the local atmospheric pressure, and it will tend to cause a sudden disruption of the spray.

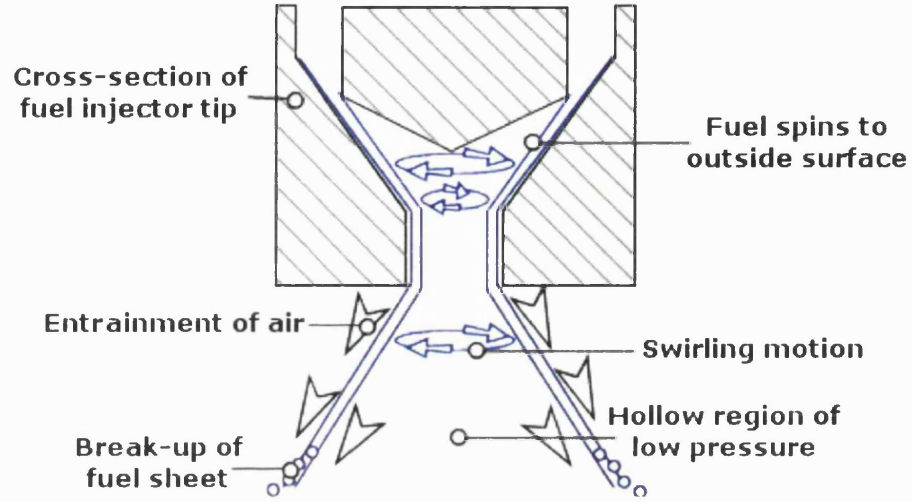

Figure 2.11 - Initial formation of the hollow cone.

In recently published work [VanDerWege, 2000a] the sprays from a high-pressure swirl injector designed for use in a GDI engine were found to change from a well-defined hollow cone to a filled-in cone with either an increase in temperature or a decrease in ambient pressure. This effect was found only to occur when using a fuel containing high volatility components. Each sequence of spray photographs was examined carefully to observe whether there were any signs of the occurrence of this phenomenon.

Appendix 1 contains a complete index of the photographs recorded. Frames of interest will be reproduced here for discussion. Note that an arrow is included to indicate the direction of approach of the light sheet.

Injector A

At ambient conditions the cone appeared to be densely filled with droplets (figure 2.12) rather than having a hollow structure.

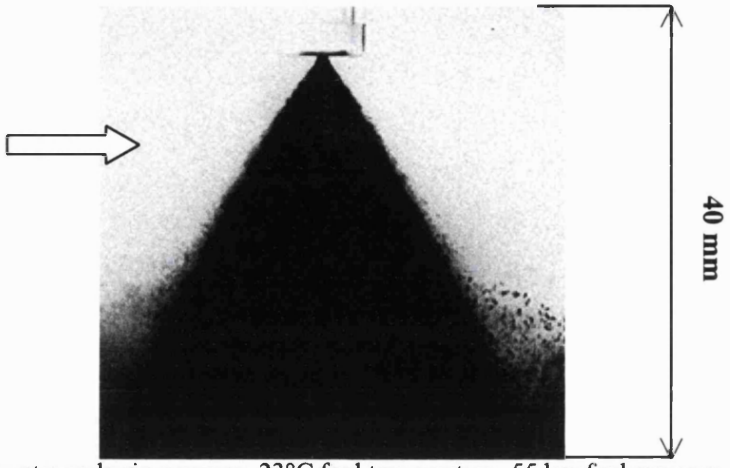

Figure 2.12 - Injector A: atmospheric pressure, 23°C fuel temperature, 55 bar fuel pressure, gasoline, 1.9 ms aSOI, figure A1.1 029.

However, this was not conclusive. It was inevitable that some light from the sheet was reflected and illuminated parts of the spray not cut by the original sheet. To investigate this further a microscope lens was used to magnify the spray. Figure 2.13 shows a section of this magnified spray. There appears to be a significant dense region on the edge of the cone, and it is believed that features of the spray structure apparent in the centre are mainly details on the outside of the spray illuminated by reflected light, suggesting that the core could be hollow after all.

Figure 2.13 - Injector A: atmospheric pressure, 23°C fuel temperature, 55 bar fuel pressure, gasoline, 1.6 ms aSOI, figure A1.1 062.

Further proof was found in the end-on view of the spray (figure 2.14). This shows the view when the camera was placed looking into the spray with the light sheet cutting the spray some 40 mm from the injector tip. A dense outer ring is visible with an apparently hollow ring inside. Although the outside ring appears to be incomplete, it is assumed to be a uniform ring. The width of the light sheet itself did not span the complete width of the spray, hence the loss of some detail. The fuel visible in the centre of the spray was probably formed from the 'slug' of fuel that issued from the injector at the start of the injection process, as apparent in Figure 2.14b. There is a tendency for the first fuel leaving the injector to travel along the axis of the injector, as the swirling motion that forms the cone takes some time to become established.

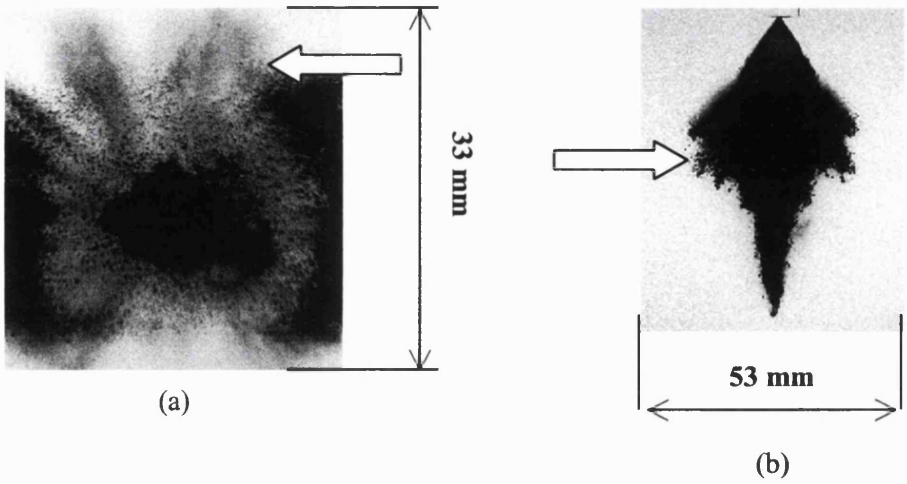

Figure 2.14 - Injector A: atmospheric pressure, 23°C fuel temperature, 55 bar fuel pressure, gasoline. (a) End-on photograph, 2.0 ms aSOI, 40 mm from injector tip, figure A1.1082. (b) Side photograph, 0.9 ms aSOI, figure A1.1024.

Injector B

At atmospheric pressure there did not appear to be a hollow cone present in the photographs taken from the side (figure 2.15a). Note that the side view has a 5 mm blank area. This is due to the need for a revised viewing arrangement to accommodate the 20° angle of the spray. The injector was mounted at 20° to the vertical so that the spray travelled axially along the cylinder, and a window was mounted in the injector holder to view the spray leaving the injector. This arrangement was used with the dummy cylinder for testing below atmospheric pressure, but also for atmospheric pressure testing. The 'anomaly' in the end-on spray view in figure 2.15b at the 9 o' clock position was thought to be a feature linked to the manufacture of the injector with a 20° inclination. The end-on view (figure 2.15b) was taken with the plane of illumination 44 mm away from the tip of the injector and supported the contention that the spray was filled.

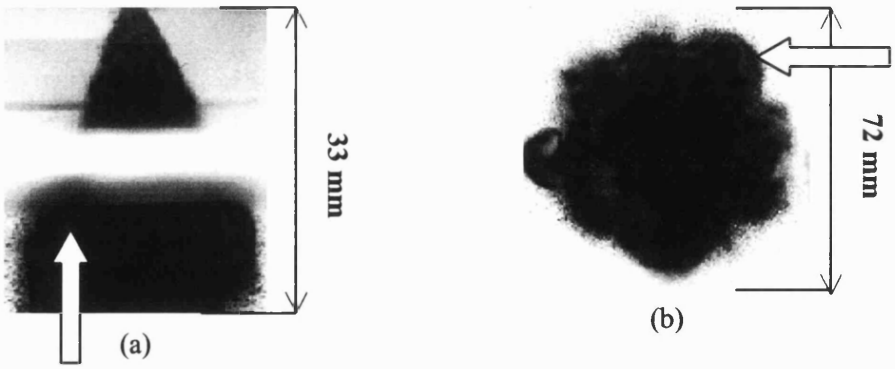

Figure 2.15 - Injector B: atmospheric pressure, 120 bar fuel pressure, gasoline. (a) Side view, 24°C fuel temperature, 0.7 ms aSOI, figure A1.2 004. (b) End-on view, 25°C fuel pressure, 1.6 ms aSOI, figure A1.2 042.

Injector C

The spray structure from injector C was seen to vary significantly with fuel pressure under atmospheric conditions. The cone appeared to be filled at all times under atmospheric conditions (figure 2.16). However, it is worth noting that the light sheet was obscured much earlier when injecting at the higher fuel pressure (100 bar). In this arrangement, the light sheet approached the spray along the axis of the injector as shown in figure 2.17. Comparing this diagram with figure 2.1, it is possible to see how the fuel may obscure the light sheet itself. This arrangement was necessary for some tests as a dummy cylinder was used to perform tests at reduced ambient pressure, and was retained for most testing as it reduced the amount of time taken to change configuration. At 100 bar injection pressure there is more fuel injected along the path of the light sheet for the same time after the start of injection, causing greater obscuration.

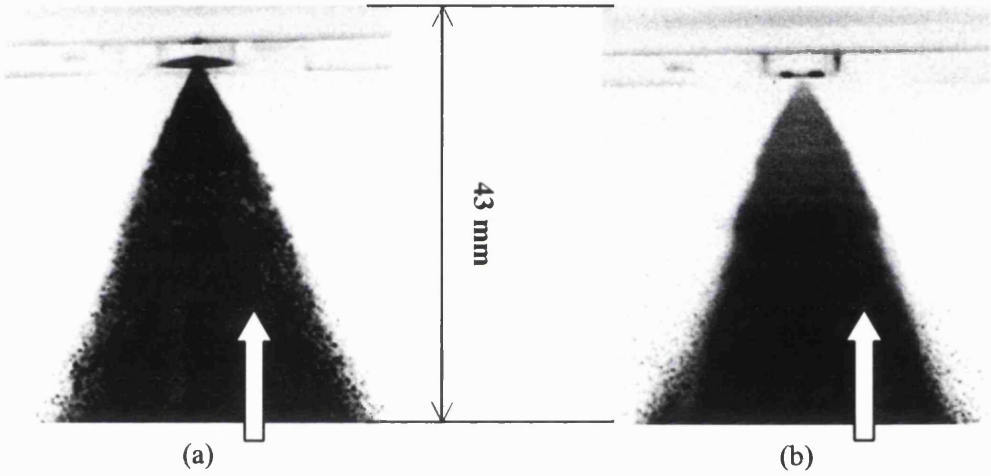

Figure 2.16 - Comparison of sprays from injector C at atmospheric pressure, 22°C fuel temperature. (a) 20 bar fuel pressure, gasoline, 2.5 ms aSOI, figure A1.3 049. (b) 100 bar fuel pressure, gasoline, 0.7 ms aSOI, figure A1.3 058.

A hollow cone structure was apparent when testing injector C at a cylinder pressure of 0.5 bar and a fuel pressure of 20 bar. Even when the injector was heated to 80°C (above the boiling point of some of gasoline's components) the cone still appeared to be hollow. Figure 2.18 illustrates the difference between injection at 20 and 100 bar under these conditions. The hollow cone structure is clearly apparent at 20 bar in figures 2.18a and 2.18c, but it is likely that the structure had changed to a filled cone at 100 bar in figures 2.18b and 2.18d. The relatively poor quality of the images is due to impaction on the window that had to be inserted in the test rig to reduce the pressure to 0.5 bar.

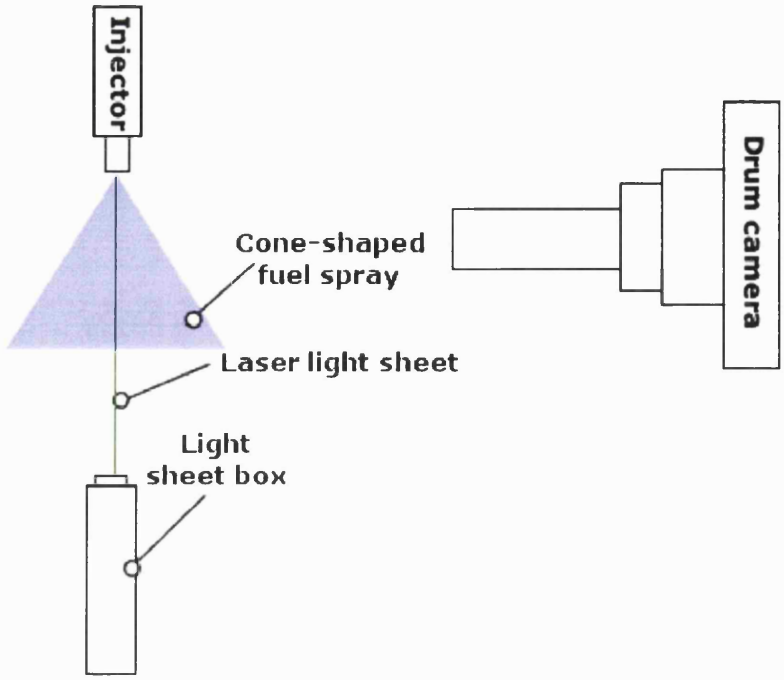

Figure 2.17 - Re-orientation of the light sheet.

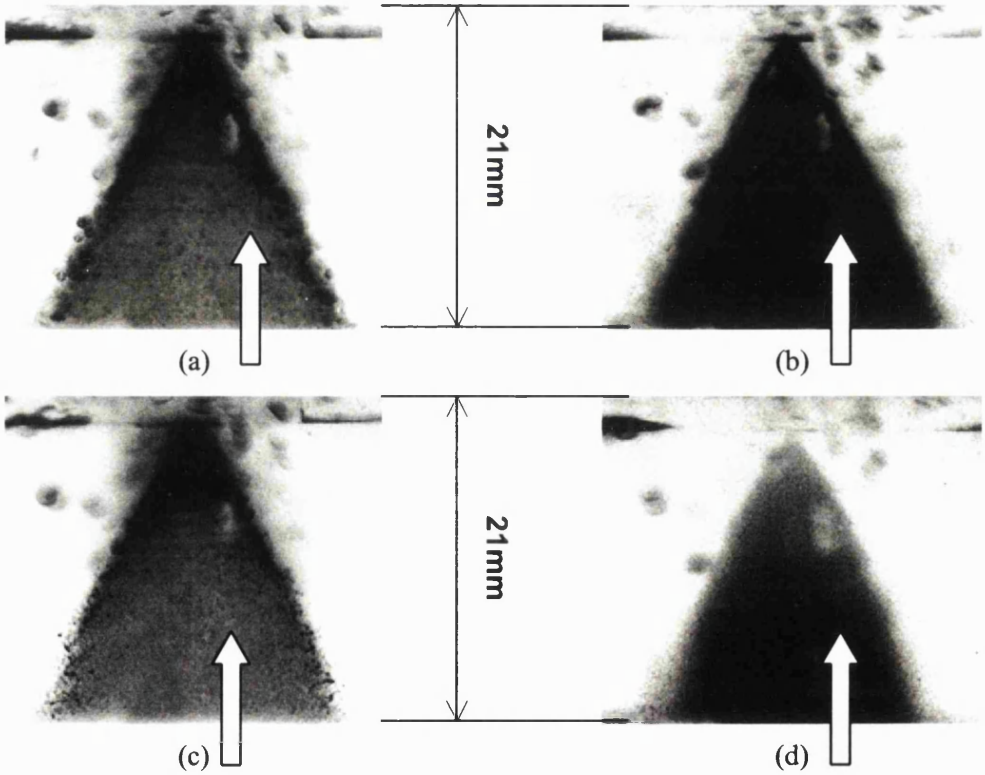

Figure 2.18 - Comparison of sprays at 0.5 bar cylinder pressure. (a) 23°C fuel temperature, 20 bar fuel pressure, gasoline, 2.2 ms aSOI, figure A1.3 120. (b) 23°C fuel temperature, 100 bar fuel pressure, 0.7 ms aSOI, figure A1.3 93. (c) 80°C fuel temperature, 20 bar fuel pressure, 1.9 ms aSOI, figure A1.3 135. (d) 80°C fuel temperature, 100 bar fuel pressure, 0.9 ms aSOI, figure A1.3 142.

Injector D

A hollow cone structure was apparent under certain conditions with injector D when spraying into atmospheric pressure. As with injector C the hollow cone was only visible at 20 bar fuel pressure. Figure 2.19 illustrates the difference between the sprays at ambient pressure and temperature.

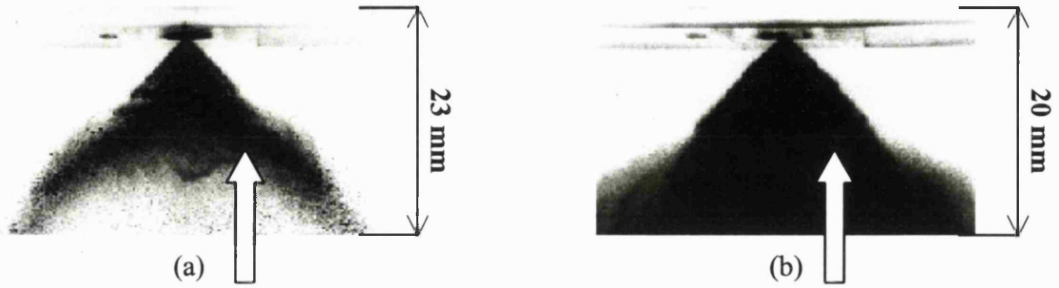

Figure 2.19 - Injector D: atmospheric pressure. (a) 25°C fuel temperature, 20 bar fuel pressure, gasoline, 1.1 ms aSOI, figure A1.4 058. (b) 21°C fuel temperature, 100 bar fuel pressure, gasoline, 1.1 ms aSOI, figure A1.4 076.

The same phenomenon was observed when injecting into a cylinder pressure of 0.5 bar. However, a relatively hollow cone was also present for testing at 100 bar fuel pressure when injecting at ambient temperature. Those results are displayed in figure 2.20. Note that the cone appears more hollow for the 20 bar case, and droplets appear larger and less 'misty'. There is some loss of definition, as with figure 2.18, due to the insertion of the viewing window for testing at reduced pressure. In figure 2.20 some of the fuel droplets appear larger than they are (especially in the 20 bar case). This indicates that they are out of focus. This was confirmed by close examination of the original film.

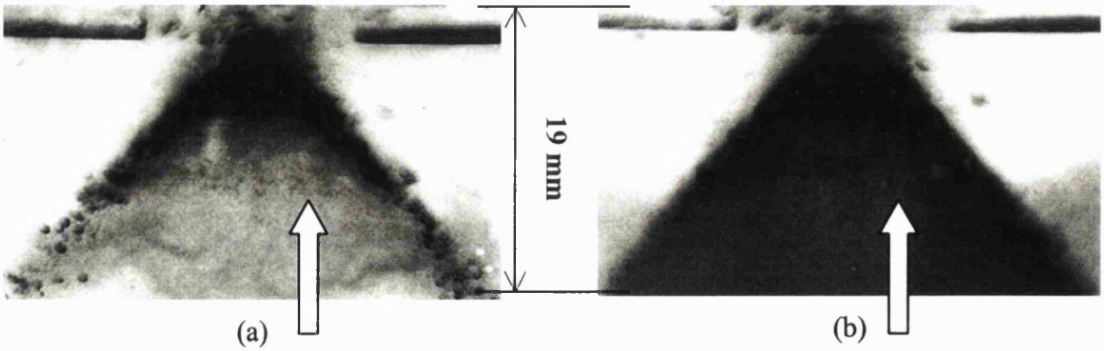

Figure 2.20 - Injector D: 0.5 bar cylinder pressure, 22°C fuel temperature, gasoline. (a) 20 bar fuel pressure, 2.1 ms aSOI, figure A1.4 169. (b) 100 bar fuel pressure, 2.1 ms aSOI, figure A1.4 149.

2.3.3 Formation of curl-up vortices

A predominant characteristic of the sprays is the formation of curl-up vortices near the leading edge of the spray. All four injectors displayed this characteristic under certain conditions. It is understood [Kume *et al*, 1996] that the formation of these curl-ups is due to the drag forces between the air and

the fuel. This causes the smaller fuel droplets on the outside of the cone to become entrained in the slower moving air, and then to join a recirculating current that is trying to fill the region from where the air has been entrained. Fuel leaves the injector as a sheet in the form of a hollow cone but this soon breaks up, sometimes with quite dramatic changes to the structure. There will be a tendency for the droplets formed on the inside of the hollow cone to be pulled inwards to the low-pressure region. There may be quite low levels of migration under some conditions but, for example, when flash boiling takes place the remaining small droplets are likely to move inwards at quite a high rate. Figure 2.21 illustrates this. Likewise, fine droplets on the outside will be pulled first outwards and then into a recirculating flow.

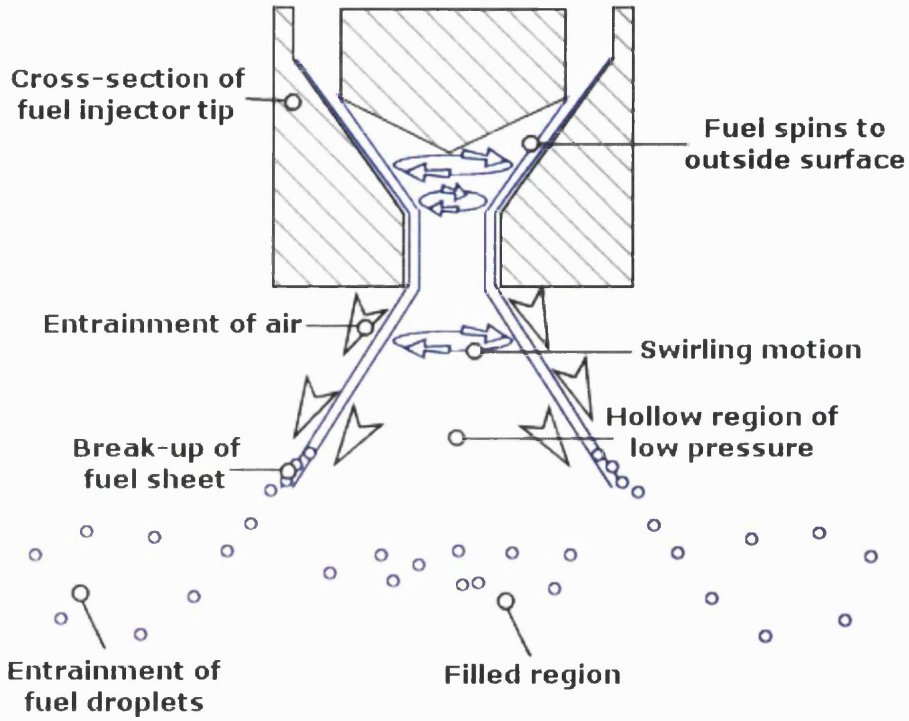

Figure 2.21 - The formation of curl-up vortices.

Injector A

Strong curl-up was observed for the injector A fuel spray at atmospheric conditions. This is consistent with the theory that the spray forms from the break-up of the hollow-cone sheet of fuel. Figure 2.22 shows an example of the curl-up vortices observed for injector A.

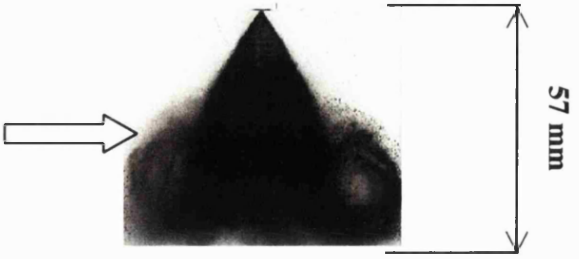

Figure 2.22 - Injector A: atmospheric pressure, 23°C fuel temperature, 55 bar fuel pressure, gasoline, 1.9 ms a SOI, figure A1.1 029.

Injector B

Under atmospheric pressure, injector B was found to produce strong curl-up at both ambient temperature (24°C) and at 80°C. Heating the gasoline had the effect of making the curl-up vortices appear more randomly ordered. This is thought not to be due to flash boiling, as substituting iso-octane for gasoline produced a similar spray. Injector B was only tested at atmospheric pressure. Figure 2.23 illustrates the difference in the curl-up formation between the hot and cold cases.

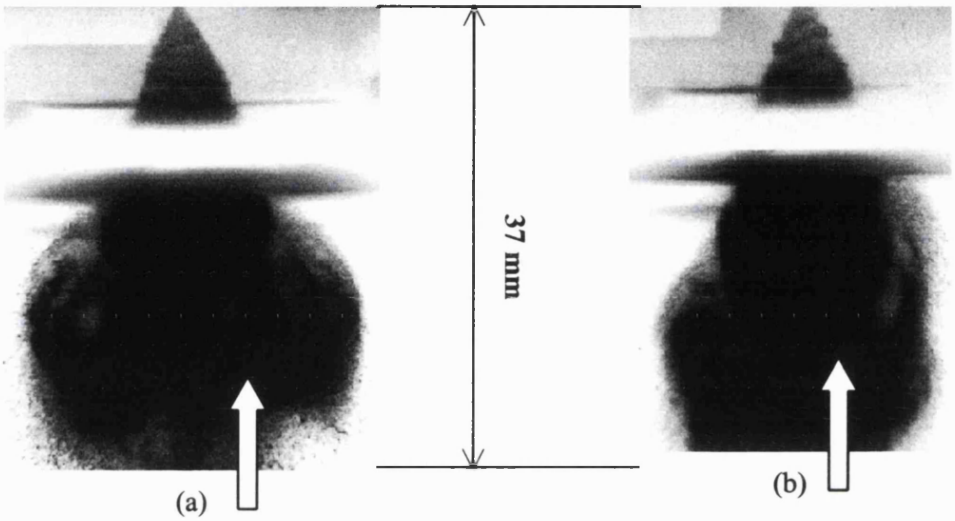

Figure 2.23 - Injector B: atmospheric pressure, 120 bar fuel pressure, gasoline. (a) 24°C fuel temperature, 1.1 ms aSOI, figure A1.2 006. (b) 80°C fuel temperature, 1.2 ms aSOI, figure A1.2 023.

Injector C

At some atmospheric conditions, injector C displayed characteristic curl-up vortices when the fuel pressure was 100 bar. However, at a fuel pressure of 20 bar, this was not apparent. Figure 2.24 compares the two conditions. As the droplets are moving slower in the 20 bar case, the shear force between them and the air is less than in the 100 bar case. The lower drag leads to delayed break-up of the fuel and also the recirculating air currents were not so strong.

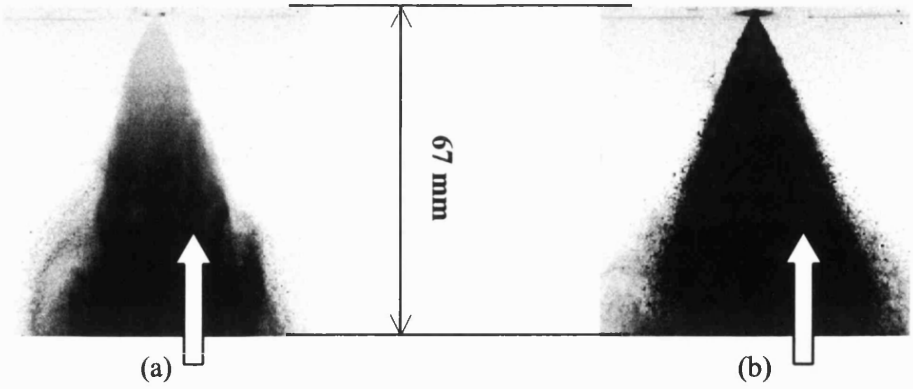

Figure 2.24 - Curl-up formation in the injector C spray at atmospheric pressure. (a) 22°C fuel temperature, 100 bar fuel pressure, gasoline, 1.3 ms aSOI, figure A1.3 061. (b) 21°C fuel temperature, 20 bar fuel pressure, 2.4 ms aSOI, figure A1.3 048.

Switching to iso-octane instead of gasoline had no discernible effect on the spray structure. Raising the temperature of the injector to 80°C did not alter the shape of the spray, but did cause more pronounced vortices to be formed when using gasoline, possibly due to the presence of flash boiling. This was not the case when using iso-octane. Reducing the cylinder pressure to 0.5 bar had the largest effect on the curl-up vortices with them disappearing almost entirely. This was true for both high and low temperature conditions. Figure 2.25 illustrates these effects at both 20 and 100 bar fuel pressures.

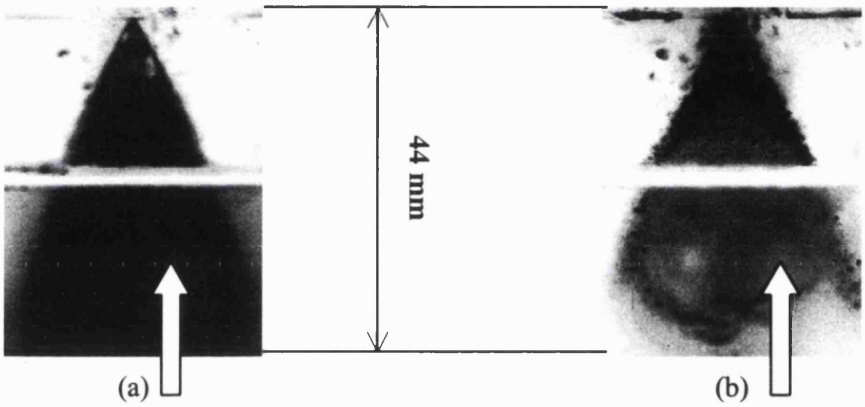

Figure 2.25 - Injector C: 0.5 bar cylinder pressure, 23°C fuel temperature, iso-octane. (a) 100 bar fuel pressure, 1.5 ms aSOI, figure A1.3 096. (b) 20 bar fuel pressure, 1.4 ms aSOI, figure A1.3 115.

Injector D

Injector D displayed considerable curl-up at many test conditions. Figure 2.26 shows the difference in the formation of the vortices under atmospheric conditions at the two different fuel pressures. Note how the curl-up vortices in the 20 bar case appear finer, as if only the lightest droplets are being entrained. The reduction in the velocity of the fuel sheet (and hence the drag forces) resulted in fewer small droplets and less air movement due to entrainment, so it was not surprising that the vortices were less pronounced.

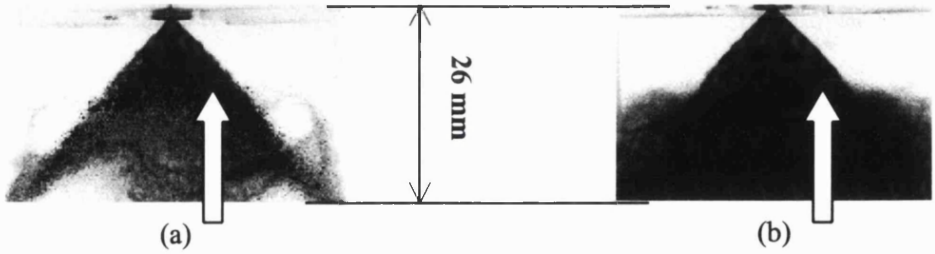

Figure 2.26 - Injector D: atmospheric pressure, gasoline. (a) 21°C fuel temperature, 20 bar fuel pressure, 3.4 ms aSOI, figure A1.4 070. (b) 25°C fuel temperature, 100 bar fuel pressure, 1.9 ms aSOI, figure A1.4 079.

Heating this injector seemed to have little effect on the curl-up formation early in the injection period. However, as the spray developed, the vortices moved with the leading edge, so in the later frames, the curl-up was more apparent towards the bottom of the picture. As with injector C,

switching to iso-octane instead of gasoline had no discernible effect on the spray structure. Reducing the cylinder pressure to 0.5 bar produced a similar effect as that observed with injector C. There was some initial curl-up, but as soon as the spray developed, the vortices seemed to disappear. The exception was when the fuel pressure was 20 bar and the injector was heated to 80°C. This is compared with the same condition at 22°C in figure 2.27. There is no visible curl-up on the outside of the spray. However, the spray shows the unusual characteristic of being most dense in the centre at the leading edge. It can be seen from viewing a complete injection sequence (see appendix 1.4) that it is likely that this effect was caused by the injector emitting an initial 'slug' of fuel. The reasons why this slug should be more pronounced in some case than others, and explanations for the series of mechanisms involved in the development of this part of the spray, cannot be easily provided.

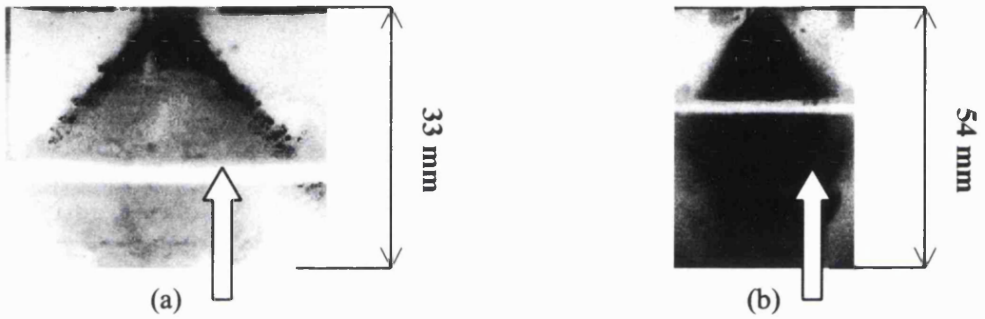

Figure 2.27 - Injector D: 0.5 bar cylinder pressure, 20 bar fuel pressure, gasoline. (a) 22°C fuel temperature, 3.3 ms aSOI, figure A1.4 175. (b) 80°C fuel temperature, 1.4 ms aSOI, figure A1.4 181.

2.3.4 Penetration rates

The speed at which a fuel spray penetrates the cylinder of an engine will strongly influence the combustion process of the engine. With high-resolution images it is possible to follow the spray frame-by-frame and measure the resulting penetration rates. The spray was broken up into two distinct areas - the leading edge (LE) and the main spray (MS). The penetrations of these areas were considered to be separate issues, as previous experience [Zhao *et al,* 1997] had shown that certain GDI injectors produced an initial slug of fuel, which was not representative of the main spray.

The penetration data was extracted from the film sequences and displayed in graphical format, in which the distance of penetration was plotted against the time taken. The accuracy of these measurements was estimated to be +/- 1.0 mm for the leading edge, +/- 2.0 mm for the main spray and -0.1 ms for the timing of the spray (as the frames are 0.1 ms apart, it is possible that the moment the spray exits the nozzle is between shots). The penetration distances were measured along the centre line of the spray axis. Figure 2.28 shows a comparison for each injector at atmospheric pressure and ambient temperature (20 - 25°C), at their highest rated fuel pressure with gasoline.

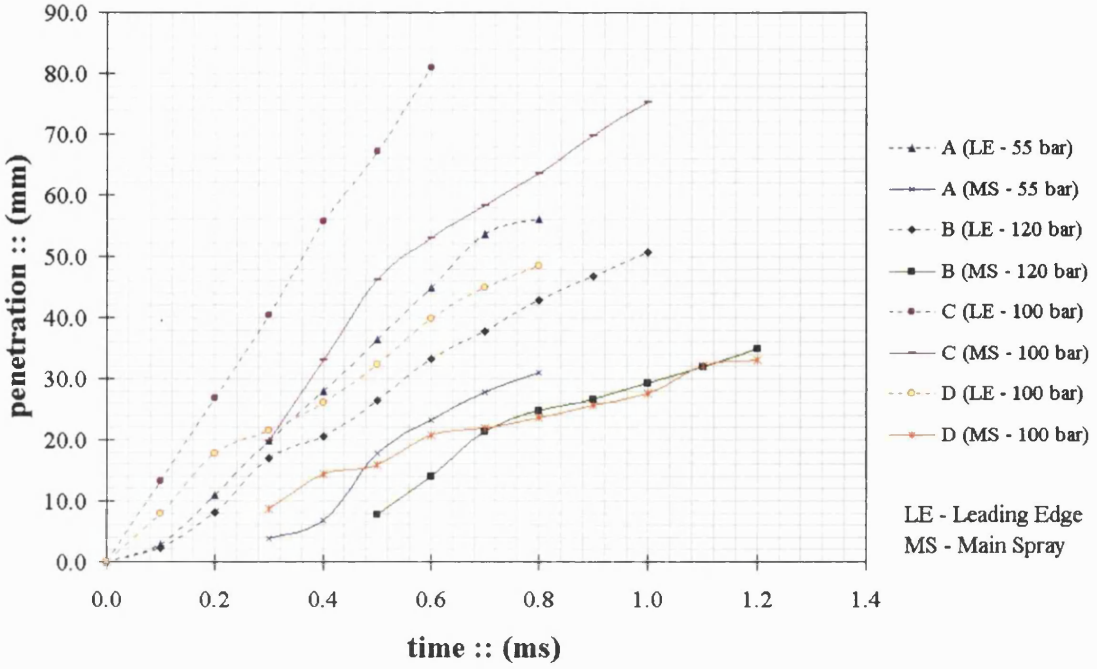

Figure 2.28 - Penetration rates, comparison of each injector (atmospheric pressure, 20-25°C fuel temperature, gasoline).

Injector C penetrated further and more quickly than the others. This may at first be surprising considering the higher fuel pressure of injector B (120 bar versus 100 bar). The included angles of the spray cones were measured at exit and again once the main spray had developed. The results are tabulated in figure 2.29, and may help to explain the penetration values.

Injector	Exit Spray Angle: degrees (+/- 2)	Developed Spray Angle: degrees (+/-2)
A	71°	61°
B	56°	43°
C	60°	40°
D	91°	79°

Figure 2.29 - Table of spray cone angles at atmospheric pressure and 20-25°C fuel temperature, gasoline.

Spray cone angles are discussed in detail in a later section. The table of penetration rates in figure 2.30 was calculated from the characteristics in figure 2.28.

Injector	Penetration rate (LE): m/s	Penetration rate (MS): m/s	Fuel pressure: bar
A	77	43	55
B	54	31	120
C	136	78	100
D	60	27	100

Figure 2.30 - Table of penetration rates at atmospheric pressure and 20-25°C fuel temperature, gasoline.

Injectors C and D (similar injectors, different spray angles) were tested at two different fuel pressures: 20 and 100 bar. As expected, injector C with its narrower cone angle, penetrated further and faster than the injector D in every comparable case. Figure 2.31 illustrates the results.

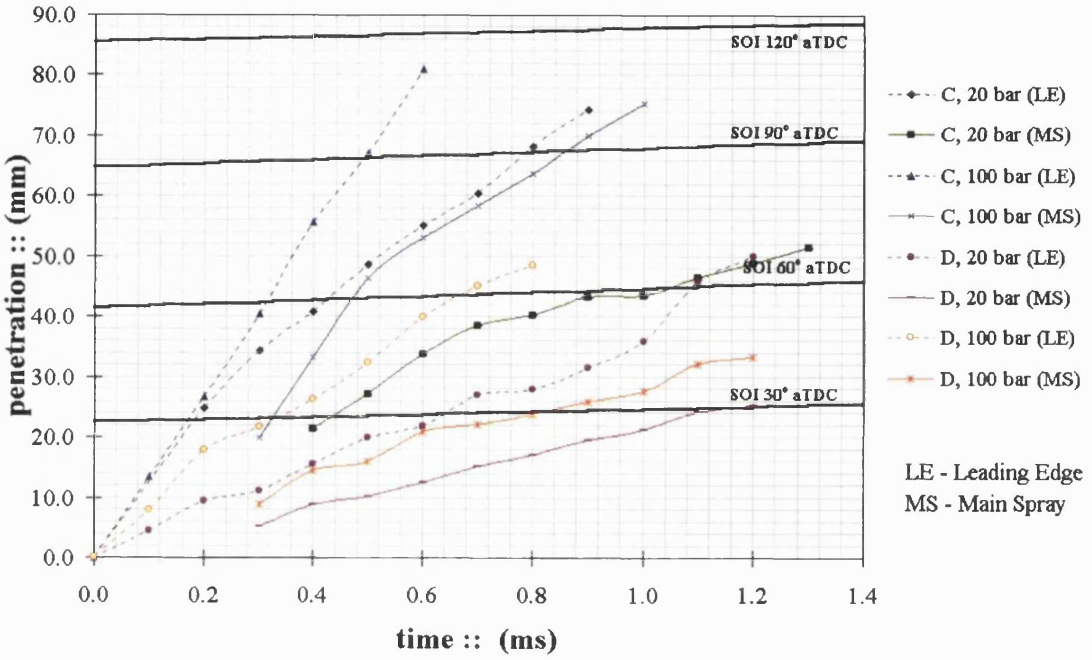

Figure 2.31 - Penetration rates for injectors C and D. The effects of fuel pressure (atmospheric pressure, 20-25°C fuel temperature, gasoline). The black lines indicate the position of a piston at different timings.

This graph has four extra lines inserted to indicate the piston's position in relation to the fuel for different injection timing. These lines were drawn assuming that the injector was mounted centrally in a pent-roof combustion chamber, and were derived using the equation describing the motion of a piston in a crankshaft/connecting-rod/piston mechanism [Stone, 1999]. The calculation was performed for an engine speed of 700 rpm. It is evident that there is the possibility of spray impaction on the piston crown with injector C (at 100 bar) even with the start of injection (SOI) at 90° after top dead centre (aTDC). Injector D would allow more timing flexibility, as significant impaction should not occur with SOI at 60° aTDC. However, the wider spread of this injector is more likely to lead to impaction on the cylinder walls.

For a given condition, the 60° injector appears to penetrate twice as quickly as the 90° injector. The fuel pressure effect is not as significant. Initial penetration appears to be unchanged by a fuel pressure increase, and then the difference develops to being within the range of around 15-35%.

Injectors C and D were used again to investigate the changes due to raising the temperature of the injector body. Figure 2.32 illustrates the effects on the leading edge of the spray.

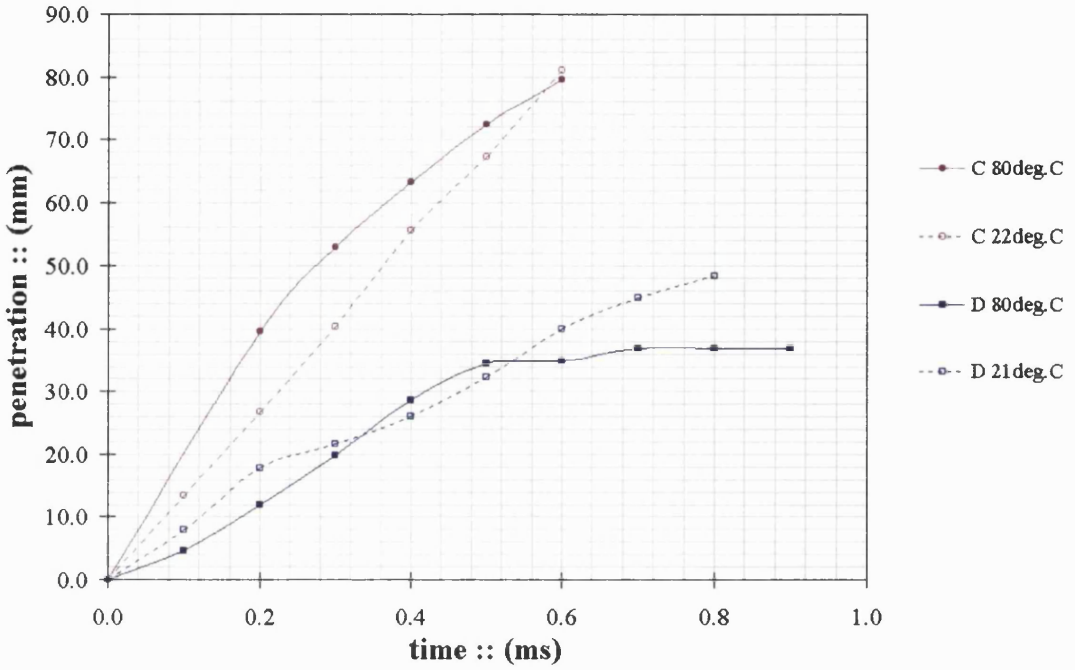

Figure 2.32 - Penetration rates for injectors C and D. The effects of temperature - leading edge of spray (atm. pressure, 100 bar fuel pressure, gasoline).

Figure 2.32 shows little difference in the penetration of the leading edges of the sprays for a change of temperature. The same conclusion can be drawn from figure 2.33, which shows the penetration of the main sprays.

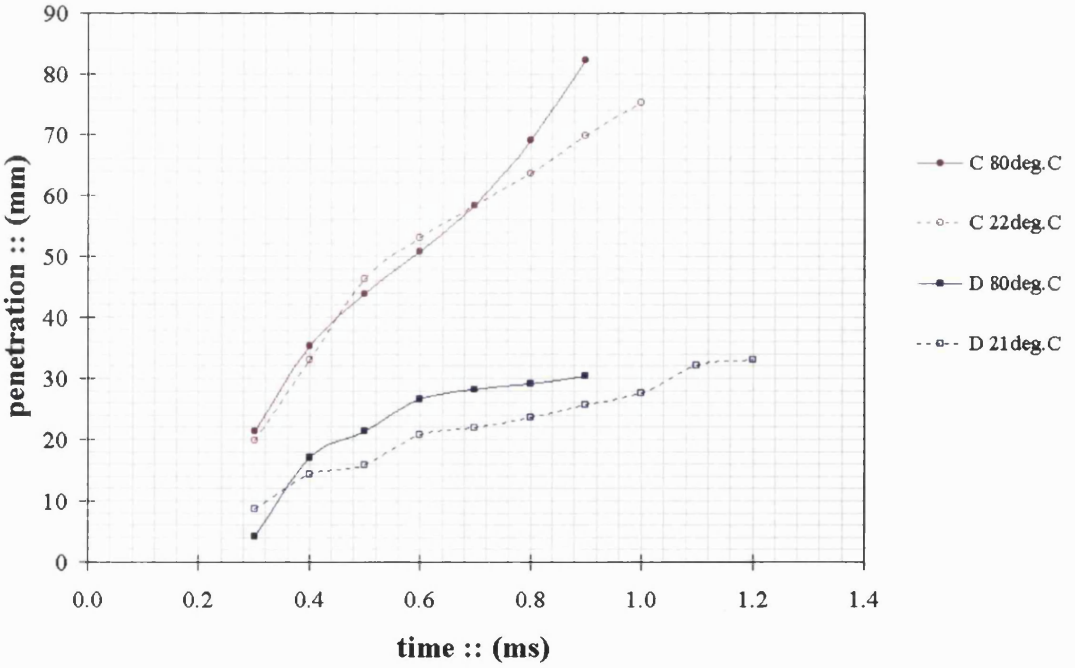

Figure 2.33 - Penetration rates for injectors C and D. The effects of temperature - main spray (atm. pressure, 100 bar fuel pressure, gasoline).

Lastly, the effects of ambient pressure were investigated for the same two injectors. Figure 2.34 shows the results for both injectors spraying into atmospheric pressure and reduced pressure (0.5 bar) at 100 bar fuel pressure, and an injector body temperature of 20-25°C.

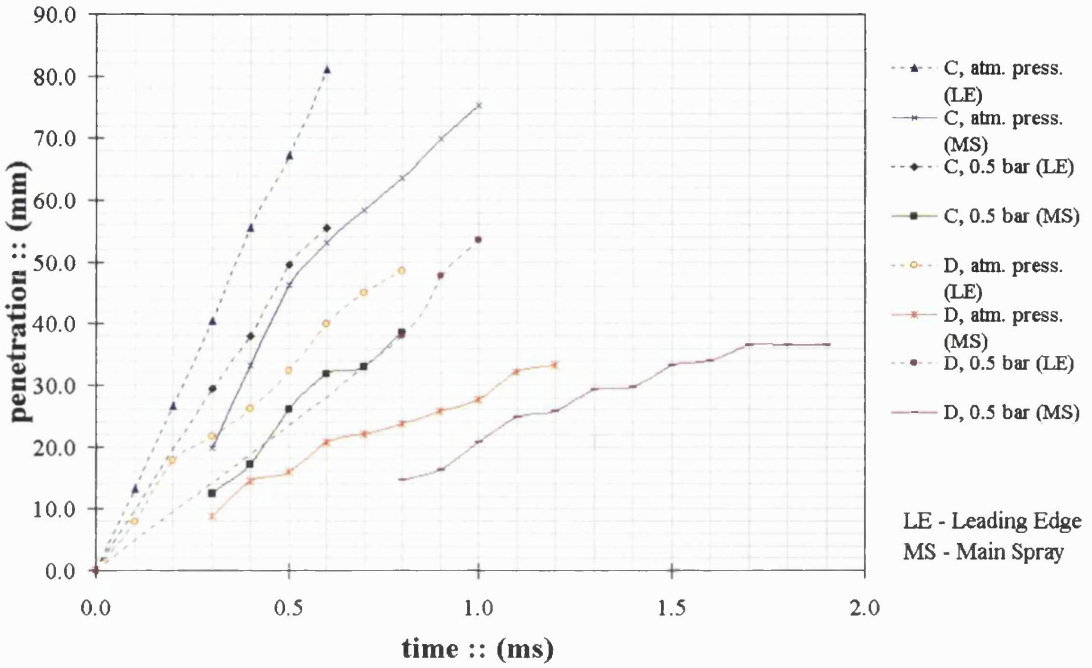

Figure 2.34 - Penetration rates for injectors C and D. The effects of ambient pressure (20-25°C, 100 bar fuel pressure, gasoline).

The penetration rates of the injectors do not appear to be very sensitive to changes in the ambient pressure. A decrease in ambient pressure decreases the rate of penetration in every case, but by no more than the effect shown by fuel pressure changes shown in figure 2.31. The effect is somewhat unexpected since it might be thought that the droplets would penetrate faster in less dense air. However, a counteracting effect may be that flash boiling is more pronounced leading to smaller droplet sizes (and hence less penetration) at reduced ambient pressure. It was also noticed that the spray cone angles in general increased at reduced ambient pressure, reducing the axial momentum of the droplets.

2.3.5 Cone spray angle

The included angle of the spray cone was measured from the photographic images. It was discovered that the initial exit angle differed from the angle of the cone once the spray had developed, so both were recorded. It was estimated that the accuracy of measurement of cone angle was +/- 2 degrees. Figure 2.35 illustrates the difference between the exit angle and developed spray angle.

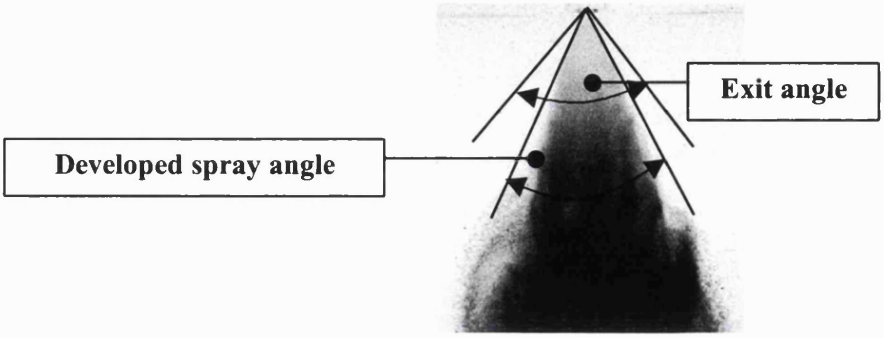

Figure 2.35 - Measuring the included angle.

A table (figure 2.36) was compiled to compare the cone angles at different conditions.

Injector	Cylinder pressure	Injector temperature: (°C)	Fuel pressure: (bar)	Fuel	Exit spray angle: (degrees)	Developed spray angle: (degrees)
A	Atm.	20-25	55	Gasoline	71	61
B	Atm.	20-25	120	Gasoline	56	43
	Atm.	80	120	Gasoline	58	37
	Atm.	20-25	120	Iso-octane	59	40
	Atm.	80	120	Iso-octane	61	40
C	Atm.	20-25	20	Gasoline	54	46
	Atm.	20-25	100	Gasoline	60	40
	Atm.	20-25	100	Iso-octane	60	40
	Atm.	80	100	Iso-octane	53	35
	Atm.	80	100	Gasoline	63	41
	0.5 bar	20-25	100	Gasoline	60	53
	0.5 bar	80	100	Gasoline	57	45
	0.5 bar	80	20	Gasoline	68	54
	0.5 bar	20-25	20	Gasoline	62	56
D	Atm.	20-25	20	Gasoline	88	83
	Atm.	20-25	100	Gasoline	91	79
	Atm.	20-25	100	Iso-octane	95	73
	Atm.	80	100	Iso-octane	93	77
	Atm.	80	100	Gasoline	92	71
	0.5 bar	20-25	100	Gasoline	93	80
	0.5 bar	80	100	Gasoline	94	62
	0.5 bar	80	20	Gasoline	86	76
	0.5 bar	20-25	20	Gasoline	92	83

Figure 2.36 - Spray cone angles.

The variations in the cone angle for different conditions are significant. Injector C, for instance, varied only from 53° to 68° on exit from the injector, but, once developed, changed from 35° to 56°. Even allowing for the accuracy of +/- 2 degrees, the variation is large. Similarly, the exit spray angle of injector D ranged from 86° to 95°. As with the 60° injector, the developed spray angle of the 90° injector varied more: 62° - 83°.

Interestingly, the angle of the cone for injector B remained consistent with temperature and fuel changes although it may have changed with ambient pressure, but no readings were taken at 0.5 bar. Both exit and developed sprays displayed this characteristic.

2.3.6 Swirling motion

It has been claimed by several injector manufacturers [Iwamoto *et al*, 1997] that the high-pressure swirl injectors do just that - produce a swirling fuel spray. Figure 2.3 displays how a swirling motion may be achieved. In reality, the situation may be very different. To investigate whether the four injectors under test produced swirling sprays, they were photographed from underneath. If swirl was present, then animating the sequence of frames should reveal it.

Injector A

The end-on shot of the spray from injector A shown in figure 2.14a was potentially easy to interpret. The periphery of the spray appeared to be made up of 'spikes' that could easily have been rotating about the injector axis. However, close examination of the sequence of photographs reveals that the spikes do not rotate. Figure 2.37 illustrates this with a number of frames from the sequence. A line has been drawn on each photograph. The spikes do not move relative to this. The complete sequence can be found in appendix 1.1.

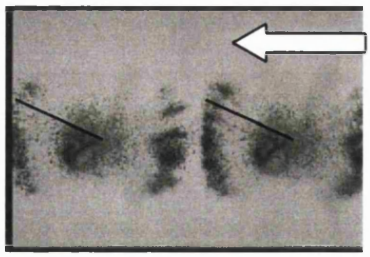

Figure A1.1 080

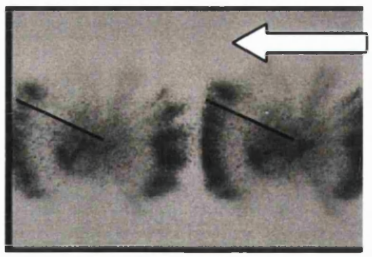

Figure A1.1 081

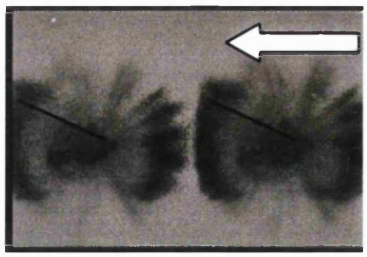

Figure A1.1 082

Figure 2.37 - Sequence of frames showing lack of swirl in the injector A spray at atmospheric pressure, 20-25°C fuel temperature, gasoline, 1.6 ms aSOI, 40 mm away from injector tip.

Injector B

Injector B was photographed from underneath under atmospheric pressure, both at ambient temperature and heated. Figure 2.38 displays six shots from a sequence to illustrate that there was no apparent swirl. However, there is a characteristic anomaly on the left of each shot in the spray.

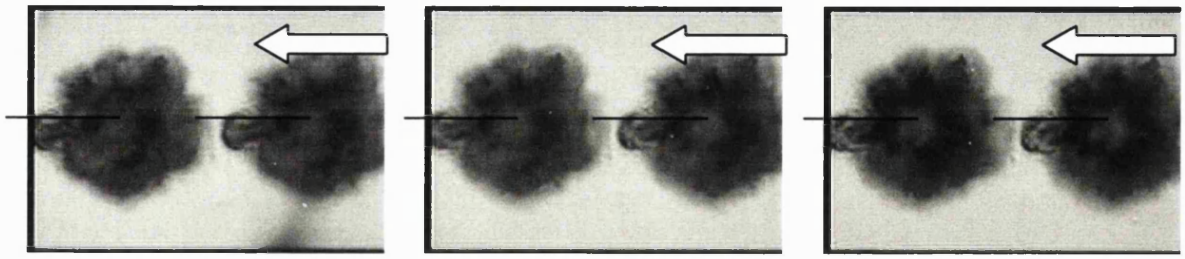

Figure A1.2 044 Figure A1.2 045 Figure A1.2 046

Figure 2.38 - Sequence of frames showing lack of swirl from injector B at atmospheric pressure, 25°C fuel temperature, gasoline, 2.0 ms aSOI, 45 mm away from injector tip.

This anomaly was apparent throughout testing with ambient conditions and is thought to be due to the fact that the spray was turned through 20° (see figure 2.5) in the injector tip with the anomaly caused by some form of machining groove. Somewhat surprisingly, it is not visible in the images of the test performed at 80°C (figure 2.39). There is no obvious reason for this. Again no swirl is apparent. The spray appears fainter as the dense fuel spray obscures the light sheet.

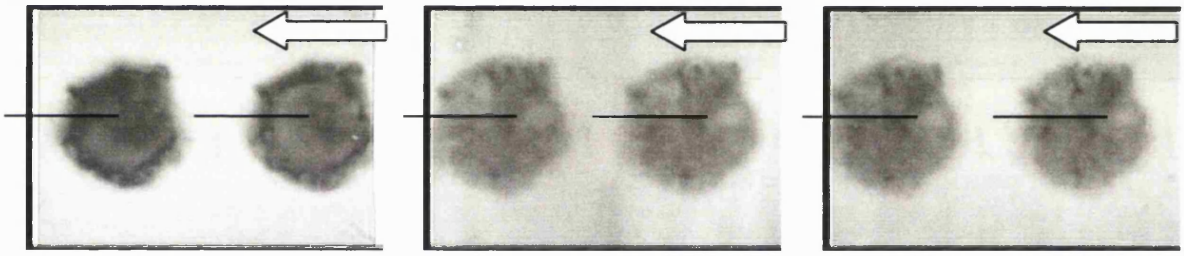

Figure A1.2 055 Figure A1.2 056 Figure A1.2 057

Figure 2.39 - Sequence of frames showing lack of swirl from injector B at atmospheric pressure, 80°C fuel temperature, gasoline, 1.4 ms aSOI, 45 mm away from injector tip.

Injectors C & D

Injector C was not photographed from underneath so it is not possible to conclude whether or not swirl was present. It is believed that it would have shown similar characteristics to injector D though. This injector was photographed under atmospheric pressure at 100 bar fuel pressure at two conditions - without heating the injector body, and with the injector heated to 80°C. The first sequence shown in figure 2.40 is the unheated case - the ambient temperature was 25°C. Lines are used in the same way to illustrate the lack of change in the developed spray.

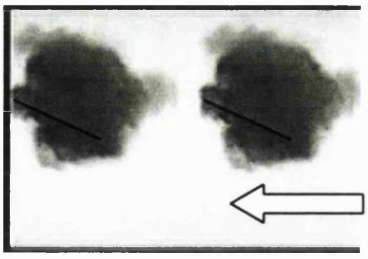

Figure A1.4 100

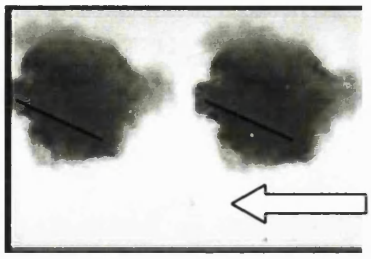

Figure A1.4 101

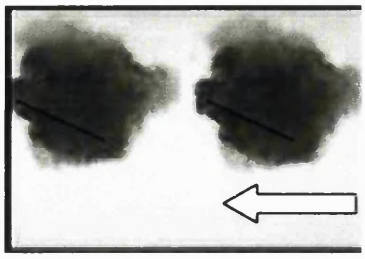

Figure A1.4 102

Figure 2.40 - Sequence of frames showing lack of swirl from injector D at atmospheric pressure, 25°C fuel temperature, gasoline, 3.1 ms aSOI, 40 mm away from injector tip.

In the heated case there were no significant changes. Figure 2.41 is a part of the sequence. The black line is used once again to illustrate the lack of a swirl motion.

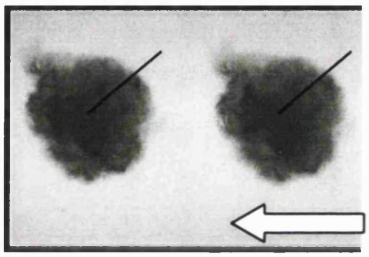

Figure A1.4 136

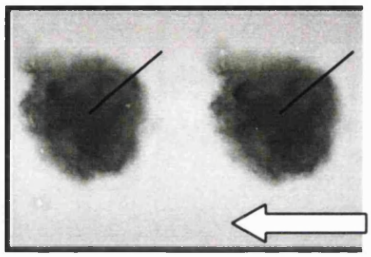

Figure A1.4 137

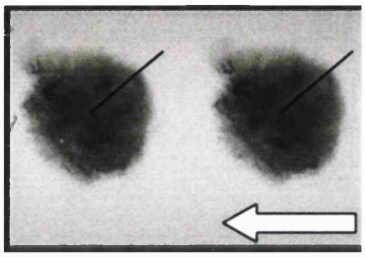

Figure A1.4 138

Figure 2.41 - Sequence of frames showing lack of swirl from injector D at atmospheric pressure, 80°C fuel temperature, gasoline, 2.5 ms aSOI, 40 mm away from injector tip.

It may be argued that the absence of any observed rotation in successive frames taken in one particular plane (as cut by the light sheet) was not positive proof of lack of swirl. Such an argument would be dependent on spray patterns following a perfectly helical path. This seemed unlikely, particularly as the leading edge of the spray could be expected to behave differently from the established spray - there was no evidence of rotation of the leading edge or the first part of the main spray.

2.3.7 Droplet size

In order to characterise a fuel spray, data is required on the droplet size distribution, and how it might vary with position within the spray and time after initiation of injection. Tests were performed with a Malvern particle sizer (section 2.2.2) in order to, at least in part, provide this data. The Malvern particle sizer takes a 'line of sight' reading. That is to say it sizes all droplets that fall within the 9 mm diameter column of the laser beam as it passes through the spray. Readings were taken as the beam was traversed across from the centre-line to the edge of the spray. If there was spatial variation in droplet size distribution then it would more likely have a ring structure (figure 2.42) than be in a series of slices. The readings displayed in this section are the 'line of sight'

readings without any attempt made to analyse the ring structure. A tomographic analysis is described later in which an attempt was made to deconvolve the ring structure.

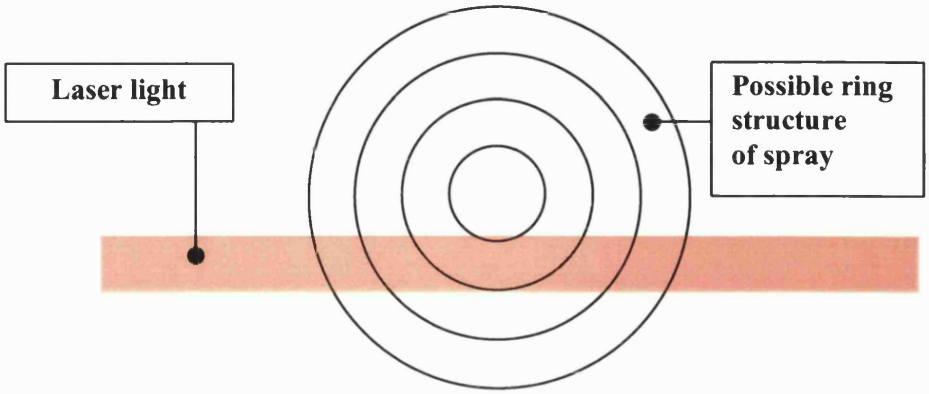

Figure 2.42 - Diagram showing how 'line of sight' laser beam cuts across possible ring structure of fuel spray.

Injector A was not included in this investigation. Also, due to the limitations of the test rig, it was not possible to obtain droplet size data for the 0.5 bar cylinder pressure conditions. The variables, therefore, were temperature, fuel pressure, fuel type and distance from the centre-line of the injector.

Injector B

Injector B was tested with both gasoline and iso-octane. The photographic evidence was that the multi-component fuel did not have a significantly different structure of spray from the single component fuel at atmospheric pressure. This is also the conclusion from figure 2.43. The gasoline and iso-octane plots are virtually identical. The temperature increase did reduce the Sauter mean diameter (SMD) of the droplets, but not by a significant margin. It can be deduced that the spray was relatively stable, and insensitive to temperature or fuel changes.

The crosses indicate readings outside the limits proposed by the manufacturer for accurate readings. The reading of obscuration is a measure of the scattered light, with a value greater than 60% indicating the danger of inaccurate results due to multiple scattering (i.e. light scattered from one droplet first and then scattered again from a second, third, etc.). A lower limit on obscuration of 5% was also observed, because readings of less would be prone to inaccuracy due to too few droplets being present. Testing showed that readings close to the centre line of the injector tended to give values of obscuration that were too high, and those nearest the edge tended to return values that were too low. Values outside the limits have been included on the plots as their accuracy diminishes progressively rather than suddenly becoming invalid. It should be noted that evaporation from the fuel droplets also affected the accuracy of the raw results. However, the technique pioneered by Williams [1994] was applied to correct for this problem.

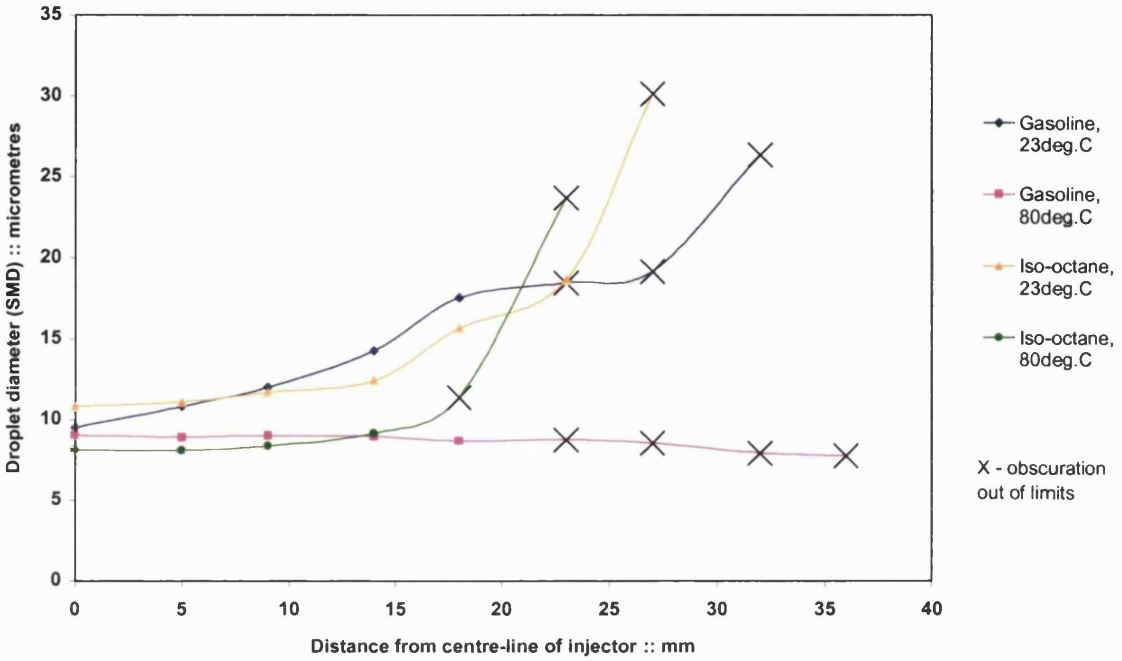

Figure 2.43 - Effects of temperature and fuel on SMD - injector B. (Readings taken across plane at 85 mm away from injector, atmospheric pressure).

Injector C

The testing of injector C is summarised in figure 2.44, where the SMD is plotted against the distance from the centre-line of the injector. The droplet size readings were recorded at a plane 85 mm along the injector axis away from the tip. Attempts to take readings any closer to the injector resulted in the obscuration reading rising to an excessive value.

The plots follow a characteristic form. The SMD remains virtually unchanged until moving 10 mm away from the centre-line. The SMD values then rise steadily as the area of investigation nears the outer edges of the cone. As expected, the smallest droplets were found at the higher fuel pressure and temperature, i.e. at 100 bar and 80°C. For the most part at this condition, the droplet diameters were around 10 μm, which is very impressive for an injector of this type. The largest droplets for injector C were at 20 bar fuel pressure and an injector temperature of 23°C. The droplet diameters were measured as below 20 μm close to the centre-line, rising to almost 40 μm at the limits of the obscuration (i.e. the edge of the spray).

Injector D

Similar tests were carried out using injector D, resulting in the characteristic shown in figure 2.45.

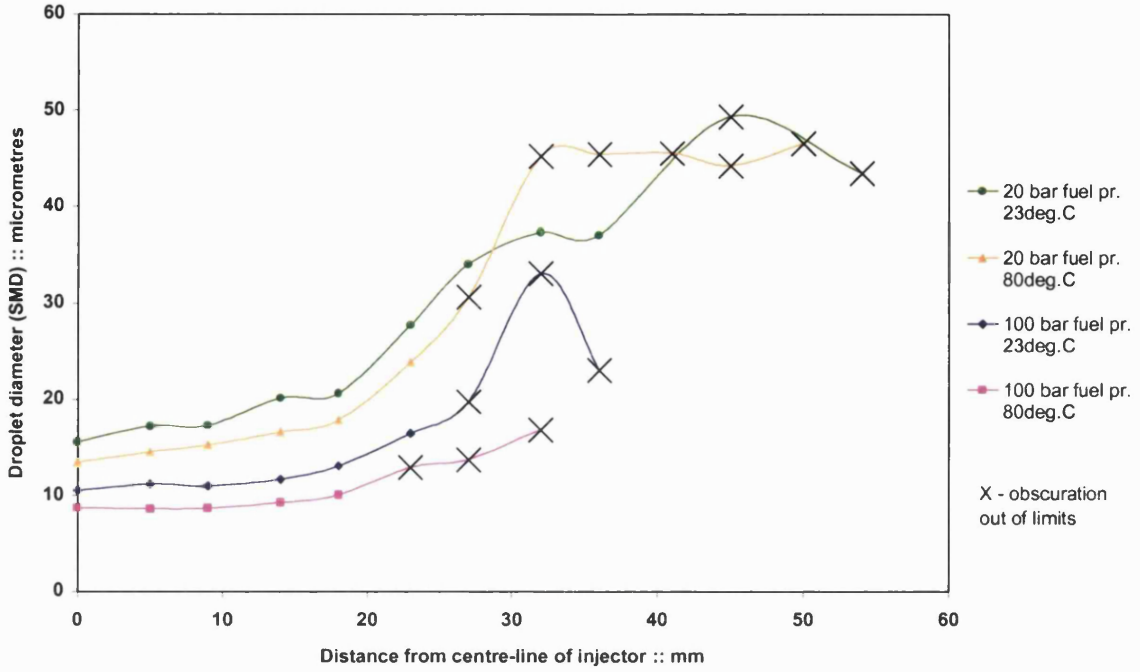

Figure 2.44 - Effects of temperature and pressure on SMD - injector C. (Readings taken across plane at 85 mm away from injector, gasoline).

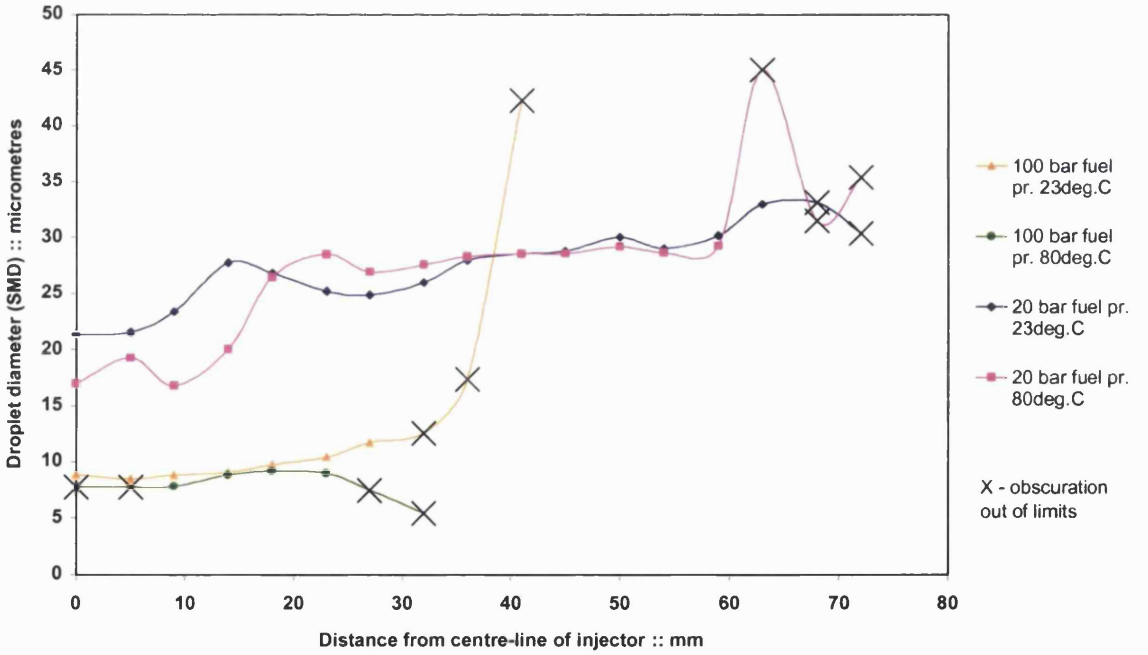

Figure 2.45 - Effects of temperature and pressure on SMD - injector D. (Readings taken across plane at 85 mm away from injector, gasoline).

The temperature effects were not as pronounced in this case, with very similar values of SMD for a given fuel pressure, regardless of the temperature. However, reducing the fuel pressure has a

significant influence on the size of the droplets in the spray, increasing the diameter size from below 10 μm to above 25 μm. The photographs of the spray support this measurement. Individual droplets were visible in the low pressure (20 bar) sprays, but appeared as a dense 'misty' cloud in the high pressure tests (figure 2.26).

As a final experiment, the injectors were tested again, but rotated 90° around their axis. This was to establish the symmetry of the sprays. In general, the spray symmetry was found to be good. Figure 2.46 illustrates the findings of this experiment. Each column represents one injector at one condition (all are at atmospheric pressure and 20-25°C). The total height is the higher of the two recorded values. The shading at the top of the column represents the difference between the higher and lower values.

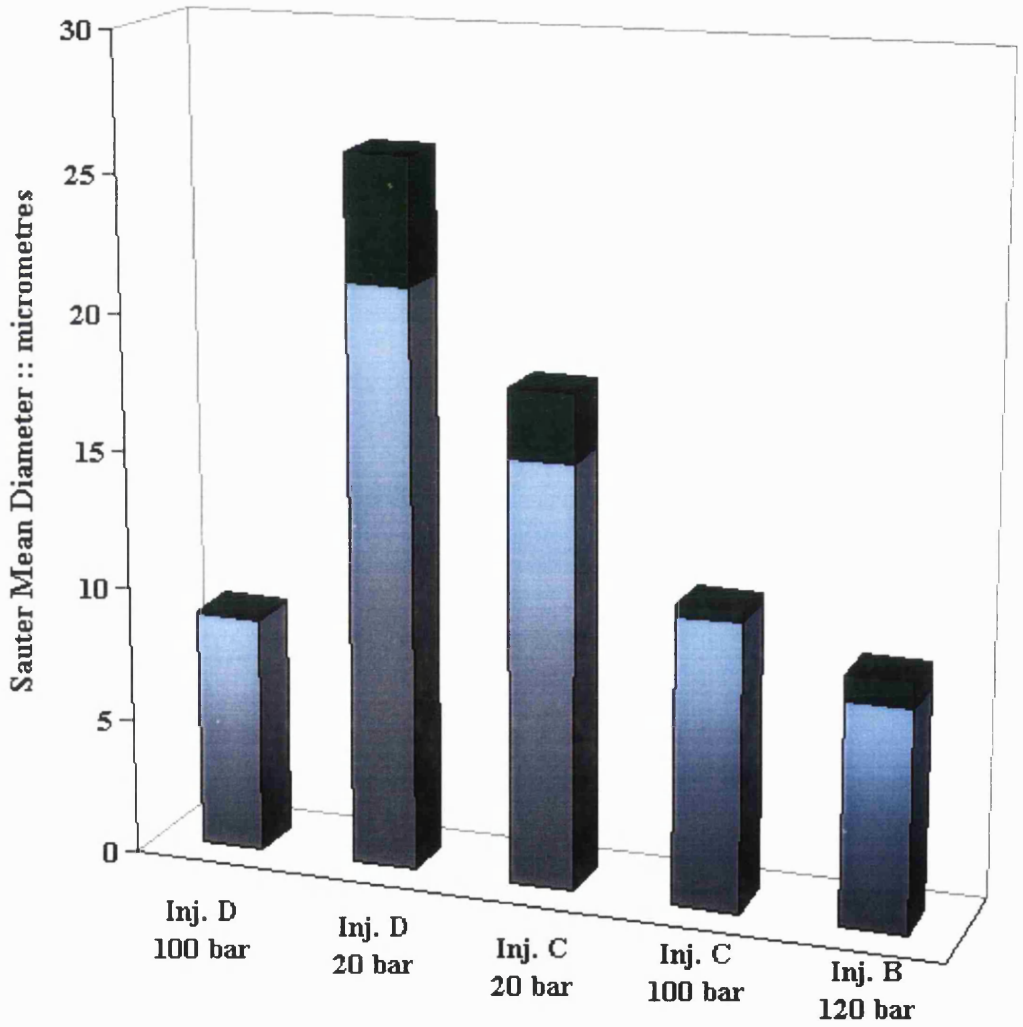

Figure 2.46 - Spray symmetry experiment (Atmospheric pressure, 20-25°C fuel temperature, gasoline, 85.0 mm away from injector tip).

2.3.8 Tomographic analysis

Further analysis of the droplet sizing data was carried out in the form of a tomographic investigation. Utilising a computer program developed by the author (algorithm provided in appendix 2), the fuel sprays were divided into rings of fuel (see figure 2.42). In each ring, SMD and fuel concentration were assumed to be uniform, enabling a relatively simple calculation, first aimed at determining the fuel concentration, and then the SMD.

Before deriving the algorithm, previous work on this subject was investigated [Lee *et al*, 1997, Yule *et al*, 1981]. These investigations utilised Fourier transforms to carry out the tomography to good effect. Unfortunately, the algorithms were not provided. The decision was taken to adopt a simpler approach, not previously applied. This method is based on the assumption that the spray may be divided into a number of rings with the same width as the laser beam, and the SMD and the fuel concentration were taken to be uniform within each ring of fuel. There may be some loss of accuracy in this method due to these assumptions. If the spray does not have a ring structure, then the calculations will produce misleading results. The restriction of the ring width being the same as the laser beam diameter also reduces the accuracy as the resolution is limited to the 9.0 mm band width. Taking further slices, which intersect, and then reprogramming the algorithm to allow for the intersections could improve this.

The tomographical method employed here requires knowledge of the concentration of liquid fuel in each ring. This may be calculated using the software supplied with the Malvern 2600 particle sizer. There are four options in the Malvern software with regards to the experiment type: particles in liquid (pil), particles in air (pia), liquid droplet sprays (lds) and metal particles in liquid (mil). Previous experience [Williams, 1994] has shown that the most accurate method for measuring the droplet diameters in a fuel spray is lds. This approach assumes light scattering through Fraunhofer diffraction and is generally considered to describe light scattered from liquid droplets down to diameters of 0.5 μm. This method was employed throughout initial calculations. However, the results from this method of calculation do not lead to accurate concentration values. To evaluate the concentration, it was necessary to change to the pil method of calculation [Wedd, 1999]. The original values for the SMD were retained, because the pil method assumes an incorrect refractive index ratio between the droplets and the air. These values were then used in conjunction with the algorithm provided in appendix 2.

The results obtained from applying the tomographic analysis program were virtually the same as those from the line-of-sight measurement. This is shown in figure 2.47 for injector C and D.

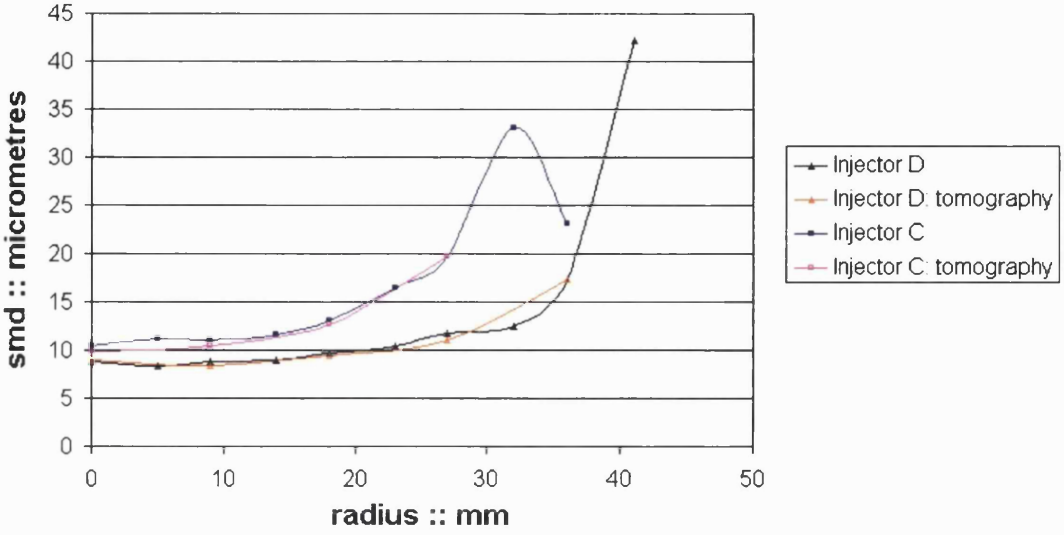

Figure 2.47 - Comparison of experimental results with data after tomography analysis.

2.3.9 Further discussion and conclusions

The driving force for performing this experimental study of injector sprays was first of all to accumulate information to support attempts to model sprays from DI gasoline injectors, and secondly to assist with the interpretation of the engine test results in chapter 4. In general, it can be observed that there were very significant differences in the sprays from one type of injector to another, and also a considerable variation in the sprays from a single injector in response to changes in operating parameters such as fuel pressure, ambient pressure, and fuel temperature. It may be deduced that the task of developing a single model to describe the observed behaviour will be extremely difficult, maybe even impossible. Ultimately, the answer could be for each injector manufacturer to supply an appropriate model for his injector so that engine manufacturers can apply appropriate predictive techniques to aid engine development. More specific conclusions are attempted in the following:

(i) Hollow or filled cone?

It has been described how swirl injectors, such as those tested, produce a conical sheet of fluid which becomes unstable and subsequently breaks down into small droplets. It was apparent from the photographs that, in some sprays, the radial momentum of the droplets was maintained to form a hollow cone, whereas in others the spray tended to narrow and fill the centre region. Injectors C and D were tested over a wide range of operating conditions and it was apparent that the form of the spray could change with operating condition. It is likely that these changes could have a profound effect on the subsequent mixing of fuel and air and an attempt is made here to conclude what variables affect the form of the spray.

1) Sprays with a larger nominal cone angle resist collapse better than those with narrower cone angles. In particular, the comparison between injectors C and D bears this out. Therefore, the more open sprays are more likely to encompass a hollow region.

2) One of the most influential variables on the spray structure is the ambient pressure into which the fuel is injected. The initial cone angle is more likely to be sustained at lower ambient pressure due to the lower aerodynamic drag, and a smaller pressure difference across the walls of the fuel spray itself. This condition would increase the likelihood of hollow sprays. As soon as the ambient pressure is increased, the sprays are found to collapse. As an engine may use many different injection timings (hence a range of ambient pressures) it will be important to understand the spray structure under each different condition.

3) Fuel pressure has two main effects on the spray structure. Increased fuel pressure would increase the overall spray momentum, creating a larger exit spray cone angle. However, as the individual droplets are smaller (reduced mass), and their momentum is a product of mass and velocity, then their individual momentum may be smaller. The droplets would then be more susceptible to entrainment into the low-pressure region at the centre of the spray, leading to a reduced developed cone angle.

4) When the fuel temperature (in a multi-component fuel) is sufficiently high to cause flash boiling, the spray has been found to collapse. The reason for this is the reduction in the number of large droplets present. Smaller droplets are easily entrained into the low-pressure core of the spray, giving the appearance of a completely-filled cone.

5) Although not investigated in full in this work, the pre-spray from the nozzle may have a significant effect on the spray structure. It is thought that a larger 'slug' of pre-spray along the axis of the injector would cause a lower pressure region in its wake within the centre of the spray core. The spray would be more likely to collapse under such conditions.

6) It was found that the above mechanisms are not always additive. Once collapsed, the spray appears to stabilise. Further heating or an increase in pressure does not tend to force the spray to collapse further. Also, the relatively sudden onset of flash boiling (and hence collapse of spray) can be brought about by the combination of two changes (e.g. increased fuel temperature and reduced ambient pressure), whereas one alone may have a relatively small effect.

(ii) Spray penetration and cone angle

Two other particularly important spray characteristics are its rate of penetration and its radial spread, the latter being touched on in the preceding section. These two parameters will determine when and where the spray will impact on combustion chamber surfaces, which in turn will determine the level of UHC emissions. The following general conclusions were made.

1) When the ambient pressure is decreased, the aerodynamic drag reduces. Under this condition it was assumed that penetration would increase. However, it has already been stated that the cone angle increases when the ambient pressure is decreased. An increase in cone angle will increase the radial momentum, but importantly, will reduce the axial momentum, hence decreasing the penetration.

2) The temperature of the fuel was found to affect the penetration rate of sprays that were not already stabilised (collapsed). For instance, with injector D, heating the fuel resulted in higher penetration rates. The increase in penetration was due to the collapse of the spray, and hence an increase in the axial momentum. However, injector C did not display this characteristic as the spray was already collapsed at ambient conditions.

3) When testing with low ambient pressure and high fuel temperature, the effects discussed above are seen to counteract each other. The exception is injector D, which appears to collapse further. This indicates that the spray was not yet fully collapsed in previous tests where the injector was heated and the fuel was injected into atmospheric pressure.

4) Increased fuel pressure was found to significantly increase the spray penetration rates from injectors C and D. Higher fuel pressures lead to decreased developed spray cone angles, but increased the exit cone angles in most cases.

(iii) Swirl

As described earlier, images were taken of the underneath of the sprays. In all cases, the photographs were of the cross-section of the spray approximately 40 mm from the injector tip. At this point there was no visible bulk rotation (swirl) of the spray periphery. This was the case for all injectors under test. What is of interest is the irregularity of the spray periphery. This is attributed to the presence to a greater or lesser extent of curl-up vortices. Overall, it was felt that the photographic evidence of lack of swirl was strong. However, only measurements of droplet velocity in three orthogonal planes could confirm this. For instance, it may be that the lack of any swirling motion within the air surrounding the spray led to the appearance of no swirl because the small droplets on the periphery of the spray were mainly influenced by the air motion.

(iv) Curl-up vortices

The following points summarise the findings with regards to the formation of curl-up vortices.

1) Curl-up vortices are caused by the smaller drops on the outside of the spray becoming entrained in the recirculating air currents set up by the motion of the spray.

2) The vortices are particularly predominant when flash boiling is present due to the presence of many small droplets. For the same reason, higher fuel pressures increase the likelihood of curl-up vortice formation.

3) It is likely that curl-up vortices will not be seen on sprays in engines as the in-cylinder flow patterns will tend to distort the recirculating air pattern.

(v) Droplet sizes

In general, the sprays exhibited an initial transient period in which the main structure was formed, and a steady state, at which time most of the droplet sizing was carried out. The following conclusions were obtained from the data.

1) The smallest droplets were found at the core of the spray. SMD values of as low as 10 μm were recorded. Measurements further away from the centre revealed that the droplet diameter increased gradually towards the periphery.

2) In general, increasing the temperature of the fuel reduced the SMD values in the spray. However, the effect was small, suggesting that flash boiling was not an important influence at the 1.0 bar atmospheric pressure used for the tests.

3) Fuel supply pressure was by far the most influential variable on droplet size. Increasing the pressure had the effect of reducing the droplet diameter. The effects of pressure and temperature were additive, though the change due to the fuel pressure was noticeably greater.

4) It was found that, at the lower fuel pressure, there was a wider distribution of droplet sizes across the spray, with the largest measured at the periphery. This is supported by the photographic work.

5) Changing the fuel from gasoline to iso-octane did not alter the droplet diameter.

Chapter 3
ENGINE AND TEST CELL DESCRIPTION

3 - Engine and test cell description

3.1 Introduction

This chapter describes the engine used for testing, the test bed and its instrumentation in more than usual detail. The reason is that none of it existed prior to the work described in this thesis and the author was responsible for all of the design and commissioning work. The starting point for the engine was a bare Ricardo Hydra cylinder block and a GDI cylinder head supplied by the Ford Motor Company. A new crankshaft had to be fitted and a cylinder block designed. Oil, water, fuel, air and ignition systems had to be assembled. On the test bed side, the dynamometer had to be installed and engine instrumentation built up and commissioned.

3.2 Engine description

The assembled engine is shown in the test cell in figure 3.1.

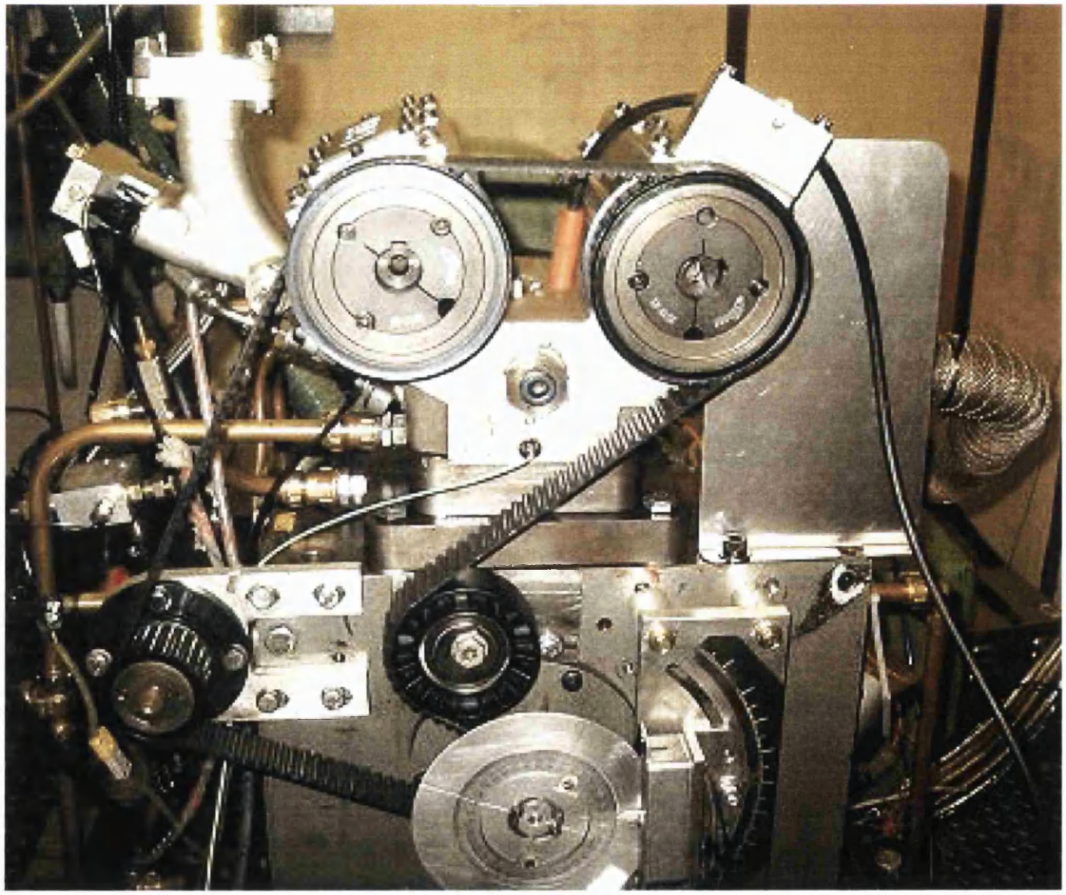

Figure 3.1 - The GDI engine assembled in the testing cell (shown without timing belt guard).

3.2.1 Combustion chamber

The engine under test was designed around a prototype, single-cylinder, Ford-manufactured, cylinder head. The head incorporated four valves (two inlet and two exhaust) and two overhead camshafts. The spark plug was located in a near-central position. There were two possible entry

points for a GDI injector: one was next to the spark plug, and the second was underneath and between the inlet valves. The diameter of the inlet valves was less than it would have been if the head had been designed for PFI operation. This reduction in size was necessary to accommodate the GDI injector mounting position. Care was taken in the design of the inlet porting to minimise any loss of volumetric efficiency due to the smaller valves [Anderson *et al*, 1996]. There was an additional drilling in the head to allow the fitting of a pressure transducer. The head had to be modified to accept the particular types of GDI injectors under test. The cylinder head is shown in figure 3.2.

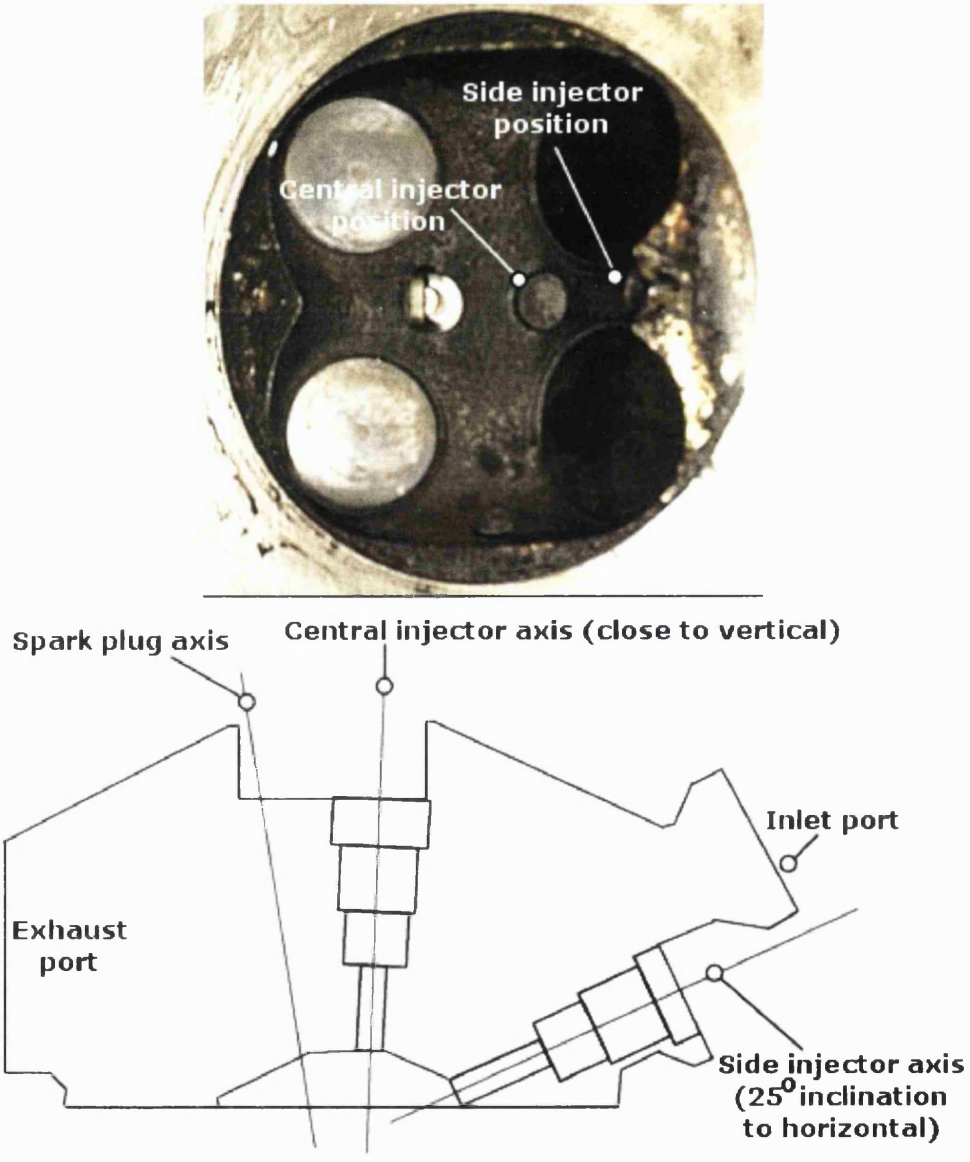

Figure 3.2 - Details of the Ford GDI cylinder head.

3.2.2 Cylinder block design

A new block was required to fit the cylinder head described above. The design was based on the Ricardo Hydra component, which is a barrel and sleeve design, between which the coolant

flows. The bore was machined to suit a production piston and connecting rod, supplied by Jaguar. The workshop drawings for these components may be found in appendix 3.

3.2.3 Camshaft and fuel pump drive arrangement

A belt drive system was utilised to drive the camshafts from the crankshaft. The camshaft pulleys had a diameter twice that of the crankshaft pulley, so that the camshafts operated at half engine speed. It was decided to drive the high-pressure fuel pump for GDI operation with the timing belt as this was thought to be easier to implement than a remote electrically-driven arrangement. The nominal pumping volume of the fuel pump was quite high for the requirement of the engine, but it was necessary to drive the pump at engine speed because its volumetric efficiency dropped rapidly at low speed (see appendix 4.1 for further details of the pump). To ease removal and adjustment a belt tensioner was added to the arrangement, as shown below in figure 3.3.

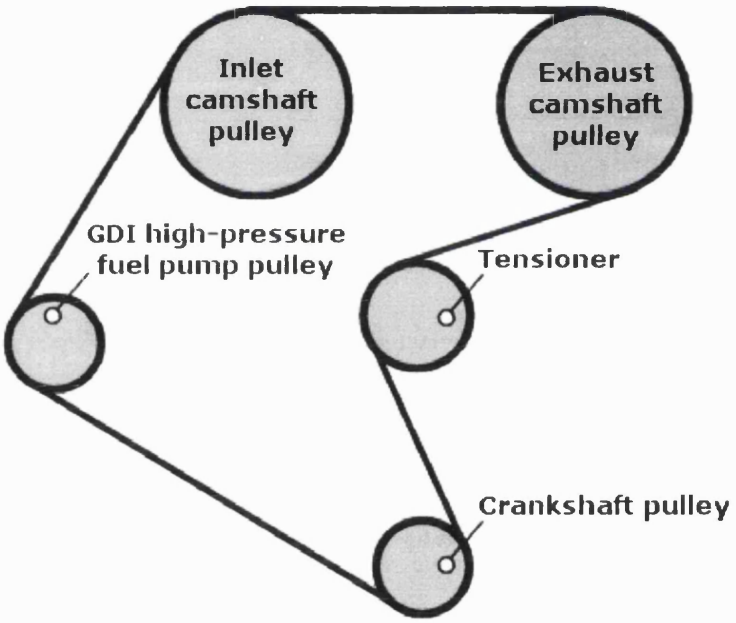

Figure 3.3 - Schematic representation of timing belt route (see also figure 3.1).

A consideration of this design was the need to easily change the position of the inlet camshaft in order to alter the inlet valve timing. For this purpose taper-lock bushes were used. These taper-lock bushes could grip the camshafts firmly when tightened, but could be loosened to allow one or both camshafts to turn, ensuring infinite adjustment. This method reduced the need to remove the timing belt during testing. Full details of the individual components are provided in figure 3.4.

Component	Details
Camshaft pulley (two off)	Fenner 043K0044.
Camshaft taper-lock bushes (two off)	Fenner Bush 029K0 025.
Crankshaft pulley	Modified Fenner 043K0022.
Fuel pump pulley	Fenner 043K0022.
Tensioner	Sourced from Ford Zetec engine.
Timing belt	Torque Drive Plus timing belt 285K0128.

Figure 3.4 - Components used in timing of engine.

3.2.4 Oil system

A high-flow oil pump, powered by a three-phase electric motor, was used to provide lubrication to the engine. The high flow rate from the pump required the selection of a high-capacity pressure relief valve. This valve was adjusted through the setting of its spring to maintain the oil pump delivery pressure at 3 bar (gauge). The excess was spilled back into the sump within the engine itself.

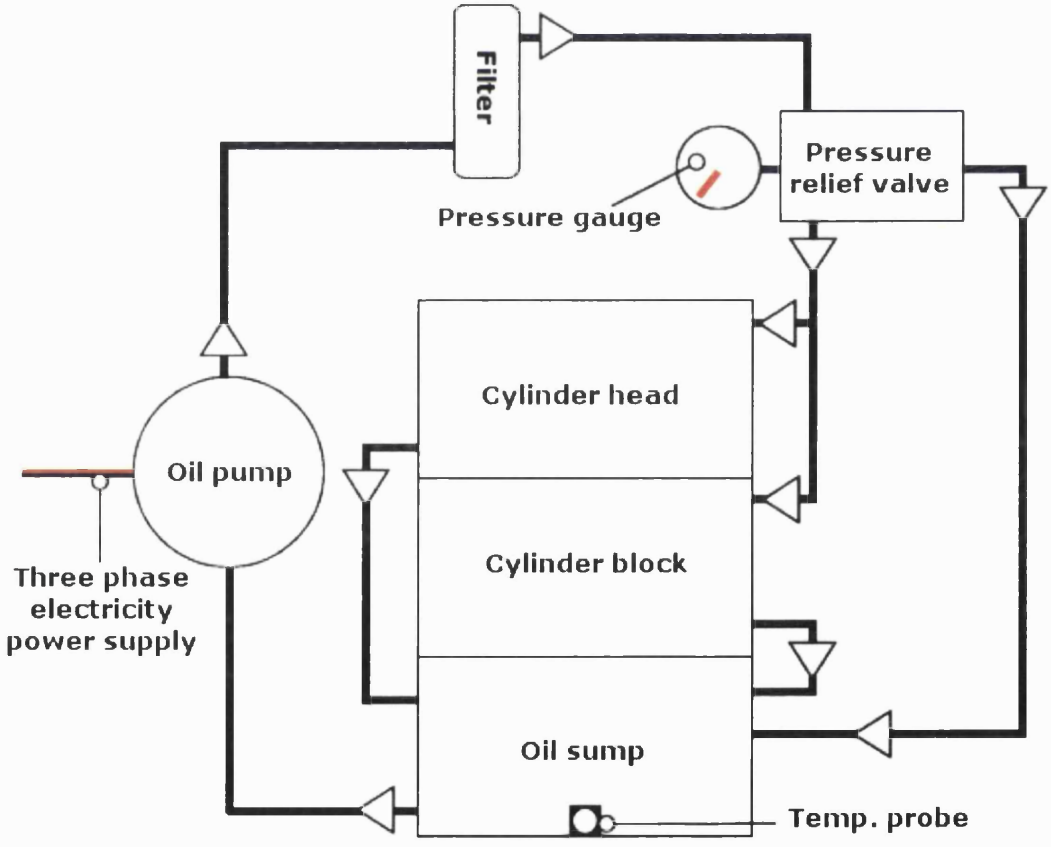

Figure 3.5 - Schematic representation of engine lubrication system.

A dual feed of oil was supplied to the cylinder head (camshaft bearings and cam surfaces) and the Hydra cylinder block (crankshaft and connecting rod bearings). Initial testing was performed

to check that a suitable balance was obtained between the two feeds. Care was taken to return the excess flow to the sump in a manner that minimised oil splashing. The crankcase was ventilated to atmosphere through a specially-constructed wire-wool filter. Full details of the individual components are provided in figure 3.6 below.

Component	Details
Oil pump	Varley double helical gear pump, model 5M3/4EXD6R/04, manufactured in cast iron, fitted with mechanical and internal safety valve. Driven by 0.55 kW EXD flameproof motor running at 960 rpm.
Filter	Parker Hannilin 15CN-1-10B-M-25-C2C2-1.
Pressure gauge	RS 110-826, bottom entry, 0-10 bar.
Temperature probe	RS 228-7445, type k, 1.5 x 50 mm.
Pressure relief valve	Hy-Pro supplied hydraulic pressure relief valve.

Figure 3.6 - Components used in engine lubrication system.

3.2.5 Water system

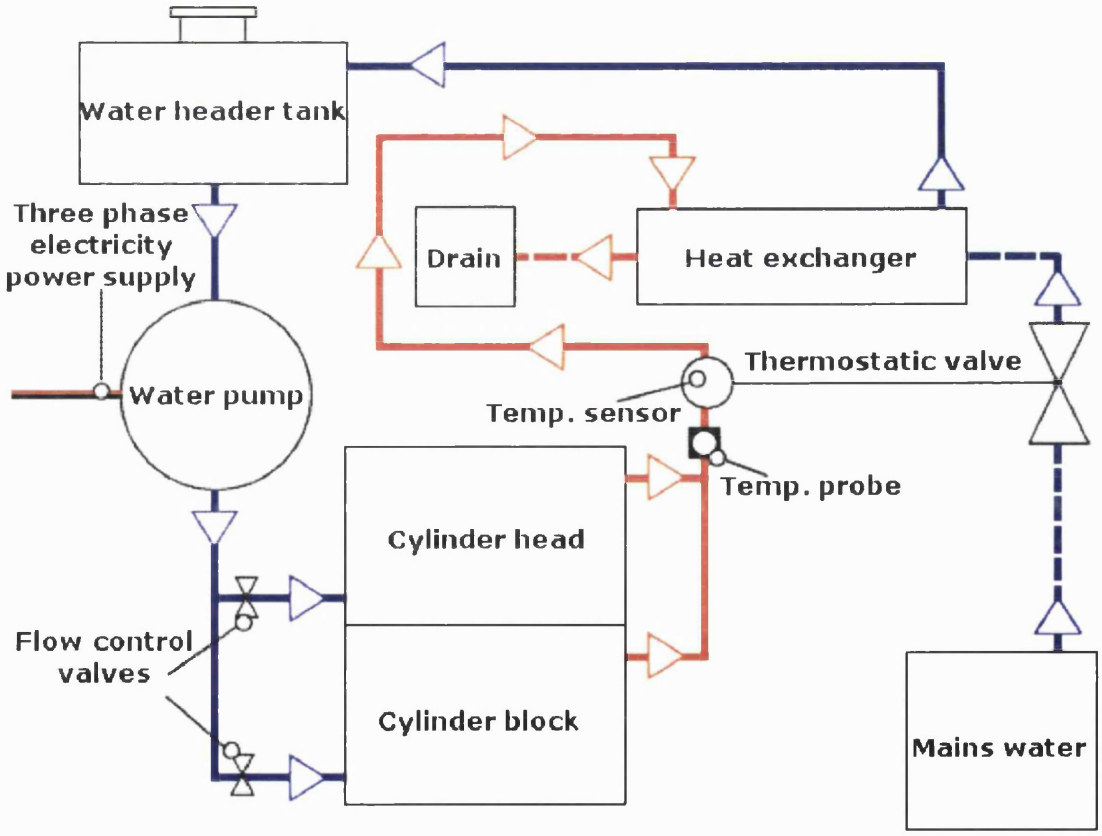

Figure 3.7 - Schematic representation of engine cooling system.

A high-flow water pump, powered by a three-phase electric motor, was used to provide cooling water to the engine. To ensure that both the cylinder head and the cylinder block received

sufficient cooling, these circuits were separated and controlled via two taps to allow system balancing. Tests were performed during the early stages of engine running to set the valves to ensure that there was an approximately equal temperature rise between the water flows in each circuit.

Component	Details
Water pump	Eurostream horizontal end suction pump, model 32/13, manufactured in cast iron, fitted with 139 mm diameter impeller and mechanical seal. Driven by a 1.5 kW EXD flameproof motor running at 2900 rpm.
Heat exchanger	Bowman FG100-1427-2, 3-pass exchanger.
Thermostatic valve	Spirax Sarco SA128 control system with a range of -20°C to 110°C.
Temperature probe	RS 228-7445, type k, 1.5 x 50 mm.

Figure 3.8 - Components used in engine cooling system.

For emissions testing, it was important to control the engine temperature. This was achieved by the use of a thermostatic valve. Once the temperature of the water exiting the engine reached 70°C the sensor of the thermostatic valve opened the flow control valve allowing cold mains water to flow through the heat exchanger. As the system was not pressurised, temperatures higher than 100°C were not attainable. Full details of the individual components are provided in figure 3.8.

3.2.6 Fuel systems

Even though the majority of the testing was carried out with a GDI fuel system, it was required to run with PFI for starting and for baseline testing. Two distinct systems were developed.

Figure 3.9 shows the more complicated GDI system. The high fuel pressure (up to 100 bar) required by the GDI injectors necessitated the development of a high-pressure fuel delivery system. Consideration was given to using the type of pressurised system employed for the injector spray measurement (see chapter 2). However, the limited capacity of such a system was considered unsuitable for engine testing. Pumps from current production GDI vehicles were very difficult to obtain, so a high-pressure hydraulic pump was used. The pump was a fixed displacement pump, containing its own lubricant. It was modified by its manufacturer (Hydro Rene Leduc) to make it suitable for pumping gasoline. The chosen item was a Micro-Pump PB36.5 ES. Technical specifications for this pump are shown in appendix 4.1. It was driven at crankshaft speed by the same belt used to drive the camshafts. A low-pressure fuel pump was required to supply fuel to the high-pressure pump. An electrically-driven unit was chosen, providing 0.3 - 0.4 bar fuel pressure.

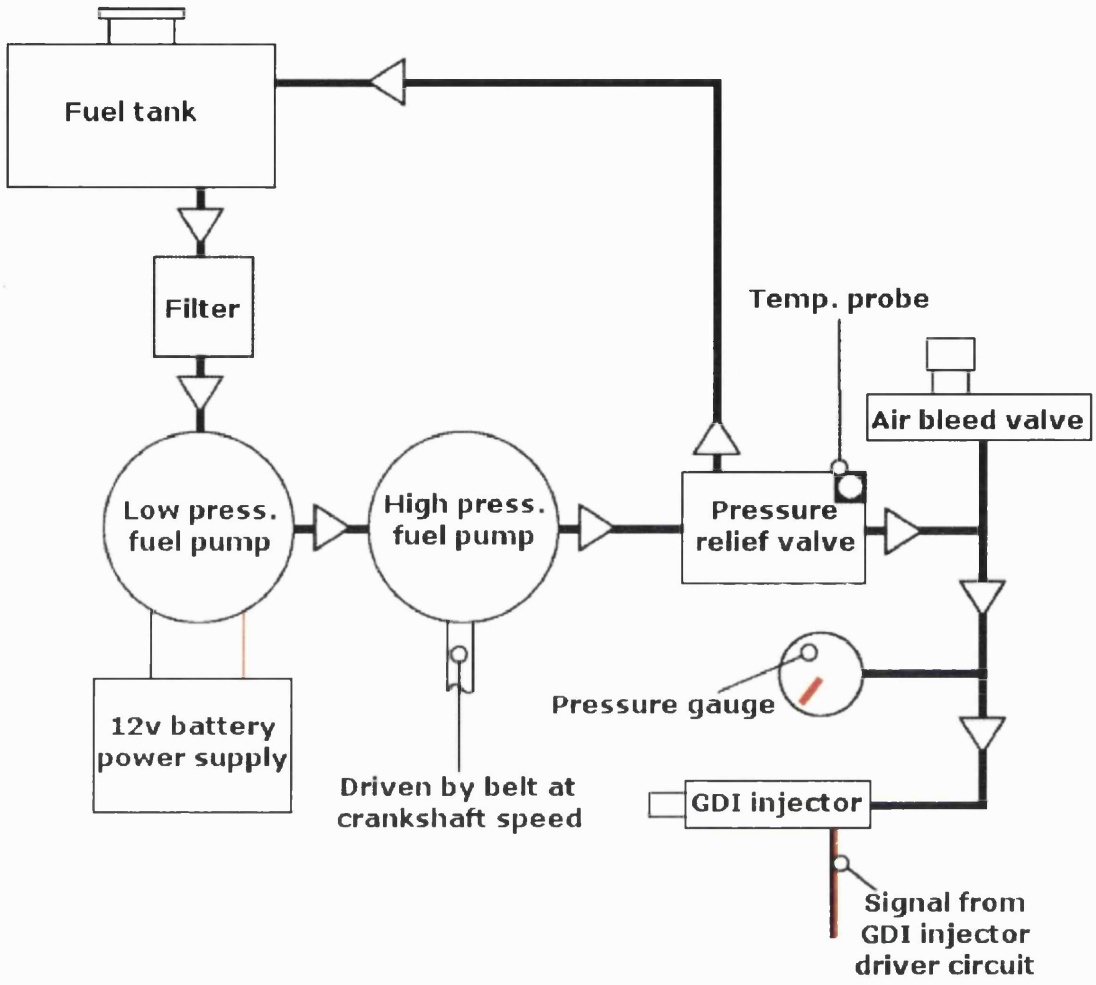

Figure 3.9 - Schematic representation of GDI fuel system.

The fuel pressure to the GDI injector was measured with a Bourdon-type pressure gauge. One of the test variables was fuel pressure, so it was imperative that this could be precisely set and maintained. The pressure was adjusted via a pressure relief valve, which was capable of fine adjustment. Excess fuel was spilled back to the main fuel tank. Full details of the individual components are provided in figure 3.10 below.

Component	Details
Low-pressure fuel pump	Facet Automotive Electronic 574A.
Filter	Facet Fuel Injection Pump Filter, 4 inch dia.
Pressure gauge	Hydraulic Equipment PGF-1001-250.
Pressure relief valve	Oil Control Ltd. 03.51.01.121.
High-pressure fuel pump	Hydro Rene Leduc Micro-Pump PB36.5 ES.
Temperature probe	RS 228-7445, type k, 1.5 x 50 mm.

Figure 3.10 - Components used in GDI fuel system.

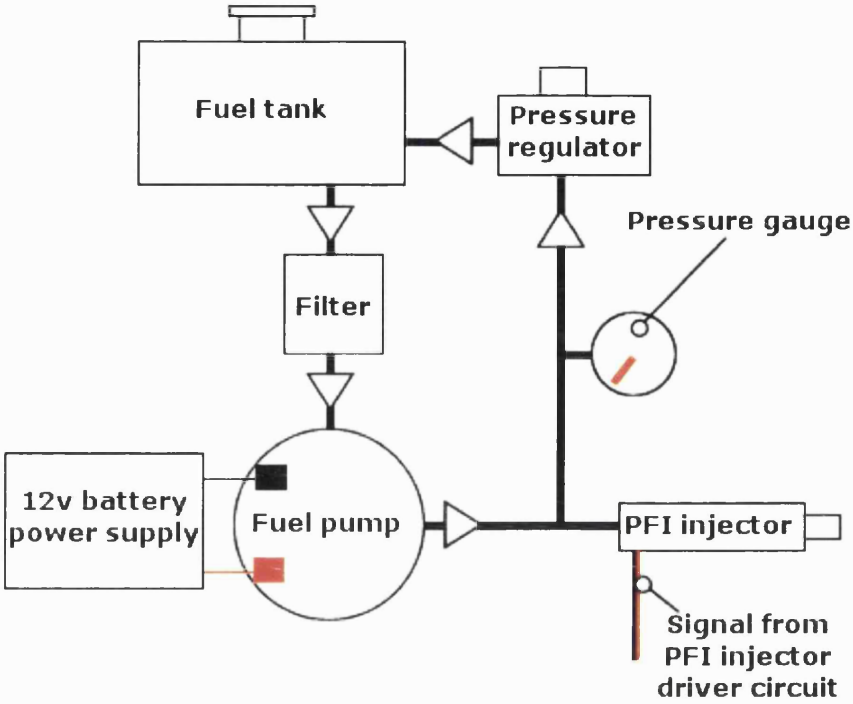

Figure 3.11 - Schematic representation of PFI fuel system.

The PFI system shown in figure 3.11 was much more straightforward. A standard electric PFI pump was used to supply fuel under pressure to twin PFI injectors. The fuel pressure was 3 bar (gauge), held constant by a pressure regulator. Full details of the individual components are provided in figure 3.12 below.

Component	Details
Fuel pump	Facet Roller Vane Fuel Pump, 98 l/h, 80 lbf/in^2.
Filter	Paper-type fuel filter.
Pressure gauge	RS 243-5919, bottom entry, 0-6 bar.
Pressure regulator	Bosch B280 500048.

Figure 3.12 - Components used in PFI fuel system.

3.2.7 Air control system

The strongly pulsating type of flow experienced in the inlet systems of single-cylinder engines can lead to engine instability. For this reason, a large plenum chamber was designed, using the calculations shown in appendix 4.2.

The first estimation of the plenum volume required to allow stable engine running as low as 500 rpm was 0.33 m^3. It was not practical to accommodate a plenum of such a size in the relatively small test cell. A compromise design had an internal volume of 0.2 m^3, and an estimated stable

minimum engine speed of 650 rpm. As most testing was conducted at 1500 rpm, this was satisfactory.

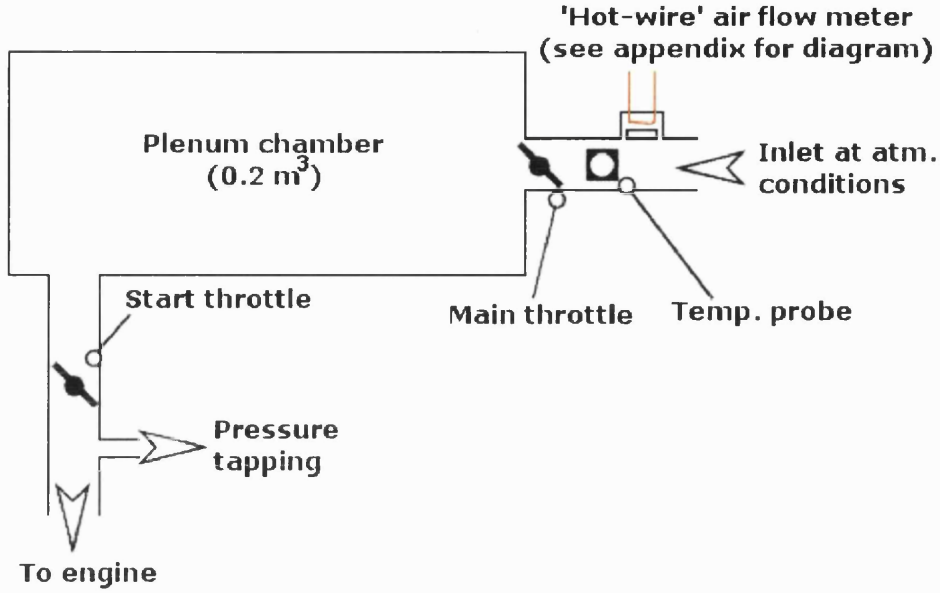

Figure 3.13 - Schematic representation of air control system.

As the plenum was still very large relative to the swept volume (500 cm^3) of the cylinder, there was a significant time delay between an adjustment being made to the main throttle and the full response of the engine. For this reason, a secondary throttle was implemented much closer to the engine to ensure that depression was attainable while starting the engine. A depression was necessary because starting the engine with an intake pressure of near ambient caused significant control problems. Under all test conditions other than starting this throttle was held wide open.

Four measurements were recorded for this system:

(i) - Atmospheric air pressure: a digital barometer was present in the test cell during testing.

(ii) - Atmospheric air temperature: a thermocouple was placed in the air stream upstream of the main throttle.

(iii) - Inlet air pressure: a simple mercury manometer was utilised to measure the depression on entry to the inlet port of the cylinder head. This reading was used for diagnostic purposes and was not used to calculate the engine's performance parameters.

(iv) - Air flow rate: a 'hot-wire' air flow meter measured the air flow at intake to the plenum chamber as shown in figure 3.13. The air flow meter was taken from the engine management system of a 4-cylinder production engine. It was modified to be more suitable for the lower air flow range of the single-cylinder test bed engine by fitting a partial blanking plate. This plate had the effect of changing the ratio of flow between the small measurement passage and the larger bypass passage. The modified flow meter was then calibrated against a rotameter, whose calibration was traceable to a national standard. The air flow meter and its calibration are detailed in appendix 4.3.

3.2.8 Ignition system

The ignition system comprised of the components shown in figure 3.14. A trigger disk was designed to be mounted on the front of the crankshaft. The opto-switch controlling the timing of ignition was fixed to a moving mechanism on the engine crankcase. This arrangement made it possible to alter the ignition timing while the engine was running, as it was not always possible to start the engine at the extreme timings of some of the test points. When the opto-switch sensed a gap in the trigger disk a signal was sent to the Lumenition control module. This then controlled the charge and discharge times of the coil itself. A ballast resistor was incorporated in the circuit to allow compensation for voltage drop during the period of starter motor operation. The circuit itself was part of the engine safety circuit which was all controlled via a conventional "ignition key" mounted on the engine control panel.

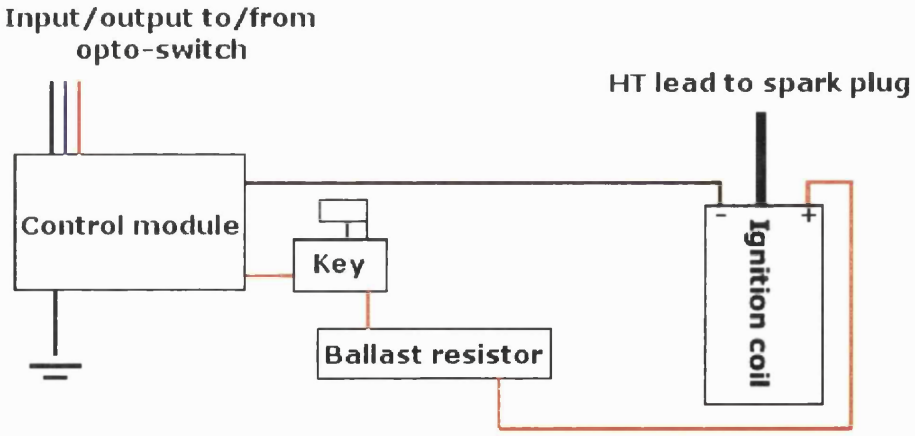

Figure 3.14 - Schematic representation of engine ignition system.

Full details of the individual components are provided in figure 3.15.

Component	Details
Control module	Lumenition Optronics Ignition.
Ballast resistor	1.7 Ω resistance.
Ignition coil	Intermotor 11100 ballast coil.

Figure 3.15 - Components used in engine ignition system.

3.3 Instrumentation

3.3.1 Dynamometer

A Schenck W130 eddy-current dynamometer was utilised for engine testing. Eddy-current dynamometers convert the mechanical work from the drive shaft into heat through first generating electricity, which is then dissipated through currents in a resistive material. Cooling water was used to remove this heat. A recirculating water system was designed for the dynamometer cooling. A schematic of this is shown in figure 3.16.

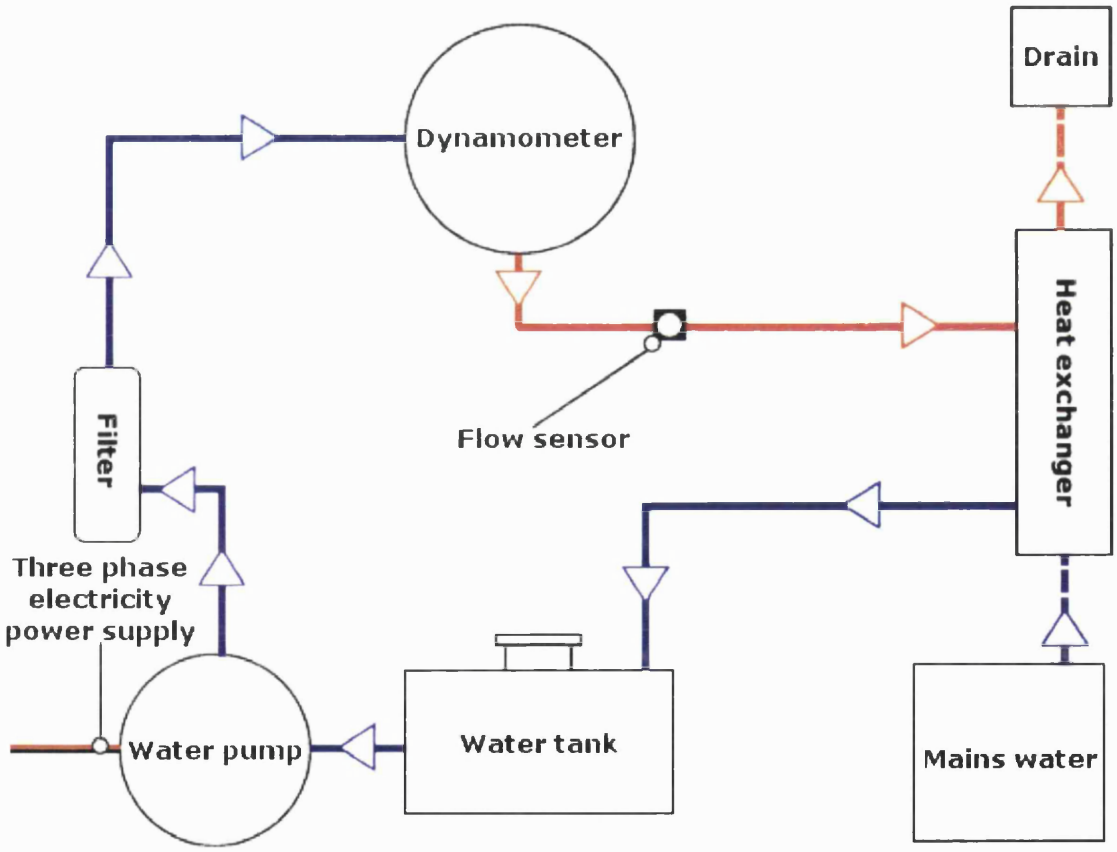

Figure 3.16 - Schematic representation of the dynamometer cooling system.

To measure the torque being produced by the engine, the dynamometer was equipped with a load cell, which incorporated a force transducer. This was linked to the Schenck torque measuring electronic unit, which converted the force on the load cell to torque displaying the

value on a digital read-out in Nm. The system was calibrated using lever arms and weights provided by Schenck.

3.3.2 Fuel flow measurement

The fuel flow rate to the engine is an important measurement. First of all, it was required to enable real-time calculation of the engine's air/fuel ratio so that the engine could be set to the specified air/fuel ratio at each test point. Secondly, it was required for the calculation of BSFC (brake specific fuel consumption), an important engine performance parameter. It was decided to measure fuel flow rate through accurate calibration of the injectors used during the test programme. It was necessary to calibrate each injector at each fuel supply pressure so they were calibrated at 20 and 100 bar fuel pressures. The results of these calibrations are detailed in appendix 4.5. The calibrations were performed with the injectors spraying into air at atmospheric pressure, whereas, on the engine, the injectors were injecting during the induction stroke when the air pressure in the cylinder was around 0.4 bar below atmospheric pressure. This difference in condition resulted in the differential pressure being 0.4% different for the 100 bar fuel supply pressure and 2.0% different at 20 bar. It was decided that these differences would have had negligible effect on engine test results at 100 bar and only a slight effect at 20 bar. Calibration of the injectors was performed at the same pulsing rate as experienced on the engine when operating at its test condition speed of 1500 rpm. Care was taken to minimise the loss of the 'light ends' of the gasoline during calibration when the injector was spraying into a measuring cylinder.

A 'macro' program was written by the author which calculated the instantaneous air/fuel ratio of the engine for a given pulsewidth, injector, fuel pressure, and the signal from the air flow meter. This method made it possible to alter the air/fuel ratio quickly and easily while the engine was running.

3.3.3 Cylinder pressure measurement

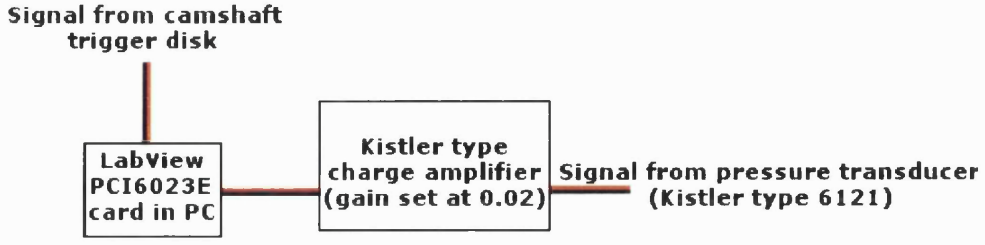

Figure 3.17 - Schematic representation of the engine data-logging system.

The cylinder pressure was recorded throughout testing. This pressure trace was useful for diagnostic purposes while the engine was running, and also to assist with analysis of the engine performance data. A Kistler pressure transducer was permanently installed in the cylinder head. 100 engine cycles were logged at each test point using a PC-based data-logging system (figure 3.17). An existing computer program [Dargains, 1998], using National Instruments LabView interface, converted this data into a useful graphical format. The cylinder pressures were displayed, along with the pressure-volume 'indicator diagram'.

The data-logging system relied on a crankshaft angle position signal to act as a reference point. A trigger disk mechanism, using an opto-switch, was already in place on the exhaust camshaft (for triggering the fuel injection circuit). This signal was also taken to the data-logging system. However, as the position of this trigger moves according to the desired injection timing, it was necessary to feed the offset into the program. The offset (measured in crankshaft angle degrees) is the distance between the signal and the TDC setting. This was determined accurately (+/- 0.5°) by motoring the engine and observing the resultant pressure-volume plot. It was assumed that when no combustion is taking place, the compression and expansion curves meet at a defined point. The offset was adjusted until the curves met at this single point. Full details of the individual components are provided in figure 3.18 below.

Component	Details
PCI control card	National Instruments PCI6023E.
Pressure transducer	Kistler type 6121, serial no. 497023.
Charge amplifier	Kistler serial no. 2464.
Opto-switch for camshaft trigger	RS303-1192.

Figure 3.18 - Components used in the cylinder pressure measurement system.

3.3.4 Exhaust gas measurements

A stainless steel exhaust system was constructed to fit directly onto the exhaust port of the single-cylinder engine. It was connected to the laboratory's exhaust extraction system. The positions of two measurements were as follows:

(i) - Exhaust gas temperature: a k-type thermocouple was placed in the gas flow approximately 0.2 m from the exhaust valves.

(ii) - Exhaust emissions: a single sampling point was positioned 1.4 m from the exhaust valves. The sample probe is shown in figure 3.20.

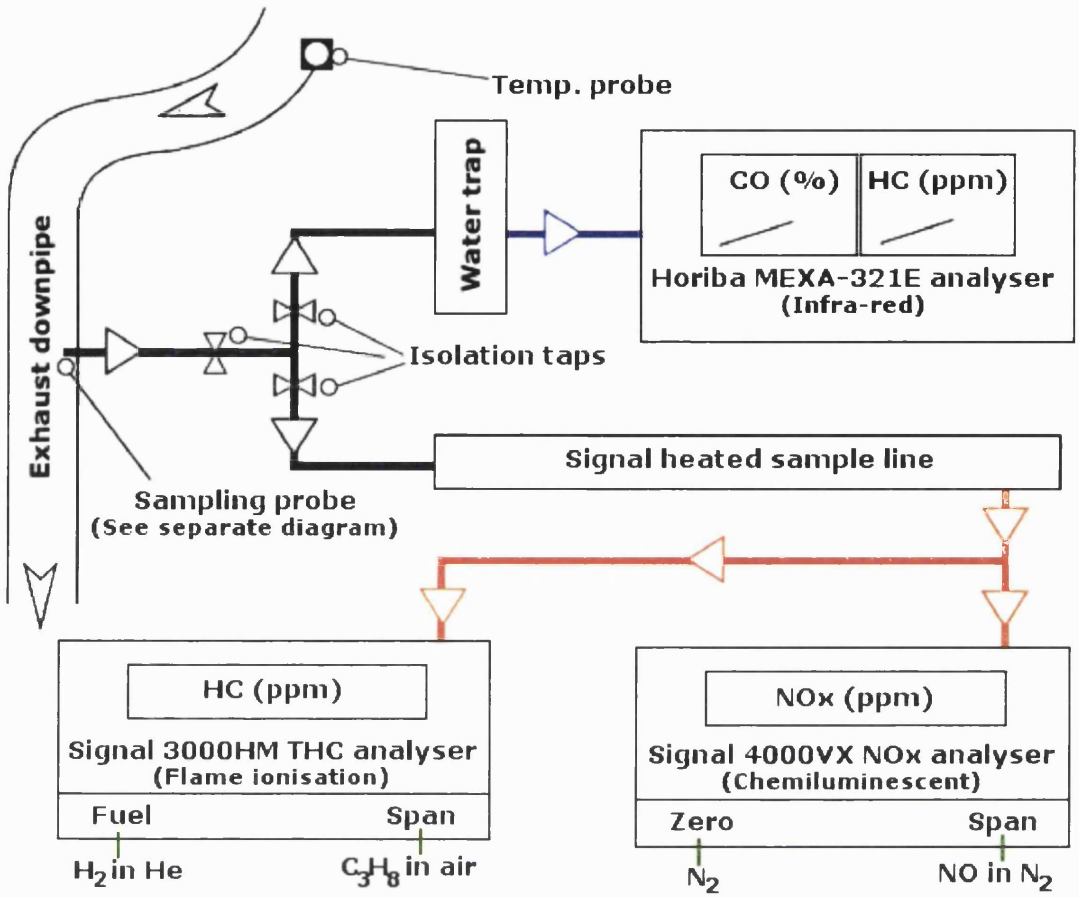

Figure 3.19 - Schematic representation of the exhaust gas measurement system.

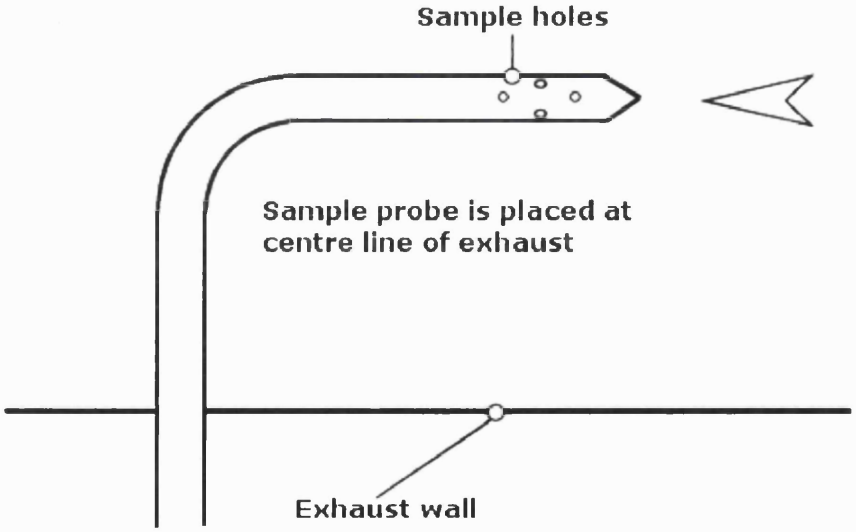

Figure 3.20 - Schematic representation of sample probe in exhaust.

Horiba analyser: CO (%) & HC (vppm)

The Horiba MEXA-321E analyser required the sample to be at a temperature of no more than 80°C. Exhaust gases were sampled at temperatures of up to around 700°C and then fed through a long (1.1 m) falling stainless steel pipe to a water trap, before being connected to the analyser through flexible tubing. This sampling system both cooled the gas and removed excess H_2O. No external gases were required during engine running. A mixture of 6.0% CO and 1800 vppm n-butane in nitrogen was used to calibrate the instrument at the beginning of each test.

Signal Instruments analysers: HC (vppm) & NOx (vppm)

The Signal Instruments analysers required the sample to be heated to 180°C. This was performed by a Signal 530 temperature controller and heated sample line. The Signal 3000HM THC analyser used hydrogen in helium as a fuel, and propane in air (2000 vppm) to calibrate the analyser. The Signal 4000VX NOx analyser required nitrogen as the zero gas and NO in nitrogen (1000 ppm) as the span gas.

Readings from the analysers were recorded in vppm (volumetric parts per million) and then converted to specific emissions values (g/kWh) using the readings of air flow rate, fuel flow rate and brake power. It was thought that this would allow more reliable comparisons to be made, particularly since air/fuel ratio (and hence exhaust gas flow rate) was one of the four test variables.

3.4 Testing

3.4.1 Fuel

Regular gasoline was chosen as the test fuel, to ensure that the results were comparable with normal engine running conditions. All the fuel was taken from a single supply of pump gasoline. Great care was taken not to allow the 'lighter ends' of the gasoline to evaporate during fuel handling. The density of the fuel was measured as 750 kg/m^3 by weighing a known volume, first of all at room temperature from the fuel tank, and secondly after pumping through the high-pressure fuel system.

3.4.2 Engine test condition

The World Wide Mapping Point (WWMP) is a commonly-used test point for engine testing. This test condition is 1500 rpm, 2.62 bar BMEP, and it has been chosen to represent a typical inner-city cruise condition on a standard size car. Care should be taken in comparing the results of the test engine at the WWMP with those of a typical production engine due to differences in FMEP (frictional mean effective pressure). Single cylinder engines normally have considerably

higher FMEP values than multi-cylinder engines. It was true that the test engine did not have to drive oil and water pumps, but the fuel pump was engine-driven and was considerably over-sized. It was estimated from measurements and calculations that the IMEP when the test engine was run at the WWMP was 4.0 bar, and this was the value used for the calculation of the specific emissions figures.

3.4.3 Engine procedures

In order to obtain consistent test results it was important that the engine should be prepared for testing in a methodical way. Details of the procedures for starting, warm-up, burn-off and shutdown are given in appendix 4.4. Burn-off testing was performed at the end of each day of testing to ensure that combustion chamber deposits did not build up as a result of continuous low-load running.

3.4.4 Central Composite Rotatable Design

Statistical methods of experiment design first became popular with researchers in the agriculture industry. The time between tests was long, for example waiting for a crop to grow, so it was important to maximise the amount of information gleaned from each experiment. In more recent years, the work of Box and Wilson [1951] has gained wider acceptance in areas of research and development. These ideas have been applied to engine testing during the last 15 years and reported on by Seabrook [1995] and Ghauri [1999]. Indeed, the computer program used by the author is based on that developed by Ghauri [1999].

In engine research, most responses are dependent on a number of variables. For instance, inlet valve timing, exhaust valve timing and ignition timing (amongst others) will all influence the emissions of NOx. Often, it is desirable to optimise (minimise in the case of NOx) a given response. The traditional approach was to change each variable one at a time. Using NOx as an example, the exhaust valve timing and the ignition timing would first of all be held constant (path AB in figure 3.21), as the optimum inlet valve timing level was determined. Inlet valve timing would then be set at that value while for instance, exhaust valve timing was altered (path BC), and so on, until a near-optimum point has been found (point D).

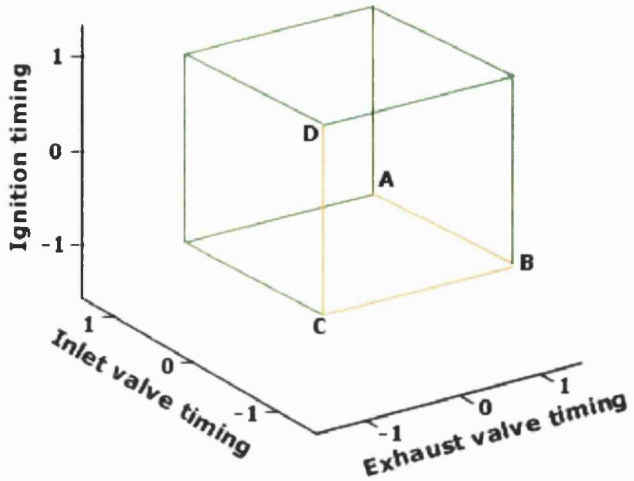

Figure 3.21 - The traditional approach to a three variable experiment at two levels.

The path followed in the example above is shown in orange, but no information may be had about the rest of the cube volume. To do this, a researcher would have to conduct a full-factorial experiment, which in a 3-variable experiment at 2 levels would require 8 test points. The number of tests necessary increases sharply with more variables and levels. Four variables at 5 levels would require 625 points. This clearly would be a very time-consuming experiment.

The Central Composite Rotatable Design (CCRD) has been found to be a particularly efficient method of dealing with multi-variable experiments where there are non-linear responses and interaction between the variables. The CCRD uses star and centre points in addition to the 2-level factorial cube shown in figure 3.21 above. Figure 3.22 shows the case for 3 variables at 5 levels. The number of centre points and the distance of the star points from the centre are two critical properties of the experiment design, and they are related to 'orthoganality' and 'rotatability' of the test matrix.

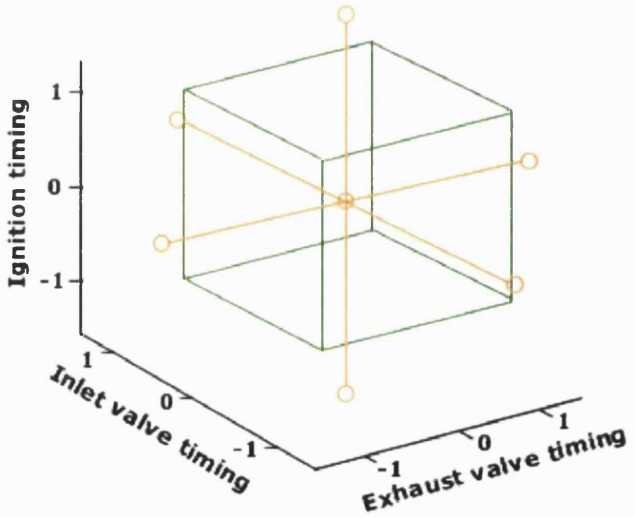

Figure 3.22 - A CCRD for an experiment with three variables at five levels.

Orthoganality allows the effect of each variable to be determined without any distortion from the others in the test. Rotatability indicates that the variance in a design is only a function of the distance from the centre points, ensuring a spherical distribution of data. There are established tests of orthoganality and rotatability, which determine the properties of an experiment design.

It was required to test the effects of four variables (inlet valve timing, ignition timing, injection timing and air fuel ratio) for the author's test programme. Thirty-one test points were necessary with a CCRD experiment, with seven of these being centre points. According to Cochran and Cox (1957) the experiment plan would be set out as follows in figure 3.23.

A	B	C	D
-1	-1	-1	-1
1	-1	-1	-1
-1	1	-1	-1
1	1	-1	-1
-1	-1	1	-1
1	-1	1	-1
-1	1	1	-1
1	1	1	-1
-1	-1	-1	1
1	-1	-1	1
-1	1	-1	1
1	1	-1	1
-1	-1	1	1
1	-1	1	1
-1	1	1	1
1	1	1	1
-2	0	0	0
2	0	0	0
0	-2	0	0
0	2	0	0
0	0	-2	0
0	0	2	0
0	0	0	-2
0	0	0	2
0	0	0	0
0	0	0	0
0	0	0	0
0	0	0	0
0	0	0	0
0	0	0	0
0	0	0	0

Figure 3.23 - CCRD experiment plan.

In this matrix, 0 represents a centre point, with -2, -1, 1 and 2 being the levels. The order of testing of this design was altered slightly to ease engine testing. For instance, during testing, it was very easy to alter the air fuel ratio and the ignition timing, but injection timing and inlet valve timing were more difficult. The final test matrix was as follows in figure 3.24.

Test point	Air fuel ratio	Ignition timing	Injection timing	Inlet valve timing
		(deg. bTDC)	(SOI deg. aTDC)	(IVO deg. aBDC)
1	17	25	100	175
2	18.5	17.5	60	162.5
3	15.5	17.5	60	162.5
4	18.5	32.5	60	162.5
5	15.5	32.5	60	162.5
6	18.5	17.5	140	162.5
7	15.5	17.5	140	162.5
8	18.5	32.5	140	162.5
9	15.5	32.5	140	162.5
10	17	25	100	175
11	18.5	17.5	60	187.5
12	15.5	17.5	60	187.5
13	18.5	32.5	60	187.5
14	15.5	32.5	60	187.5
15	18.5	17.5	140	187.5
16	15.5	17.5	140	187.5
17	18.5	32.5	140	187.5
18	15.5	32.5	140	187.5
19	17	25	100	175
20	14	25	100	175
21	20	25	100	175
22	17	10	100	175
23	17	40	100	175
24	17	25	20	175
25	17	25	180	175
26	17	25	100	175
27	17	25	100	150
28	17	25	100	200
29	17	25	100	175
30	17	25	100	175
31	17	25	100	175

Figure 3.24 - Test matrix used for engine testing.

The variable ranges were chosen after a series of star points (i.e. extreme points) were tried on the engine. Obviously, the wider the range, the more information that could be gleaned about the engine and its operating envelope. On the other hand, inclusion of points of unstable running (e.g. very lean) would lead to inaccuracies in the results as the program attempts to fit an equation to the experimental data. The initial checks involved running at the required test condition. The criterion for inclusion of a point within the test matrix was that the engine should run in a stable manner without unduly high hydrocarbon emissions.

Multiple regression analysis was applied in the MATLAB computer program to compute a regression function for each response from two independent variables while the other two variables were set to their centre points. There are four useful multiple regression models [Devore, 1991]: the first-order model, the second-order no interaction model, the first-order

interaction model and the second-order model with interaction. The latter was used in this work, and is of the form:

$$y = b_0 + b_1x_1 + b_2x_2 + b_3x_1^2 + b_4x_2^2 + b_5x_1x_2 + \varepsilon$$

y = dependent variable (e.g. NOx emissions)

b_0 - b_5 = constants

x_1 - x_2 = independent variables (e.g. air/fuel ratio)

ε = a random error which is assumed to be normally distributed

The use of such a complex model is necessary, particularly with regards to engine emissions, as the interaction between independent variables has been established. The presence of these terms of interaction in the model illustrates that, even if one of the variables is held constant, the effect of changing the other will not be fully understood unless the actual value of the first is known.

An example of a typical set of results is shown in figure 3.25. The particular example taken is for HC emissions with the 60° injector mounted in the side position, supplied with fuel at 100 bar at the standard test condition of 1500 rpm and 2.62 BMEP. There are three types of graph in use. The first (figure 3.25a) is a plot of standardised residual values (i.e. a measure of the difference between the position of the actual test point and that predicted by the model) against case number (equivalent to test point) produced from the regression analysis. As well as the actual residual values, error bars at the 95% confidence limits are added. The addition of these bars quickly indicates any outliers. It follows that an outlier is a point for which the model has failed to provide a satisfactory fit. More specifically, it is a point for which the model prediction lies outside the 95% confidence limit boundaries applied to the actual test point. The 95% confidence limits are calculated from the measured variation in the variable at the centre-point setting. The MATLAB program automatically highlights outliers in red. For the model to be adequate, the residuals should be randomly scattered. Any trend in the residuals will indicate an abnormality, and often clearly points to the test point of interest.

The second type of graph (as seen in figure 3.25(b)) is a bar graph, used as a plot of the most influential variables. The regression model identifies the factors found to be significant with a confidence greater than 95%. The influence of each factor is then converted to the standardised t value indicated, so that its relative influence to the other factors may be illustrated. The main factors are A (air/fuel ratio), B (ignition timing), C (injection timing) and D (inlet valve timing). Additionally, there is the possibility of squared factors (e.g. AA, BB) and an interaction between factors (e.g. AB, BD).

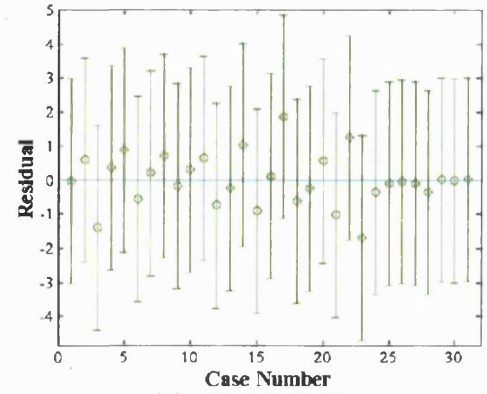

(a) - Residuals plot.

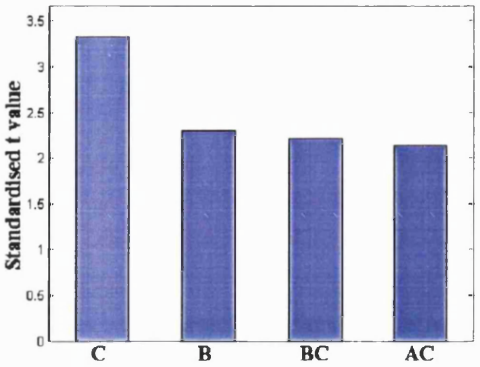

(b) - Influential variables.

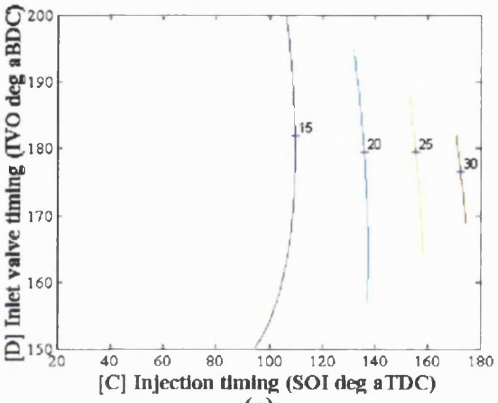

(c)

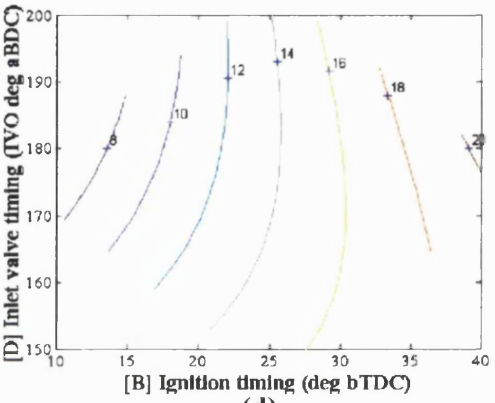

(d)

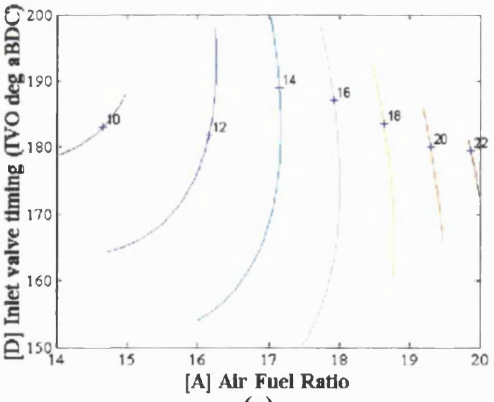

(e)

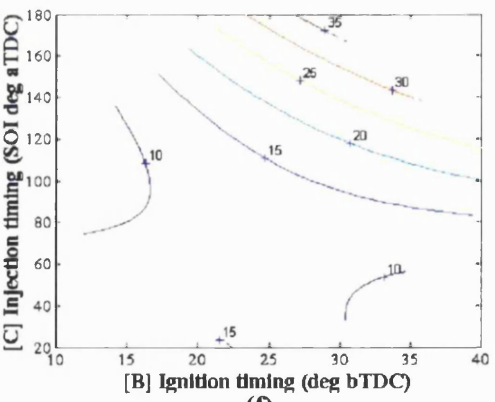

(f)

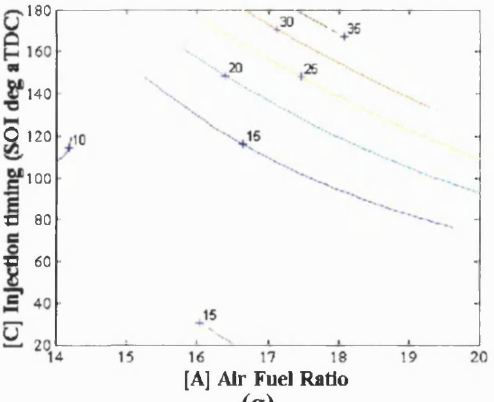

(g)

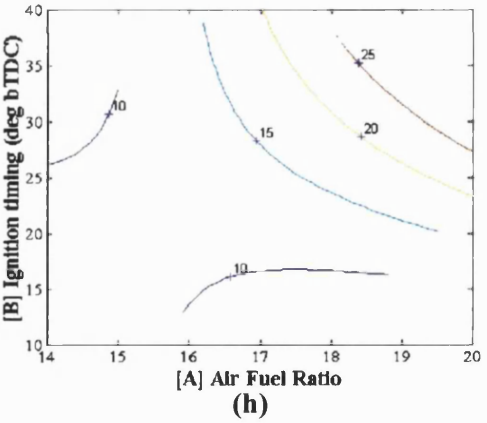

(h)

Figure 3.25 - Example results for HC emissions (g/kWh). 60° injector, side injection, 100 bar fuel pr.

The remaining graphs are plots of the results from the modelled responses. The regression equation calculated by the program is used to plot a series of contour maps. Each plot shows the effect of two variables on the response while the other two variables are set to their centre point values. Figures 3.25(c) - 3.25(h) are examples of a set of such plots. Particular care must be taken in using plots where there is a variable that interacts with another variable, and only one of the variables is plotted. For instance, figure 3.25(b) shows that there is a BC interaction and figure 3.25(c) is a plot of C and D at the centre-point value of B. The relationship between C and D is likely to be different if it were to be examined at another value of B.

Chapter 4
ENGINE TEST RESULTS

4 - Engine test results

4.1 Introduction

This chapter can be considered as two separate parts. In the first part, the results from each configuration are looked at in isolation with a view to understanding the form of the responses. Each section from 4.2 to 4.7 covers an individual configuration. They are sub-divided into the four individual responses (HC emissions, NOx emissions, BSFC and exhaust gas temperature). For each response, a summary table is supplied providing information on the result, the results are discussed, and there is a page of graphs as described in 3.4.4.

In the second part (section 4.8), there is an attempt to amalgamate all the test data into a single cohesive picture of the engine's performance. The configurations are compared, and the most efficient one discussed in detail. In this section, some of the more unusual results are also discussed with the aid of interpretation diagrams. The engine settings are referred to as A, B, C and D throughout this chapter. The key is as follows:

A = Air/fuel ratio
B = Ignition timing (measured in CA degrees bTDC)
C = Fuel injection timing (measured in CA degrees aTDC)
D = Inlet valve timing (measured in CA degrees aBDC)

4.2 90° injector, 100 bar fuel pressure, side injection

4.2.1 Hydrocarbon emissions

No. of outliers	4
Influential variables	C, AC, A, BC, CC
Highest t value	8.5

Figure 4.1 - Summary of CCRD results for HC emissions.

Injection timing is the most influential variable on HC emissions with this configuration. In figure 4.5(c), (f) and (g) it is shown that later injection timing increases HC emissions. This is as expected. As fuel injection is delayed, there is less time for the fuel to mix with the air. Poor mixture preparation is a common cause of high HC emissions. The values of specific HC emissions are quite high compared with most of the other configurations tested (see later sections). This again suggests poor mixture preparation leading to locally rich areas.

As there are four outliers, it is worth looking at the model in more depth to retain confidence in the response curves. The four outliers correspond to test points 6, 14, 21 and 25 of the testing matrix (figure 3.24). Test point 6 corresponds to a relatively lean air/fuel ratio (18.5:1) and a

relatively late injection timing (140° aTDC). The poor mixture preparation resulting from the latter, combined with the lean average air/fuel ratio, might well have caused unstable combustion resulting in the HC emissions being considerably higher than the predicted value, as apparent in figure 4.5(a). Test point 21 was found to be the most common outlier in all testing. At this test point, the engine is running at an air/fuel ratio of 20:1 which is the leanest setting of the test sequence. This setting was close to or on the lean limit of the various configurations tested with instability promoted by slow and inconsistent combustion. Similarly, test point 25 was not always stable. It represented the latest injection timing setting (180° aTDC), reducing the amount of time available for the fuel and air to mix. Such instability would cause large cycle-to-cycle variability, and may lead to HC emissions not predicted by the model.

4.2.2 NOx emissions

No. of outliers	2
Influential variables	B, C, A, CC, AA, AD, BC
Highest t value	12

Figure 4.2 - Summary of CCRD results for NOx emissions.

Ignition timing has the largest influence on NOx emissions in this configuration, followed by injection timing, and then air/fuel ratio. Figure 4.6(d), (f) and (h) all illustrate lower NOx emissions when the ignition timing is retarded. Retarded timing has the effect of reducing peak pressures and temperatures within the combustion chamber, leading to a reduction in the formation of NOx.

Running the engine lean, as shown in figure 4.6(e), (g) and (h) reduced the NOx emissions. Lean mixtures produce lower peak combustion temperatures, reducing the formation of NOx.

Additionally, later injection timing, as shown in figure 4.6(c) and to a lesser extent in figure 4.6(g), reduced NOx emissions. This is thought to be an effect due to cooling of the intake air, and is discussed further in section 4.8.

The model itself appears to be a good fit, with many of the data points lying close to their predicted positions, and only two outliers. Test point 15 (the second and more significant outlier) is another test point that combines the relatively lean air/fuel ratio of 18.5:1 with the relatively late injection timing of 140° aTDC. Again it is likely to be susceptible to cycle-to-cycle variability.

4.2.3 Brake specific fuel consumption

No. of outliers	0
Influential variables	C, AC
Highest t value	5

Figure 4.3 - Summary of CCRD results for BSFC.

Injection timing is the single variable of significance to influence BSFC with this configuration. This is borne out by figure 4.7(f). Earlier injection leads to marked reductions in BSFC, due to the increased time available for mixture preparation ensuring complete combustion.

4.2.4 Exhaust gas temperature

No. of outliers	0
Influential variables	D, B, BB, AD
Highest t value	2.5

Figure 4.4 - Summary of CCRD results for exhaust gas temperature.

The variables responsible for changes in exhaust gas temperature (in this configuration) are mainly inlet valve timing, followed closely by ignition timing. Figure 4.8(d) is the plot of these two variables with the other two variables at their centre points. The main trend from this graph is that the temperature is reduced when ignition timing is advanced, until a timing of approximately 30° before TDC, at which point the temperature increases once more. The reduction in temperature results from more efficient conversion of chemical energy in the fuel into work. The minimum exhaust gas temperature at a timing of 30° bTDC suggests that this is the most efficient ignition timing. This is supported by the BSFC plots in figure 4.7(d) which indicates that the BSFC does tend to give a minimum value at this condition, although the variation at other ignition timings is not great. The effect of the inlet valve timing is quite pronounced, though there is a complex trend for a decrease in the temperature when the inlet valve timing is earlier. This is also in figures 4.8(c) and 4.8(e). Again this can be explained by the more efficient conversion of chemical energy to work, this time because the earlier inlet valve opening results in the inlet valve closing closer to BDC, giving a higher effective compression ratio.

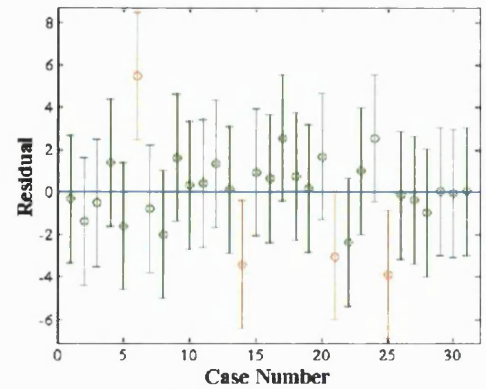

(a) - Residuals plot.

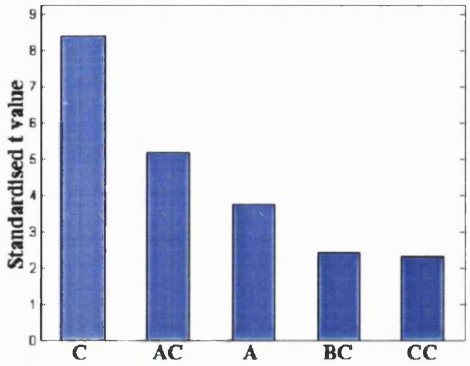

(b) - Influential variables.

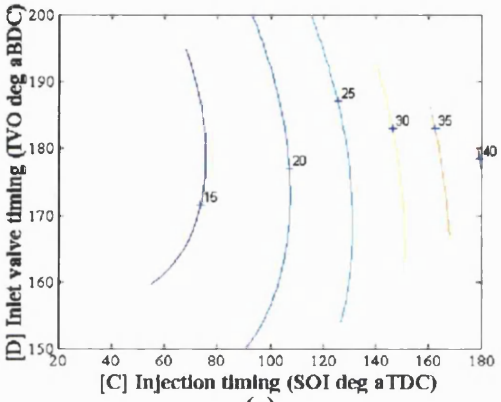

(c)

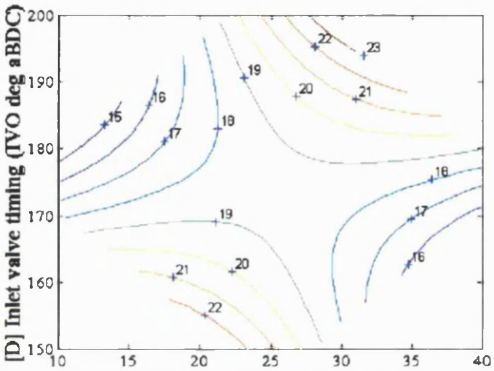

(d)

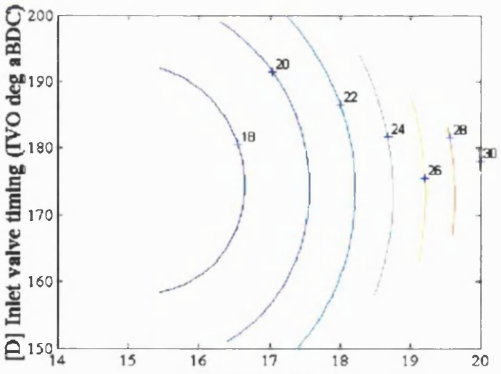

(e)

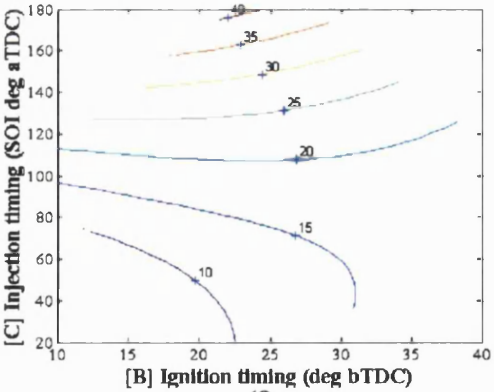

(f)

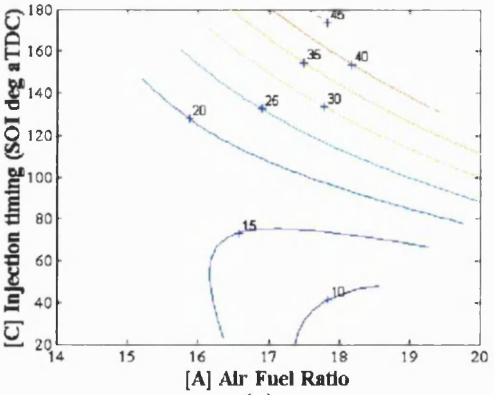

(g)

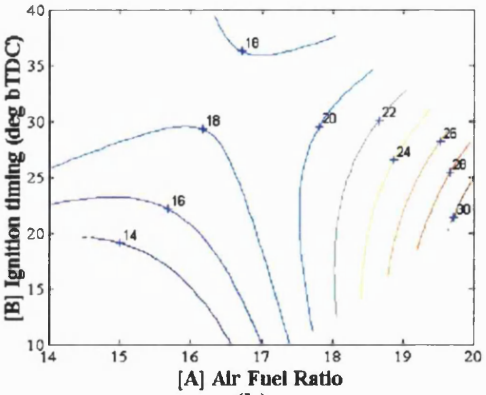

(h)

Figure 4.5 - Results set for HC emissions (g/kWh). 90° injector, side injection, 100 bar fuel pressure.

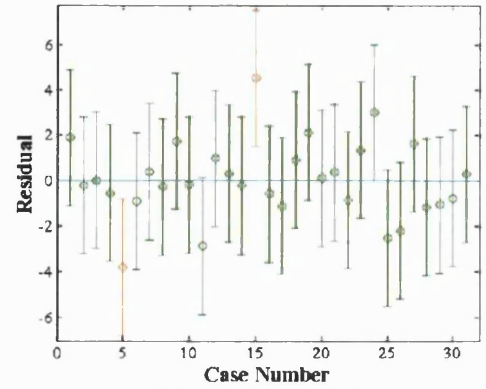

(a) - Residuals plot.

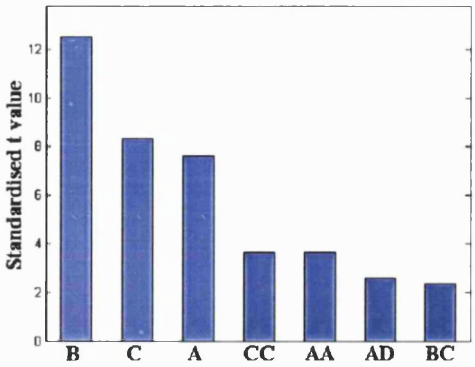

(b) - Influential variables.

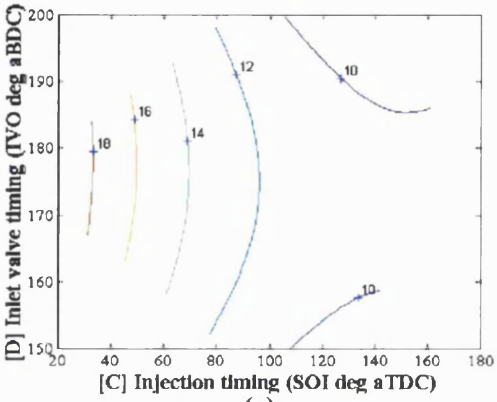

(c)

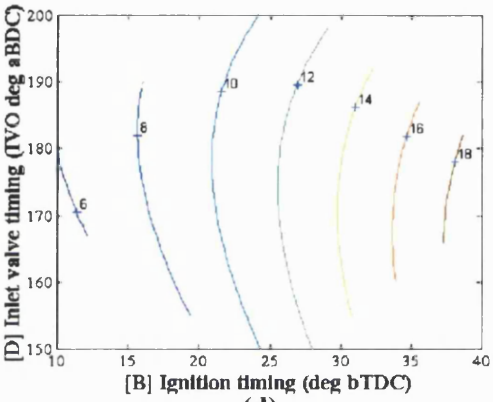

(d)

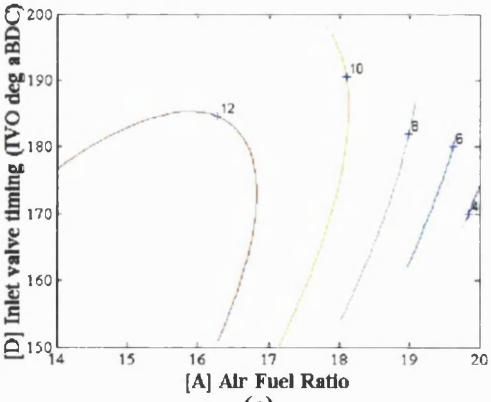

(e)

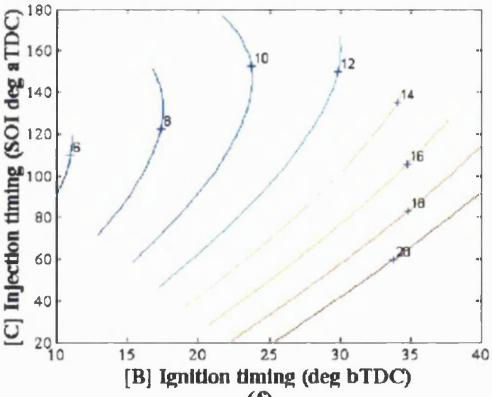

(f)

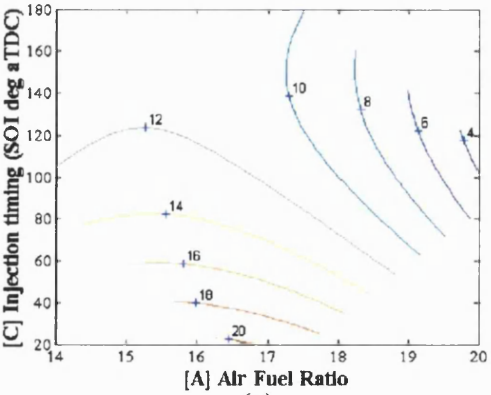

(g)

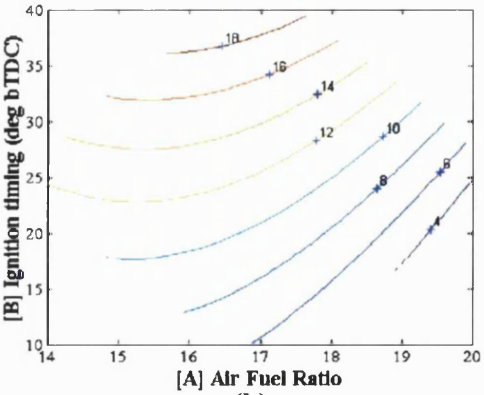

(h)

Figure 4.6 - Results set for NOx emissions (g/kWh). 90° injector, side injection, 100 bar fuel pressure.

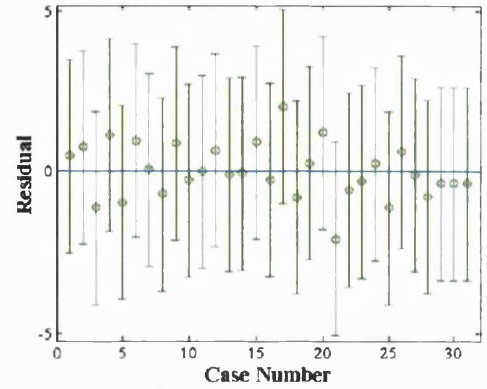

(a) - Residuals plot.

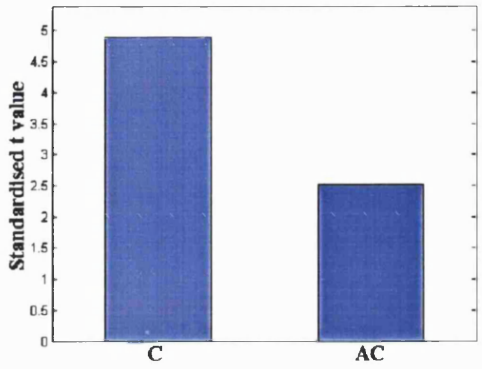

(b) - Influential variables.

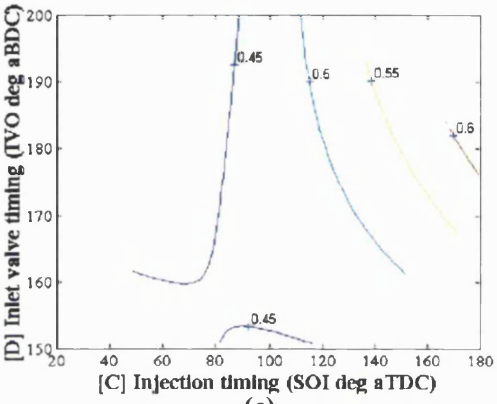

(c)

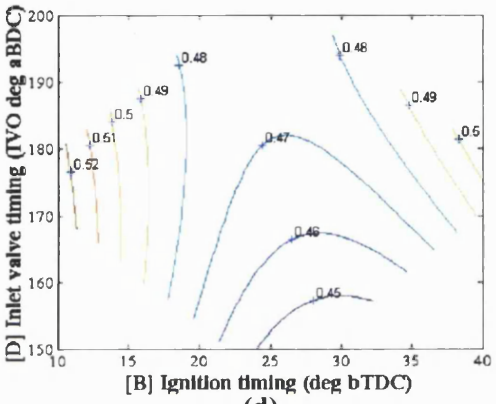

(d)

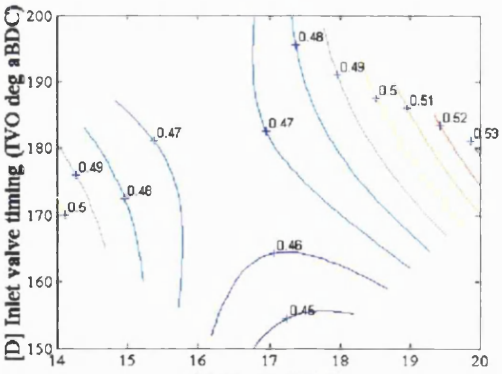

(e)

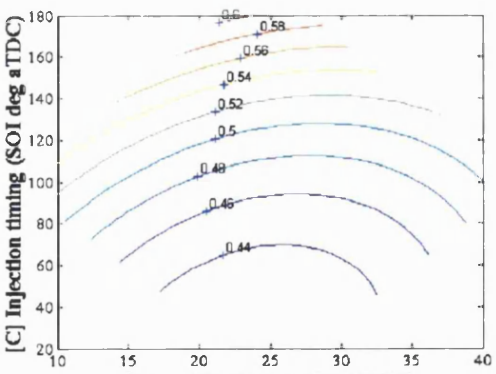

(f)

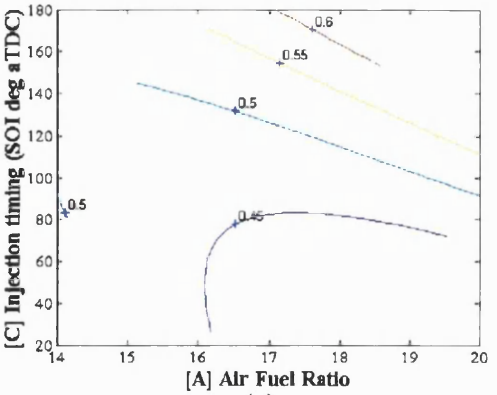

(g)

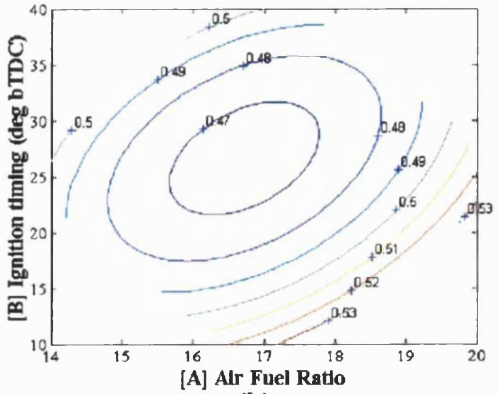

(h)

Figure 4.7 - Results set for BSFC (kg/kWh). 90° injector, side injection, 100 bar fuel pressure.

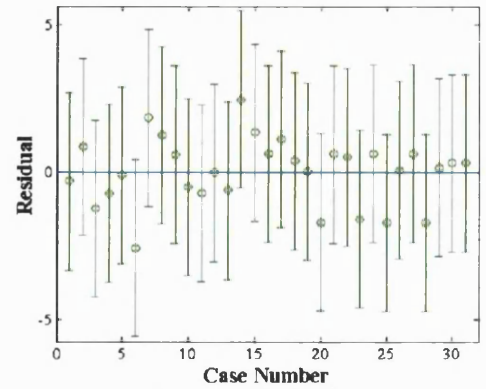

(a) - Residuals plot.

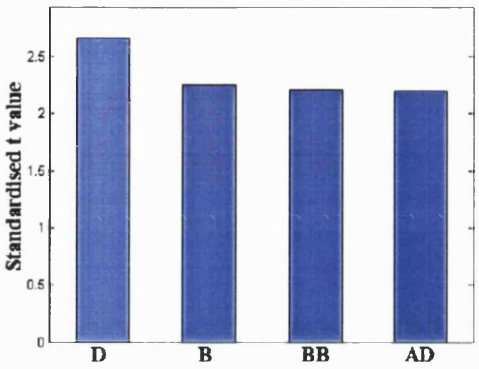

(b) - Influential variables.

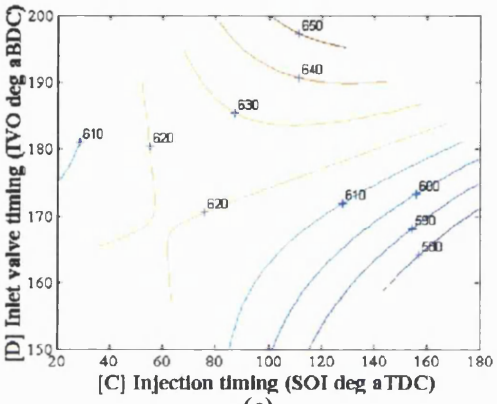

(c)

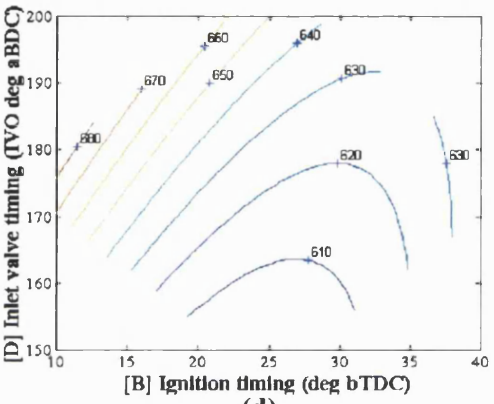

(d)

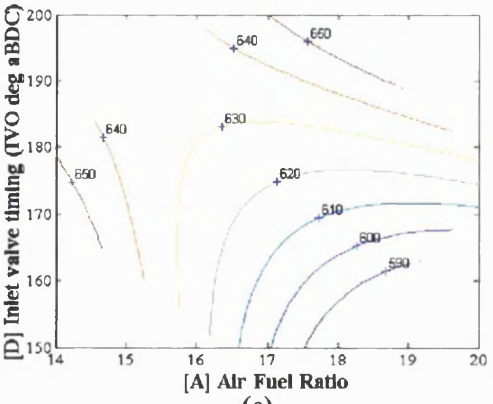

(e)

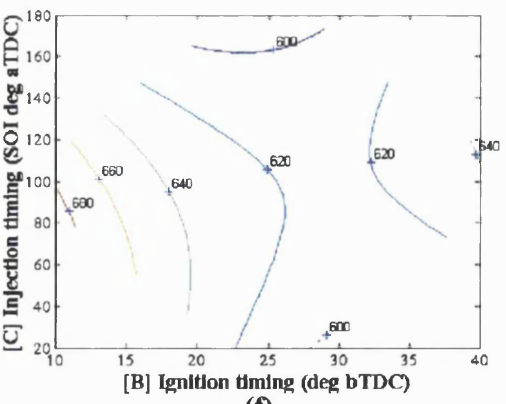

(f)

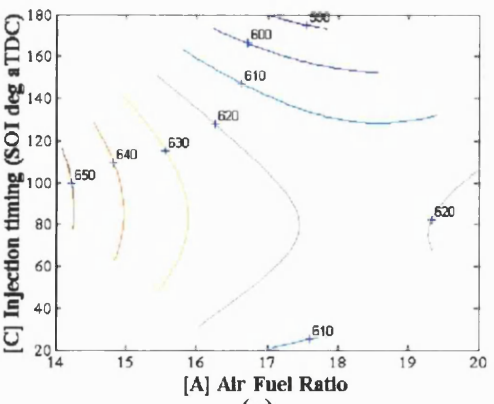

(g)

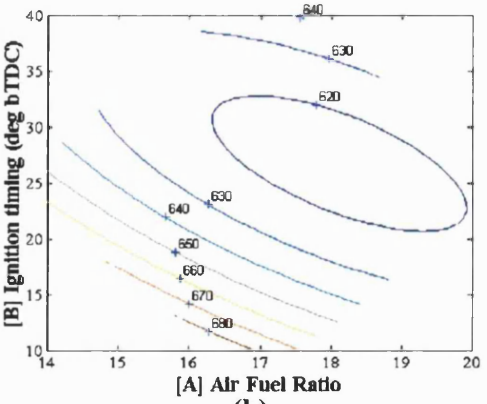

(h)

Figure 4.8 - Results set for exhaust gas temperature (°C). 90° injector, side injection, 100 bar fuel pr.

4.3 90° injector, 100 bar fuel pressure, central injection

4.3.1 Hydrocarbon emissions

No. of outliers	11
Influential variables	A, AA, BB, CD, AD, C
Highest t value	16

Figure 4.9 - Summary of CCRD results for HC emissions.

The air/fuel ratio is by far the most influential variable on HC emissions with this configuration. The individual response curves bear this out. Figures 4.13(e), (g) and (h) all show that HC emissions reduce with lean running, with a minimum in this case formed at an air/fuel ratio of approximately 18:1. This agrees with established understanding, and is explained by virtue of excess air ensuring that all fuel is burned. The reason HC emissions increase once again in mixtures leaner than the minimum point is due to the slower and often less complete burning of the mixture.

Unfortunately, it appears that the model may not be very reliable. It is apparent from figure 4.13(a) that there are no less than 11 outliers out of the 31 test points. There are two pieces of evidence that suggest that the problem is that a quadratic model of the HC response is not able to follow the complex pattern of the actual engine behaviour. The first observation is that the HC emissions are generally much lower than the previous series of tests with side injection (see figure 4.5 for comparison). This suggests reasonably complete combustion. The second point is that models for the other responses (i.e. for NOx, BSFC and exhaust gas temperature) all show good fits, two with no outliers, and the remaining response with only one outlier. The high 't' values for both A and AA (figure 4.13(b)) give confidence that the air/fuel ratio does have a strong effect on HC emissions, but the actual shape of the response curves are probably in error.

4.3.2 NOx emissions

No. of outliers	0
Influential variables	B, C, D, AA
Highest t value	6

Figure 4.10 - Summary of CCRD results for NOx emissions.

Ignition timing is the most influential variable on NOx emissions with this configuration, closely followed by injection timing, and then inlet valve timing. In figure 4.14(d) it is obvious that ignition timing exerts greater influence over NOx emissions than inlet valve timing, though the latter has some influence. In this case, earlier ignition timing leads to higher values of NOx emissions. The same trend is illustrated in figures 4.14(f) and 4.14(h). Advancing the ignition increases the peak pressures and temperatures in the cylinder. This increases NOx formation.

The response curves suggest that emissions of NOx decrease with later fuel injection timings. This is shown in figures 4.14(c) and 4.14(g) and to a lesser extent in figure 4.14(f). This is thought to be due to increased charge cooling, which will have the effect of reducing the peak combustion temperature, reducing the formation of NOx. This is discussed further in section 4.8.

Inlet valve timing is the third most influential variable. As already mentioned, this is shown in figures 4.14(c) and 4.14(d). The strongest response is illustrated in figure 4.14(e), though the same trend is observed throughout. That is, later inlet valve opening tends to reduce NOx emissions. It could be argued that the reduced residuals with late inlet valve timing should increase the NOx emissions due to reduced levels of EGR, but it is thought that the reduction of the effective compression ratio is a more dominant effect in this case. It is also possible that the more vigorous charge motion associated with late inlet valve opening may also have a part to play in the response. This is investigated further in section 4.8.

The NOx emissions did not peak at the expected value of around 15.5:1. In fact, there was a surprisingly weak link between NOx and air/fuel ratio, which meant that it was difficult to accurately identify the air/fuel ratio for peak emissions.

4.3.3 Brake specific fuel consumption

No. of outliers	0
Influential variables	A, AA, BB
Highest t value	10

Figure 4.11 - Summary of CCRD results for BSFC.

The air/fuel ratio is by far the most influential variable on BSFC with this configuration. This is obvious from figures 4.15(e), (g) and (h) where the lowest BSFC is obtained at the leaner test points, though the curves all appear to be nearing a minimum BSFC at an air/fuel ratio of approximately 19.5:1. The main effect of operating lean is the extra air requirement means that the engine is less throttled, leading to lower pumping work and hence greater efficiency. Eventually though, the air-fuel mixture will approach the flammability limits of the fuel.

4.3.4 Exhaust gas temperature

No. of outliers	1
Influential variables	B, A, BB, AA, D, CD, C
Highest t value	23

Figure 4.12 - Summary of CCRD results for exhaust gas temperature.

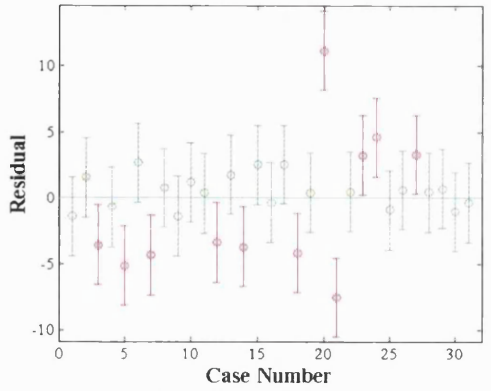

(a) - Residuals plot.

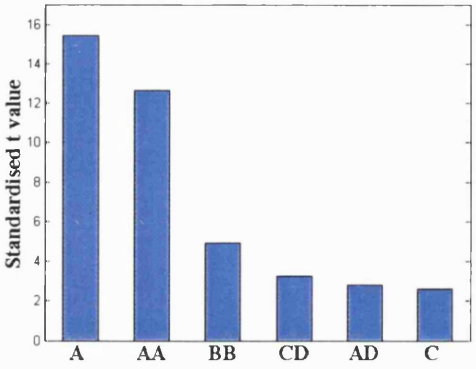

(b) - Influential variables.

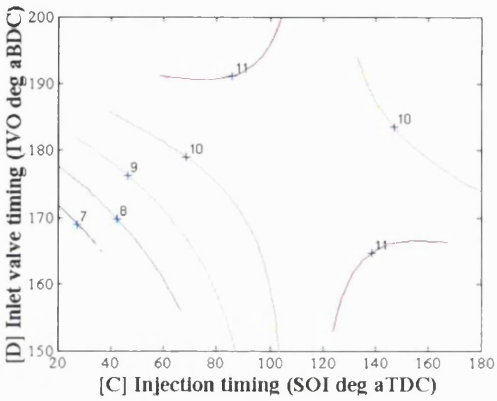

(c)

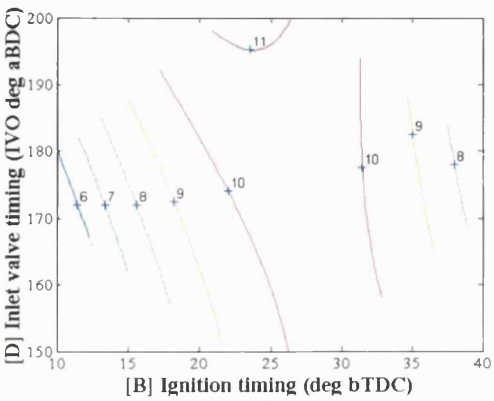

(d)

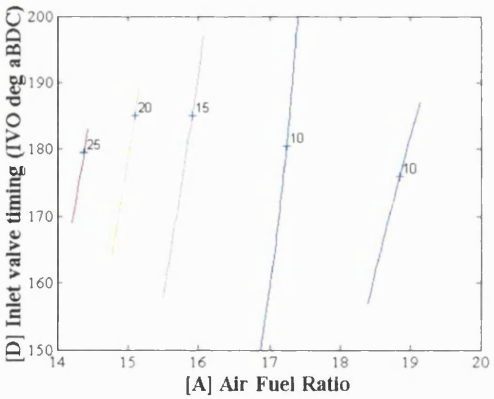

(e)

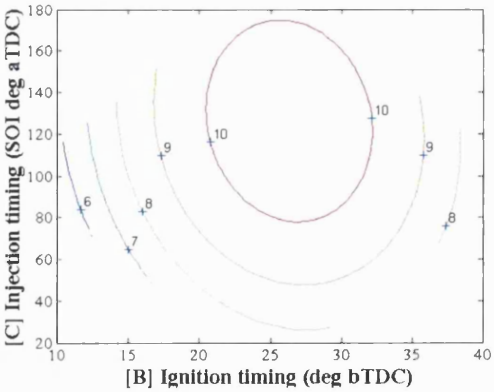

(f)

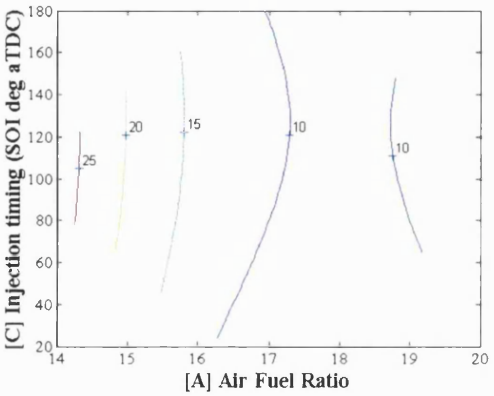

(g)

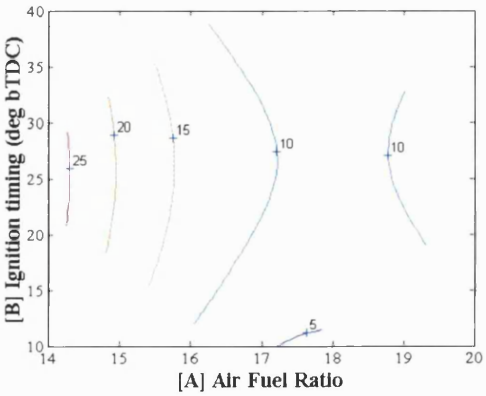

(h)

Figure 4.13 - Results set for HC emissions (g/kWh). 90° injector, central injection, 100 bar fuel pr.

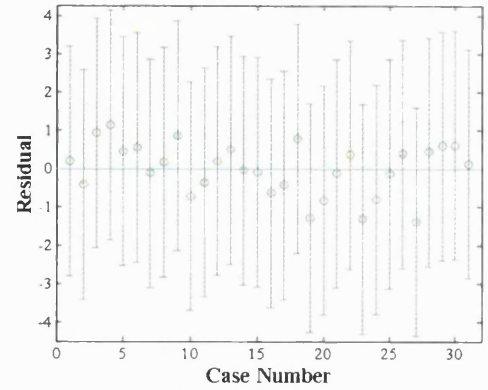

(a) - Residuals plot.

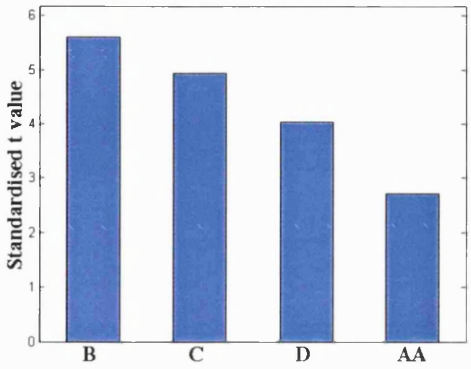

(b) - Influential variables.

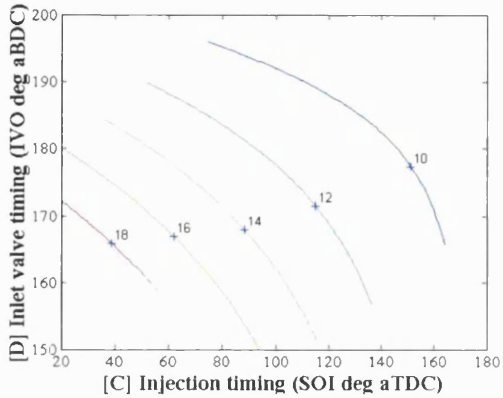

(c)

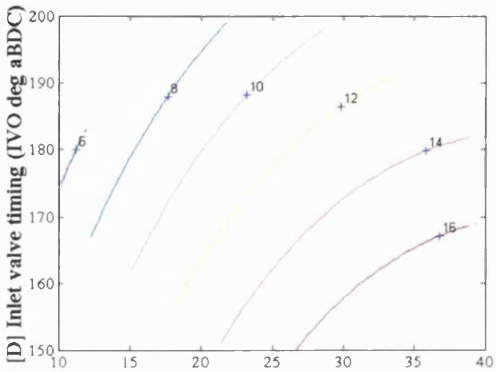

(d)

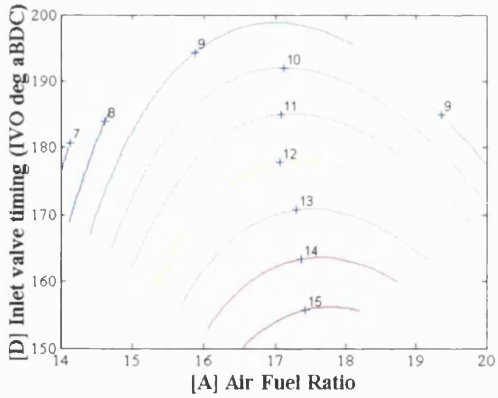

(e)

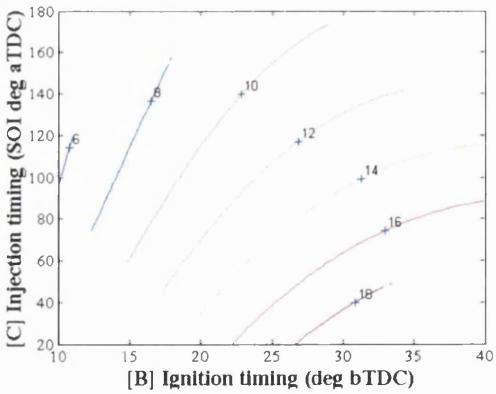

(f)

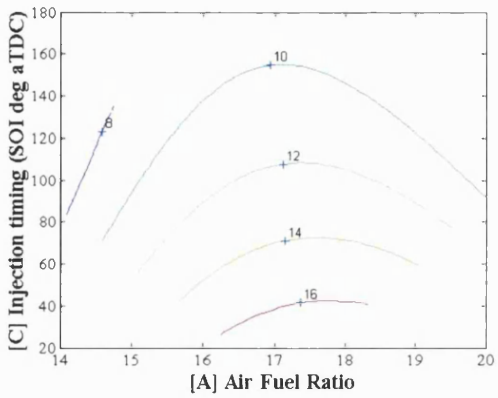

(g)

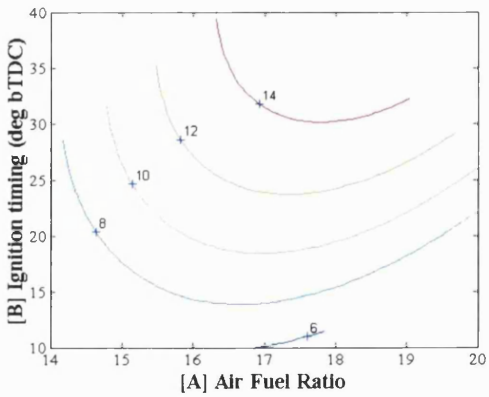

(h)

Figure 4.14 - Results set for NOx emissions (g/kWh). 90° injector, central injection, 100 bar fuel pr.

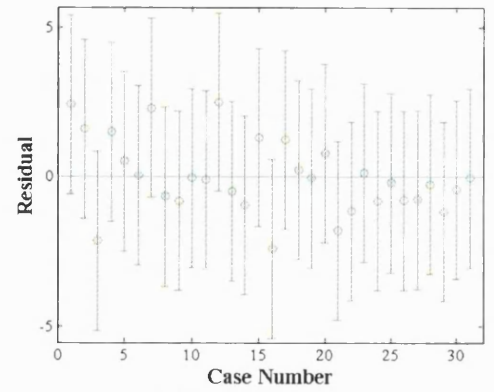

(a) - Residuals plot.

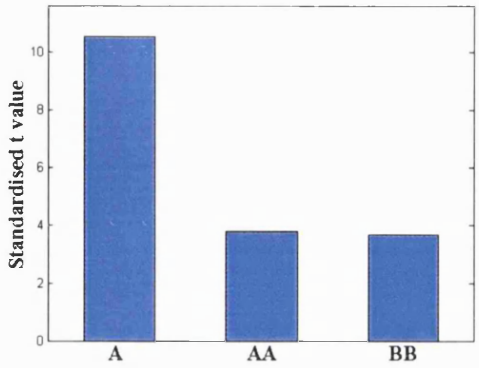

(b) - Influential variables.

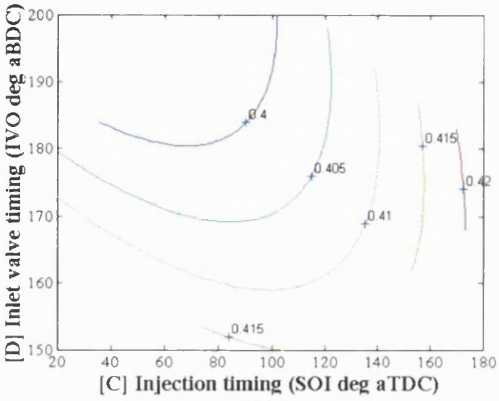

(c)

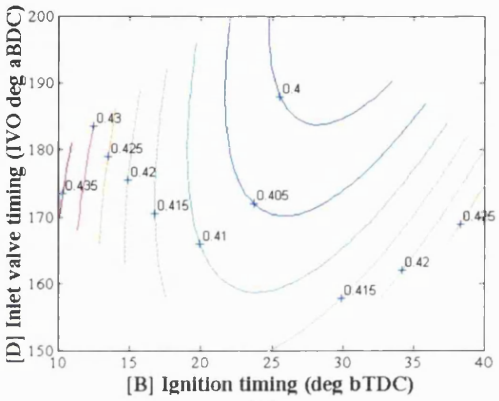

(d)

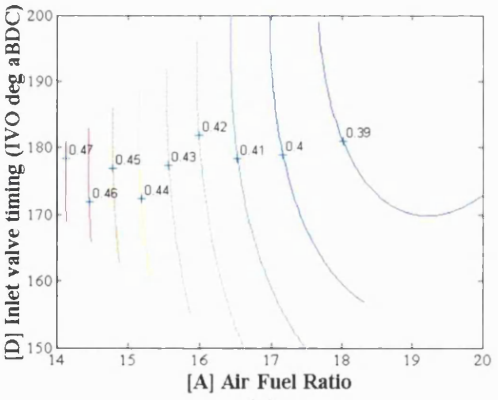

(e)

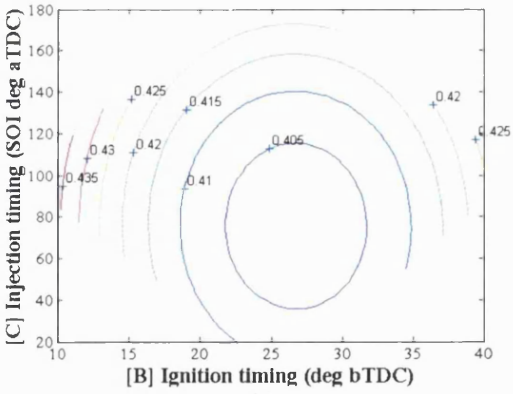

(f)

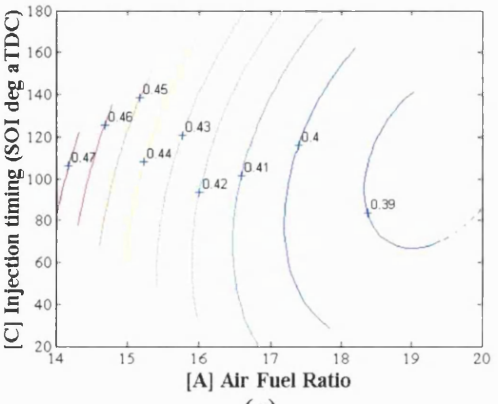

(g)

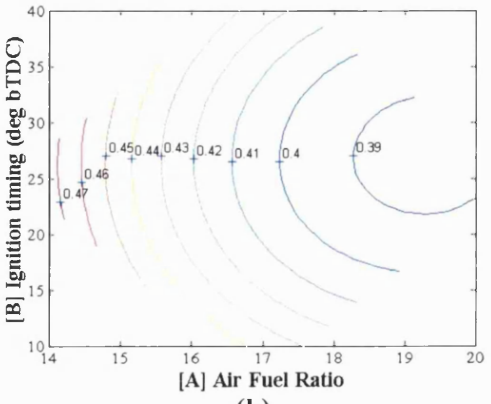

(h)

Figure 4.15 - Results set for BSFC (kg/kWh). 90° injector, central injection, 100 bar fuel pressure.

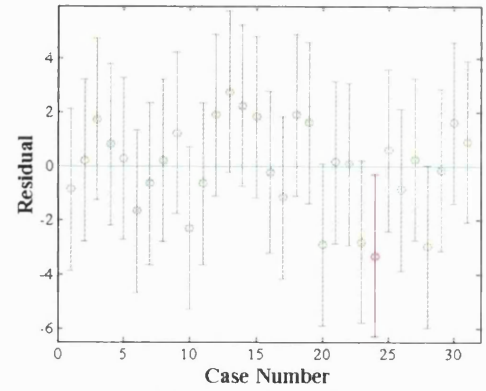

(a) - Residuals plot.

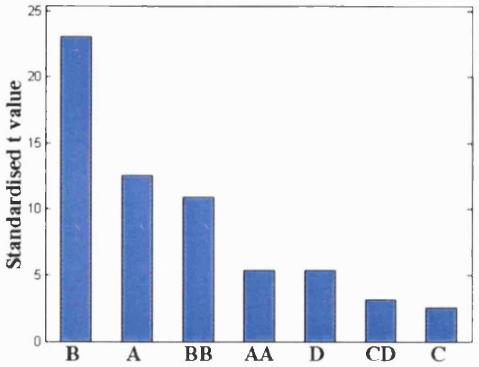

(b) - Influential variables.

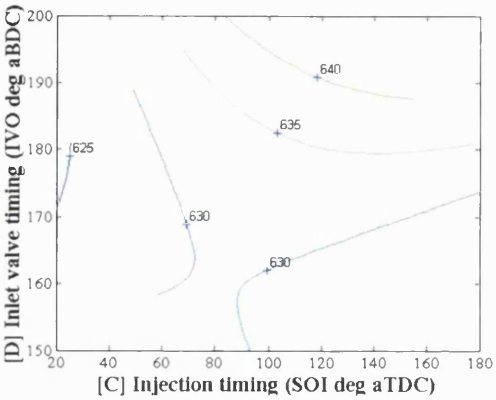

(c)

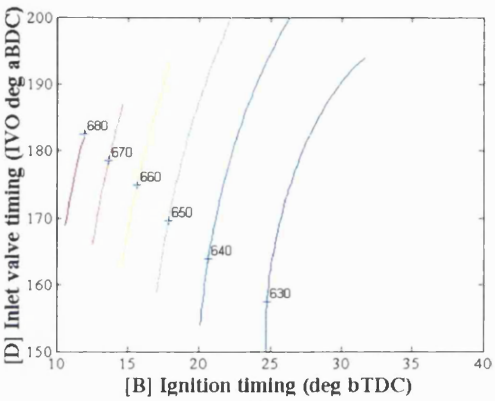

(d)

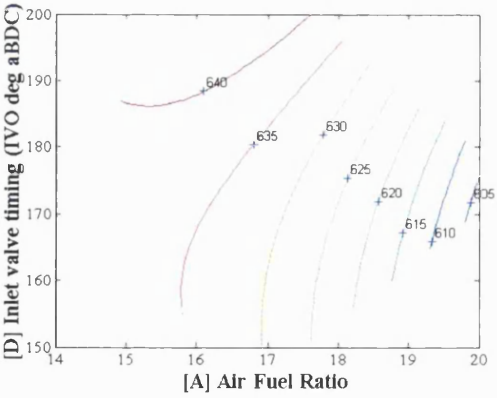

(e)

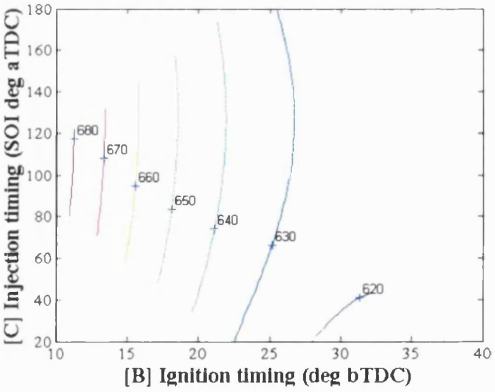

(f)

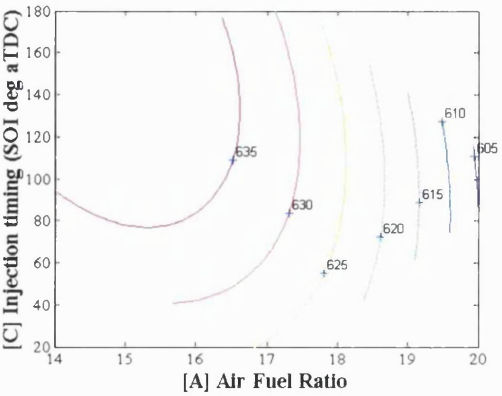

(g)

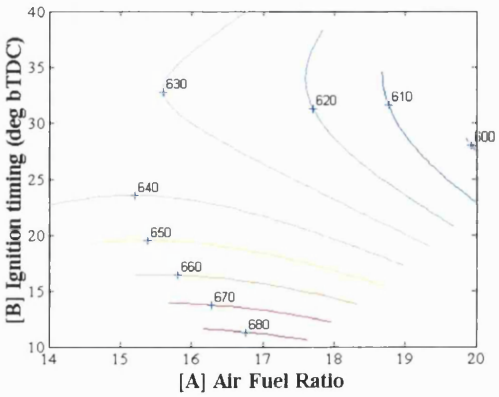

(h)

Figure 4.16 - Results set for exhaust gas temp. (°C). 90° injector, central injection, 100 bar fuel pr.

Ignition timing is easily the most significant variable affecting exhaust gas temperature with this configuration. Air/fuel ratio comes in second. Figures 4.16(d), (f) and (h) all illustrate the trend for a lower temperature with advanced ignition timing. Advancing the timing of the ignition leads to the heat release (i.e. burning) taking place nearer to the minimum volume condition, which is thermodynamically more efficient. This, in turn, means that more of the chemical energy from the fuel is converted to work, with the consequent effect of a lower exhaust gas temperature.

The only outlier in figure 4.16(a) corresponds to test point 24. At this point, the ignition timing is retarded to its lowest figure (10° bTDC) which suggests that the model is not able to follow the engine's behaviour at this particularly retarded ignition timing.

4.4 60° injector, 100 bar fuel pressure, side injection

4.4.1 Hydrocarbon emissions

No. of outliers	0
Influential variables	C, B, BC, AC
Highest t value	3.5

Figure 4.17 - Summary of CCRD results for HC emissions.

Injection timing is the main variable affecting HC emissions with this configuration, closely followed by ignition timing. Figures 4.21(c), (f) and (g) all display a general trend for lower HC emissions with earlier injection timings. This suggests that the mixture has more time to form a homogeneous charge as the injection is moved to an earlier timing.

Retarding the ignition timing reduces the HC emissions in this configuration. This is apparent in figures 4.21(d) and (f). The change in ignition timing has the effect of increasing the exhaust gas temperature. According to Heywood [1988], a higher exhaust gas temperature is usually accompanied by a reduction in HC emissions, quite likely due to further oxidation of the unburnt HC emissions after the flame has extinguished.

The fit of the model is good with no outliers and most points close to their predicted values (figure 4.21(a)).

4.4.2 NOx emissions

No. of outliers	1
Influential variables	A, B, CC, CD, AA
Highest t value	10

Figure 4.18 - Summary of CCRD results for NOx emissions.

Air/fuel ratio has the most effect on NOx emissions with this configuration, closely followed by ignition timing. Figures 4.22(e), (g) and (h) all clearly demonstrate the trend of reduced NOx emissions while running the engine with lean mixtures. Most of the testing matrix was performed lean of stoichiometric, so this result is as expected. Leaner mixtures produce lower combustion temperatures, reducing the formation of NOx. It would be expected that the NOx emissions would peak at an air/fuel ratio of around 15.5:1 (figure 1.2). One explanation why no peak is evident within the range of air/fuel ratios covered by the plots is that some of the fuel injected found its way into a very rich region, meaning that the air/fuel ratio of the burning charge was actually leaner than calculated from air and fuel inputs.

Retarding the ignition timing appears to have the effect of reducing NOx emissions according to figures 4.22(d) and 4.22(f) and to a lesser extent (due to the influence of the air/fuel ratio) figure 4.22(h). By retarding the ignition timing, the peak pressure in the cylinder is reduced (and hence the peak temperature). This leads to a reduction in the NOx emissions.

The one outlier is test point 23 which has the most advanced ignition timing (40° bTDC) of all the test points, and again it is the case that the model cannot follow engine behaviour at this more extreme condition. The actual NOx emissions are significantly higher than predicted by the model.

4.4.3 Brake specific fuel consumption

No. of outliers	1
Influential variables	C, AC
Highest t value	5.5

Figure 4.19 - Summary of CCRD results for BSFC.

Injection timing is by far the most important variable in its effect on BSFC with this configuration. Figures 4.34(c), (f) and (g) all illustrate the same trend - earlier injection reduces BSFC. Early injection increases the amount of time for mixture preparation, ensuring that there will be complete combustion, minimising the BSFC.

Notably, the only outlier corresponds to test point 20, which is the richest air/fuel ratio setting (14:1). In general, the model fit appears to be quite good, with most points close to their predicted values.

4.4.4 Exhaust gas temperature

No. of outliers	8
Influential variables	B, A, BB, CC, AB, BC, AA, D, C, AC, DD
Highest t value	12

Figure 4.20 - Summary of CCRD results for exhaust gas temperature.

Ignition timing is again the most influential variable on the temperature of the exhaust gases, with some additional influence in this configuration from the air/fuel ratio. As expected, the lower exhaust gas temperatures are achieved with more advanced ignition timings, as shown in figures 4.24(d), (f) and (h).

Figures 4.24(e), (g) and (h) illustrate a lower gas temperature as the engine is run lean as would be expected. The response curves do appear to approach a minimum value, corresponding to an air/fuel ratio of approximately 19.5:1. This can be explained by the excess air acting as a dilutent to the combusting charge, reducing gas temperature throughout the combustion and post-combustion periods.

Unfortunately, some outside influence appears to have affected the results according to figure 4.24(a). Before test point 19, most of the data is above the values predicted by the model, but from test point 20 onwards, most of the data is below the model. This pattern of behaviour suggests that the cause was some external influence on exhaust temperature, rather than problems with the fit of the model or unstable running points. One possibility is that the change was due to all the variable settings at test point 19 being adjusted back to their centre-point values. Centre points were often used as a natural break in engine testing. It may be possible that ambient conditions changed over this time causing a step change in the exhaust gas temperature, although test records show no great change in engine intake temperature.

The relatively high 't' values for ignition timing and air/fuel ratio give confidence that these variables were the major influences on exhaust gas temperature, but the high number of outliers means that there is doubt in the accuracy of the actual shape of the characteristics.

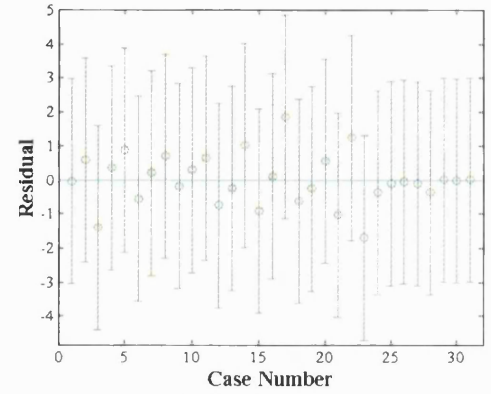

(a) - Residuals plot.

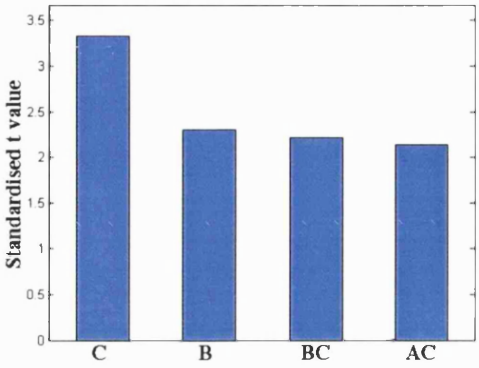

(b) - Influential variables.

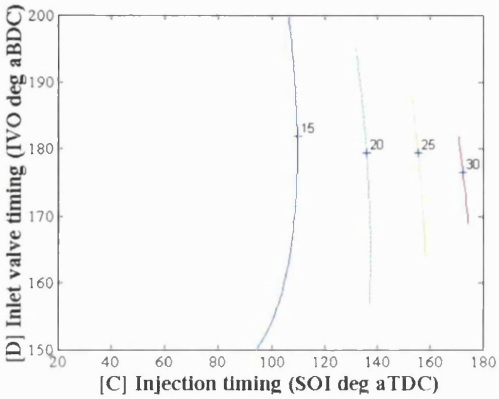

(c)

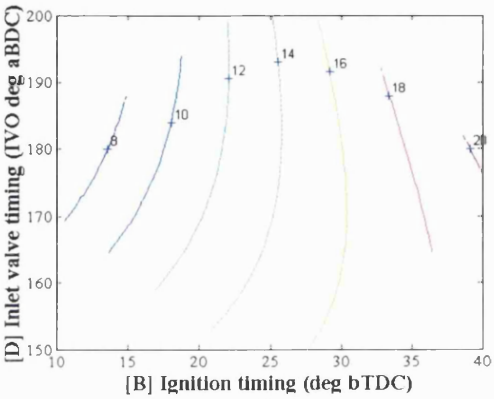

(d)

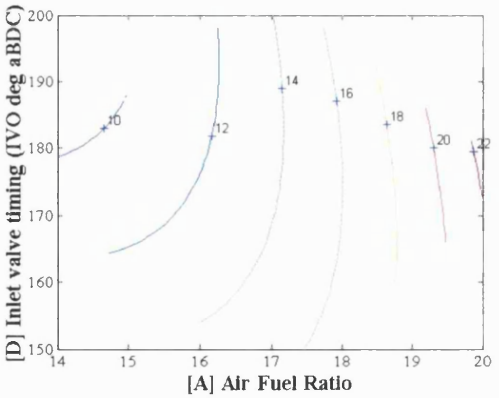

(e)

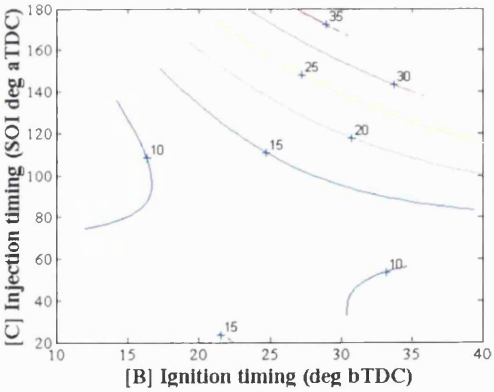

(f)

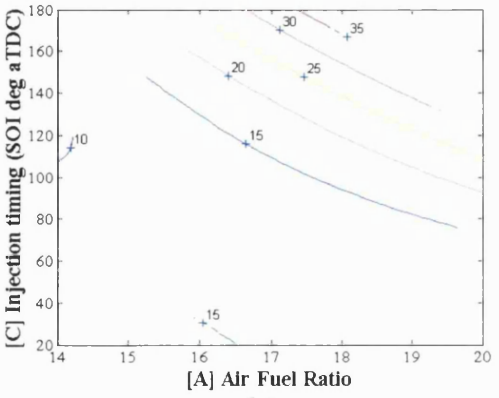

(g)

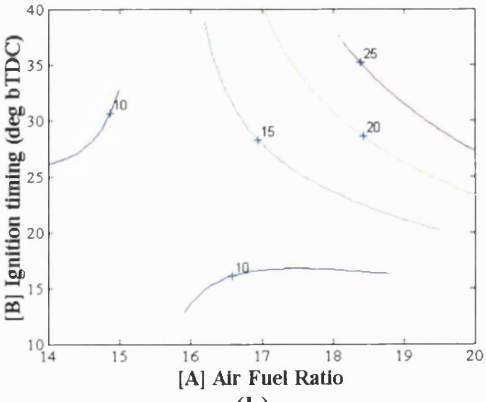

(h)

Figure 4.21 - Results set for HC emissions (g/kWh). 60° injector, side injection, 100 bar fuel pressure.

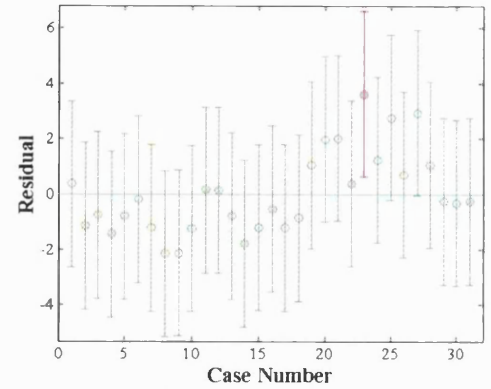

(a) - Residuals plot.

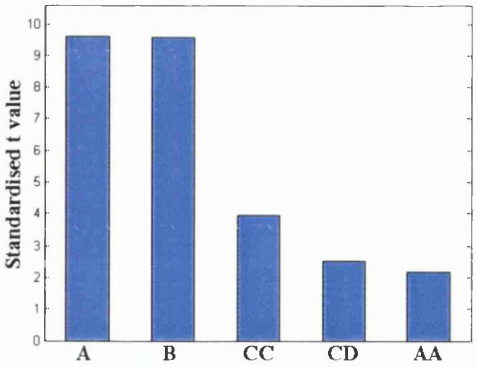

(b) - Influential variables.

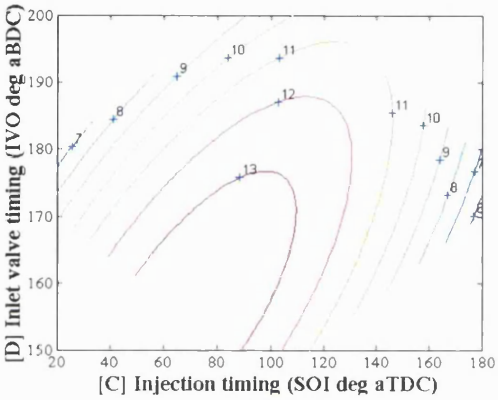

(c)

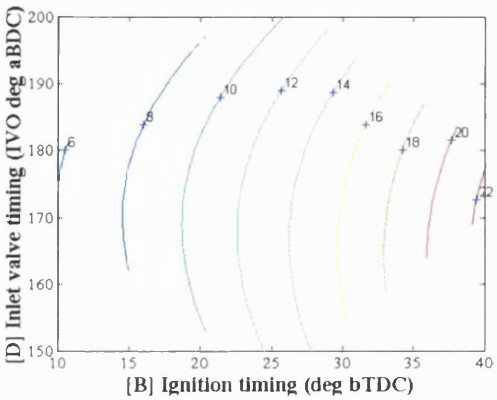

(d)

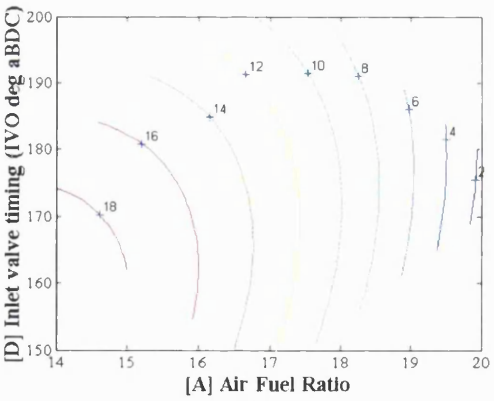

(e)

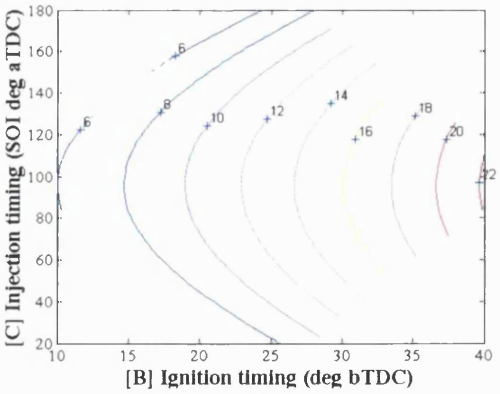

(f)

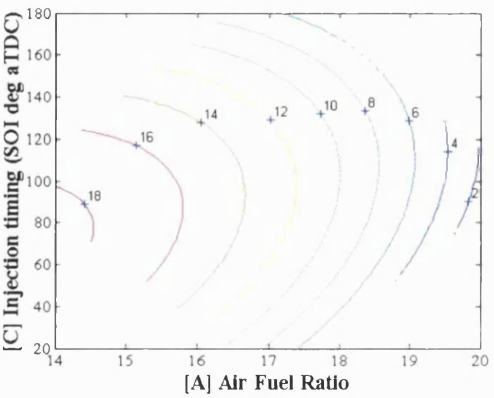

(g)

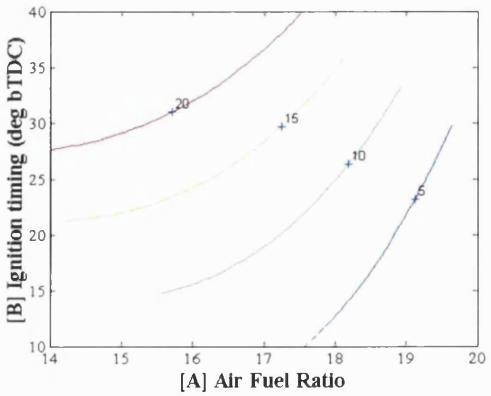

(h)

Figure 4.22 - Results set for NOx emissions (g/kWh). 60° injector, side injection, 100 bar fuel pressure.

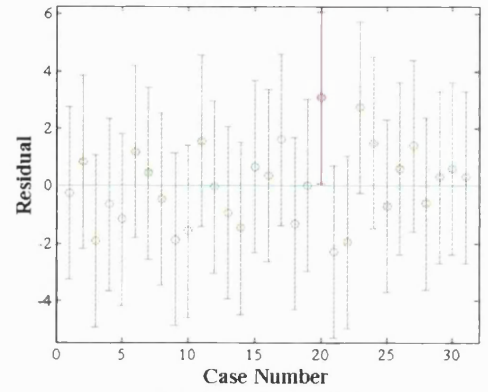

(a) - Residuals plot.

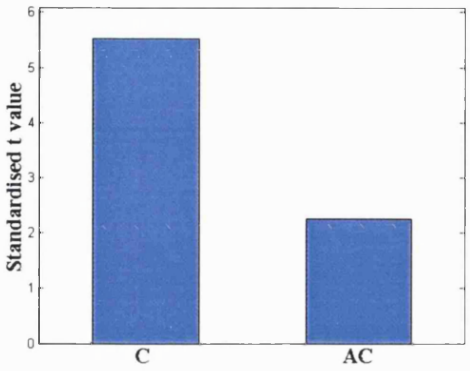

(b) - Influential variables.

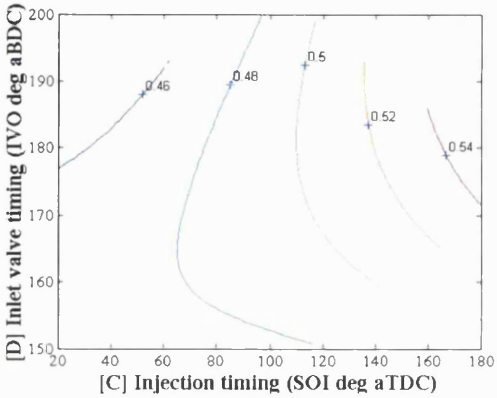

(c)

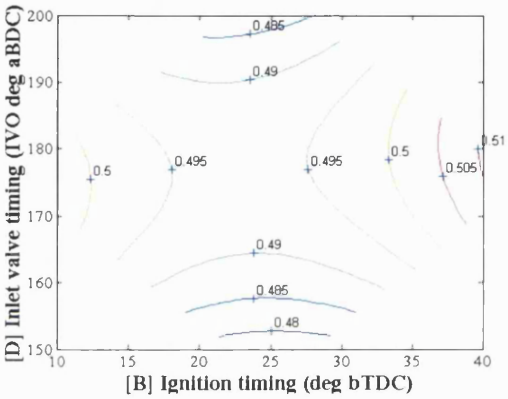

(d)

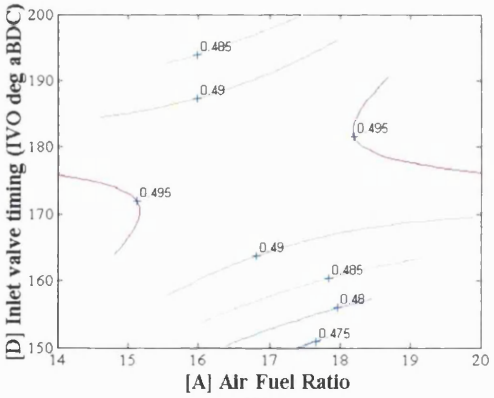

(e)

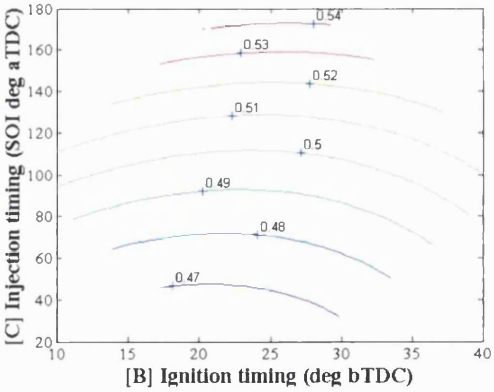

(f)

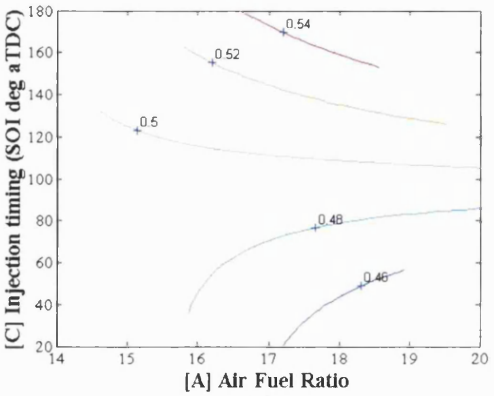

(g)

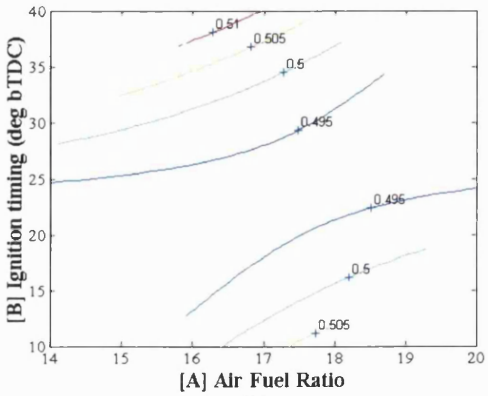

(h)

Figure 4.23 - Results set for BSFC (kg/kWh). 60° injector, side injection, 100 bar fuel pressure.

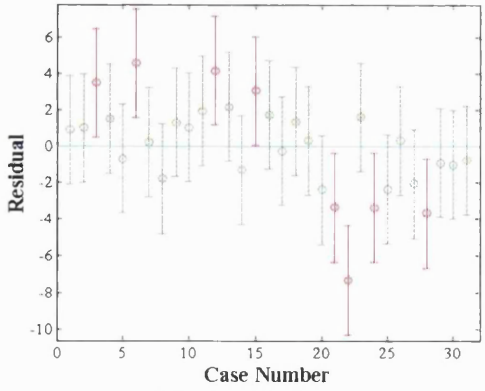

(a) - Residuals plot.

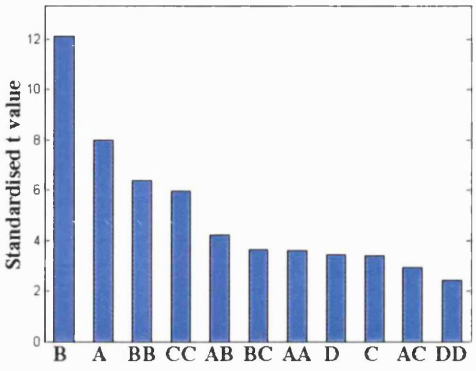

(b) - Influential variables.

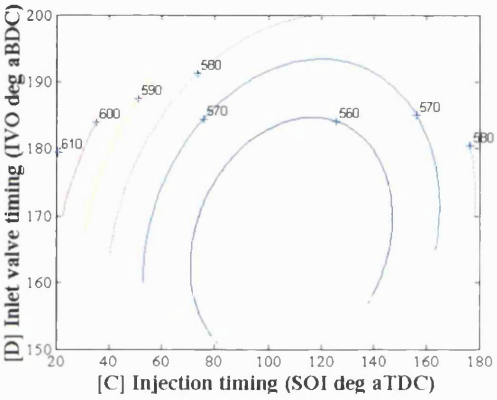

(c)

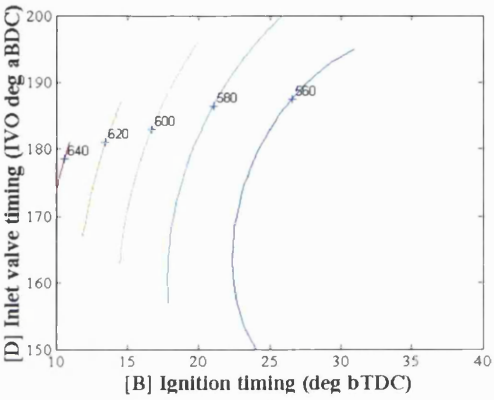

(d)

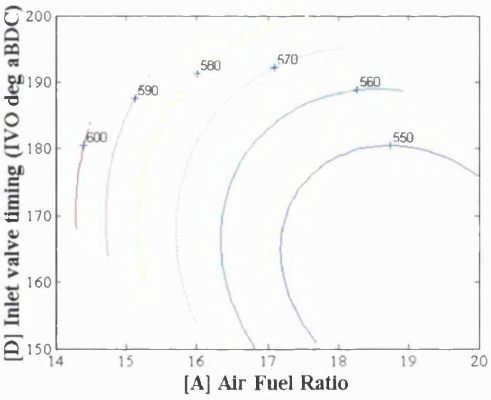

(e)

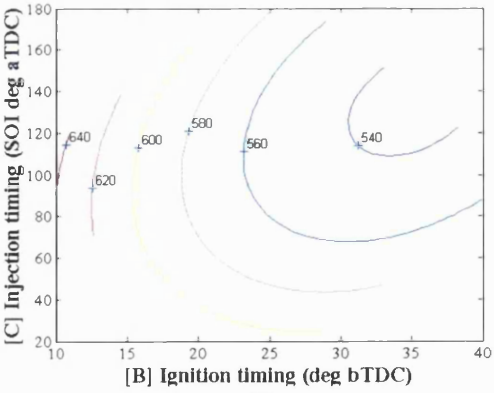

(f)

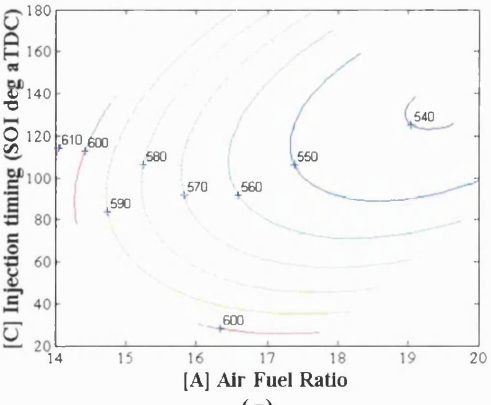

(g)

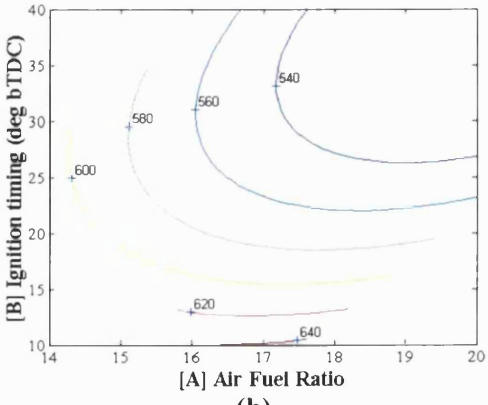

(h)

Figure 4.24 - Results set for exhaust gas temperature (°C). 60° injector, side injection, 100 bar fuel pr.

4.5 60° injector, 100 bar fuel pressure, central injection

4.5.1 Hydrocarbon emissions

No. of outliers	0
Influential variables	A, B, CC, BB
Highest t value	7

Figure 4.25 - Summary of CCRD results for HC emissions.

Air/fuel ratio is the most important variable in its effect on HC emissions with this configuration, followed by ignition timing. Figures 4.29(e), (g) and (h) show a reduction of HC emissions at rich air/fuel mixtures. This is not the obvious relationship until it is realised that the test range is nearly all in the region lean of stoichiometric, so excess air would have been available for nearly all of the test conditions. Under these circumstances, the lower exhaust gas temperatures of the leaner settings can be expected to adversely affect HC emissions due to less post-flame oxidation of unburnt hydrocarbons.

The two most obvious plots incorporating ignition timing, figures 4.29(d) and 4.29(f), show a maximum HC level at an ignition timing of approximately 30° bTDC. The timing for maximum emissions approximately corresponds to the most efficient operating condition of the engine (figure 4.31) and therefore the lowest exhaust gas temperature (figure 4.32). The same argument as above applies as to the reason for the high hydrocarbons.

4.5.2 NOx emissions

No. of outliers	0
Influential variables	B, A, BB, AC, CD, DD
Highest t value	10

Figure 4.26 - Summary of CCRD results for NOx emissions.

Ignition timing is the most influential variable on NOx emissions with this configuration, followed by air/fuel ratio. As in 4.4.2, retarding the ignition timing has the effect of reducing NOx emissions. This is illustrated in figures 4.30(d) and 4.30(f) and to a lesser extent in figure 4.30(h). By retarding the ignition timing, the peak pressure in the cylinder is reduced (and hence the peak temperature), leading to a reduction in the NOx emissions.

In all three response curves (figures 4.30(e), (g) and (h)) it is apparent that increasing the air/fuel ratio (lean running) reduces the NOx emissions. As discussed in section 4.4.2, leaner mixtures (maximum NOx emissions occur just lean of stoichiometric) produce lower combustion temperatures, reducing the formation of NOx. Once again, there is no peak apparent at around 15.5:1 as would be expected with homogeneous combustion. The fact that an air/fuel ratio is

quite near the edge of the experimental space does make it more difficult to locate a peak accurately. In fact, the star point of the CCRD for the richest air/fuel ratio is test point 20 with a value of 14:1. The next richest setting is 15.5:1, approximately where the peak in NOx values would be expected. Examination of figure 4.30(a) shows that the recorded NOx value was less than that predicted by the model, lending weight to there being a peak lean of stoichiometric.

4.5.3 Brake specific fuel consumption

No. of outliers	0
Influential variables	AB
Highest t value	2

Figure 4.27 - Summary of CCRD results for BSFC.

AB represents an interaction between A and B (air/fuel ratio and ignition timing respectively). The influence of the combined effects of these variables is illustrated in figure 4.31(h). The timing of ignition has a direct influence on the power output (which is related directly to BSFC). If ignition is too early then the peak pressure occurs before TDC of the compression stroke, reducing the power output (and increasing BSFC). However, if ignition is too late, then heat is not released at the most thermodynamically efficient timing of around TDC, thereby leading to an increase in the BSFC. In this configuration, the optimum ignition timing appears to be 30° before TDC. The 't' value of the AB interaction is relatively low indicating that the combined effect of these variables does not have a great influence on BSFC.

4.5.4 Exhaust gas temperature

No. of outliers	3
Influential variables	B, BB, AB, AD, CD, D, BD, C, BC, A
Highest t value	14

Figure 4.28 - Summary of CCRD results for exhaust gas temperature.

Ignition timing is by far the most influential variable again on exhaust gas temperature. The expected trend is shown in figures 4.32(d), (f) and (h) where advancing the ignition timing has the effect of reducing the exhaust gas temperature, with a minimum value for an ignition timing slightly more advanced then 30° bTDC.

Though not greatly significant, there are three outliers in figure 4.32(a). These correspond to test points 5, 15 and 21. Test points 15 and 21 have been discussed before as potential problem points as 15 combines a lean air/fuel ratio (18.5:1) with a late injection timing (140° aTDC) and 20 is the leanest running point (20:1).

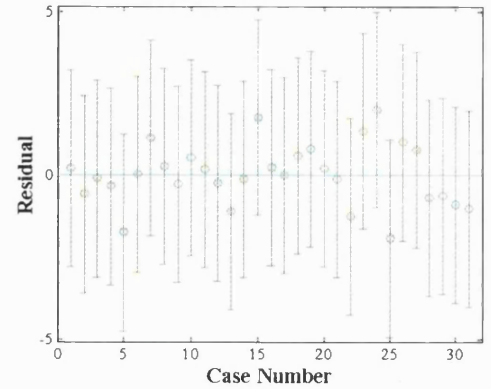

(a) - Residuals plot.

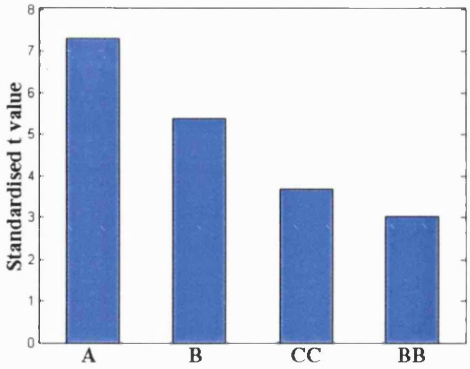

(b) - Influential variables.

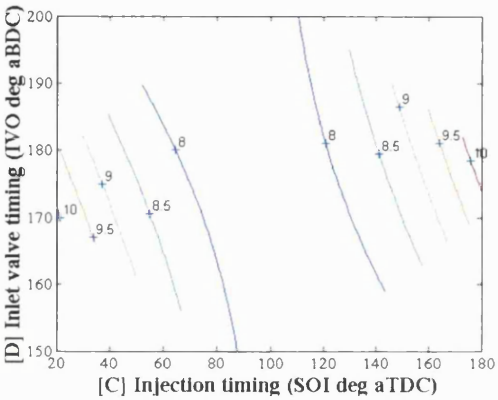

(c)

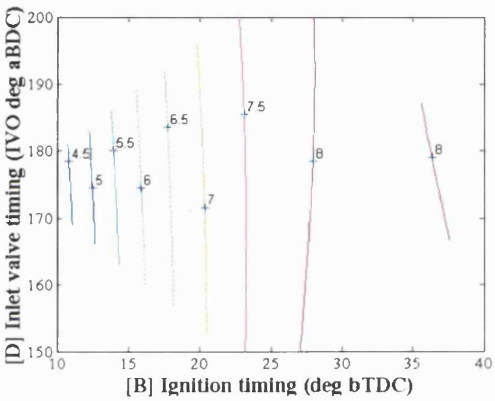

(d)

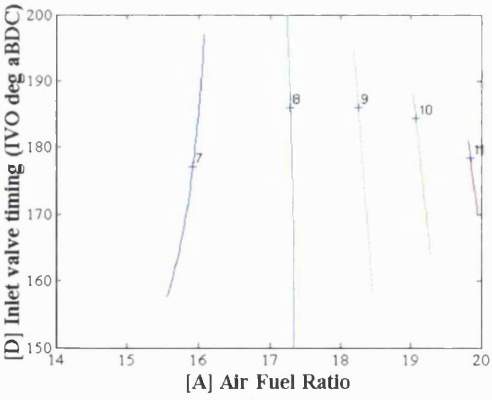

(e)

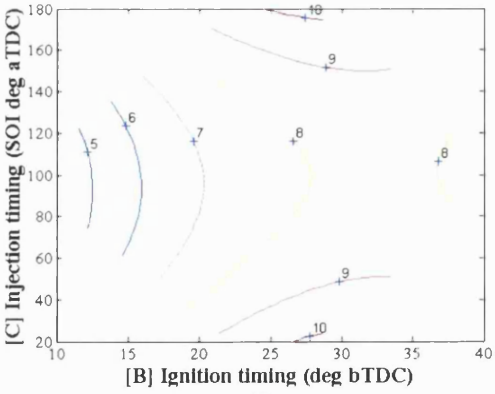

(f)

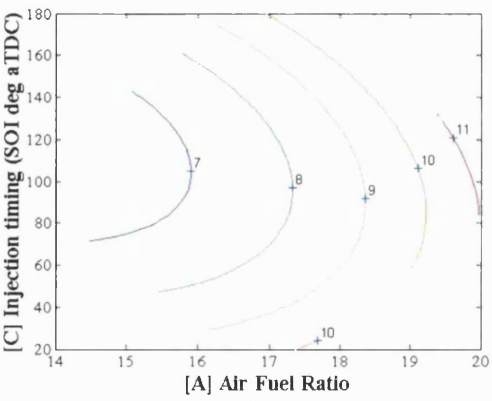

(g)

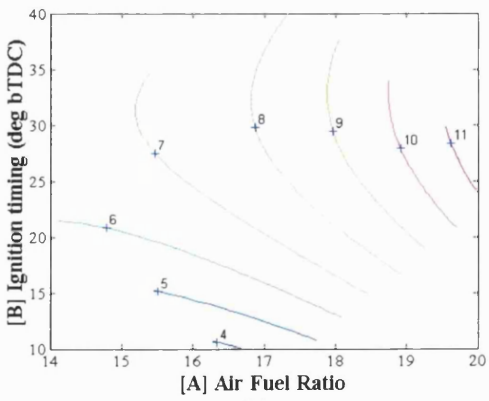

(h)

Figure 4.29 - Results set for HC emissions (g/kWh). 60° injector, central injection, 100 bar fuel pr.

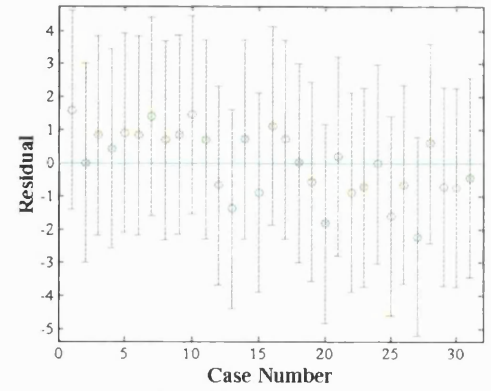

(a) - Residuals plot.

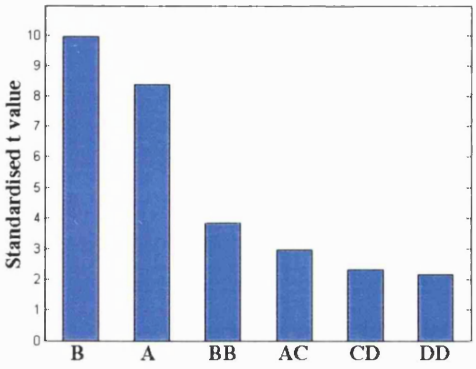

(b) - Influential variables.

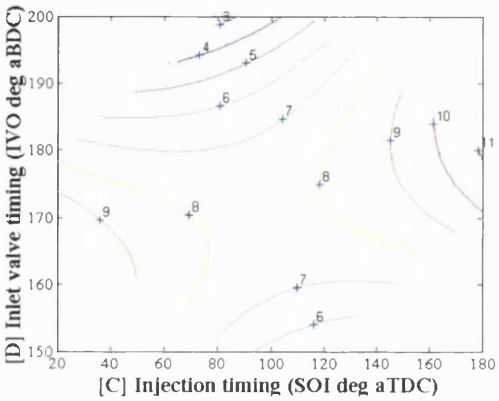

(c)

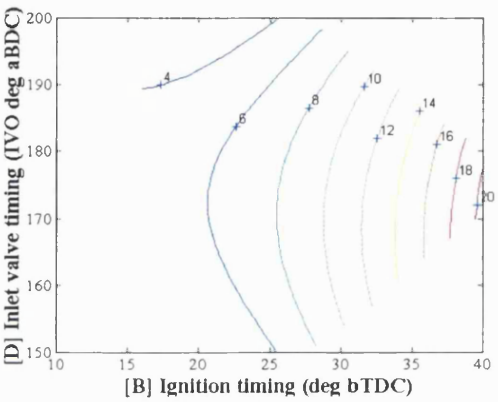

(d)

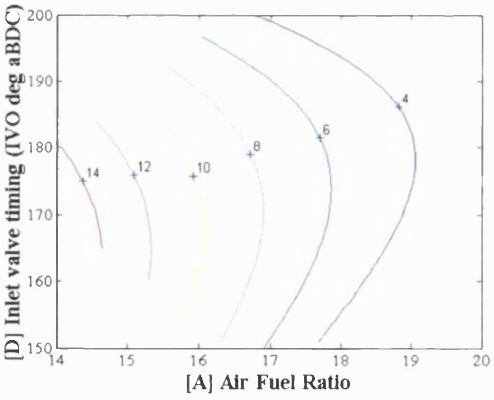

(e)

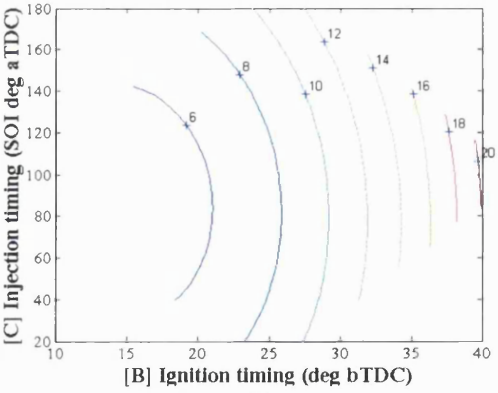

(f)

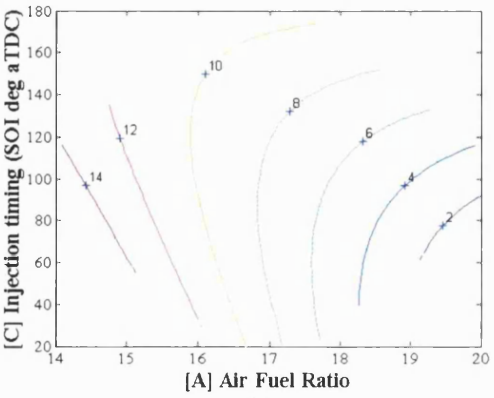

(g)

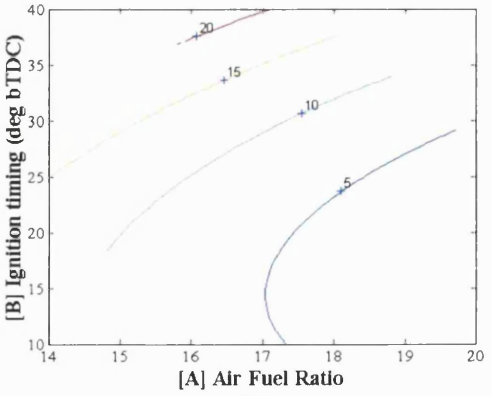

(h)

Figure 4.30 - Results set for NOx emissions (g/kWh). 60° injector, central injection, 100 bar fuel pr.

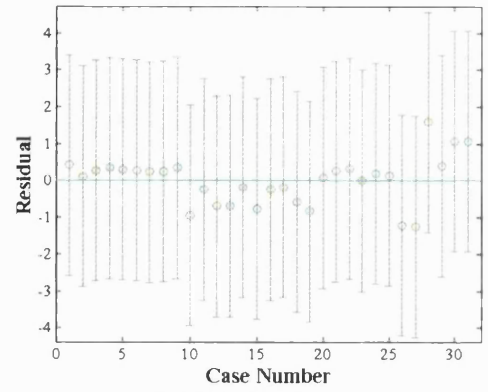

(a) - Residuals plot.

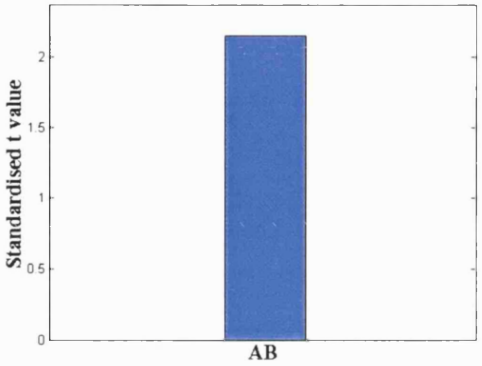

(b) - Influential variables.

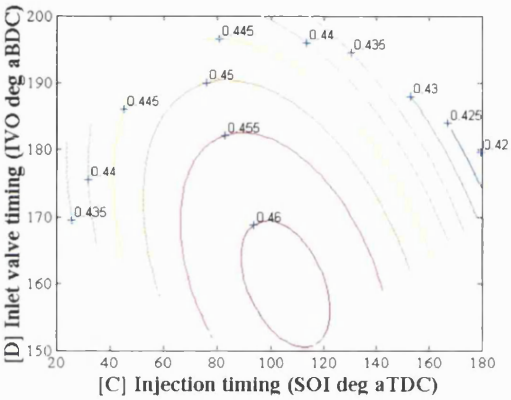

(c)

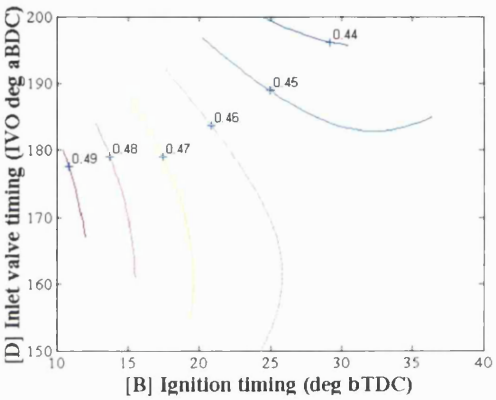

(d)

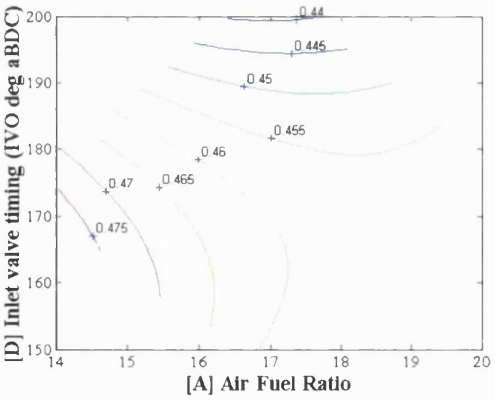

(e)

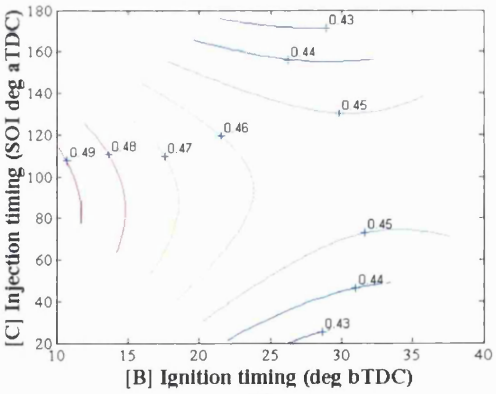

(f)

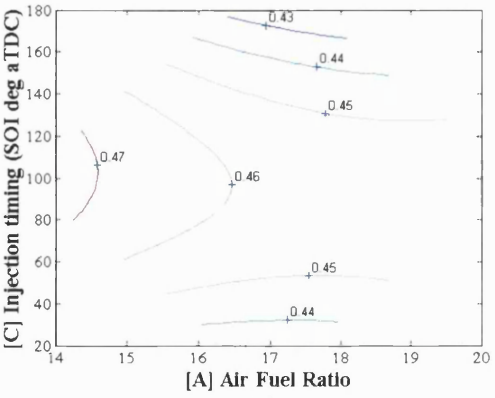

(g)

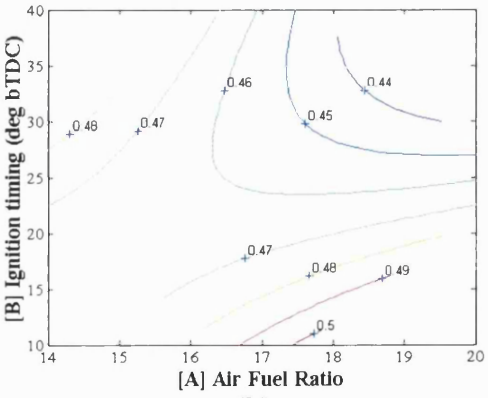

(h)

Figure 4.31 - Results set for BSFC (kg/kWh). 60° injector, central injection, 100 bar fuel pressure.

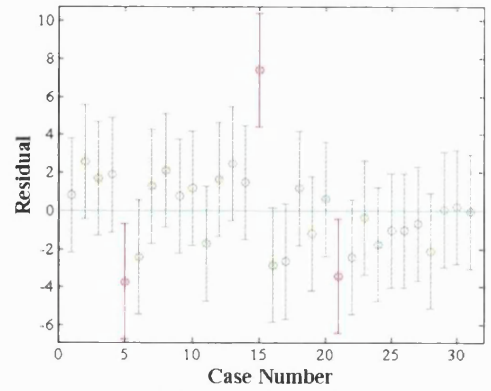

(a) - Residuals plot.

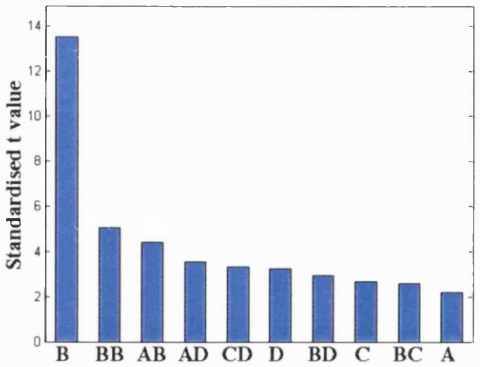

(b) - Influential variables.

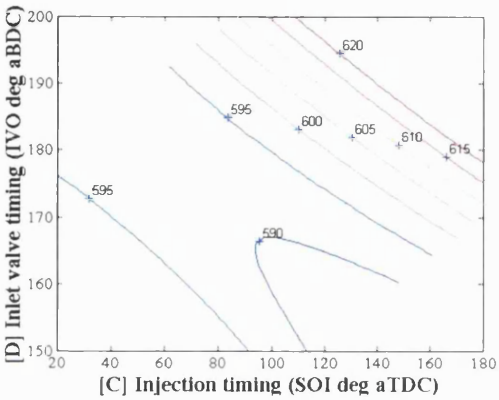

(c)

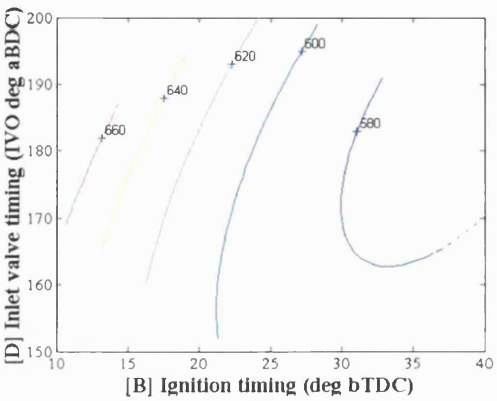

(d)

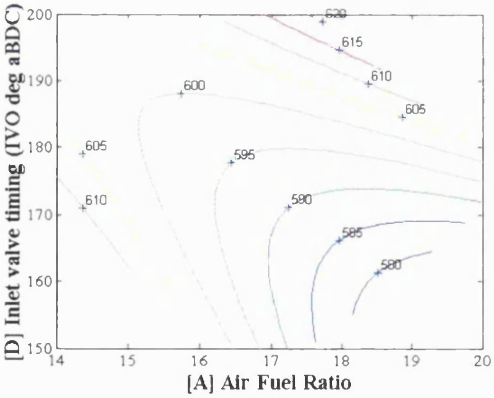

(e)

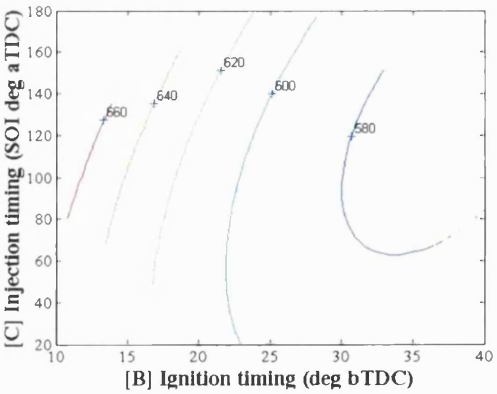

(f)

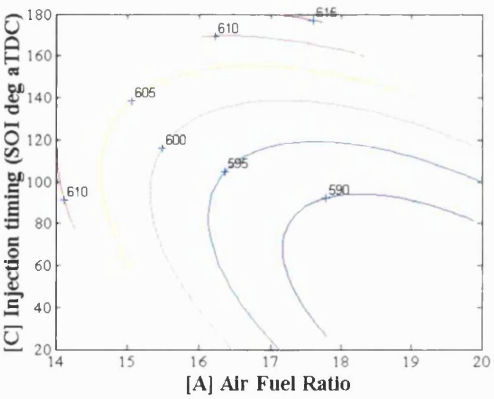

(g)

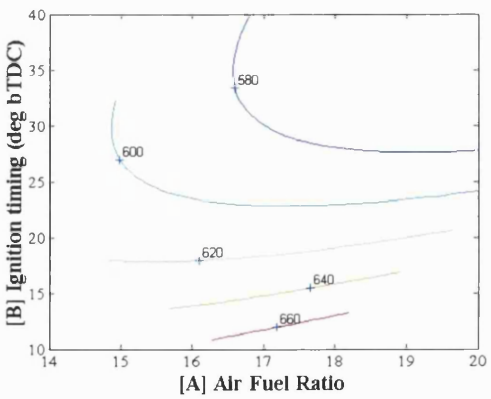

(h)

Figure 4.32 - Results set for exhaust gas temp. (°C). 60° injector, central injection, 100 bar fuel pr.

4.6 60° injector, 20 bar fuel pressure, side injection

4.6.1 Hydrocarbon emissions

No. of outliers	1
Influential variables	A, AA, B, BB
Highest t value	7.5

Figure 4.33 - Summary of CCRD results for HC emissions.

Air/fuel ratio is the most significant variable in its effect on HC emissions with this configuration, followed by ignition timing. There is a minimum level of HC emissions at an air/fuel ratio of approximately 15.5:1 according to figures 4.37(e), (g) and (h). The explanation is the same as for the 60° injector with 100 bar fuel pressure as detailed in 4.5.1.

HC emissions peak at an ignition timing of 30° before TDC in figures 4.37(d), (f) and (h). This is again thought to be due to the reduced post-flame oxidation reactions caused by the comparatively low exhaust gas temperature (figure 4.40). The levels of HC emissions are fairly similar to those obtained with the same configuration with 100 bar fuel supply pressure (figure 4.21). This lack of sensitivity to fuel supply pressure can be explained because there is likely to be impingement of the spray on the piston for many injection timings, making the quality of the spray less important.

High levels of HC emissions are a feature of side injection as switching to the 90° injector gives even higher values (figure 4.5). In contrast, HC emissions with central injection are considerably reduced for both the 60° and 90° injectors (figures 4.29 and 4.13). This is discussed in more detail later in the chapter.

Though the model fit appears to be very good (figure 4.37(a)), there is one outlier which is a significant distance away from the model. On further investigation, the outlier corresponds to test point 21, which, as previously discussed, has the leanest air/fuel ratio of all test points, leading to unstable running.

4.6.2 NOx emissions

No. of outliers	0
Influential variables	B, A, CC
Highest t value	13

Figure 4.34 - Summary of CCRD results for NOx emissions.

Ignition timing has the greatest effect on NOx emissions with this configuration, closely followed by air/fuel ratio. The influence of ignition timing is obvious from figure 4.38(h), and

more so in figures 4.38(d) and 4.38(f), where NOx emissions are reduced at retarded ignition timings. Again, this is simply due to the reduced peak pressure and temperature in the cylinder.

Figures 4.38(e), (g) and (h) clearly illustrate the strong influence the air/fuel ratio has over the level of NOx emissions. The trend is for reduced NOx at lean air/fuel ratios, as expected from earlier results, apart from the lack of a peak around 15.5:1. Particularly low values of NOx emissions are evident at retarded ignition timings and lean air/fuel ratios. Values are even lower then the same configuration with 100 bar fuel supply pressure (figure 4.22) and significantly lower than the other configurations (figures 4.6, 4.14 and 4.30). Low values of NOx are consistent with poor mixture preparation as suggested by the high HC emissions.

4.6.3 Brake specific fuel consumption

No. of outliers	0
Influential variables	BB, D, AA, C, AB
Highest t value	2.5

Figure 4.35 - Summary of CCRD results for BSFC.

All four variables are shown to influence BSFC, with ignition timing and air/fuel ratio showing a quadratic relationship. As there are so many variables influencing the results in this case it is more difficult to decipher the response curves. In the plots showing air/fuel ratio figures, 4.39(g) and 4.39(h), the only trend is the apparent minimum BSFC at an air/fuel ratio of approximately 18:1. It is expected to have lower BSFC with leaner running, until the reduction in the flammability of the mixture increases the BSFC again.

There is a minimum level of BSFC apparent with regards to ignition timing also. As discovered earlier, it occurs when ignition timing is approximately 25-30° bTDC. This is shown in figures 4.39(d), (f) and (h). Figures 4.39(c), (d) and (e) share the same trend for inlet valve timing - opening the inlet valves later appears to reduce BSFC. This will be discussed in more detail later in the chapter.

4.6.4 Exhaust gas temperature

No. of outliers	0
Influential variables	B, BB, A
Highest t value	6

Figure 4.36 - Summary of CCRD results for exhaust gas temperature.

Ignition timing is the most influential variable on the temperature of the exhaust gases. Figures 4.40(d), (f) and (h) all illustrate a reduction in temperature with advanced ignition timings.

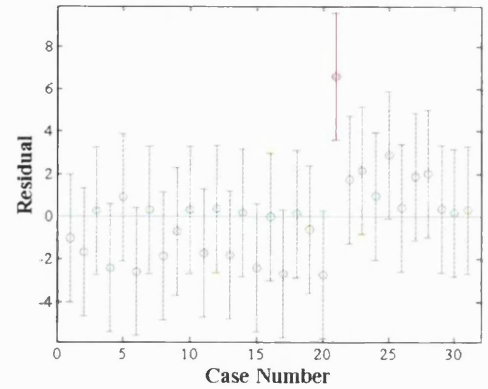

(a) - Residuals plot.

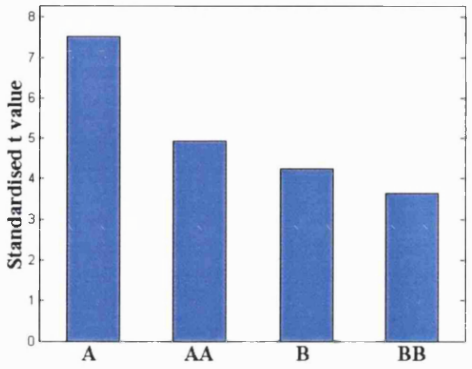

(b) - Influential variables.

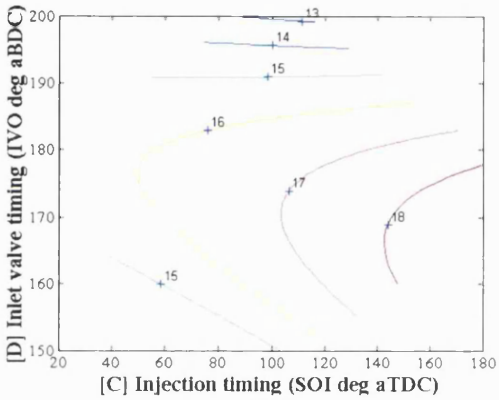

(c)

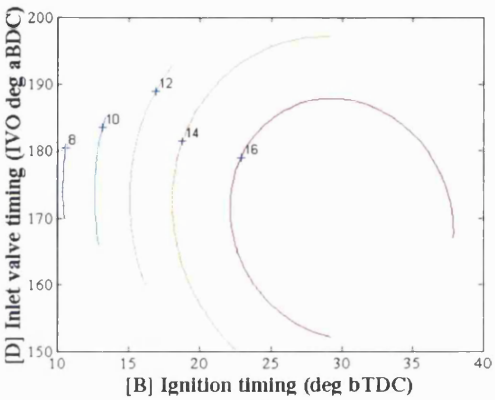

(d)

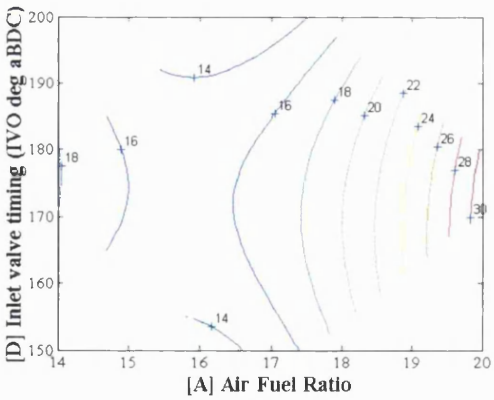

(e)

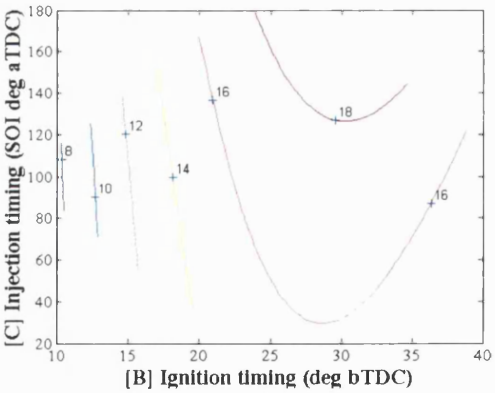

(f)

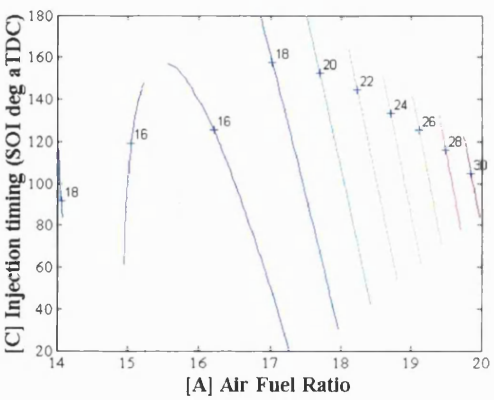

(g)

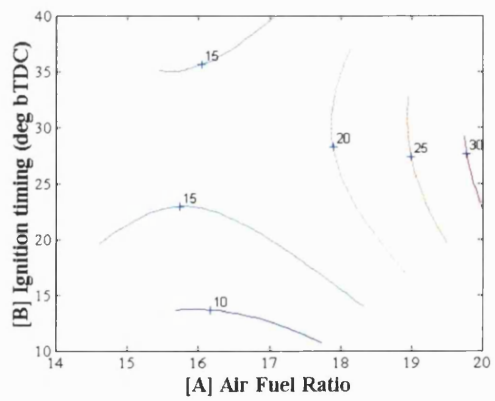

(h)

Figure 4.37 - Results set for HC emissions (g/kWh). 60° injector, side injection, 20 bar fuel pressure.

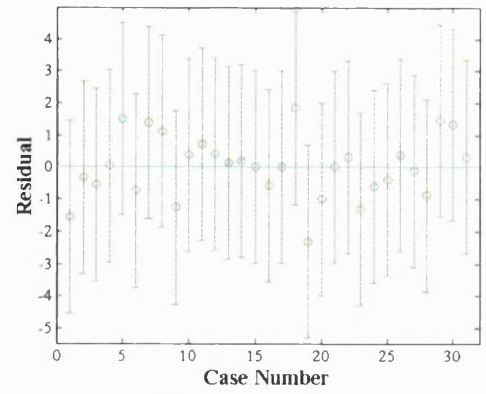

(a) - Residuals plot.

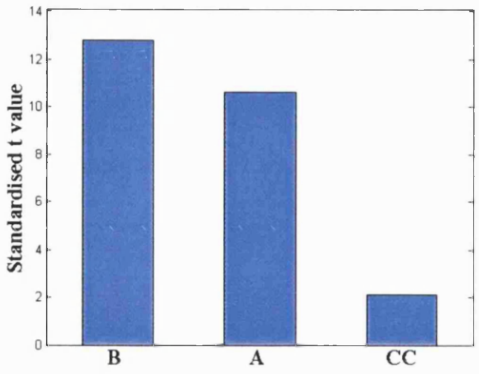

(b) - Influential variables.

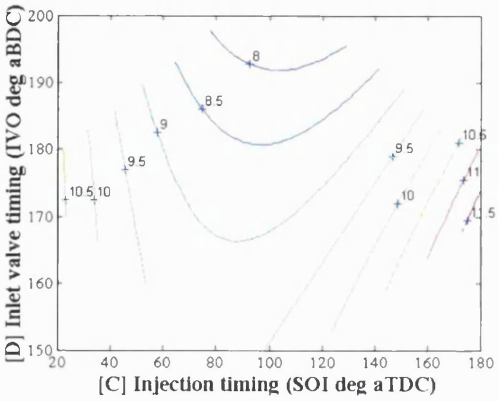

(c)

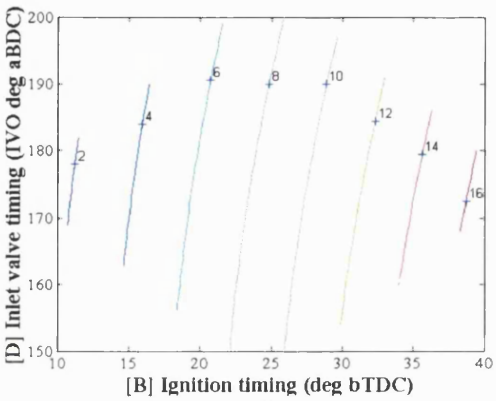

(d)

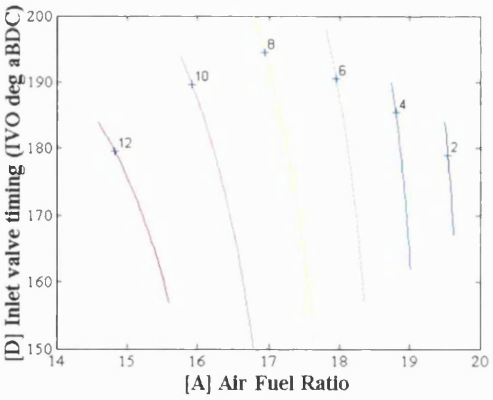

(e)

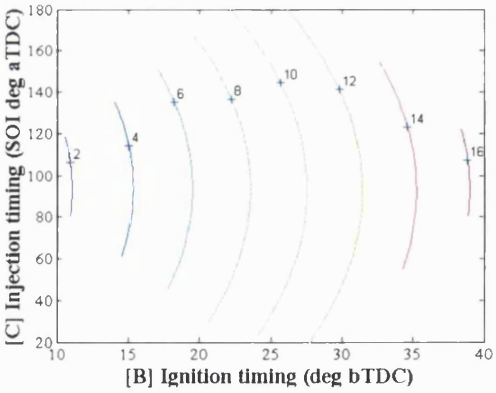

(f)

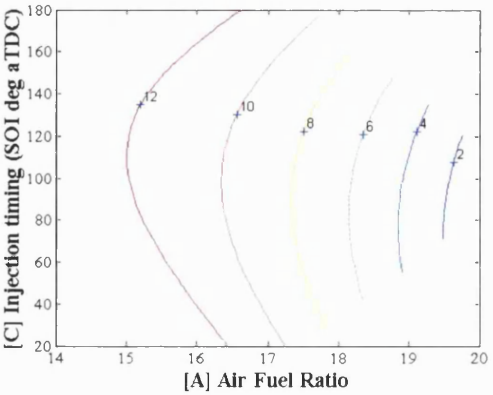

(g)

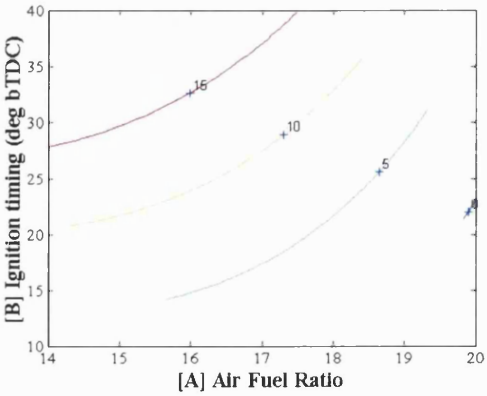

(h)

Figure 4.38 - Results set for NOx emissions (g/kWh). 60° injector, side injection, 20 bar fuel pressure.

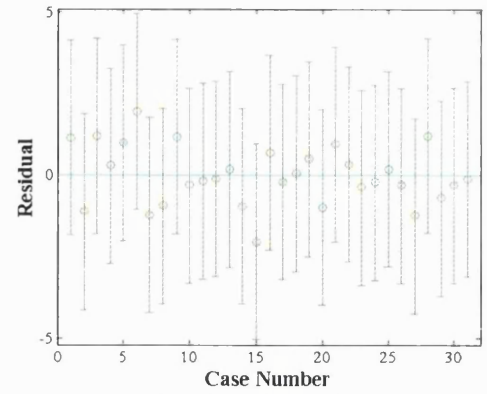

(a) - Residuals plot.

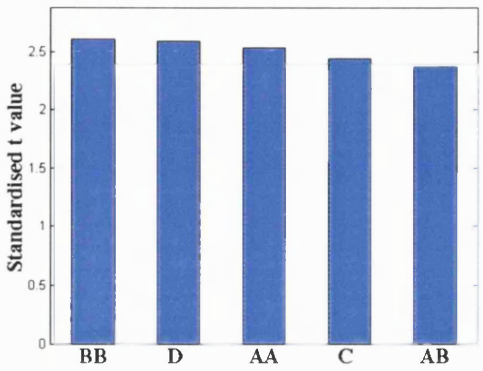

(b) - Influential variables.

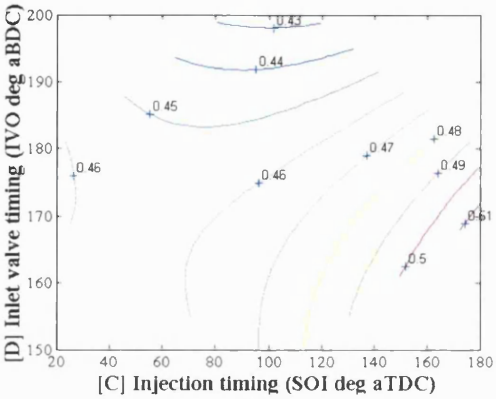

(c)

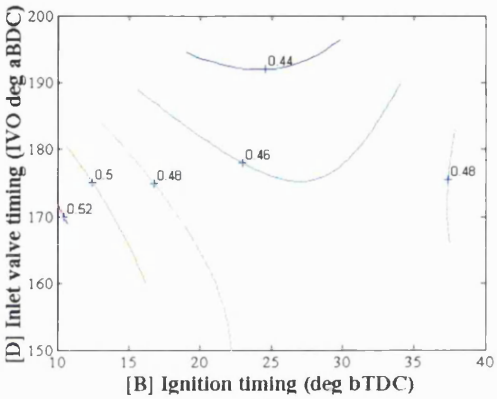

(d)

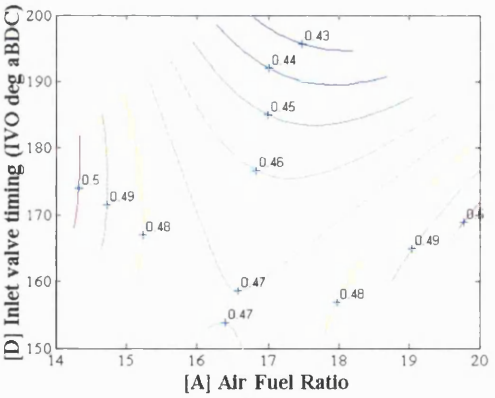

(e)

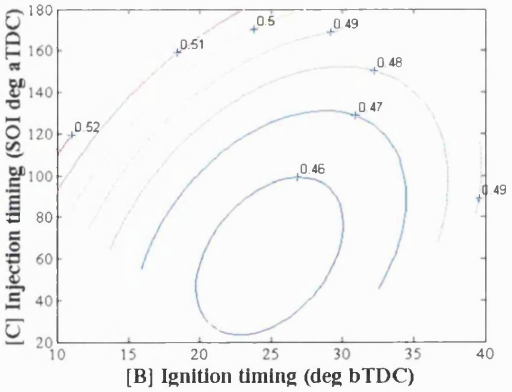

(f)

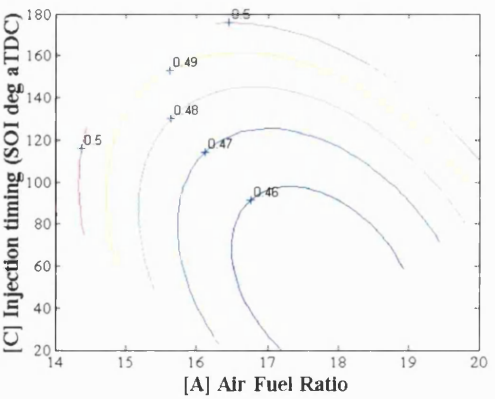

(g)

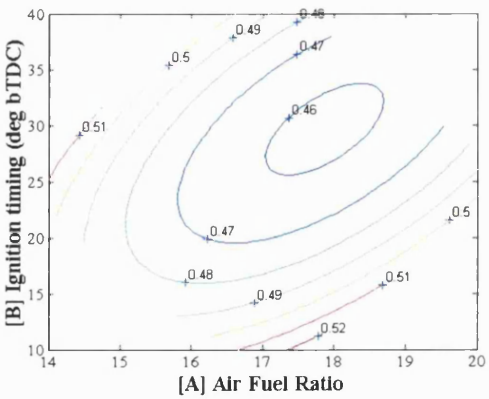

(h)

Figure 4.39 - Results set for BSFC (kg/kWh). 60° injector, side injection, 20 bar fuel pressure.

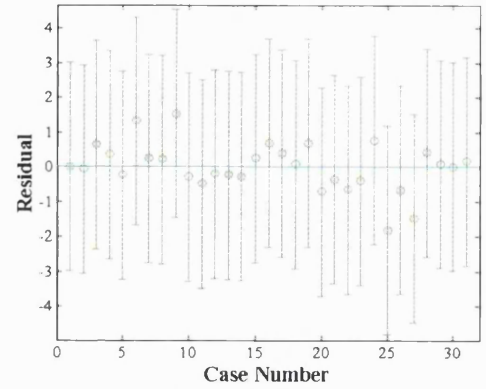

(a) - Residuals plot.

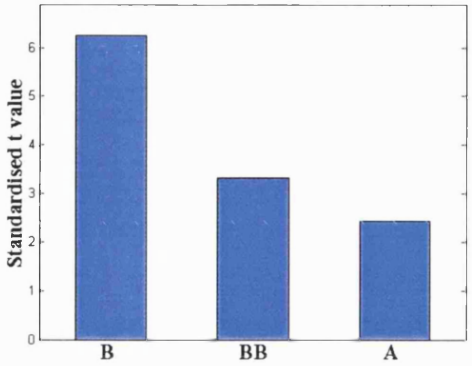

(b) - Influential variables.

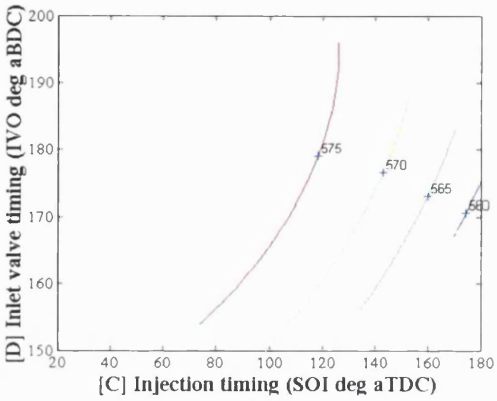

(c)

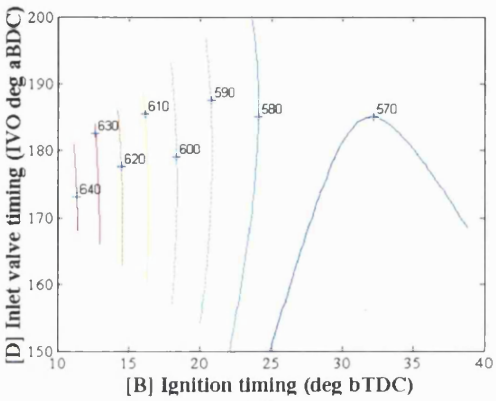

(d)

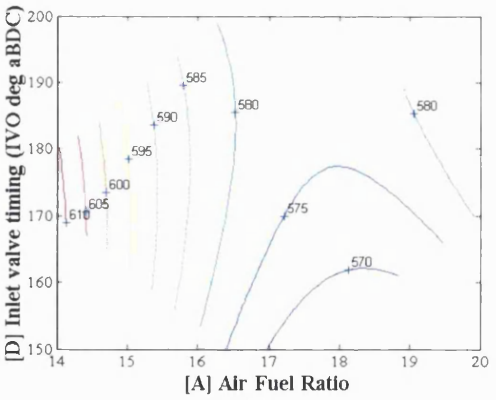

(e)

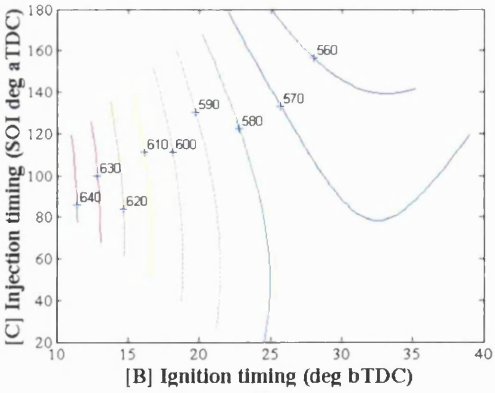

(f)

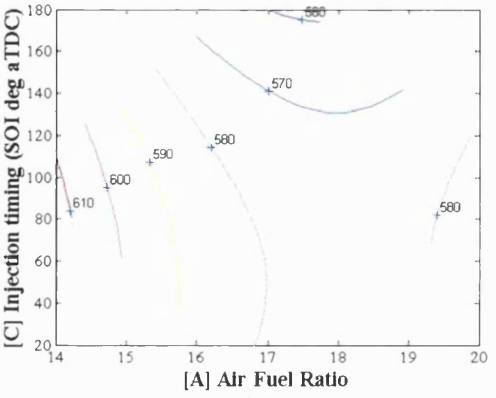

(g)

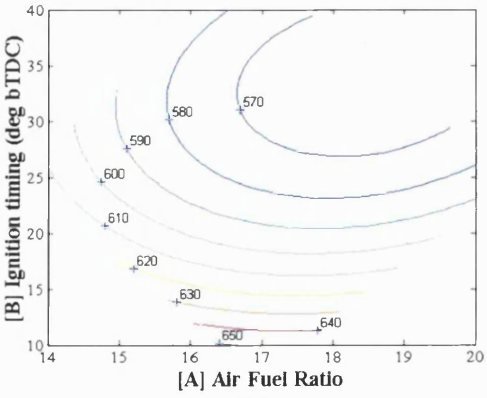

(h)

Figure 4.40 - Results set for exhaust gas temperature (°C). 60° injector, side injection, 20 bar fuel pr.

4.7 Port fuel injection, 3 bar fuel pressure

4.7.1 Hydrocarbon emissions

No. of outliers	0
Influential variables	BB, C, B
Highest t value	4

Figure 4.41 - Summary of CCRD results for HC emissions.

Ignition timing is the most important variable in its effect on HC emissions with this configuration, followed by injection timing. Figures 4.45(d), (f) and (h) all agree in that HC emissions peak at an ignition timing of between 25° and 30° bTDC. This was also experienced with other configurations as explained earlier.

Lower HC emissions are achieved with later injection timings in this configuration. This can be explained for the port fuel injection arrangement by the fact that late injection timings correspond to closed valve injection once the transit time of the fuel between injector and the intake valves is taken into account. Closed valve injection allows the fuel sufficient residence time on the back of the inlet valves to be fully vaporised by the start of the induction process, hence leading to good mixture preparation. This trend is visible in figures 4.45(c), (f) and (g).

4.7.2 NOx emissions

No. of outliers	2
Influential variables	AA, B, AD, C, D, BB, AB, DD
Highest t value	12

Figure 4.42 - Summary of CCRD results for NOx emissions.

The air/fuel ratio, followed by ignition timing are the most significant variables with regards to influencing the formation of NOx in this configuration. The NOx emissions are seen to peak at an air/fuel ratio of approximately 16:1 in figures 4.46(g) and (h) and to a lesser extent in figure 4.46(e). It is expected that peak NOx figures are obtained at an air/fuel ratio just lean of stoichiometric, with substantial reductions either side of this point. The response curves show this with a steep gradient away from the maximum.

As expected, retarded ignition timings have the effect of reducing NOx emissions due to the reduced peak temperature in the combustion chamber. This is illustrated in figures 4.46(d) and 4.46(f).

4.7.3 Brake specific fuel consumption

No. of outliers	11
Influential variables	A, AA, BB, B, C, AD, AB
Highest t value	8

Figure 4.43 - Summary of CCRD results for BSFC.

Air/fuel ratio is by far the most influential variable in this configuration on the BSFC. The response is typical of a port-injected engine with a fairly flat response lean of stoichiometric and a minimum of 17.5:1. There is the expected rapid deterioration at air/fuel ratios rich of stoichiometric. However, there are doubts over the validity of the model. There are 11 test points flagged up as outliers in the residual plot shown in figure 4.47(a). The spread of the data in this figure indicates that there was a systematic change in the results from, perhaps, as early as test point 14 onwards. This change meant that the results fell to levels under those predicted by the model up until test point 28 where there were indications of a recovery. The systematic nature of the change suggests that there was some influence affecting either or both of the two parameters compounded to calculate BSFC (i.e. fuel flow rate or engine power). It is not apparent from the examination of the raw test data what the influence might be. The relatively high 't' values of the air/fuel ratio and ignition timing leaves little doubt that these are the main parameters affecting BSFC, and so it is only the shape of the responses that are in question.

4.7.4 Exhaust gas temperature

No. of outliers	1
Influential variables	A, B, D, BB
Highest t value	10

Figure 4.44 - Summary of CCRD results for exhaust gas temperature.

The most influential variable on exhaust gas temperature in this configuration is air/fuel ratio, closely followed by ignition timing. Figures 4.48(e), (g) and (h) illustrate a trend for lower exhaust gas temperatures at high air/fuel ratio values, as expected. The effect of ignition timing (shown in figures 4.48(d) and 4.48(f) and to a lesser extent in figure 4.48(h)) is a reduction in the temperature of the gases when the timing is advanced. This has been discussed in an earlier section.

The one outlier is test point 20. This corresponds to the richest air/fuel ratio (14:1) and the indication is that the model is predicting a temperature that is too high for this setting.

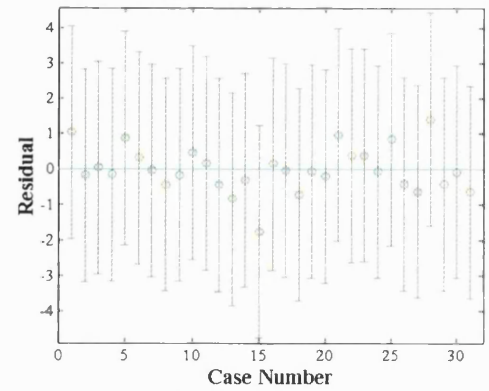

(a) - Residuals plot.

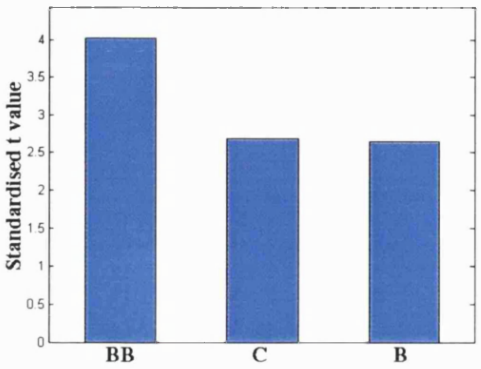

(b) - Influential variables.

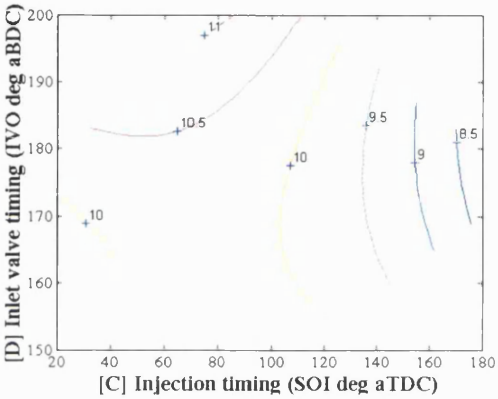

(c)

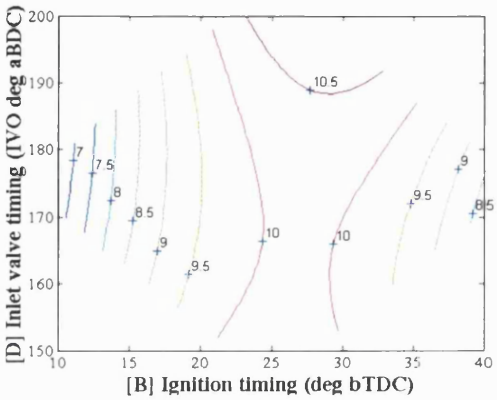

(d)

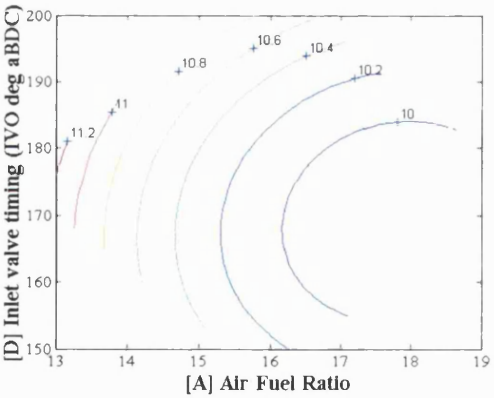

(e)

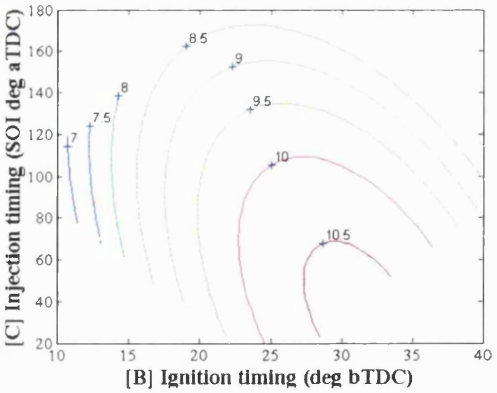

(f)

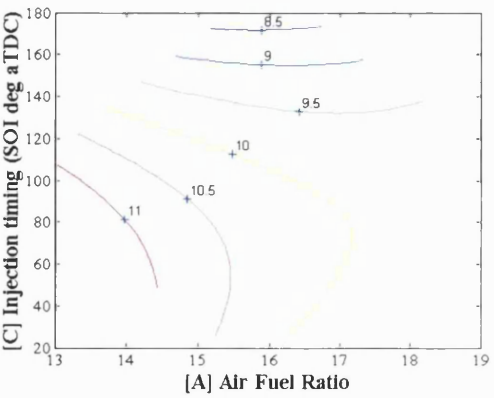

(g)

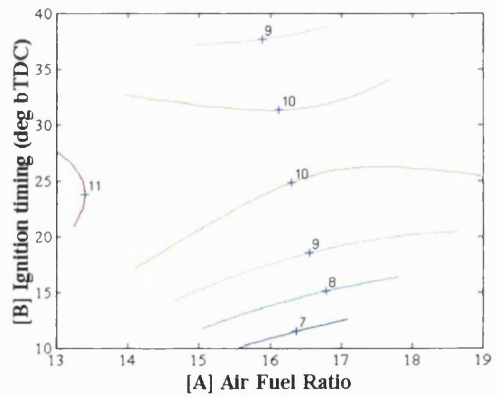

(h)

Figure 4.45 - Results set for HC emissions (g/kWh). Port fuel injection, 3 bar fuel pressure.

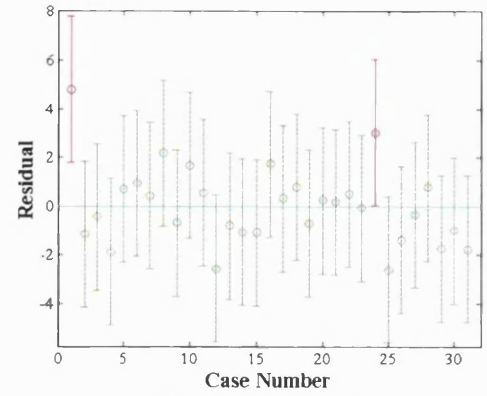

(a) - Residuals plot.

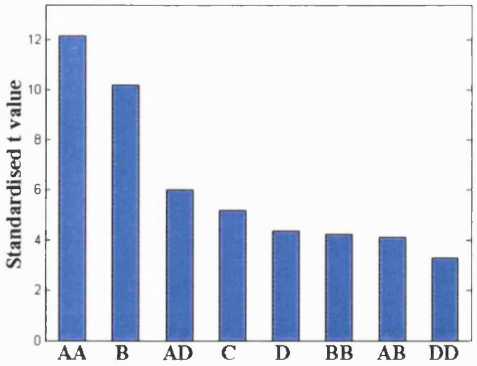

(b) - Influential variables.

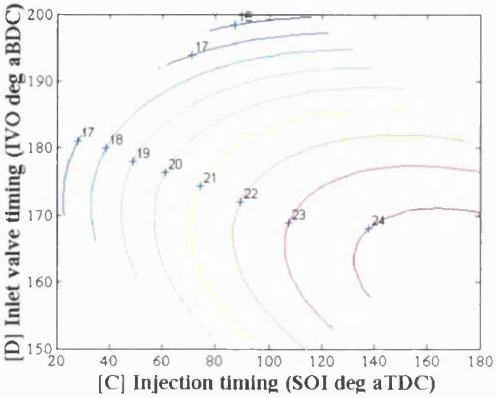

(c)

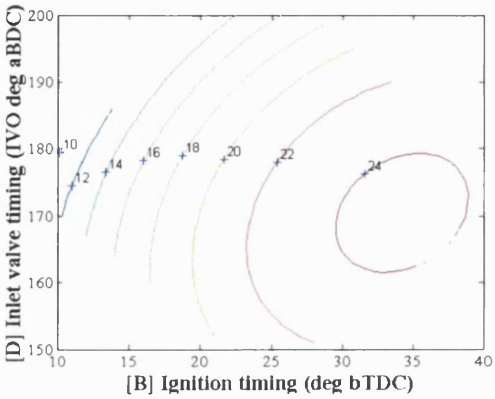

(d)

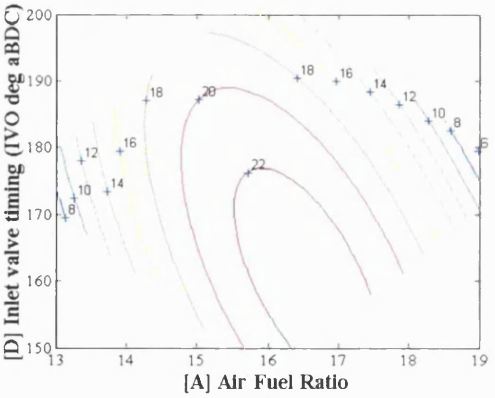

(e)

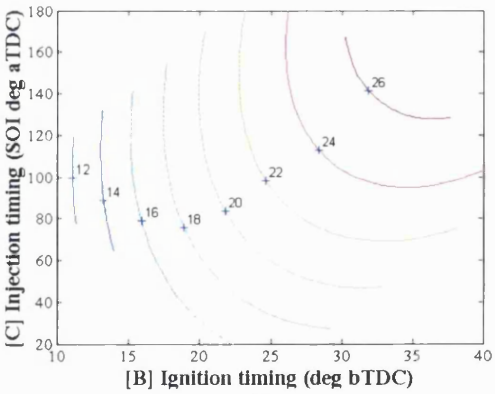

(f)

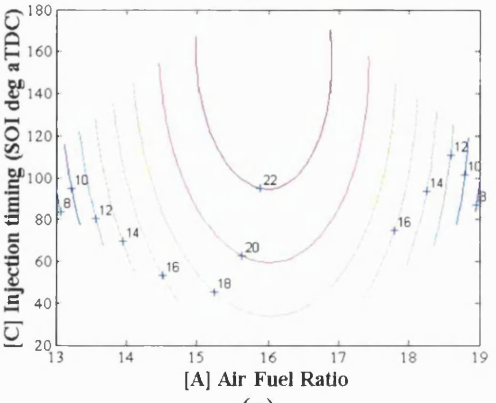

(g)

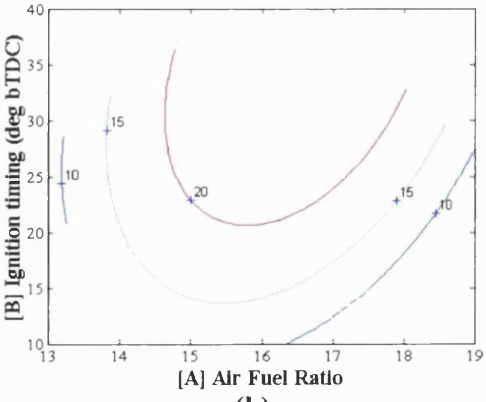

(h)

Figure 4.46 - Results set for NOx emissions (g/kWh). Port fuel injection, 3 bar fuel pressure.

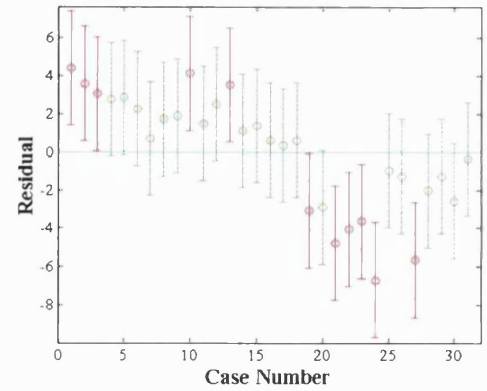

(a) - Residuals plot.

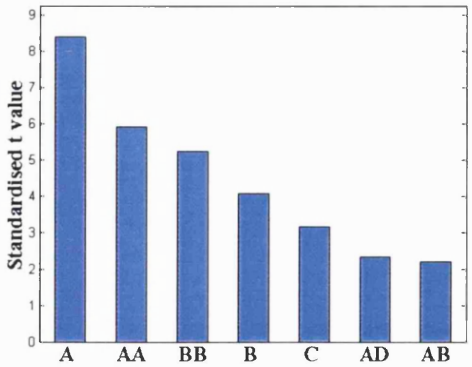

(b) - Influential variables.

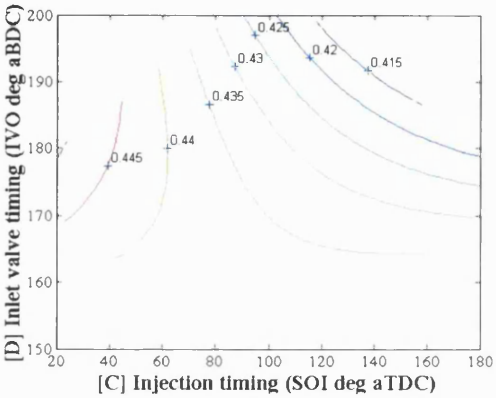

(c)

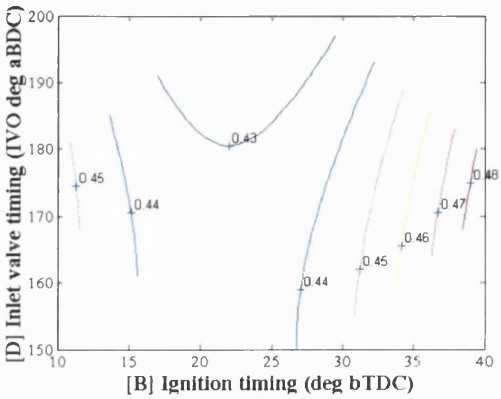

(d)

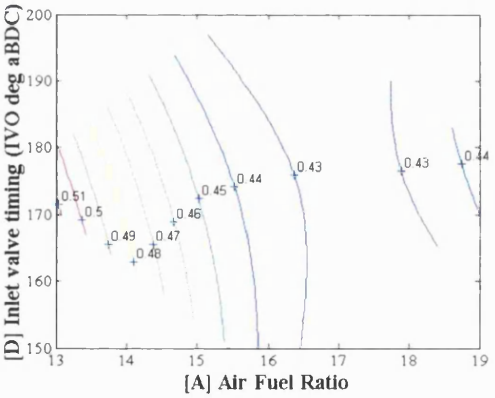

(e)

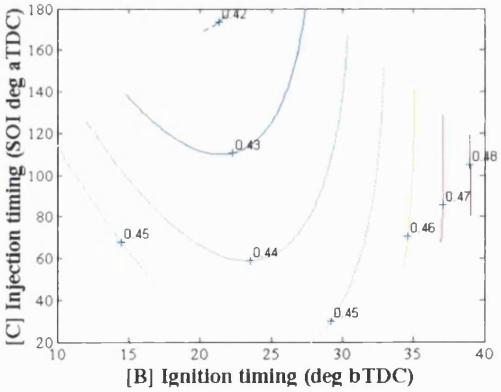

(f)

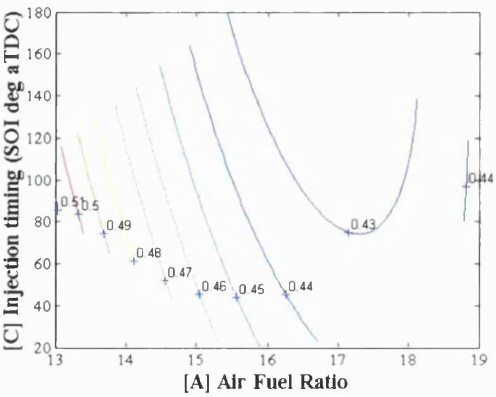

(g)

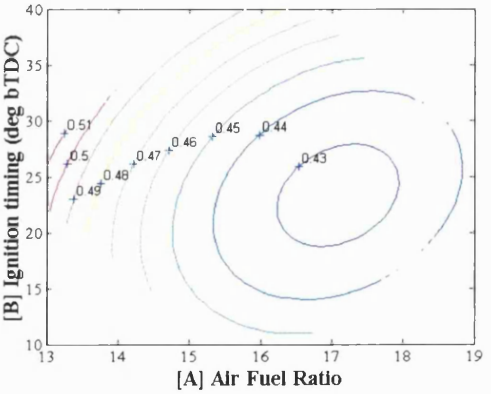

(h)

Figure 4.47 - Results set for BSFC (kg/kWh). Port fuel injection, 3 bar fuel pressure.

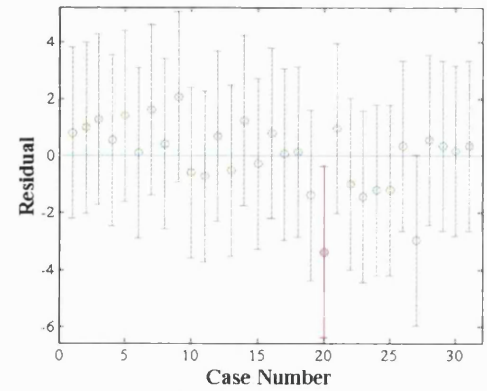

(a) - Residuals plot.

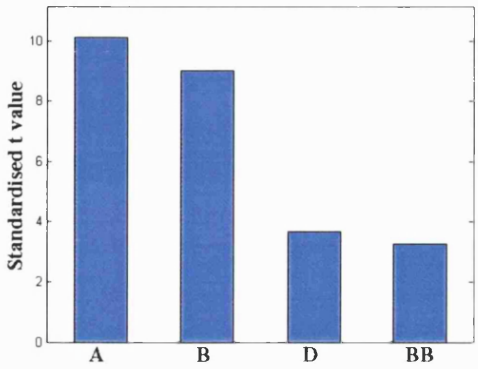

(b) - Influential variables.

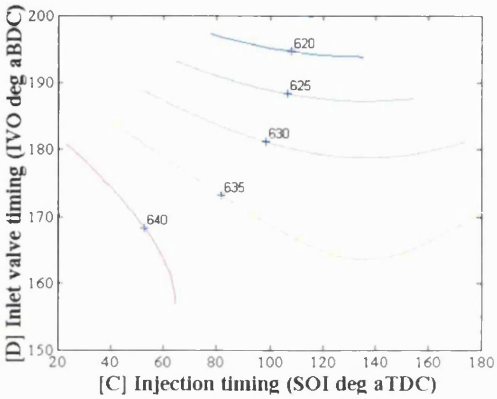

(c)

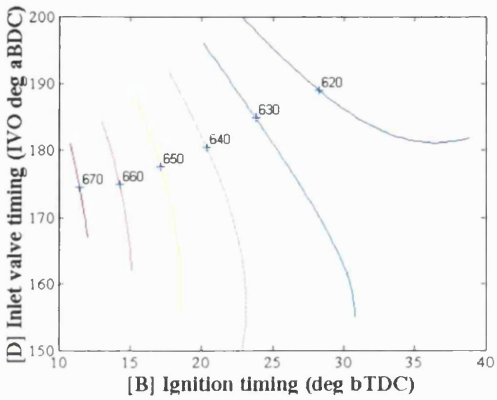

(d)

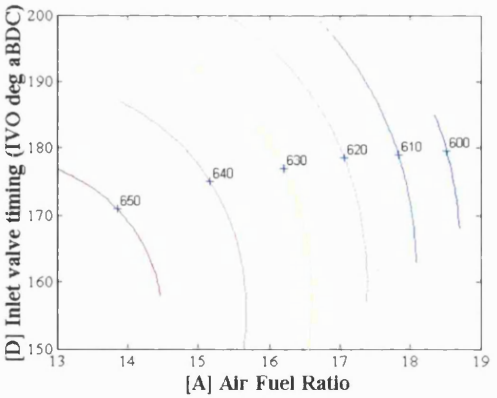

(e)

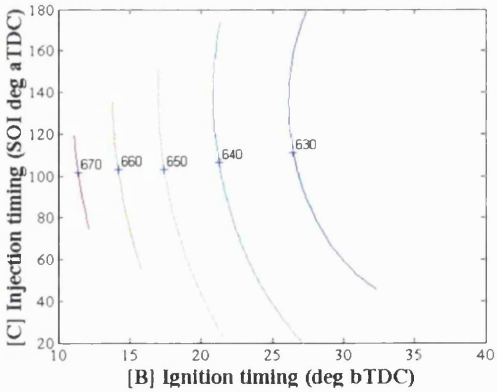

(f)

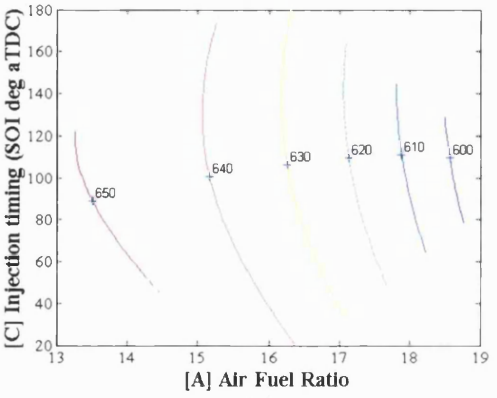

(g)

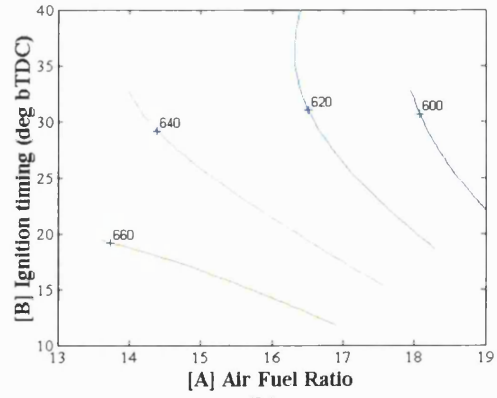

(h)

Figure 4.48 - Results set for exhaust gas temperature (°C). Port fuel injection, 3 bar fuel pressure.

4.8 Discussion of engine test results in relation to the fuel spray structures

The method by which the fuel was introduced into the combustion chamber is the difference under investigation between the various configurations tested. An understanding of the results must therefore be based on a study of the differences between the fuel sprays. The earlier test rig results (chapter 2) provided a considerable amount of basic spray information. It was decided to apply this information to interpret the engine test results by superimposing suitably scaled images from the test rig onto accurate diagrams of the internal layout of the cylinder and combustion chamber.

This approach is limited in a number of ways. The combustion chamber of the engine, for instance, is more confined than the test rig used for the spray photographs particularly when injection timing is early and the piston is close to TDC. At many of the engine's operating conditions, the fuel spray would impact on the piston, as shown in the superimposed diagrams. No attempt has been made to remove the portion of the spray that has apparently impacted on the piston, as it was felt that the spray envelope gives a visual measure of the extent of the likely impaction, and therefore, the amount of fuel that may or may not reside on the piston. When interpreting the diagrams, it should be remembered that injecting in the proximity of a wall (as for some engine cases) would affect the form of the spray when compared to a free-air spray.

For each condition illustrated, two injection timings are shown: one near the mid-point of the injection period and the second at the end of injection. In each of the seven diagrams provided, a fuel injection sequence from the rig testing was chosen to closely reflect the actual in-engine conditions. For instance, during engine testing with GDI operation, the fuel was hot throughout testing due to its path through the fuel pump and the pressure relief valve. All spray images used in these diagrams were taken from sequences where the fuel was heated. Likewise, the pressure in the cylinder. Though this did vary in the engine itself, the pressure in the cylinder was always approximately 0.5 bar during the injection period. Rig tests were performed at this pressure also, enabling accurate replication of the conditions. One effect that is not allowed for in this superposition technique is the influence of airflow on the spray structure. However, the existence of a parallel project, which recorded images of sprays within a firing optical engine of the same design, allowed an assessment to be made and this is discussed later in this section.

One of the main outcomes of this superposition approach is an indication of the likelihood of impaction of the spray on either the descending piston or the opening inlet valves with central and side injection, and both 60° and 90° injectors. Rather than examine every case, the following study is concentrating on the extremes: earliest injection timing (when the danger of piston impaction is greatest) and latest timing (when the danger is least). Likewise the most

adverse combination of injection and inlet valve timing is included to investigate the possibility of fuel spray impaction on the valves.

The first of the obvious "extreme cases" is shown in figure 4.49. The 60° injector has the highest penetration rates at 100 bar, and the timing of the fuel injection is just 20° aTDC, which is the earliest setting used during testing. Even at around the mid-point of the 1.9 ms injection duration (figure 4.49(a)) there is significant impingement on the piston crown. By the end of injection (figure (4.49(b)), it is likely that a large amount of this fuel will have impacted on the cylinder wall due to the momentum of the spray in that direction. In fact, the situation is worse than it appears, as the image of the spray is truncated where it has penetrated the furthest. The reason for this truncation is that the frame size of the rig test images was not large enough to record all of the spray (see figure A1.3 147). Some fuel will evaporate from the hot piston surface, but some will almost certainly reach the cylinder wall. The effect of this on the HC emissions can be compared to the case where the injector is mounted centrally (figure 4.51). According to the CCRD model, the side injection case has an HC emissions value of 13.5 g/kWh, whereas the central injection case, with the same settings, emits only 9.8 g/kWh. The cylinder wall is significantly cooler than the piston, so the fuel may reside on the walls and in the boundary layer, eventually being scraped into the top piston ring crevice. This fuel would then be detected in the exhaust as unburned HC emissions, because combustion does not penetrate this area. As there is less fuel being wasted in this way with central injection, its BSFC figure is lower (0.43 kg/kWh against 0.46 for the side injection case).

Figure 4.49 is a two-dimensional representation of what is a three-dimensional situation. It appears that the spray impacts on the inlet valves, but this is far from obvious in practice as the injector is mounted in a plane between the inlet valves rather than in the same plane as one of them. In fact, the chance of impaction is obviously less for the 60° injector that for the 90° injector. The situation for the 90° injector is discussed later.

The second case under investigation is similar to the first, but the fuel pressure is lowered to just 20 bar. The injection period is necessarily extended for the 20 bar case in order to deliver the same amount of fuel. This has the effect that the piston has descended further by the halfway point and completion points of the spray period. Also, the penetration rate is considerably less due to the slower exit velocity from the injector. As can be seen from figure 4.50, there is still some fuel sprayed onto the piston crown. This, together with a mixture which is not as well prepared as the high-pressure case, increased the HC value to 15.5 g/kWh (13.5 g/kWh for the 100 bar case). The increase is not as large as might be expected, and it may be due to the 20 bar

fuel pressure reducing the penetration of the fuel spray, so that less fuel resides on the cylinder walls.

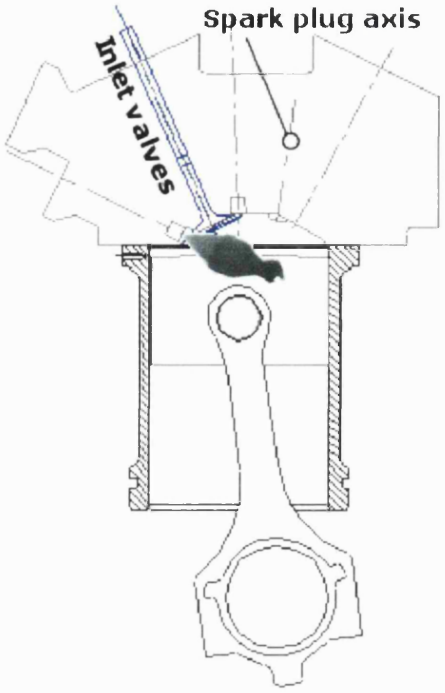

(a)

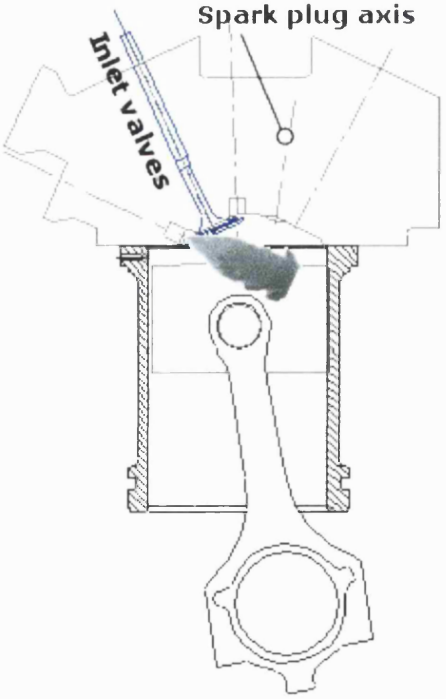

(b)

Figure 4.49 - a) Engine timing diagram. 60° injector, 100 bar fuel pressure, 1.0 ms aSOI, IVO 5° bTDC, engine position 388.6° CA, valve lift 2.77 mm. (Photograph figure number A1.3 142)
b) Engine timing diagram. 60° injector, 100 bar fuel pressure, 1.9 ms aSOI, IVO 5° bTDC, engine position 397.1° CA, valve lift 3.73 mm. (Photograph figure number A1.3 147)

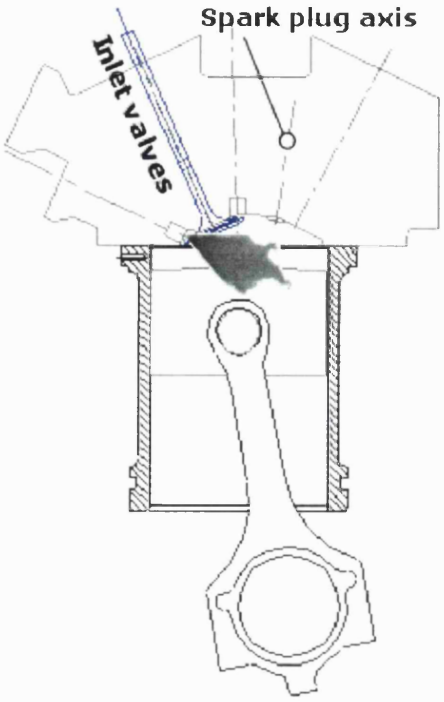

(a)

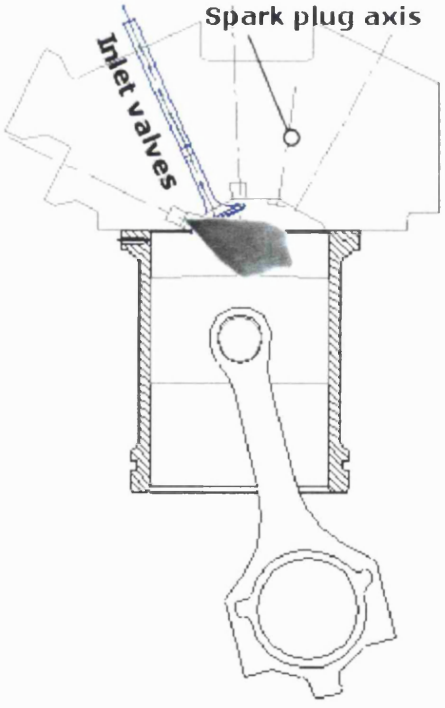

(b)

Figure 4.50 - a) Engine timing diagram. 60° injector, 20 bar fuel pressure, 2.2 ms aSOI, IVO 5° bTDC, engine position 399.8° CA, valve lift 3.83 mm. (Photograph figure number A1.3 137)

b) Engine timing diagram. 60° injector, 20 bar fuel pressure, 2.7 ms aSOI (spray fully developed), IVO 5° bTDC, engine position 419.6° CA, valve lift 5.83 mm. (Photograph figure number A1.3 139)

As discussed earlier, the emissions performance of the engine with the 60° injector mounted centrally is far better than with the same injector mounted in the side injection position. HC emissions in particular are dramatically reduced by injecting centrally, supporting the theory that side injection causes a significant amount of fuel to reside on the cylinder walls. Even in the case shown in figure 4.51, where fuel injection is at its earliest setting (20° aTDC), leading to significant impaction on the piston, the value of HC emissions (9.8 g/kWh) is much lower than the worst case for side injection.

Some of the fuel impacting on the piston will spread outwards, but the radial momentum with the 60° cone angle is likely to be low, giving a longer residence time and more chance of evaporation from the piston crown. Some of the spray is likely to 'splash' back into the combustion chamber, either impacting on the combustion chamber surface or forming droplets, probably quite small in size, and becoming entrained in the general gas motion.

As with the 60° injector in the side position, figure 4.52 demonstrates that a significant amount of fuel impacts on the piston crown when the 90° injector is utilised with the earliest injection timing (20° aTDC). However, the HC emissions are lower when using the 90° injector (11.8 g/kWh versus 13.5 g/kWh for the 60° injector) at the early fuel injection timing. This is thought to be due to the lower penetration rates from the 90° injector, which reduces the amount of fuel impacting the cylinder wall. The BSFC is also improved by using the 90° injector (0.42 kg/kWh versus 0.46 kg/kWh for the 60° injector). The lower penetration rate is partly evident by comparing figure 4.52(b) with 4.49(b), and is confirmed by the penetration plots shown in figures 2.33 and 2.34 (injector C is the 60° injector and injector D is the 90° injector).

The wider spray angle of the 90° injector means that there is more danger of impaction on the inlet valves. The most critical time for this is when the combination of inlet valve and injection timing is such that injection is complete at around the time of maximum inlet valve lift (9.0 mm). This combination is shown in figure 4.53.

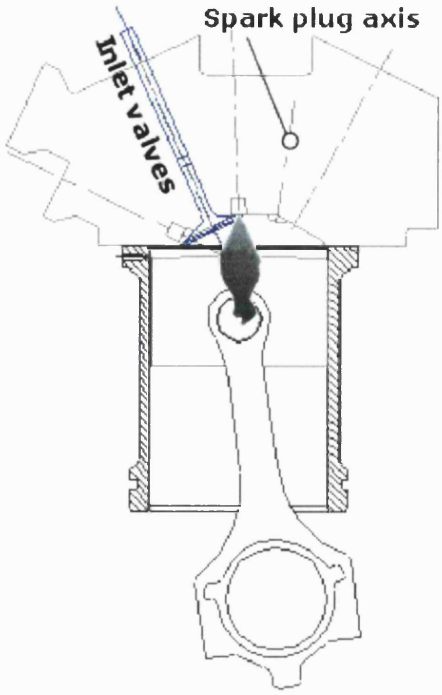

(a)

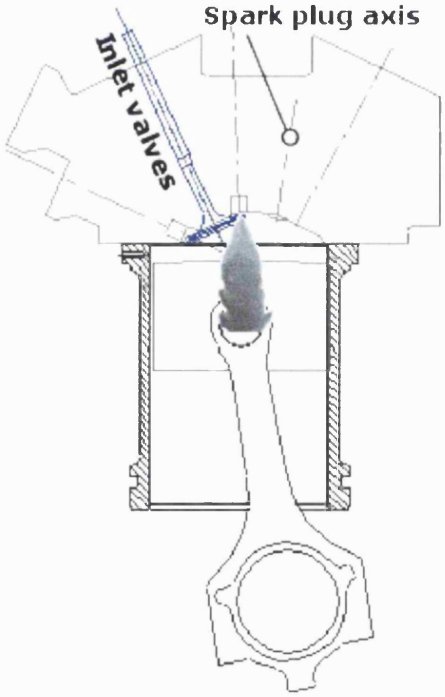

(b)

Figure 4.51 - a) Engine timing diagram. 60° injector, 100 bar fuel pressure, 1.0 ms aSOI, IVO 5° bTDC, engine position 388.6° CA, valve lift 2.73 mm. (Photograph figure number A1.3 142)
b) Engine timing diagram. 60° injector, 100 bar fuel pressure, 1.9 ms aSOI, IVO 5° bTDC, engine position 397.1° CA, valve lift 3.73 mm. (Photograph figure number A1.3 147)

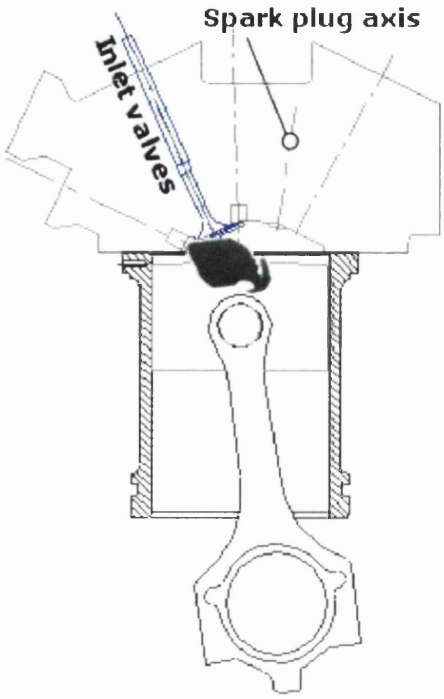

(a)

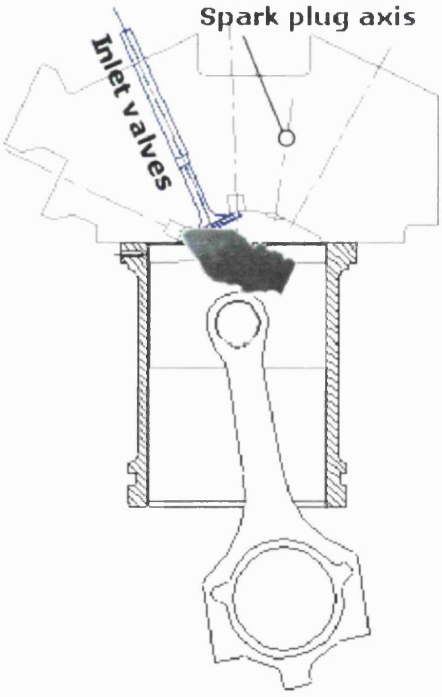

(b)

Figure 4.52 - a) Engine timing diagram. 90° injector, 100 bar fuel pressure, 0.9 ms aSOI, IVO 5° bTDC, engine position 388.1° CA, valve lift 2.68 mm. (Photograph figure number A1.4 005)
b) Engine timing diagram. 90° injector, 100 bar fuel pressure, 1.8 ms aSOI, IVO 5° bTDC, engine position 396.2° CA, valve lift 3.43 mm. (Photograph figure number A1.4 009)

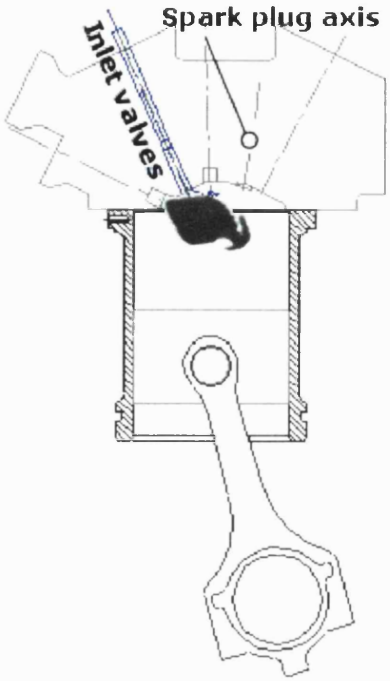

(a)

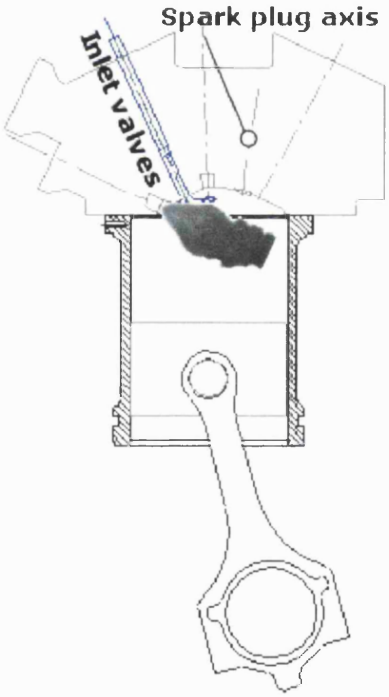

Figure 4.53 - a) Engine timing diagram. 90° injector, 100 bar fuel pressure, 0.9 ms aSOI, IVO 5° bTDC, engine position 468.1° CA, valve lift 8.68 mm. (Photograph figure number A1.4 005)
b) Engine timing diagram. 90° injector, 100 bar fuel pressure, 1.8 ms aSOI, IVO 5° bTDC, engine position 476.2° CA, valve lift 8.83 mm. (Photograph figure number A1.4 009)

Figure 4.53 shows the geometry of the engine with the 90° injector and with the inlet valves opening 5° bTDC and injection starting 100° aTDC. The inlet valves are nearly fully open throughout injection in this situation, leading to suspicions that impaction may occur on the backs of the valves, adversely affecting the HC emissions and BSFC. Indeed, the model indicates a value of 18.7 g/kWh for HC emissions for this test point versus only 11.8 g/kWh for the same configuration with early injection (figure 4.52). As can be seen in figure 4.53, there is no significant fuel impaction on the piston, but some spray may travel straight across the combustion chamber in any case and land on the cylinder wall. This may cause high HC emissions, but then so may impaction on the backs of the inlet valves. The likelihood of the impaction is investigated in figure 4.54. The lines in figure 4.54(a) represent the width of the spray measured from the image corresponding to the spray at the end of injection. These lines are then transposed as ellipses in figure 4.54(b) on the assumption that the spray is conical in form. It is clear from this that there should be a significant amount of fuel hitting the backs of the inlet valves. Even with the 60° injector, it is likely that there would be some impaction.

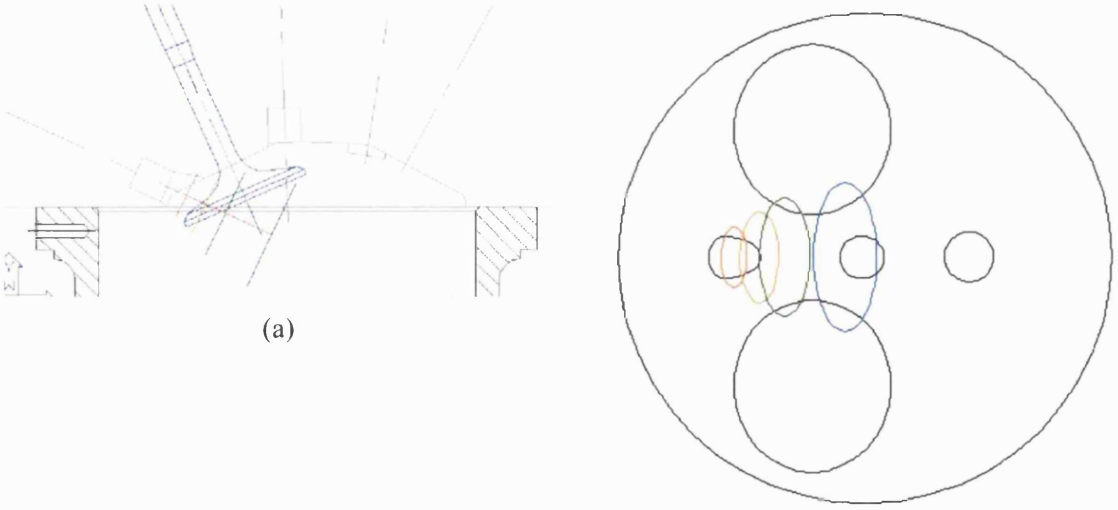

(a)

(b)

Figure 4.54 - Schematic representation of the 90° fuel spray and its impaction on the inlet valves.

It is difficult to predict what would happen when the fuel spray encounters the inlet valves. Some fuel would splash into the intake port, while some would adhere to the valves. These and other possibilities are likely to detract from the preparation of a homogeneous mixture of fuel and air for combustion.

There are several other timing combinations that will result in possible impaction on the backs of the inlet valves. Early inlet valve timing (150° aBDC), with start of injection at 100° aTDC results in injection starting when the valves are fully open at 9.0 mm lift. Late fuel injection (140° aTDC) has the same effect coupled with inlet valve timing of 187.5° aBDC - injection

with the valves fully open. There are other cases where the valves may not be 100% open, but nearly, which could cause impaction, certainly with the 90° injector. The increased likelihood of impaction with side injection provides another explanation why the central injection configuration performs better than side injection.

Figure 4.55 illustrates early injection timing with a centrally mounted 90° injector injecting at 100 bar fuel pressure. The early injection timing corresponds to a period of low inlet valve lift so the risk of fuel injection on the back of the intake valves is quite small. As with the 60° injector, central injection with the 90° injector (10.4 g/kWh) has superior HC emissions over the side injection case (18.7 g/kWh). This is thought to be due to less impaction on the cylinder wall, though there is still a large amount of fuel impacting the piston crown.

A condition is shown in figure 4.56 with the 90° injector mounted centrally, in which the inlet valves are more or less fully open throughout fuel injection. This corresponds to an injection timing of 100° aTDC and an inlet valve opening time of 5° bTDC. Another schematic (figure 4.57) was created to investigate whether or not significant impaction occurred on the back of the inlet valves in this case. Impaction was not expected because the HC emissions were less with this configuration in any case as discussed earlier. Side injection with the same settings resulted in a HC figure of 18.7 g/kWh, but this case only emitted 10.4 g/kWh. Figure 4.57 does not conclusively rule out impaction as the spray cone appears to pass very close to the valves, though if there is impaction, it certainly is not to the same extent as with side injection. Air flow into the cylinder would tend to deflect the fuel away from the valves, but the spray angle has been seen to be affected by changes in fuel temperature and ambient pressure so the possibility of some interference is present. However, the generally low HC emissions and BSFC values with this configuration suggest that any influence from inlet valve impaction is minimal.

To investigate the effect of the airflow in the cylinder on the spray structure, and validate the use of the diagrams above, reference is made to a parallel project, which resulted in images being obtained from a firing engine of the same design as this project. Figure 4.58 shows examples of the images obtained for the 60° and 90° injectors. The inlet valve timing (IVO 5° bTDC) is the same as the centre-point setting used for the CCRD. It can be seen from the images that the airflow from the inlet ports has not noticeably distorted the shape of the spray. As all interpretation diagrams refer to an inlet valve timing of 5° bTDC, it is concluded that the airflow would have a negligible effect on the structure of the sprays shown in the various interpretation diagrams. Interpretation diagrams matching the timings of the engine images are

provided for comparison. It is concluded that the diagrams have been a successful method of illustrating some of the engine's characteristics.

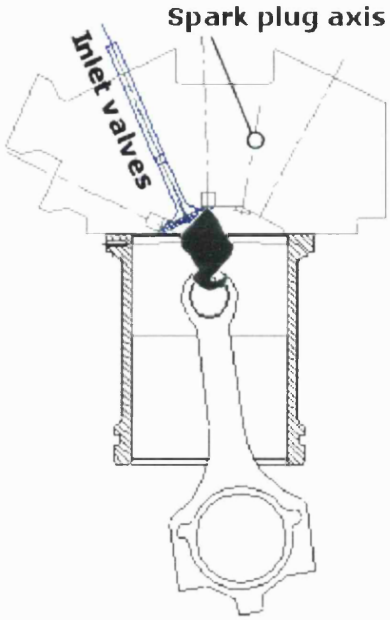

(a)

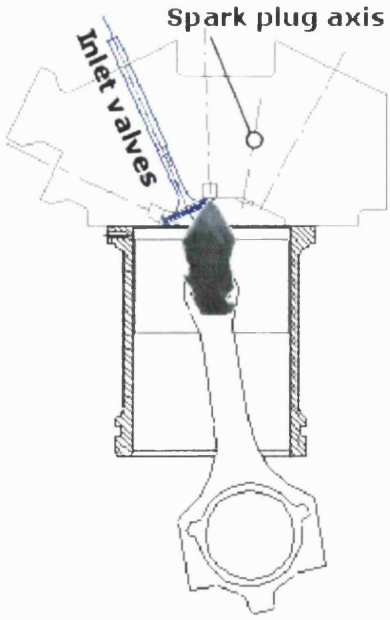

Figure 4.55 - a) Engine timing diagram. 90° injector, 100 bar fuel pressure, 0.8 ms aSOI, IVO 5° bTDC, engine position 387.2° CA, valve lift 2.56 mm. (Photograph figure number A1.4 004)
b) Engine timing diagram. 90° injector, 100 bar fuel pressure, 1.6 ms aSOI, IVO 5° bTDC, engine position 394.4° CA, valve lift 3.23 mm. (Photograph figure number A1.4 008)

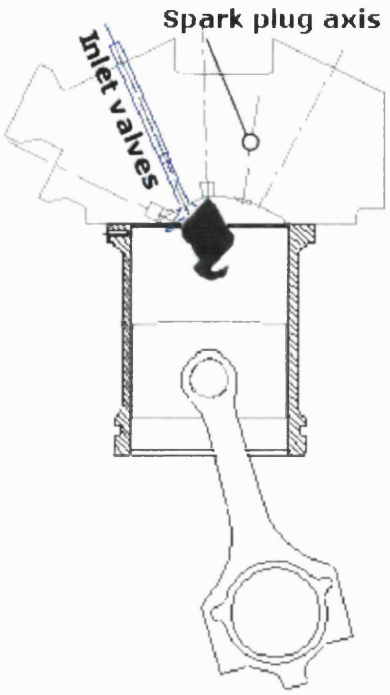

(a)

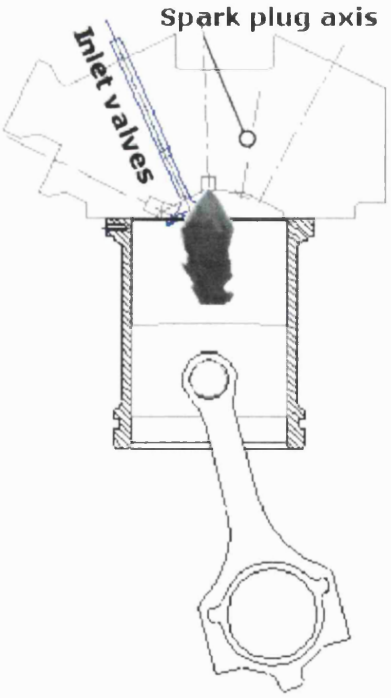

(b)

Figure 4.56 - a) Engine timing diagram. 90° injector, 100 bar fuel pressure, 0.8 ms aSOI, IVO 5° bTDC, engine position 467.2° CA, valve lift 8.67 mm. (Photograph figure number A1.4 004)
b) Engine timing diagram. 90° injector, 100 bar fuel pressure, 1.6 ms aSOI, IVO 5° bTDC, engine position 474.4° CA, valve lift 8.78 mm. (Photograph figure number A1.4 008)

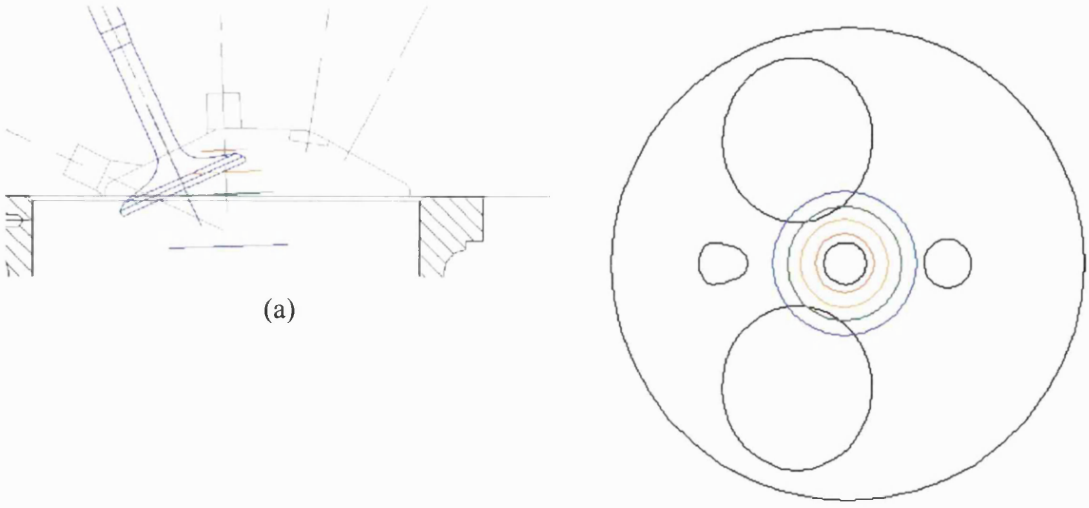

(a) (b)

Figure 4.57 - Schematic representation of the 90° fuel spray and its impaction on the inlet valves.

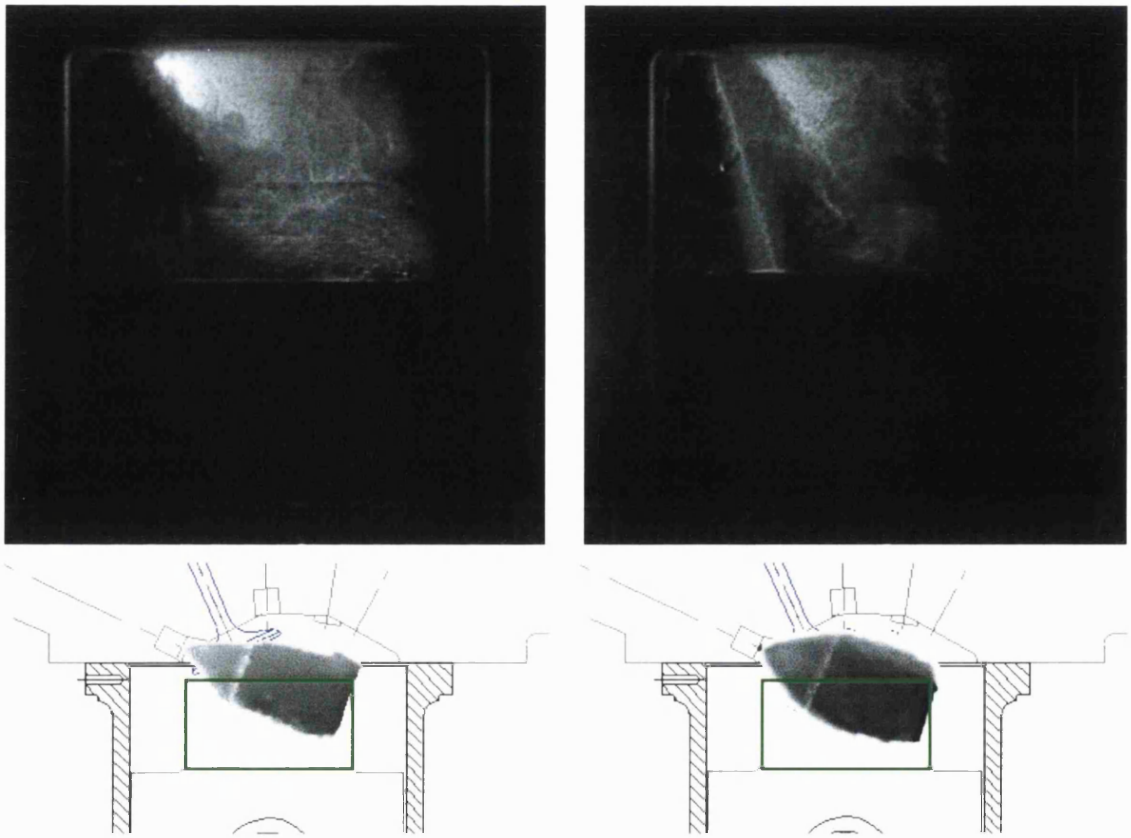

(a): 60° injector (b): 90° injector

Figure 4.58 - Photographs of the fuel spray inside the engine with side injection (adapted from the work described by Boheimer [2002]) and the associated interpretation diagrams: SOI 60° aTDC, IVO 18° bTDC, images are taken at 1.0 ms aSOI, 100 bar fuel pressure. The green outline is the viewing window.

Having now analysed the data from each configuration in isolation it will be useful to compare the different configurations, and their effect on the engine's performance as a whole.

Comparison of the sets of characteristics shown in the earlier sections of this chapter would be very difficult due to their complexity. A somewhat simpler method of comparison was derived. The MATLAB software effectively produces curve fits of the experimental data leading to mathematical equations that describe the behaviour of each response to changes in the four test variables (air/fuel ratio, ignition timing, fuel injection timing and inlet valve timing). For each configuration, the BSFC equations were examined to find the minimum value within the test range and the corresponding values of the four test variables were determined. This identified the point of maximum engine efficiency. The corresponding values of the four test variables were then substituted in the equations describing the responses of the emissions (HC and NOx), and their values found for the minimum BSFC point. The data is tabulated in figure 4.59.

Configuration	Minimum BSFC: kg/kWh	A	B: bTDC	C: aTDC	D: aBDC	HC: g/kWh	NOx: g/kWh
90°, 100 bar, side	0.41	17.8	25	60	188	12.7	13.8
90°, 100 bar, centre	0.38	18.5	18.8	80	188	8.3	7.8
60°, 100 bar, side	0.46	18.5	25	60	188	10.9	4.1
60°, 100 bar, centre	0.42	18.5	32.5	140	188	10.9	11.9
60°, 20 bar, side	0.43	17	25	100	200	12.9	7.6
PFI	0.42	16.8	21.3	140	188	9.0	15.0

Figure 4.59 - Comparison of settings for lowest BSFC values. A: air/fuel ratio. B: ignition timing. C: fuel injection timing. D: inlet valve timing.

The most efficient configuration appears to be the 90° injector mounted centrally, injecting fuel at 100 bar. HC emissions are also the lowest of all arrangements and the NOx figure is one of the lowest three figures. This is perhaps not too surprising as the GDI cylinder head was initially designed to be operated with central injection. It is thought that there are two mechanisms at work. First of all, the centrally-mounted fuel injector has been found to produce less HC emissions than the side injector in all cases, which is explained by the reduced impaction of fuel on the cylinder walls and the back of the inlet valves. Additionally, the 90° injector spreads the fuel more evenly across the combustion chamber and at lower penetration rates, so it is assumed that less fuel impacts on the piston. As there is more fuel in the air stream, maximum charge cooling can occur, reducing the charge temperature during compression and leading to lower NOx production.

Side injection with the 90° injector has a minimum BSFC value near to the central injection case, but the emissions values are considerably higher as discussed earlier.

Comparison of BSFC values suggests that the best GDI configuration is more efficient than PFI, but the other GDI configurations either give similar or worse values. The accuracy of the readings should be discussed at this point. The statistical analysis applied to the test results is able to determine the repeatability of BSFC through examination of the variation of centre-point values. The extent of the variation, in terms of a standardised residual, is marked on the plots shown earlier in the chapter (for example, figure 4.5(a)). For a closer examination of this variation, the residuals were plotted as absolute values (i.e. kg/kWh) for two cases as shown in figure 4.60. The maximum variation for the 90° injector case (figure 4.60(a)) is 0.02 kg/kWh, with a maximum variation of 0.04 kg/kWh for the PFI configuration (figure 4.60(b)).

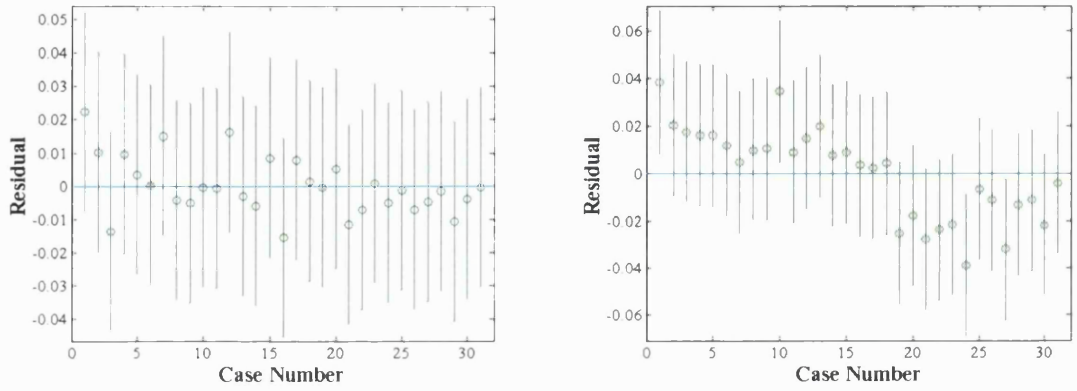

(a) (b)

Figure 4.60 - Residuals plots in absolute units (kg/kWh) for BSFC. a) 90° injector, 100 bar fuel pressure, central injection. b) PFI, 3 bar fuel pressure.

This variation is likely to be due to such factors as difficulty in keeping the engine running at its required test settings and variations in atmospheric conditions, and does not reflect the inaccuracies in measuring BSFC itself. However, it should still be considered when comparing configurations.

Two parameters are involved in the calculation of BSFC: fuel flow rate and engine power. It is estimated that engine power can be measured to an accuracy of ±1% and fuel flow rate to ±2%, giving a combined inaccuracy of ±3% (±0.012 kg/kWh). This still indicates that the best GDI configuration was more efficient than the PFI arrangement, but caution must be exercised as to the actual scale of the difference, especially when the maximum variation between points according to the residuals plot in figure 4.60 is 0.06 kg/kWh. Confidence in the greater efficiency of GDI is strengthened if the BSFC values of the 31 test points are plotted against each other (figure 4.61). The advantage of GDI is evident.

As discussed in chapter 1, a GDI engine has the potential to offer gains over the PFI engine in several respects. However, most of these are concerned with the basic operating parameters themselves, such as the ability to use a higher compression ratio with GDI. So, how is a GDI engine more efficient than a PFI unit at identical settings? It is apparent from figure 4.59 that the minimum BSFC value for 90°, central injection, 100 bar GDI configuration was obtained with a reduced ignition advance compared to the other configurations. This implies a faster burn rate, which in turn means that the heat release could be concentrated more at around the minimum volume condition. Basic heat engine cycle analysis shows that this gives the highest thermal efficiency. The faster burn rate can be explained by more even mixture preparation, because combustion would be very slow if there were local areas where the air/fuel ratio deviated significantly away from the mean value of 18.5:1 in the lean direction. It is to be expected that the 90°, central, 100 bar configuration should produce better mixture preparation than the other GDI configurations, but it is not expected that it should be better than the engine with PFI. One explanation is that the targeting of the port-mounted injectors (twin injectors were used) may not have been optimised for the engine as it was designed primarily for GDI.

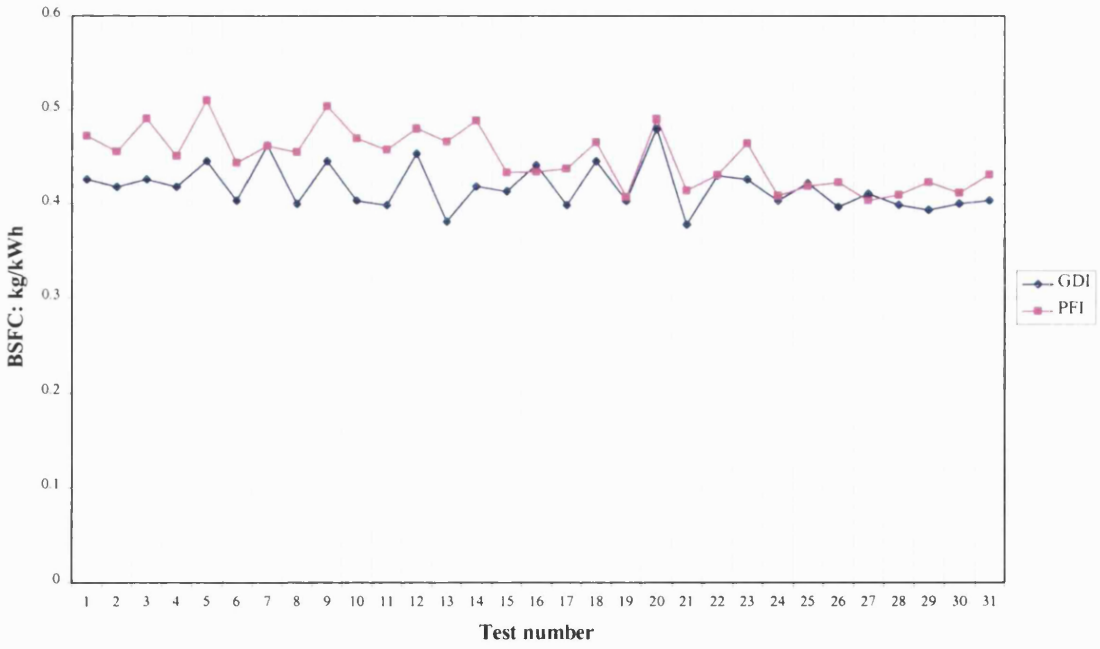

Figure 4.61 - Comparison of actual values of BSFC throughout testing. (GDI configuration is 90° injector, 100 bar fuel pressure, central injection).

Interestingly, all minimum BSFC values were obtained with late inlet valve timings. Typically the minimum BSFC was obtained with the inlet valves starting to open 8° aTDC (figure 4.59). Valve lift is relatively low for the next 20° by which time the piston has descended, inducing a relatively high intake velocity. The charge motion should be more vigorous under these

conditions, increasing the speed of burn in the cylinder, and hence improving the engine's efficiency. This could be an easier method to increase turbulence in the cylinder than designing sophisticated inlet ports, and would be particularly useful at low engine speeds.

The parallel project [Boheimer, 2002] using optical engines included laser Doppler measurements of the in-cylinder axial air flow velocities on the same geometry of engine, and a comparison between late inlet valve opening (figure 4.62(d)) and a more conventional timing (figure 4.62(c)) shows an approximately threefold increase in the peak velocity for the later opening. In figures 4.62 and 4.63, the Normalised Velocity is the ratio of the airflow velocity to the piston mean velocity.

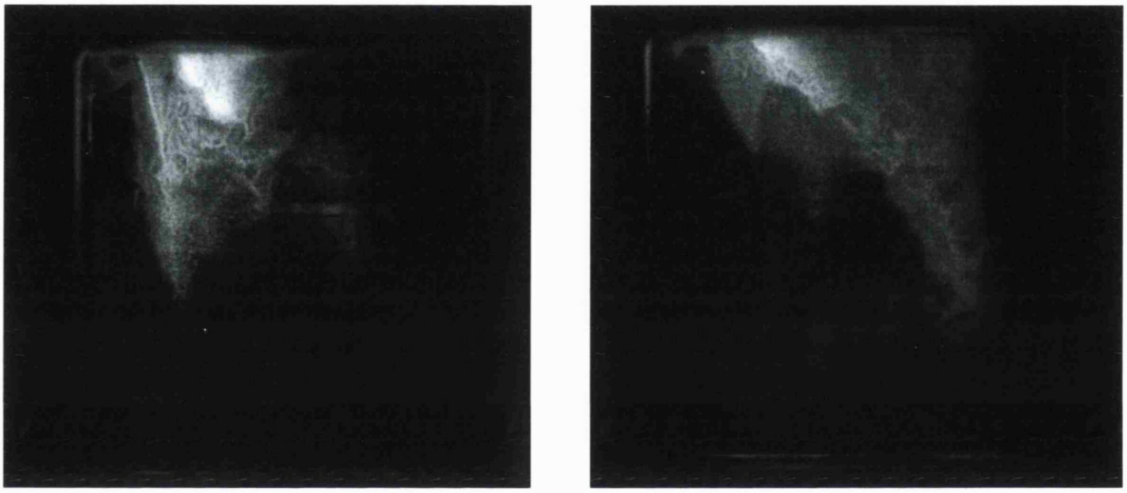

(a): IVO 18° bTDC (b): IVO: 22° aTDC

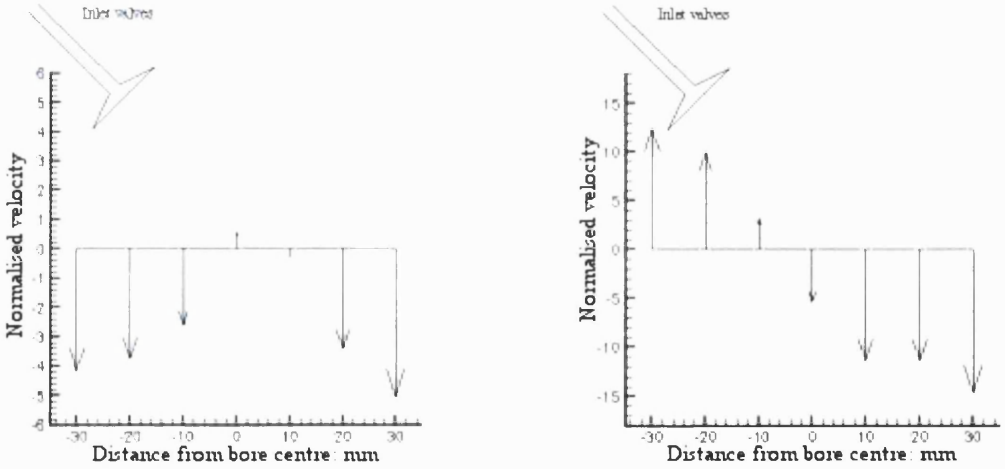

(c) (d)

Figure 4.62 - Photographs of the fuel spray inside the engine with side injection, and an axial velocity vector diagram at the same condition. SOI 100° aTDC using the 90° injector. Engine position is 109° aTDC in both cases. The axial velocities were measured across the diameter bisecting the two inlet (and exhaust valves at a distance 40 mm down from the cylinder head.

The higher airflow velocities have a considerable influence on the development of the sprays as indicated in the comparison shown in figure 4.62(a) and 4.62(b). The high velocity incoming air is flowing down the right-hand side of the cylinder, pulling with it that side of the spray. This effect was even more noticeable with the later injection timing setting of 140° aTDC, as shown in figure 4.63. Even though there is the possibility of further wall-wetting when the fuel is forced closer to the cylinder wall, it is believed that the increased velocities will result in faster burn rates through the resulting higher turbulence levels. This is reflected in the results where the minimum BSFC values were all obtained at retarded inlet valve timings.

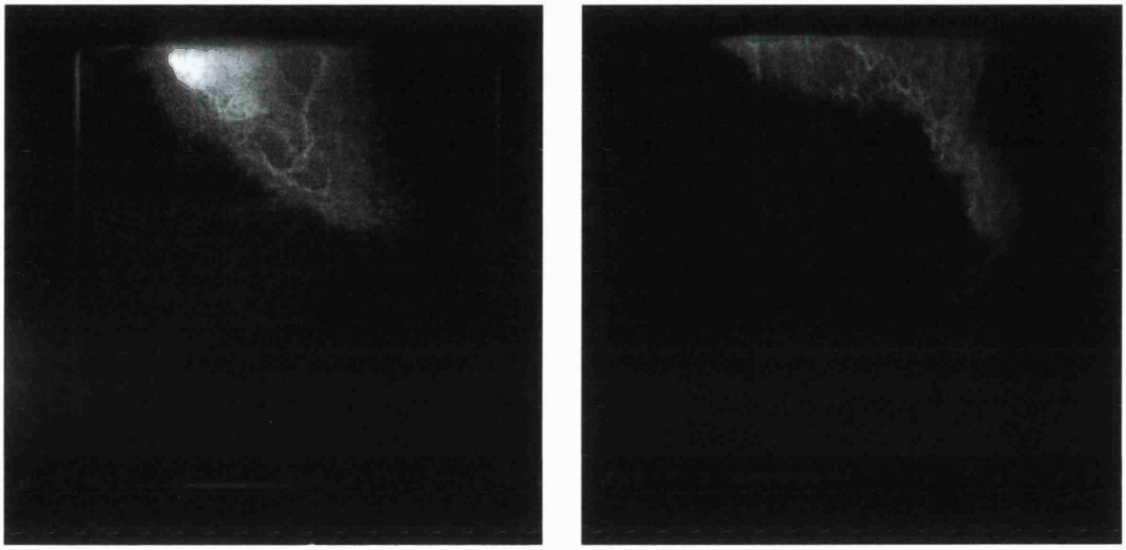

(a): IVO 18° bTDC (b): IVO: 22° aTDC

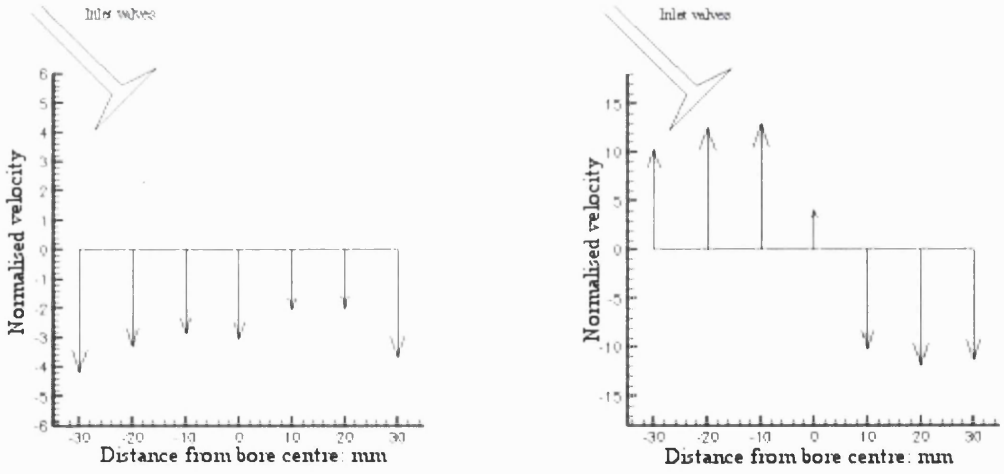

(c) (d)

Figure 4.63 - Photographs of the fuel spray inside the engine with side injection, and an axial velocity vector diagram at the same condition. SOI 140° aTDC using the 60° injector. Engine position is 149° aTDC in both cases. The axial velocities were measured across the diameter bisecting the two inlet (and exhaust valves at a distance 40 mm down from the cylinder head.

4.9 Summary of test results

In this chapter, the results were presented from engine testing on five GDI engine configurations along with PFI as a comparison. The standard test point was an engine speed of 1500 rpm, with a load setting of 2.62 bar BMEP. A CCRD was carried out using four variables (air/fuel ratio, ignition timing, fuel injection timing and inlet valve timing) to investigate their effect on four engine responses (HC emissions, NOx emissions, BSFC and exhaust gas temperature). Certain features of the emissions results could be explained by the knowledge gained on spray behaviour from the rig tests (chapter 2).

In most cases it was found that the CCRD model, which allowed for second order effects and interactions between pairs of variables, was sufficient to provide a relatively accurate description of each response. There were occasions where engine instability was a problem, at the leanest settings for instance, and this sometimes resulted in the engine test point being branded as an outlier.

In general, the responses for the engine in the various GDI configurations fell into similar patterns to its behaviour with PFI. For example, NOx emissions would tend to peak lean of stoichiometric and then fall for leaner mixtures and BSFC would decrease for leaner mixtures, showing a minimum value at 17:1 air/fuel ratio or leaner. There were differences in the levels of the responses between the various engine configurations.

The most efficient (i.e. lowest BSFC) configuration was GDI with a 90° injector mounted centrally, supplied with fuel at 100 bar pressure. This configuration also tended to have the lowest emissions levels compared with the other GDI configurations and with PFI. In general, central injection returned lower BSFC values and HC emissions than with side injection. As expected, injecting at a fuel pressure of 100 bar was better than at 20 bar, although the difference was more modest than would have been predicted. The minimum BSFC for all configurations was obtained with late inlet valve openings. This could be explained using the results of a parallel project, which showed that the in-cylinder air motion was far more vigorous under these conditions.

An attempt was made to construct interpretation figures, which illustrated the position of the piston and inlet valves in relation to the superimposed fuel spray image. These were found to be useful in understanding some of the emissions figures, such as higher HC emissions with side injection due to impaction on the cylinder wall. The possibility of inlet valve impaction was also illustrated. Further understanding was obtained by examining images from inside a firing engine. This showed the effects of airflow on the spray structure. These engine test results are

reviewed again in the following chapter in an attempt to summarise the findings of the overall research project.

Chapter 5
CONCLUSIONS AND FUTURE RESEARCH

5 - Conclusions and future research

5.1 Conclusions from the test results

Having conducted an extensive review of the literature in chapter 1, it is concluded that GDI is indeed an emerging technology, likely to play a large part in the development of the SI engine into the foreseeable future. There are currently two different approaches to utilising GDI - stratified charge and homogeneous charge. The former has potentially higher gains in fuel economy and has been the focus of the majority of the development work by industry with the first GDI production vehicle (Mitsubishi) being powered by such a unit. The latter approach has received some interest from industry (Renault) and is also relevant to the development of the former as stratified-charge engines operate with homogeneous charge at higher loads. Homogeneous charge GDI may take on a new relevance if Homogeneous Charge Compression Ignition (HCCI) combustion [Stanglmaier, 1999] is shown to be a practical proposition as this has great potential for reducing the emissions from gasoline engines. In any case, the full potential of GDI is yet to be realised as the understanding and subsequent control of the fuel-air mixing processes are so complex.

Two areas that will contribute to the understanding of the complex interactions between the fuel spray and the airflow in the cylinder were drawn out of the literature survey. The first is the need for more knowledge about fuel injector sprays, such as the variation between different types of injector and the effects of ambient conditions. This knowledge would be relevant to the application of both stratified and homogeneous charge GDI engines. An investigation was performed on this topic and is reported in chapter 2. The second is the requirement to tackle the extra challenge of integrating GDI with variable valve timing (the latter has a very significant effect on in-cylinder flows and hence on the fuel-air mixing processes). This was researched through a series of single-cylinder engine tests using a prototype cylinder head designed for homogeneous GDI. The results of the engine testing are described in chapter 4.

The fuel spray investigation was successfully carried out on four different swirl-type injectors, under a wide range of testing conditions. Whether a fuel spray is hollow or filled was one of the aspects under scrutiny. It was found that the more open sprays (i.e. injector designed to produce a wider cone angle) are more likely to encompass a hollow region. One of the most influential variables on the cone filling is the ambient pressure of the atmosphere into which the fuel is injected. The sprays were found to retain their initial cone angle if injecting into a lower than atmospheric pressure (0.5 bar absolute), but increasing the ambient pressure to atmospheric had the effect of reducing the cone angle, and with it, the likelihood of a hollow region at the core. Increased fuel pressure was found to have two opposing effects on the spray. First of all, the

radial momentum of the fuel from the injector tip is higher if the initial cone angle is greater. However, as the droplets are smaller, they are more likely to be entrained into the core of the spray, reducing the likelihood of a hollow region. It was found that increased fuel temperature could also reduce the cone angle of the spray, particularly if combined with reduced ambient air pressure. The photographs of tests under these conditions were observed to take on a misty appearance and it was thought that 'flash' boiling of some of the constituents of the gasoline was occurring leading to reduced droplet size as well as increased vapour production.

As mentioned above, the structure of the spray depends on the ambient conditions as well as the fuel pressure, temperature and construction of the injector. The resulting cone angle of the spray is an important factor, as it governs the impaction of the spray on the various surfaces within the combustion chamber of an engine. In general, the cone angle and penetration rate of a given injector are closely related. As would be expected, a larger cone angle reduces the axial rate of penetration. Factors that reduce the cone angle (and increase penetration) include increases in the ambient pressure, fuel temperature and fuel pressure.

Curl-up vortices are caused by the smaller drops on the outside of the spray becoming entrained in the recirculating air currents set up by the motion of the spray. Though these were present on many of the fuel sprays in the rig work, it is thought that this may not be particularly relevant to engine work as the airflow in an engine should be stronger than the currents produced by the fuel spray.

The distribution of droplet diameters was also measured, as this is an accepted method to analyse the ease with which a homogeneous mixture could be formed. Sprays with the smallest droplets had SMD values as low as 10 μm, these being found mainly at the centre of the sprays. The most influential variable on the droplet size was the fuel pressure. Increasing the pressure significantly reduced the droplet size. To a lesser extent, increasing the fuel temperature also reduced the measured diameters. An interesting discovery was that there is a wider range of droplet sizes throughout the spray with lower fuel pressures. It was also noted that the fuel type did not affect the droplet size under the test conditions for the two fuels investigated.

From the spray work, it was obvious how important it is to obtain data on the actual injector to be used. The injectors under test were nominally of the same type, but showed marked differences in their behaviour. Many of these differences are a result of their internal construction, which unfortunately is quite difficult to examine accurately. Modellers working on GDI sprays face the challenge of developing a generic spray model, with input parameters

defined by the individual nozzle design. Likewise, it is a challenge to model the flash-boiling phenomenon. Yet, it has been found to have a useful tendency to reduce the droplet sizes.

In chapter 4, data was presented from a series of engine tests that used a Central Composite Rotatable Design (CCRD) of experiment. The CCRD was capable of modelling the engine's behaviour for the four responses under investigation (HC emissions, NOx emissions, BSFC and exhaust gas temperature) over a moderately wide range of variables. The variables were air/fuel ratio, ignition timing, injection timing and inlet valve timing. CCRD experiments were performed for several different engine configurations at a nominal test condition (1500 rpm, 2.62 bar BMEP). The different GDI configurations included side and central injection, two different types of injector and two fuel pressures. A further CCRD was performed on the same engine converted to port fuel injection (PFI). Interpretation diagrams were produced by superimposing fuel spray images onto accurately drawn schematics of the cylinder, combustion chamber and piston. The validity of this superposition approach was demonstrated by reference to in-cylinder images from a parallel project indicating that the airflow had little effect on the fuel spray at most, but not all, of the conditions under scrutiny.

The most efficient configuration for engine running was using a 90° injector, mounted centrally, injecting at 100 bar fuel pressure. PFI was a close second, though HC and NOx emissions values for the GDI case were lower than the PFI configuration at their most efficient settings. The highest BSFC figure was recorded for the 90° injector mounted at the side, and this configuration also gave the highest HC emissions value. Side injection was less successful than central injection in terms of higher BSFC and HC emissions, probably due to impaction on the cylinder wall and, under some conditions, on the backs of the inlet valves. The profiled piston of stratified charge GDI engines would tend to overcome part of this problem, as would a narrower spray. Somewhat surprisingly, reducing the fuel pressure from 100 bar to 20 bar did not have such a detrimental effect on BSFC and HC emissions. This was probably due to the fact that the test was only run for side injection and a considerable proportion of the fuel injected would have impacted on the piston and cylinder walls for both fuel pressures.

The lowest HC emissions value obtained (4.2 g/kWh) was for a GDI configuration utilising the 60° injector in its central position at 100 bar fuel pressure. The 90° injector has a slightly higher minimum (5.3 g/kWh) in this position, possibly due to impaction on the back of the inlet valves.

The 90° injector, side mounted, provided the lowest NOx figure (0.4 g/kWh). A possible explanation is that relatively poor mixture preparation led to slow burning and a consequent

reduction in the peak temperature of the burning gases. Interestingly, the nearest competitor was the 20 bar configuration, with a minimum NOx value of only 0.6 g/kWh. The highest NOx value was obtained with PFI.

The lowest BSFC figure for each configuration was obtained with retarded inlet valve timing. The results of a parallel project have demonstrated that the velocities of the air motion induced within the cylinder rose significantly at this setting, increasing the resulting turbulence. This enhanced burning, and hence improved the BSFC. It follows that this strategy could be employed for low speed running as a means of increasing engine stability.

5.2 Original aspects of the research

It is claimed that the research reported in this thesis contains the following elements of original work:

(i) The test rig work performed on fuel sprays provided the most comprehensive set of data yet published on the variations in spray formation between different designs of swirl-type GDI injectors. In particular, the range of test conditions examined was wider than previously attempted. The range of variables investigated has given new insight into the effects of temperature and pressure on a spray's cone angle and penetration. It was also possible to conduct an in-depth study of cone filling from this data. The majority of work was performed using gasoline rather than a single-component test fluid. Gasoline is prone to 'flash' boiling which will have a considerable effect on the air-fuel mixing processes in running engines, so, the use of gasoline made the rig test results particularly relevant.

(ii) The development of a simple tomographic technique applicable to the laser diffraction method of droplet sizing to elucidate the distribution of droplet sizes within a spray is thought to be novel. It involves certain simplifying assumptions compared to the existing more complex approaches, but it is thought that the lack of accuracy did not significantly compromise the overall results because there are inevitably other sources of error (e.g. evaporation effects) which are likely to be greater. However, caution should be exercised when utilising this methodology, as it is relatively unproven.

(iii) The data obtained from the engine tests is believed to be the most comprehensive that has yet been published in terms of comparing different GDI engine configurations. It is also thought to be the first published systematic study of the effects of inlet valve timing on GDI engine performance.

(iv) The attempt to explain the engine results of the different GDI configurations using interpretation diagrams incorporating fuel spray images from rig tests has novelty. This has helped to identify the probable causes of high HC emissions and the corresponding poor efficiency of the engine for some of the configurations.

5.3 GDI development since this project was started

In 1998, when this project was started, there were very few GDI engines in production (see chapter 1). Admittedly, it was known that many manufacturers were seriously investigating the production of GDI engines. As this thesis is completed, there are few major engine-producing manufacturers that have not launched a GDI engine range. Those that have not, inevitably will.

It is interesting to note that GDI is also being applied to performance engines as well as to engines designed to comply with future emissions and fuel economy legislation. For instance, Audi dominated the 2001 and 2002 Le Mans races with their prototype sports car, which was powered by a GDI-equipped V8 engine. It is also known that several Formula One teams are investigating the technology for use on the track.

It was explained at the beginning of this chapter that the GDI engine is still not optimised. Considerable research effort has been focussed on the stratified-charge approach, but homogeneous charge GDI may also have a considerable future, certainly in racing engine applications and perhaps in the application of advanced combustion technologies (e.g. HCCI). The steps for further research are discussed in section 5.4.

5.4 Recommendations for further research

The data obtained from the engine and spray testing in this PhD is being used to validate a CFD model in another parallel project. It is thought that the model would benefit from further integration between the testing and the modelling itself. Modelling helps to explain the various phenomena observed during testing and is probably ultimately the way forward in terms of designing future engines. In particular for GDI engines, there is much unknown territory with regards to the fuel spray structure and its influence on engine parameters investigated in this thesis. Comparison of test results with a CFD model is an iterative process, as each new set of results may improve the accuracy of the model. The link between the data presented in this thesis and the CFD model being developed in the parallel project will be presented by another PhD student as the work is not yet complete.

One aspect of the spray testing that should be investigated in more detail is the structure of the spray very close to and possibly inside the fuel injector nozzle. It is likely that this would be achieved by close co-operation between testing and modelling.

Aside from a closer link to the CFD modelling, the next logical stage of research would involve an investigation based on the use of stratified charge. This is the area in which interest is highest due to the potential gains in fuel economy and emissions. It is thought, however, that the CCRD described in this thesis may not be sufficient to model the engine's response when running with a stratified charge combustion system. A significant part of the research could be to develop a tool capable of predicting the responses of a more complex system.

Since this PhD began, interest in the HCCI engine has come to the fore. The technology is still in relative infancy. A research project centred on a HCCI combustion system would be particularly interesting with regards to GDI running with extreme levels of EGR. It is thought that such a project would open up a vast area of possibilities.

APPENDICES

A1 - CATALOGUE OF FUEL SPRAY IMAGES

A1.1 - Injector A

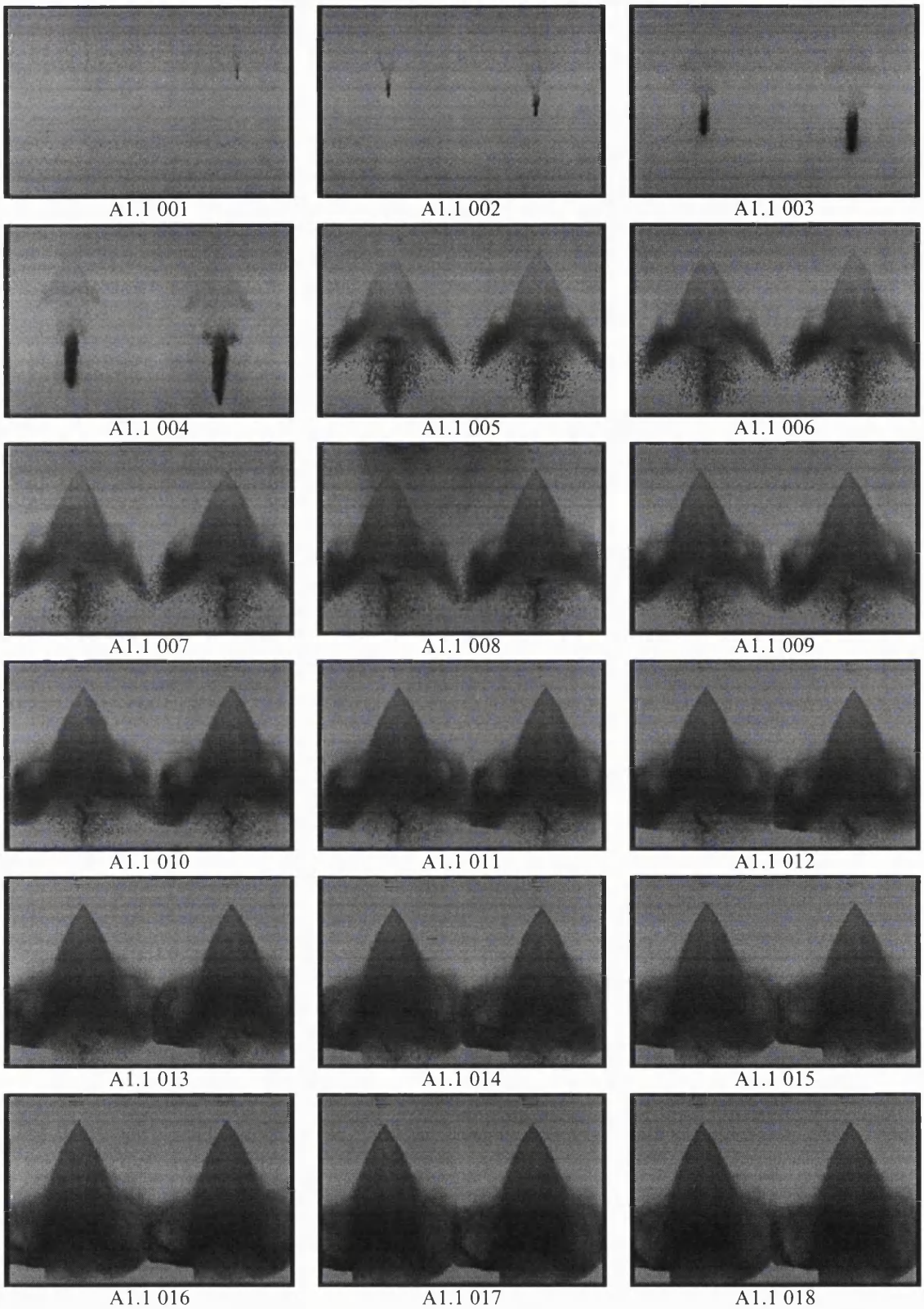

Variables: atmospheric pressure, 20 - 25°C fuel temperature, 55 bar fuel pressure, gasoline, light sheet approaching spray from left hand side.
Scale: width x height of frame represents 134.0 mm x 89.0 mm.
Notes: 0.1 ms between shots. 2 shots per frame.

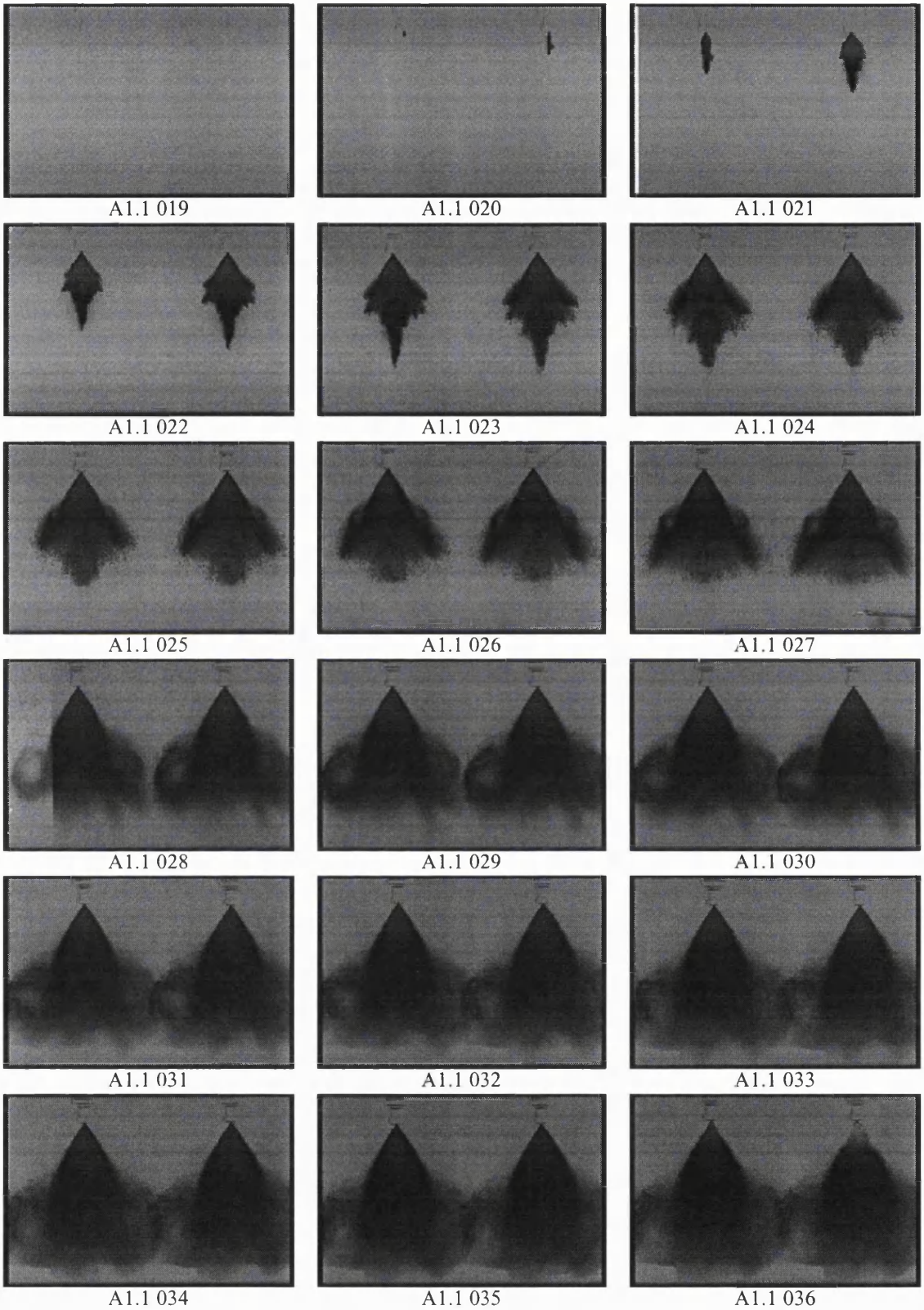

Variables: atmospheric pressure, 20 - 25°C fuel temperature, 55 bar fuel pressure, gasoline, light sheet approaching spray from left hand side.
Scale: width x height of frame represents 134.0 mm x 89.0 mm.
Notes: 0.1 ms between shots. 2 shots per frame.

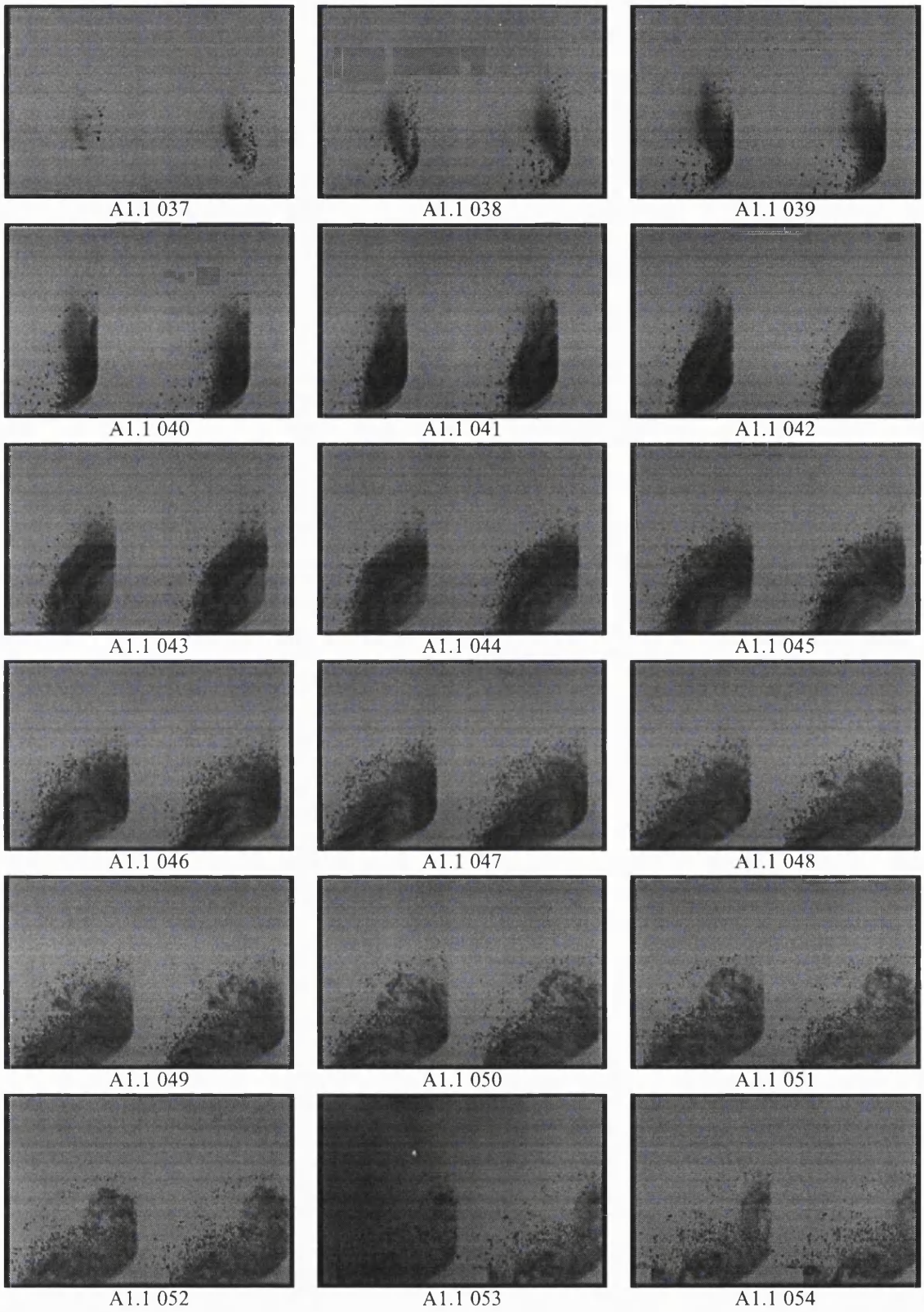

Variables: atmospheric pressure, 20 - 25°C fuel temperature, 55 bar fuel pressure, gasoline, light sheet approaching spray from left hand side.
Scale: width x height of frame represents 54.0 mm x 35.0 mm.
Notes: 0.1 ms between shots. 2 shots per frame. Camera is focussed on curl-up vortices at edge of spray.

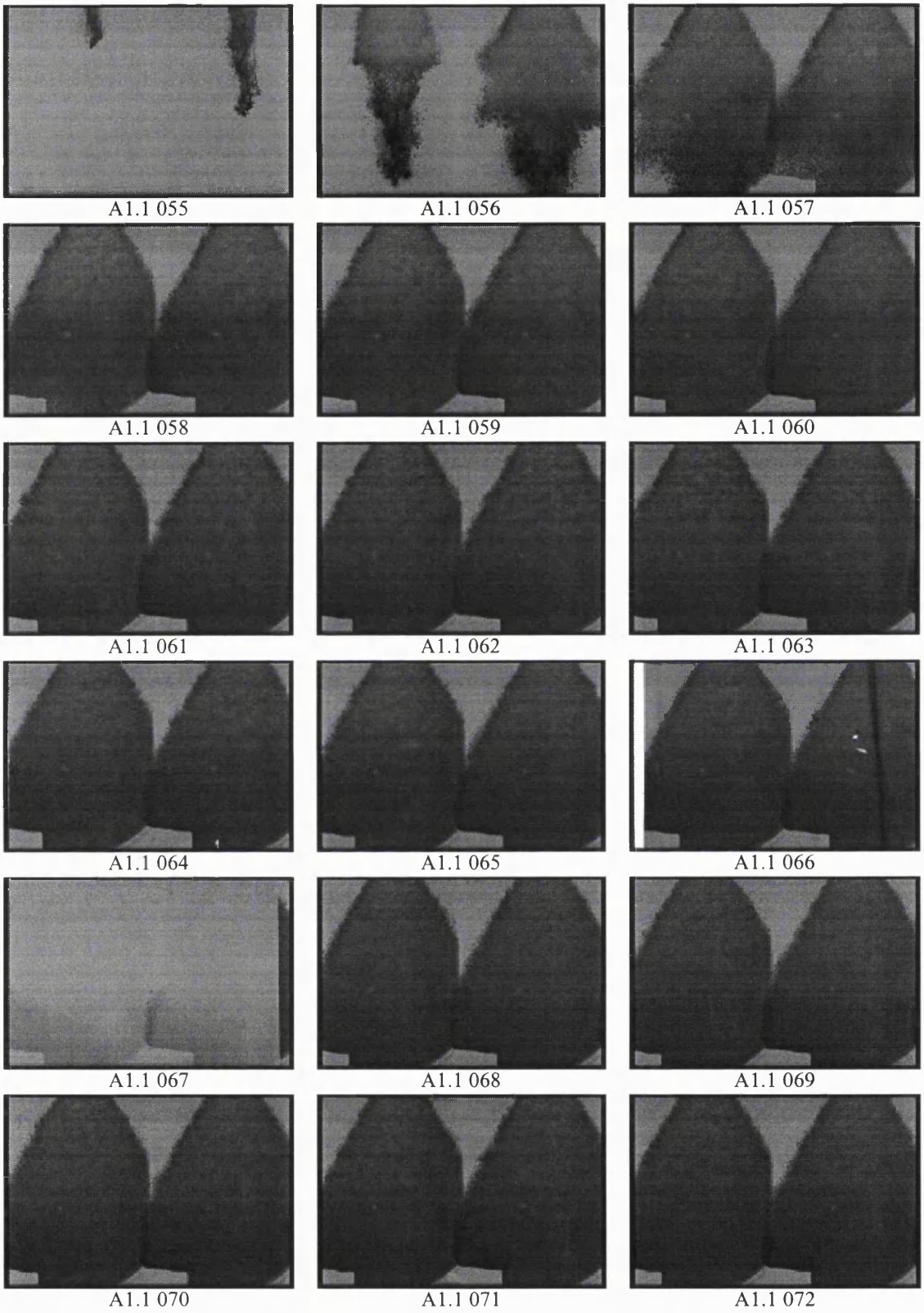

A1.1 055 A1.1 056 A1.1 057

A1.1 058 A1.1 059 A1.1 060

A1.1 061 A1.1 062 A1.1 063

A1.1 064 A1.1 065 A1.1 066

A1.1 067 A1.1 068 A1.1 069

A1.1 070 A1.1 071 A1.1 072

Variables: atmospheric pressure, 20 - 25°C fuel temperature, 55 bar fuel pressure, gasoline, light sheet approaching spray from left hand side.
Scale: width x height of frame represents 36.0 mm x 24.0 mm.
Notes: 0.1 ms between shots. 2 shots per frame. Top of frame is 5.0 mm from injector tip.

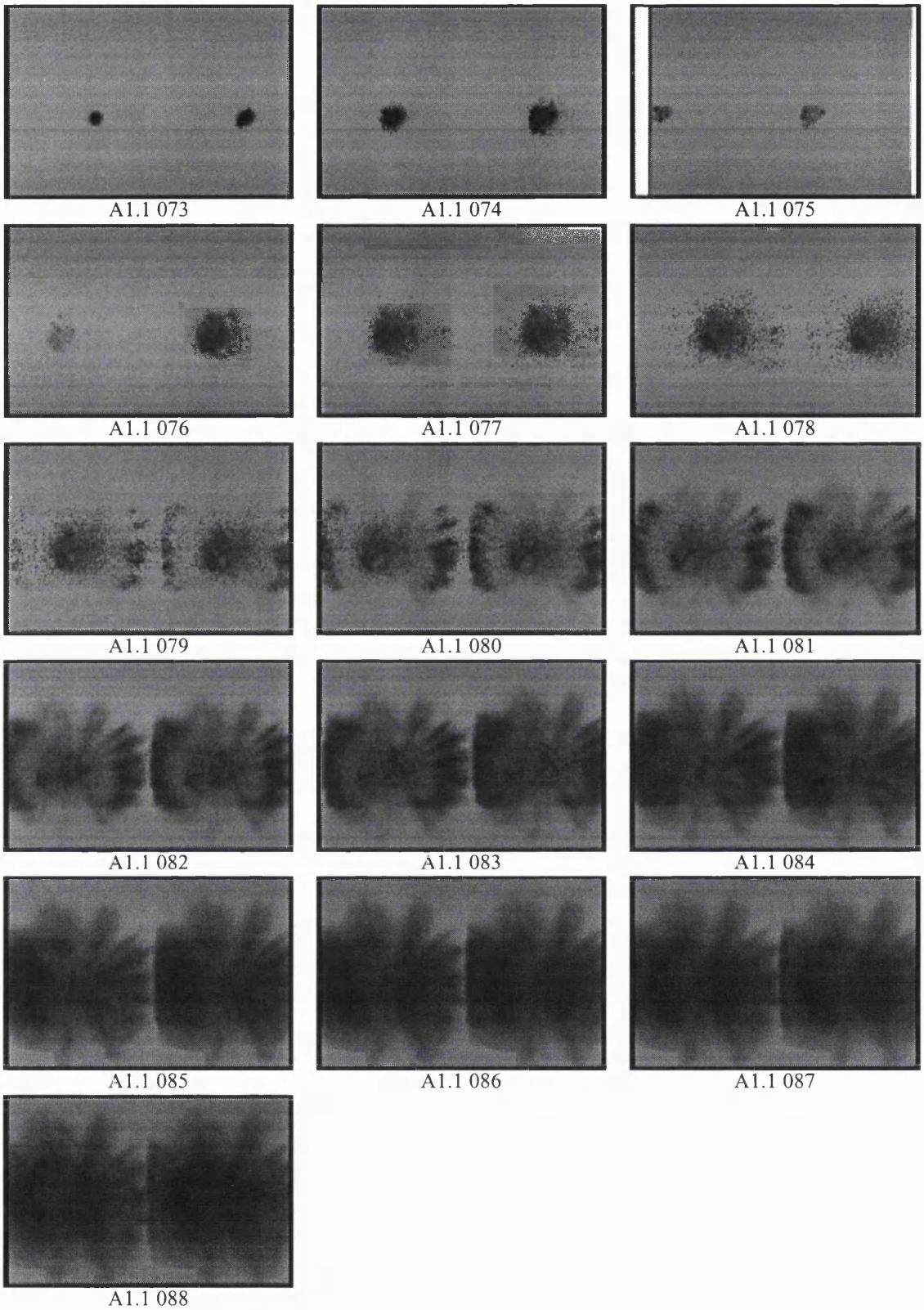

A1.1 073 A1.1 074 A1.1 075

A1.1 076 A1.1 077 A1.1 078

A1.1 079 A1.1 080 A1.1 081

A1.1 082 A1.1 083 A1.1 084

A1.1 085 A1.1 086 A1.1 087

A1.1 088

Variables: atmospheric pressure, 20 - 25°C fuel temperature, 55 bar fuel pressure, gasoline, light sheet approaching spray from left hand side.
Scale: width x height of frame represents 77.0 mm x 51.0 mm.
Notes: 0.1 ms between shots. 2 shots per frame. Light sheet plane is 40.0 mm from injector tip. End-on view.

A1 - CATALOGUE OF FUEL SPRAY IMAGES

A1.2 - Injector B

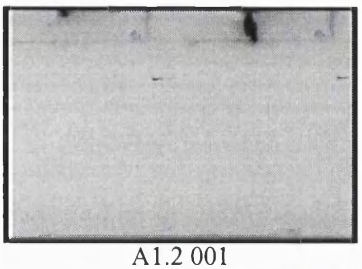
A1.2 001

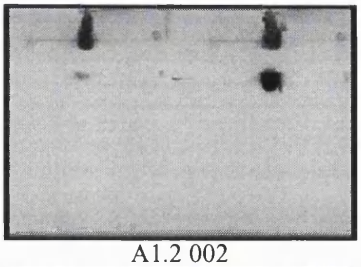
A1.2 002

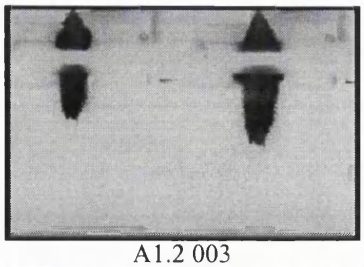
A1.2 003

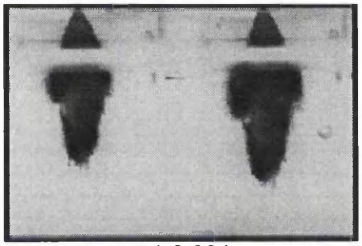
A1.2 004

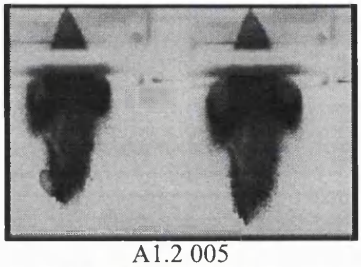
A1.2 005

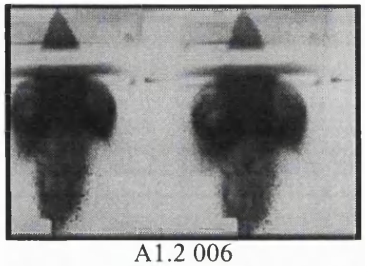
A1.2 006

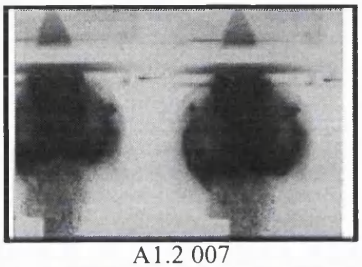
A1.2 007

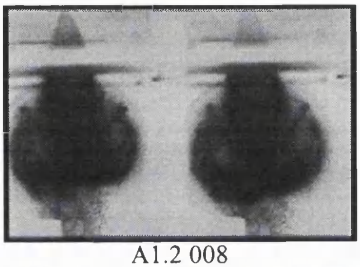
A1.2 008

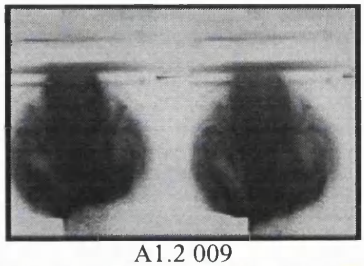
A1.2 009

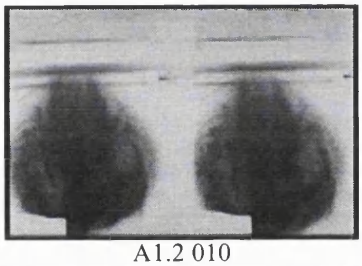
A1.2 010

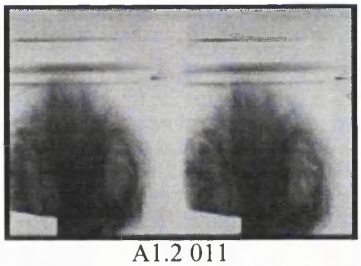
A1.2 011

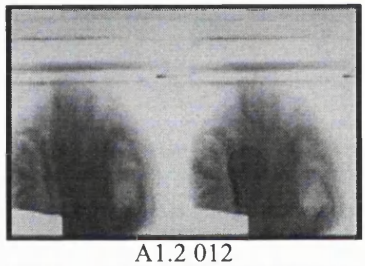
A1.2 012

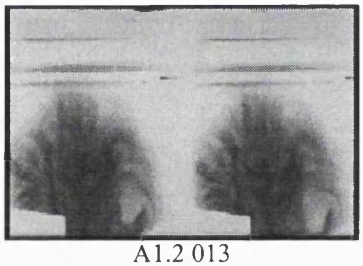
A1.2 013

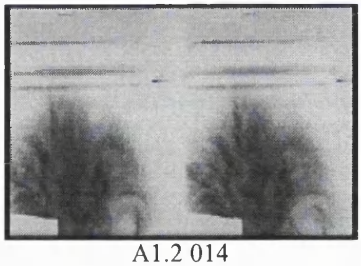
A1.2 014

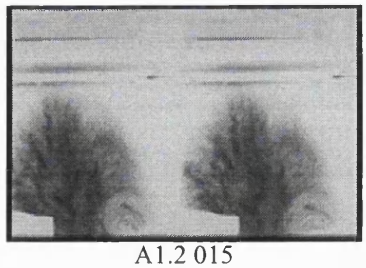
A1.2 015

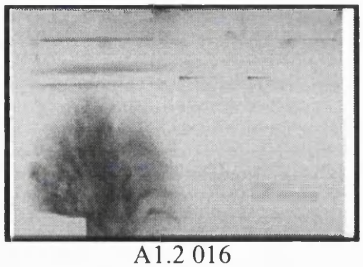
A1.2 016

Variables: atmospheric pressure, 24°C fuel temperature, 120 bar fuel pressure, gasoline, light sheet approaching spray from underneath.
Scale: width x height of frame represents 82.0 mm x 54.0 mm.
Notes: 0.1 ms between shots. 2 shots per frame. Part of spray obscured by test rig.

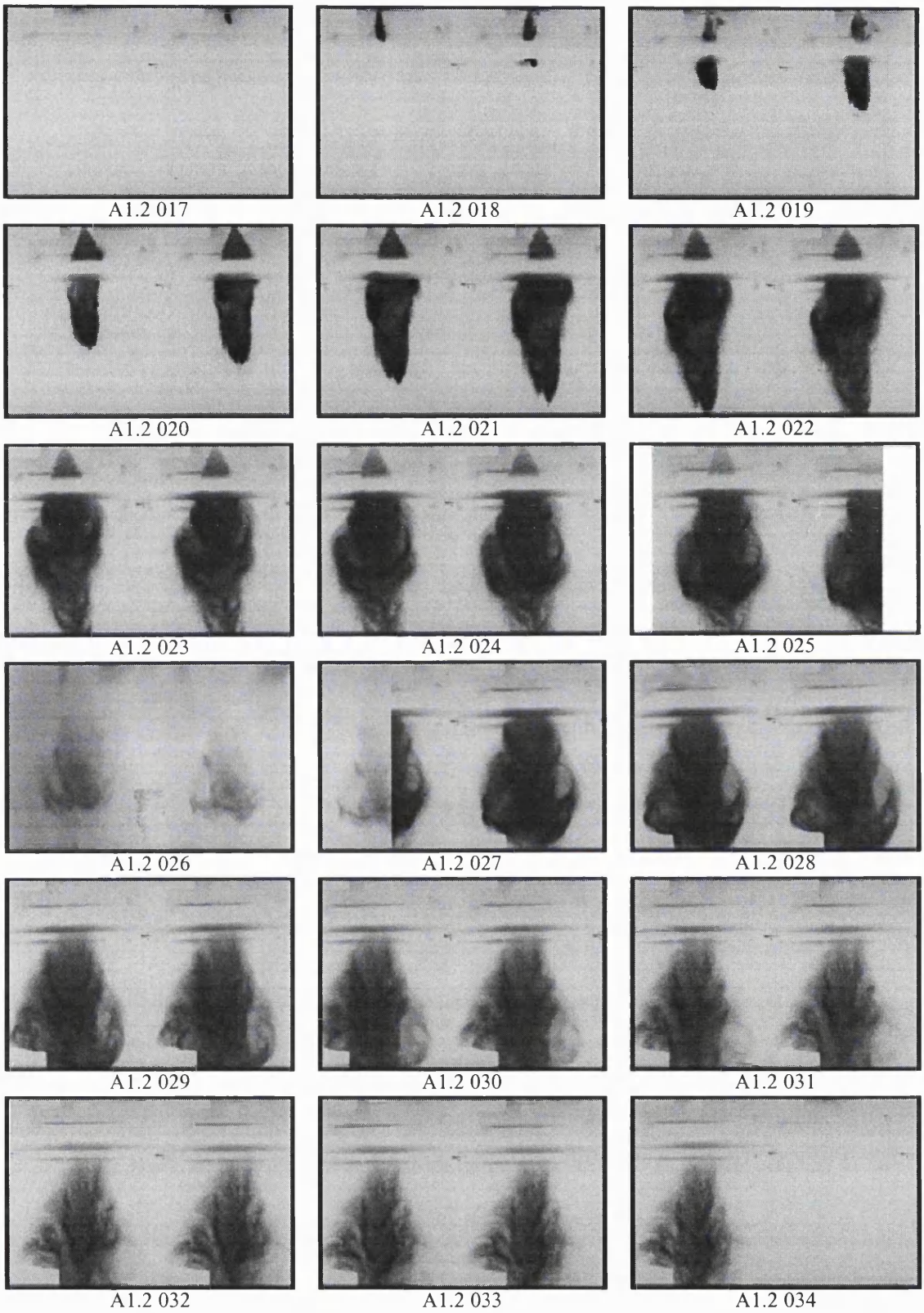

Variables: atmospheric pressure, 80°C fuel temperature, 120 bar fuel pressure, gasoline, light sheet approaching spray from underneath.
Scale: width x height of frame represents 82.0 mm x 54.0 mm.
Notes: 0.1 ms between shots. 2 shots per frame. Part of spray obscured by test rig.

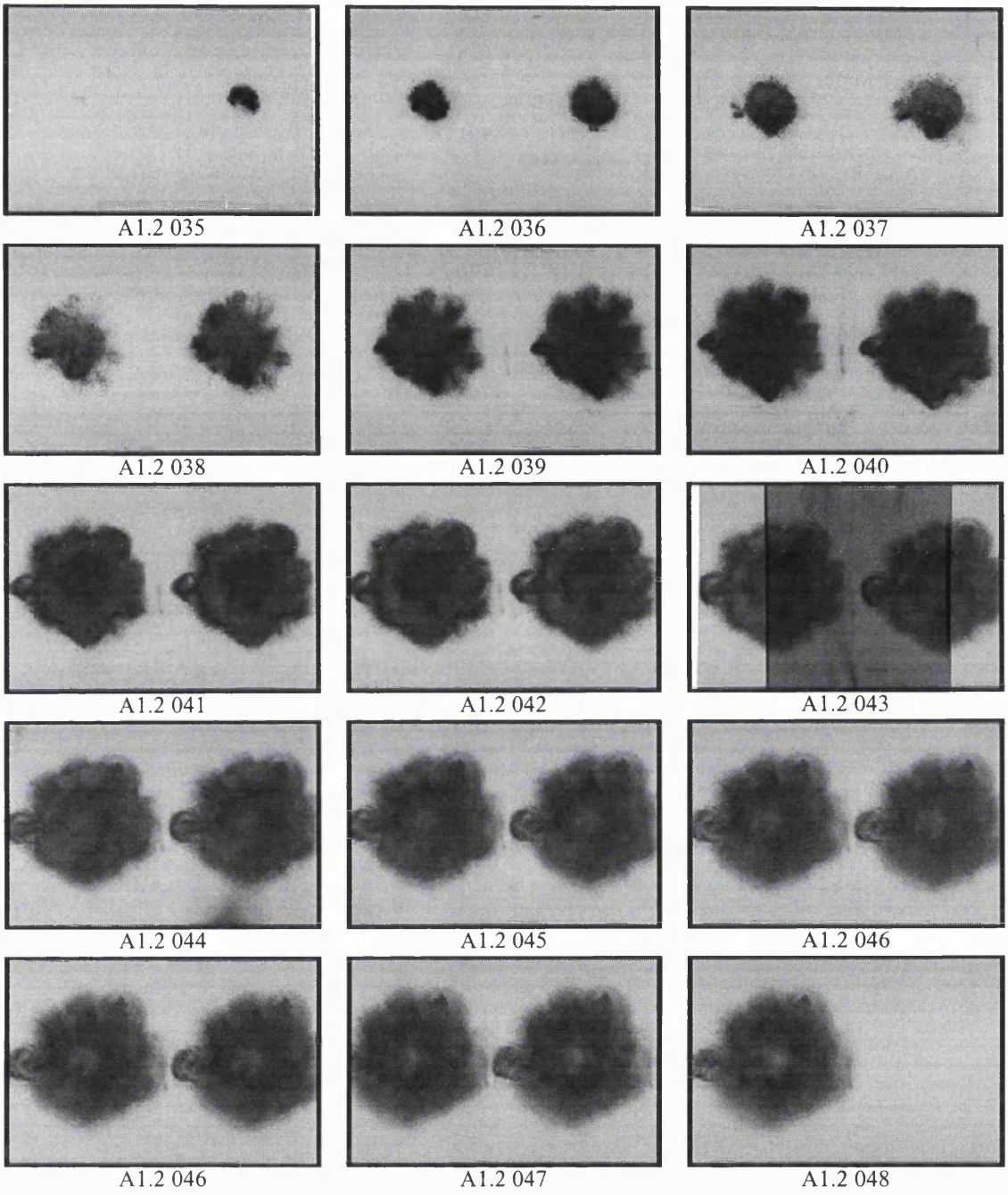

Variables: atmospheric pressure, 25°C fuel temperature, 120 bar fuel pressure, gasoline, light sheet approaching spray from left hand side.
Scale: width x height of frame represents 155.0 mm x 103.0 mm.
Notes: 0.1 ms between shots. 2 shots per frame. End-on view.

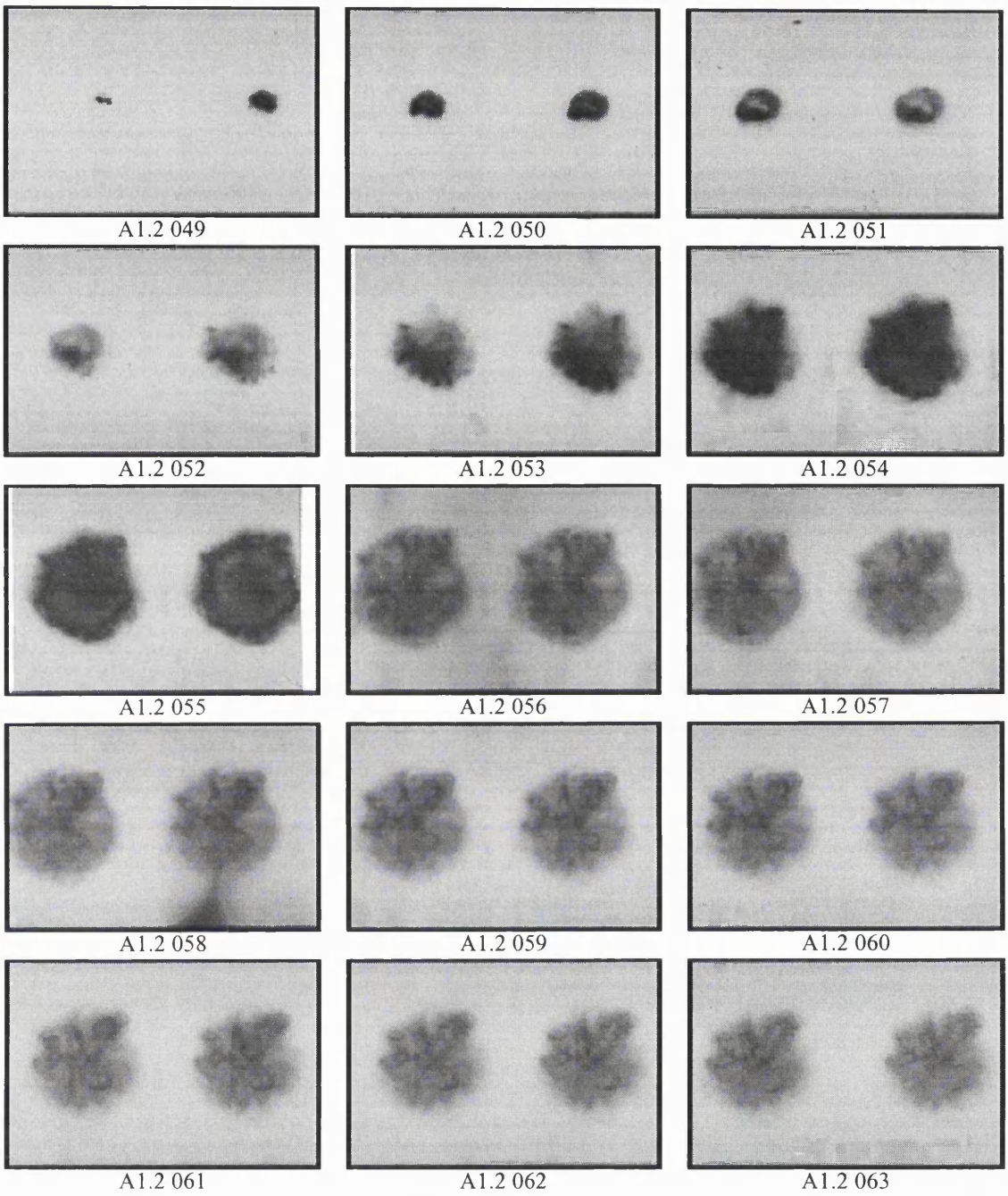

Variables: atmospheric pressure, 80°C fuel temperature, 120 bar fuel pressure, gasoline, light sheet approaching spray from underneath.
Scale: width x height of frame represents 155.0 mm x 103.0 mm.
Notes: 0.1 ms between shots. 2 shots per frame. End-on view.

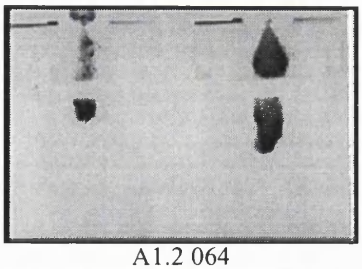
A1.2 064

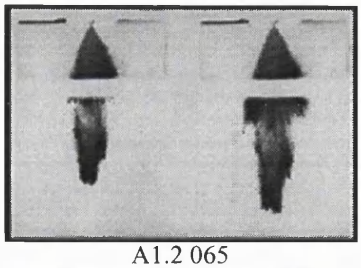
A1.2 065

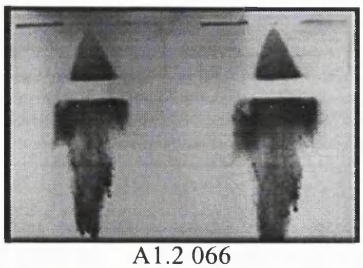
A1.2 066

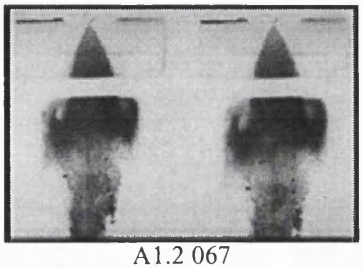
A1.2 067

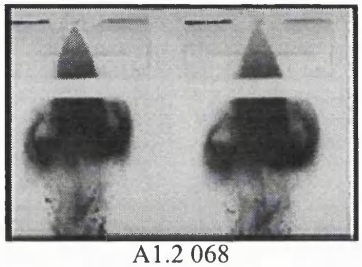
A1.2 068

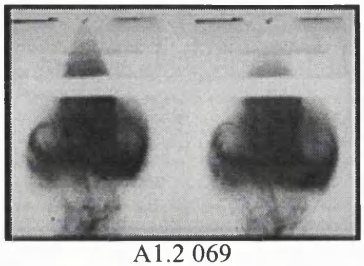
A1.2 069

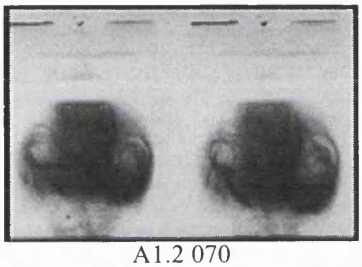
A1.2 070

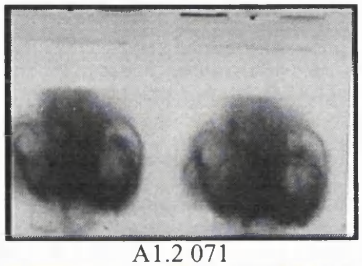
A1.2 071

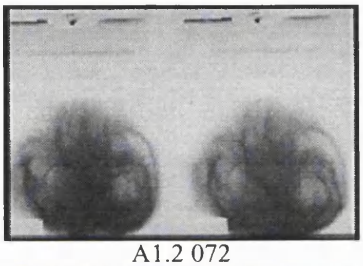
A1.2 072

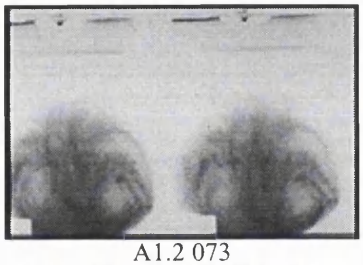
A1.2 073

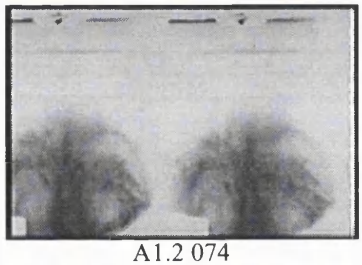
A1.2 074

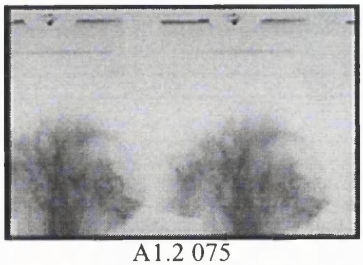
A1.2 075

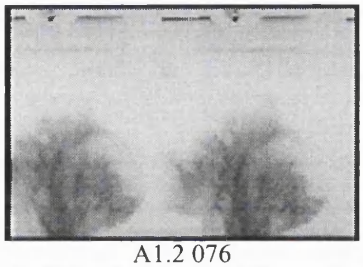
A1.2 076

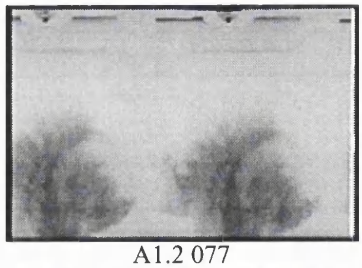
A1.2 077

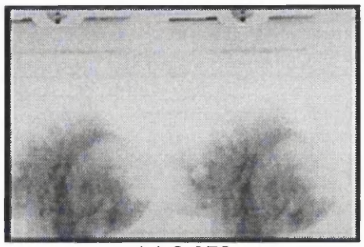
A1.2 078

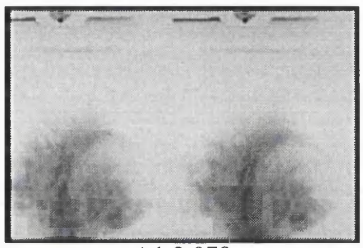
A1.2 079

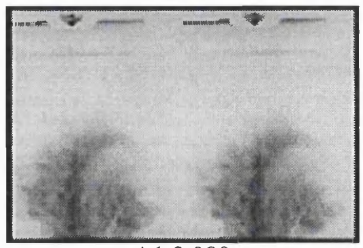
A1.2 080

Variables: atmospheric pressure, 23°C fuel temperature, 120 bar fuel pressure, iso-octane, light sheet approaching spray from underneath.
Scale: width x height of frame represents 104.0 mm x 69.0 mm.
Notes: 0.1 ms between shots. 2 shots per frame. Part of spray obscured by test rig.

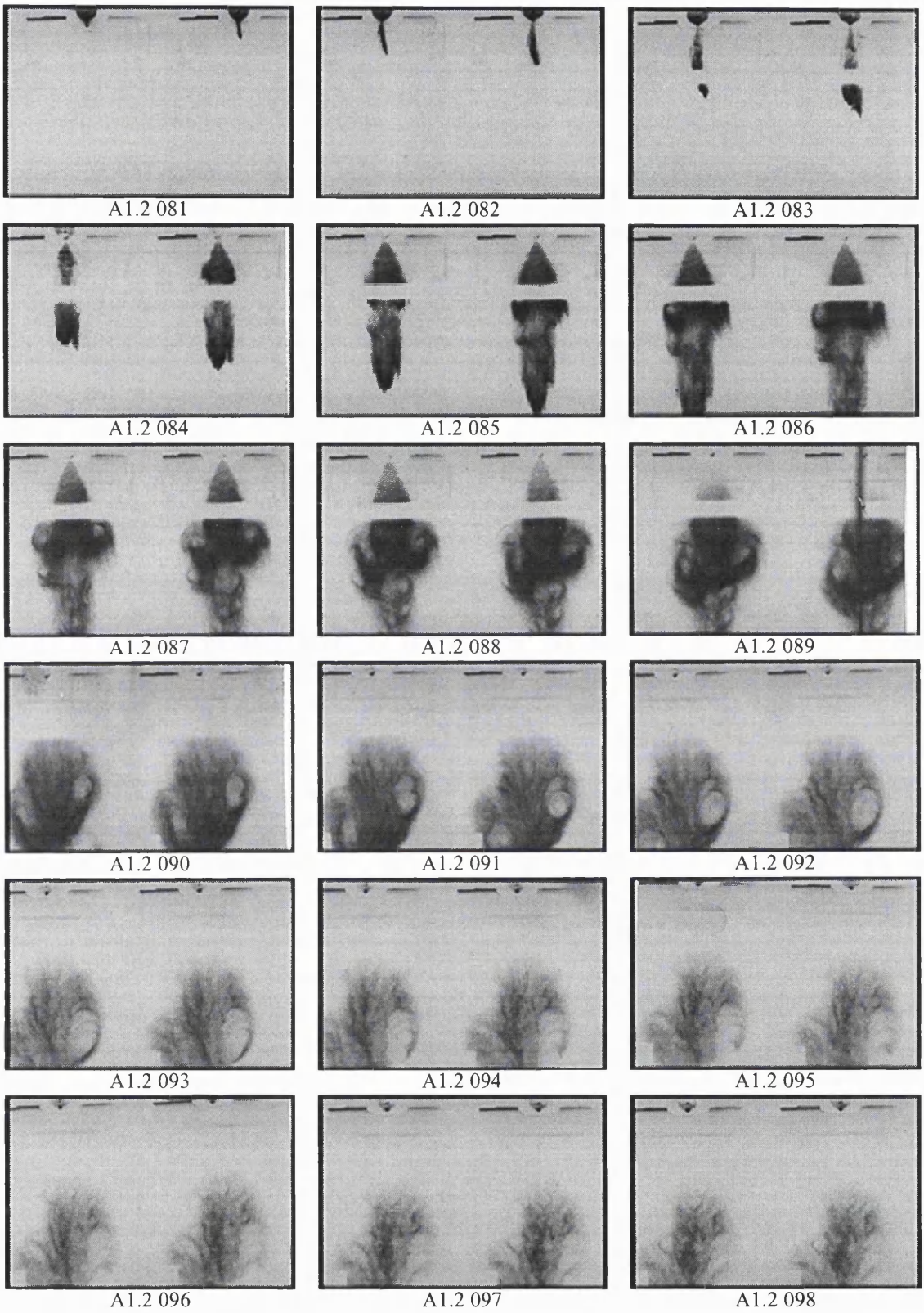

Variables: atmospheric pressure, 80°C fuel temperature, 120 bar fuel pressure, iso-octane, light sheet approaching spray from underneath.
Scale: width x height of frame represents 104.0 mm x 69.0 mm.
Notes: 0.1 ms between shots. 2 shots per frame. Part of spray obscured by test rig.

A1 - CATALOGUE OF FUEL SPRAY IMAGES

A1.3 - Injector C

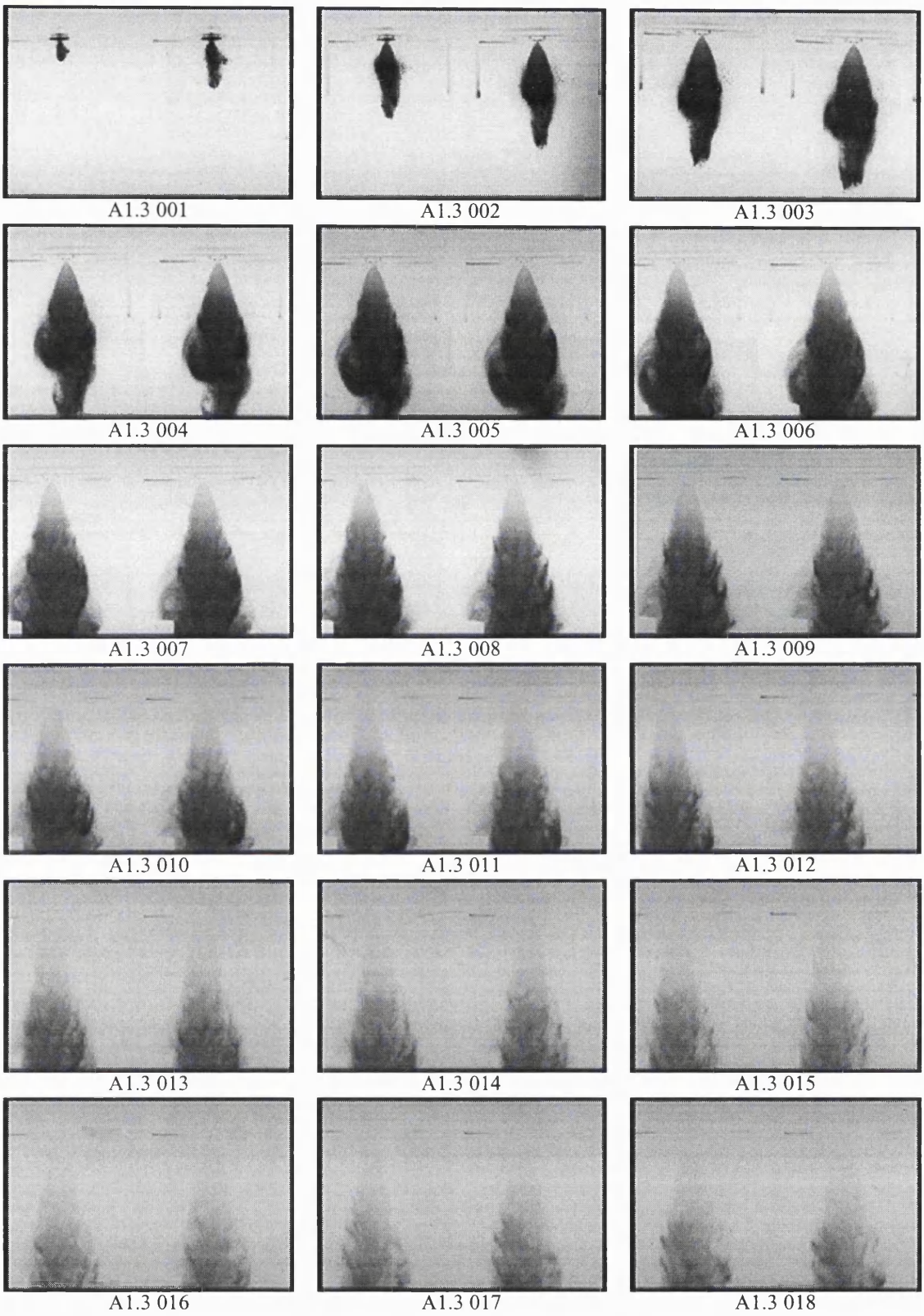

Variables: atmospheric pressure, 25°C fuel temperature, 100 bar fuel pressure, iso-octane, light sheet approaching spray from underneath.
Scale: width x height of frame represents 154.0 mm x 102.0 mm.
Notes: 0.1 ms between shots. 2 shots per frame.

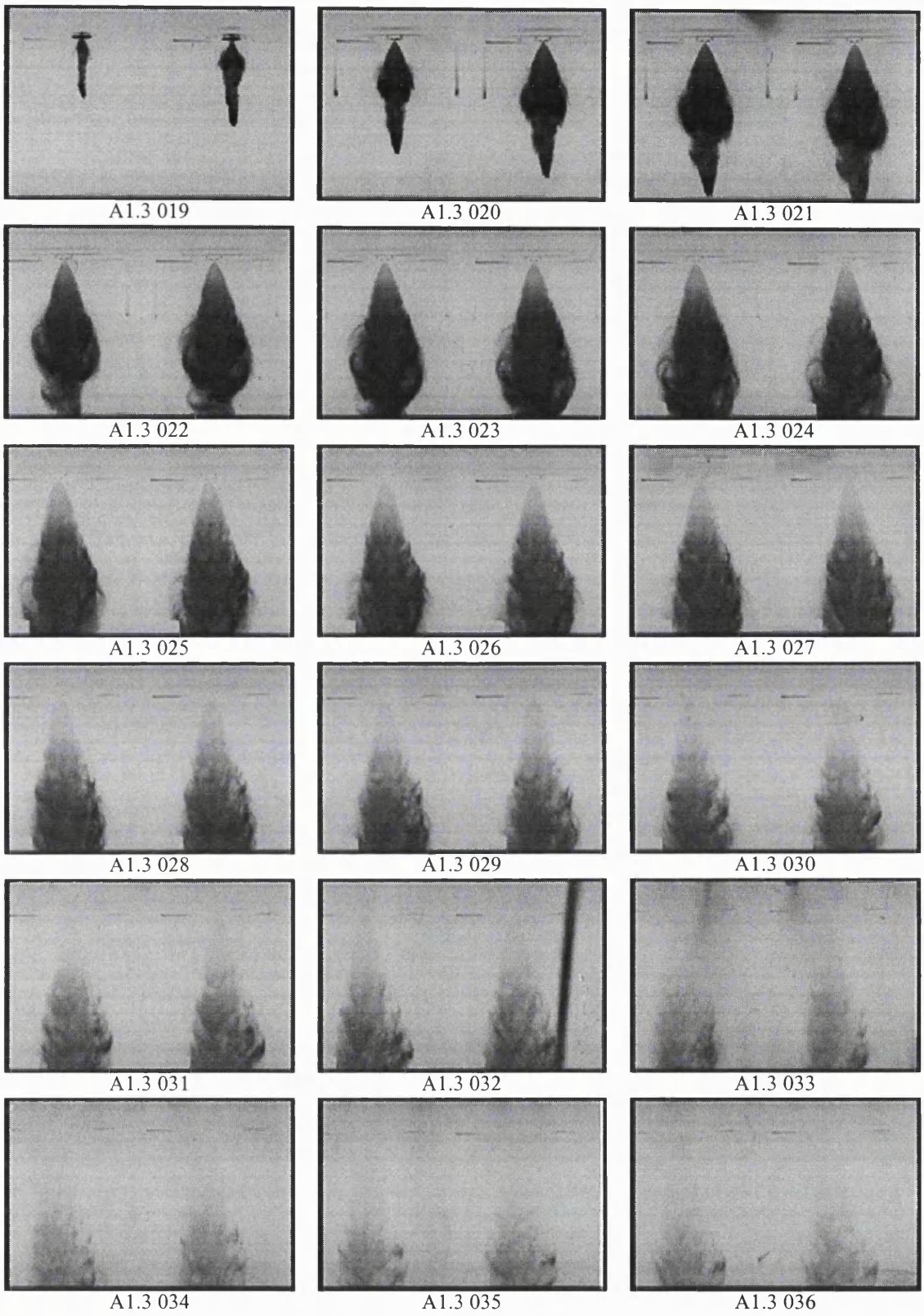

Variables: atmospheric pressure, 80°C fuel temperature, 100 bar fuel pressure, iso-octane, light sheet approaching spray from underneath.
Scale: width x height of frame represents 154.0 mm x 102.0 mm.
Notes: 0.1 ms between shots. 2 shots per frame.

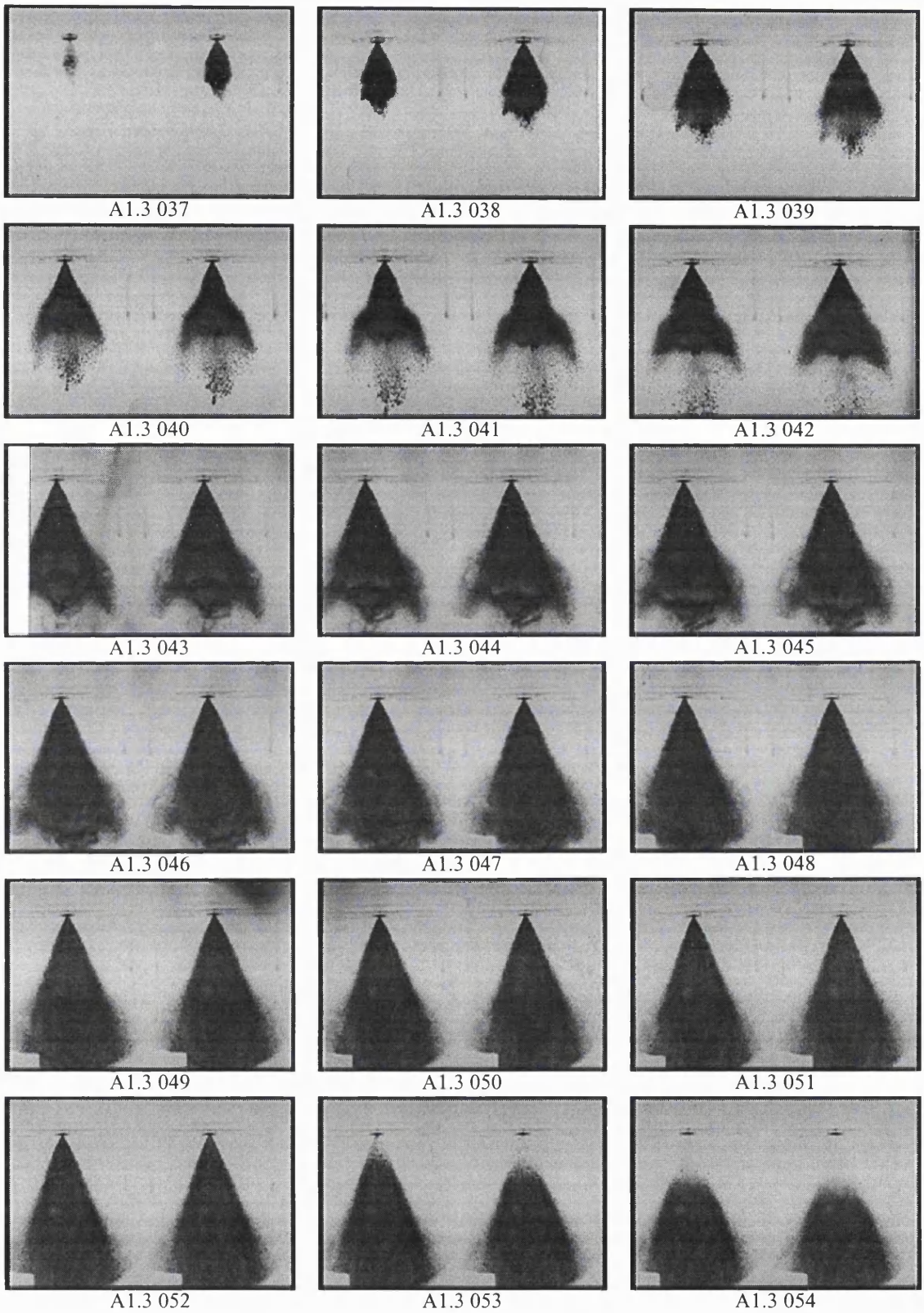

Variables: atmospheric pressure, 21°C fuel temperature, 20 bar fuel pressure, gasoline, light sheet approaching spray from underneath.
Scale: width x height of frame represents 154.0 mm x 102.0 mm.
Notes: 0.1 ms between shots. 2 shots per frame.

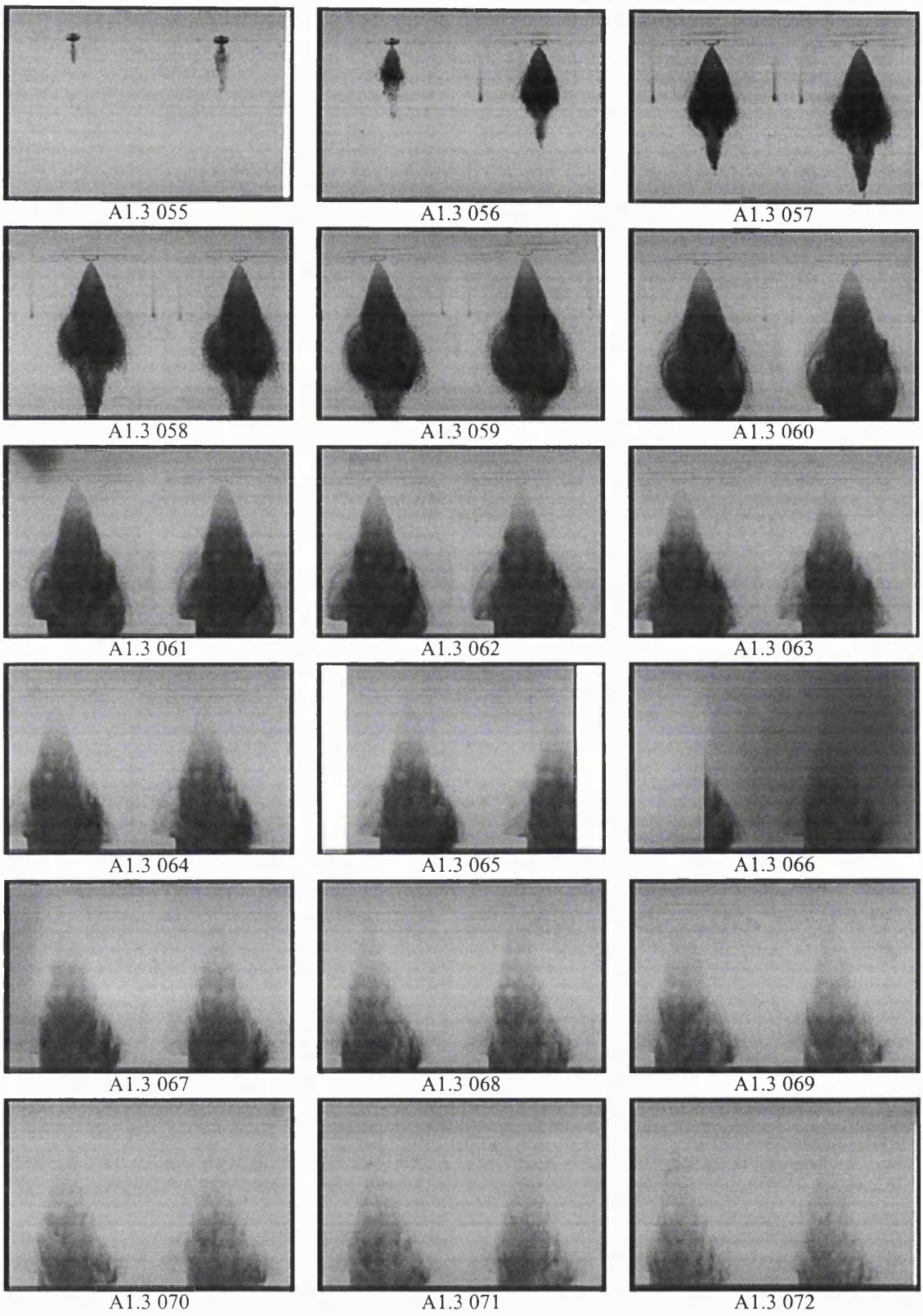

Variables: atmospheric pressure, 22°C fuel temperature, 100 bar fuel pressure, gasoline, light sheet approaching spray from underneath.
Scale: width x height of frame represents 154.0 mm x 102.0 mm.
Notes: 0.1 ms between shots. 2 shots per frame.

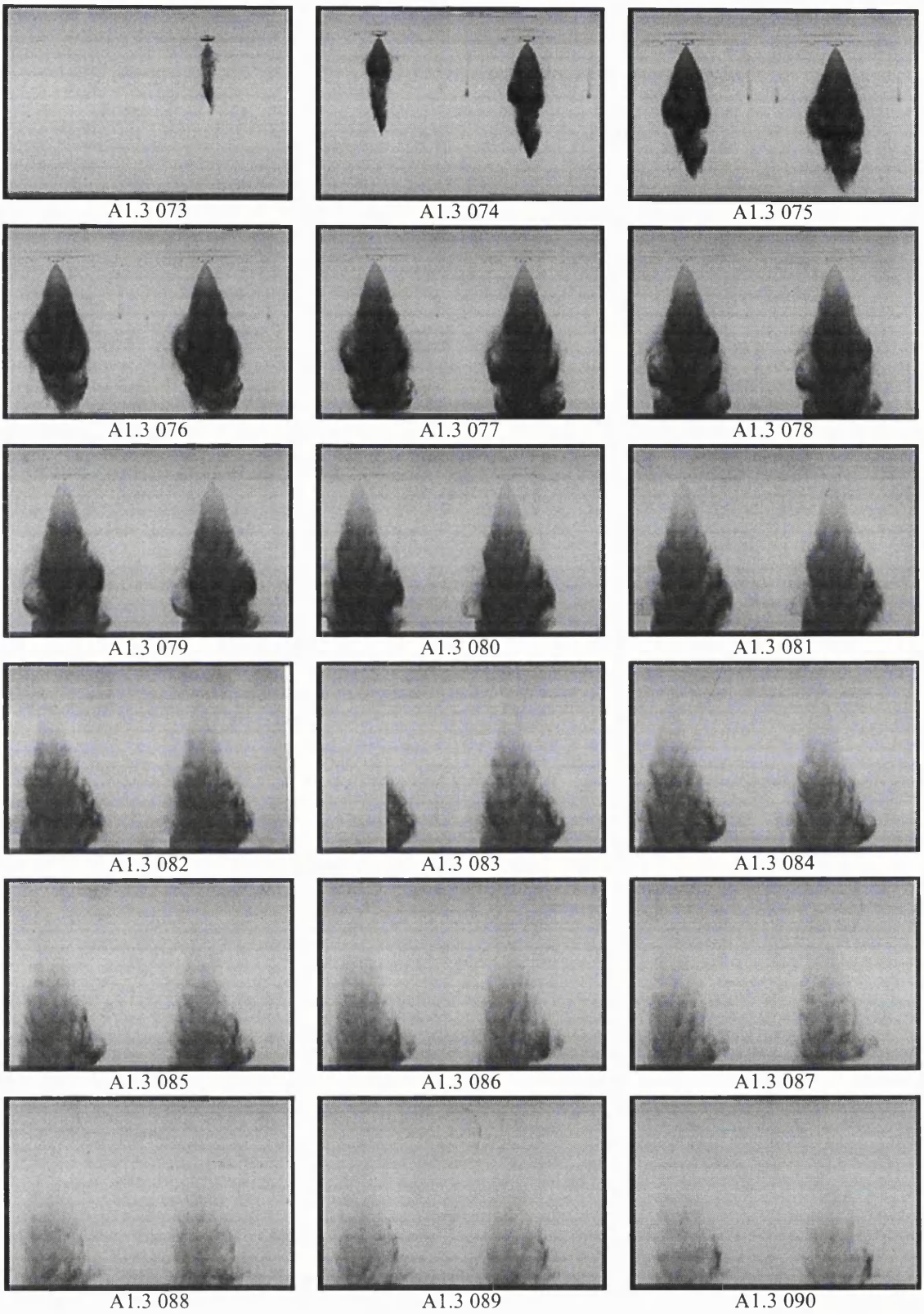

Variables: atmospheric pressure, 80°C fuel temperature, 100 bar fuel pressure, gasoline, light sheet approaching spray from underneath.
Scale: width x height of frame represents 154.0 mm x 102.0 mm.
Notes: 0.1 ms between shots. 2 shots per frame.

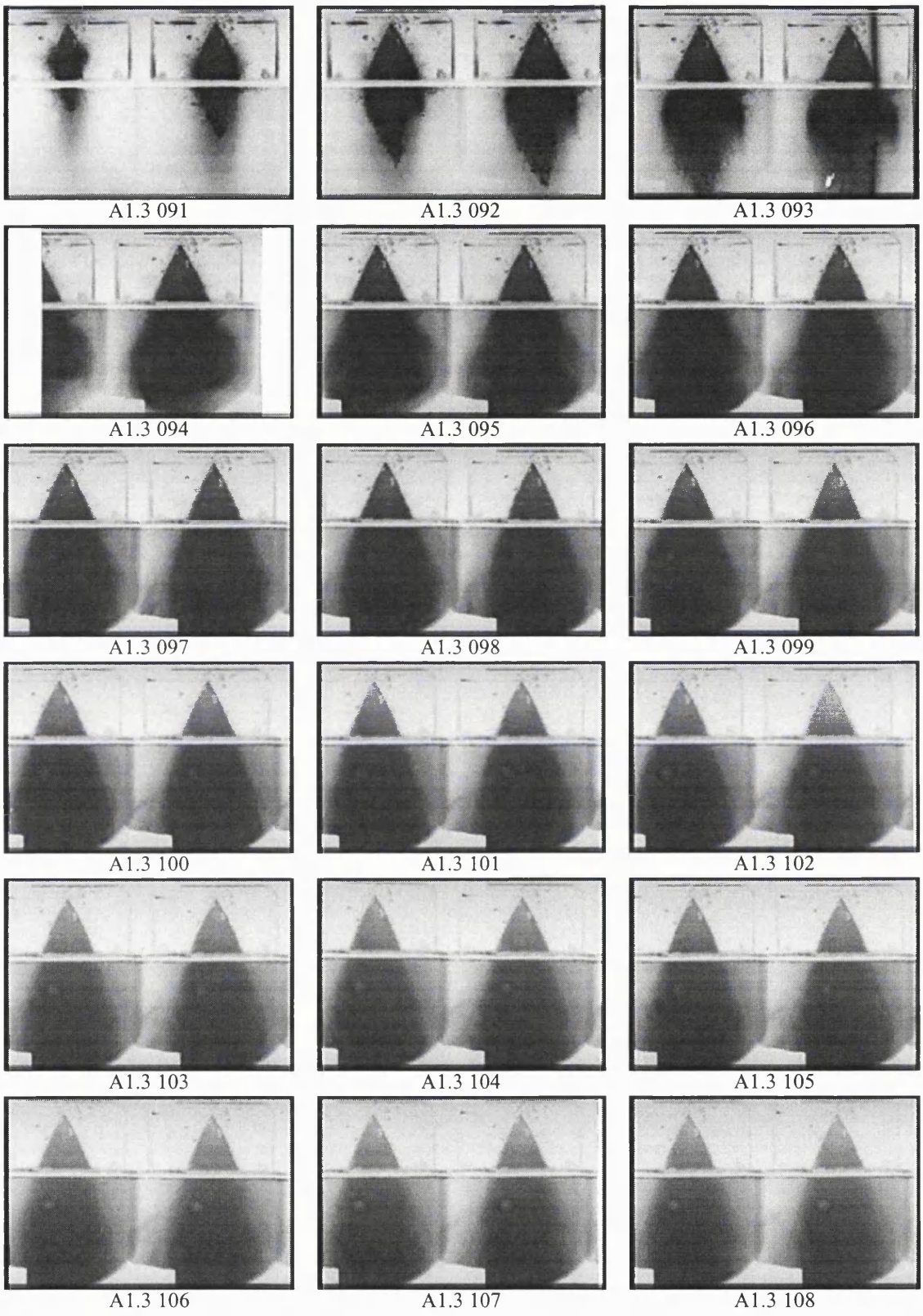

Variables: 0.5 bar ambient pressure, 23°C fuel temperature, 100 bar fuel pressure, gasoline, light sheet approaching spray from underneath.
Scale: width x height of frame represents 96.0 mm x 64.0 mm.
Notes: 0.1 ms between shots. 2 shots per frame. Part of spray obscured by test rig.

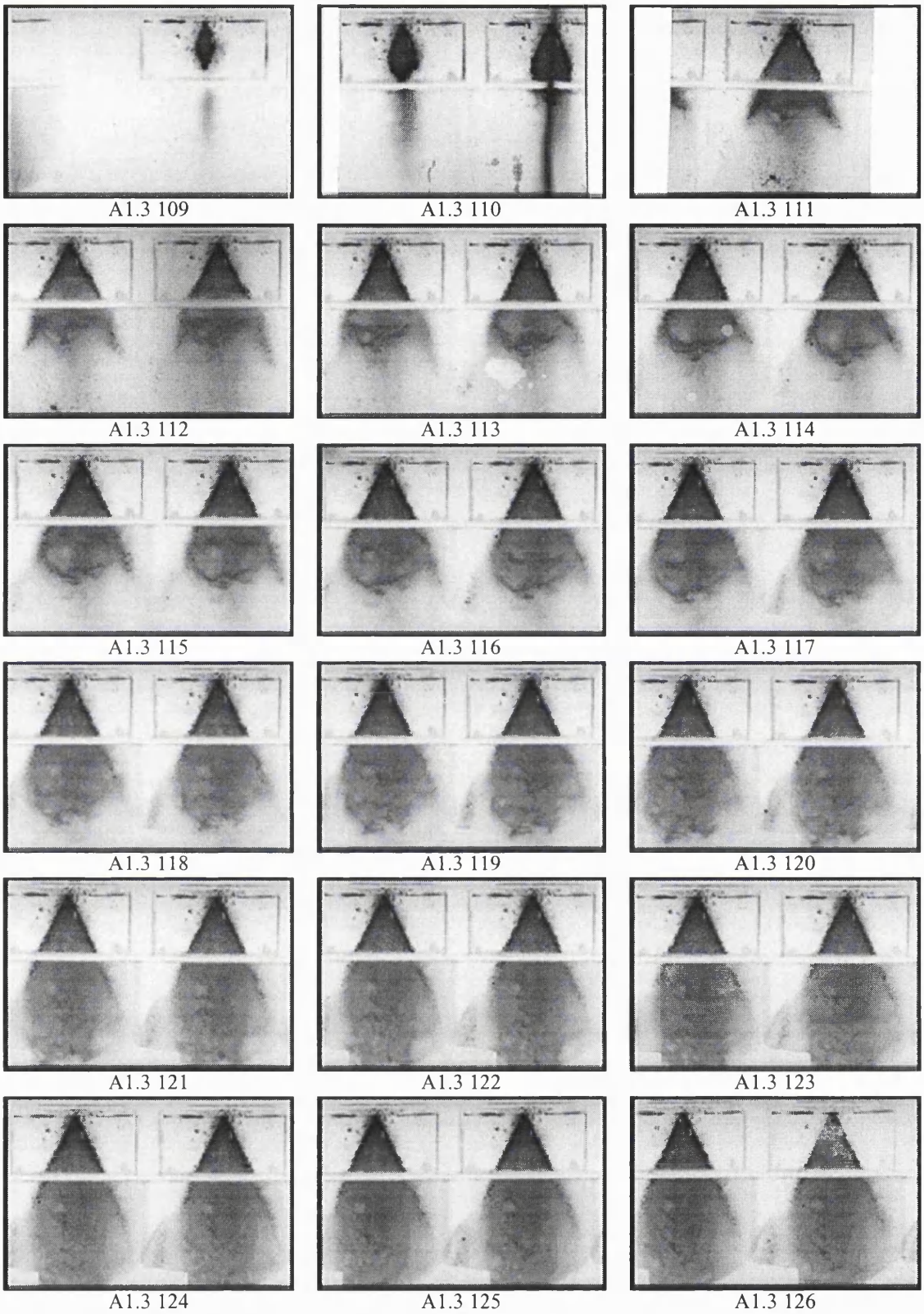

Variables: 0.5 bar ambient pressure, 23°C fuel temperature, 20 bar fuel pressure, gasoline, light sheet approaching spray from underneath.
Scale: width x height of frame represents 96.0 mm x 64.0 mm.
Notes: 0.1 ms between shots. 2 shots per frame. Part of spray obscured by test rig.

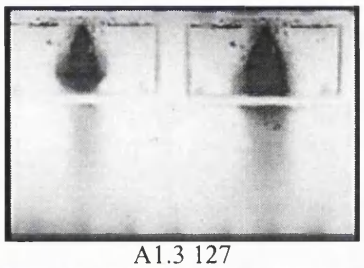
A1.3 127

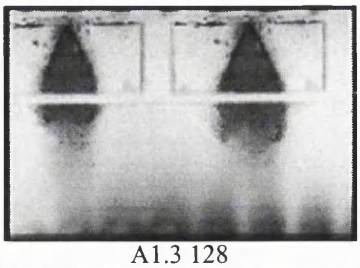
A1.3 128

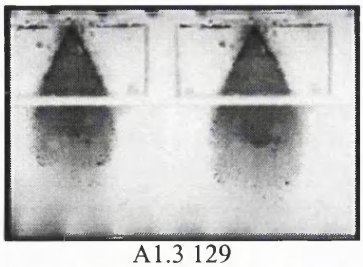
A1.3 129

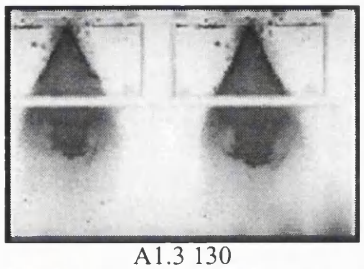
A1.3 130

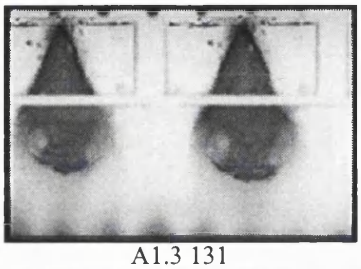
A1.3 131

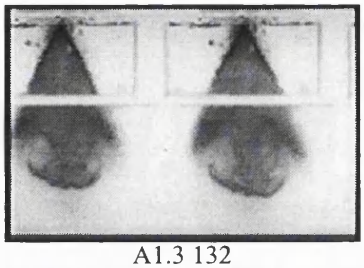
A1.3 132

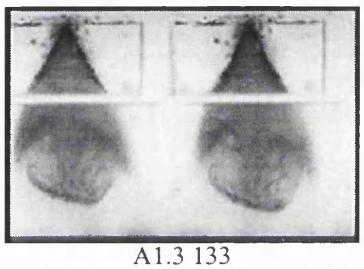
A1.3 133

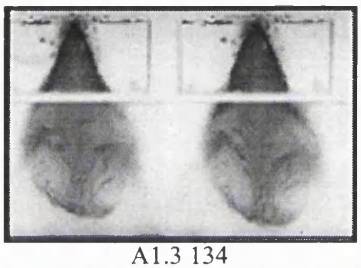
A1.3 134

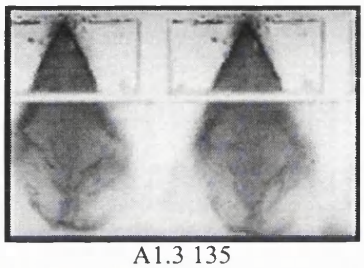
A1.3 135

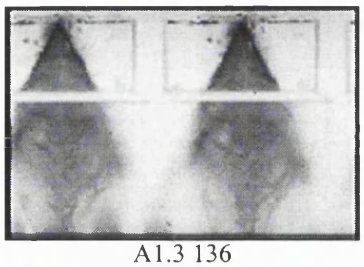
A1.3 136

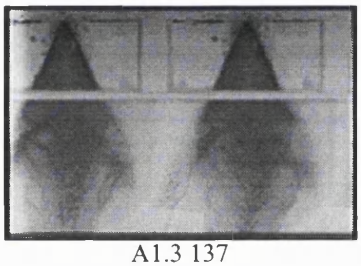
A1.3 137

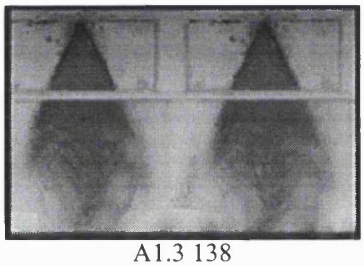
A1.3 138

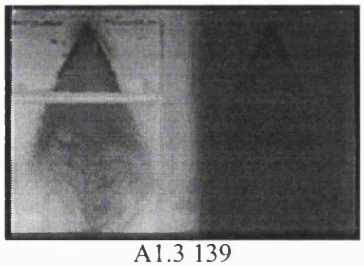
A1.3 139

Variables: 0.5 bar ambient pressure, 80°C fuel temperature, 20 bar fuel pressure, gasoline, light sheet approaching spray from underneath.
Scale: width x height of frame represents 96.0 mm x 64.0 mm.
Notes: 0.1 ms between shots. 2 shots per frame. Part of spray obscured by test rig.

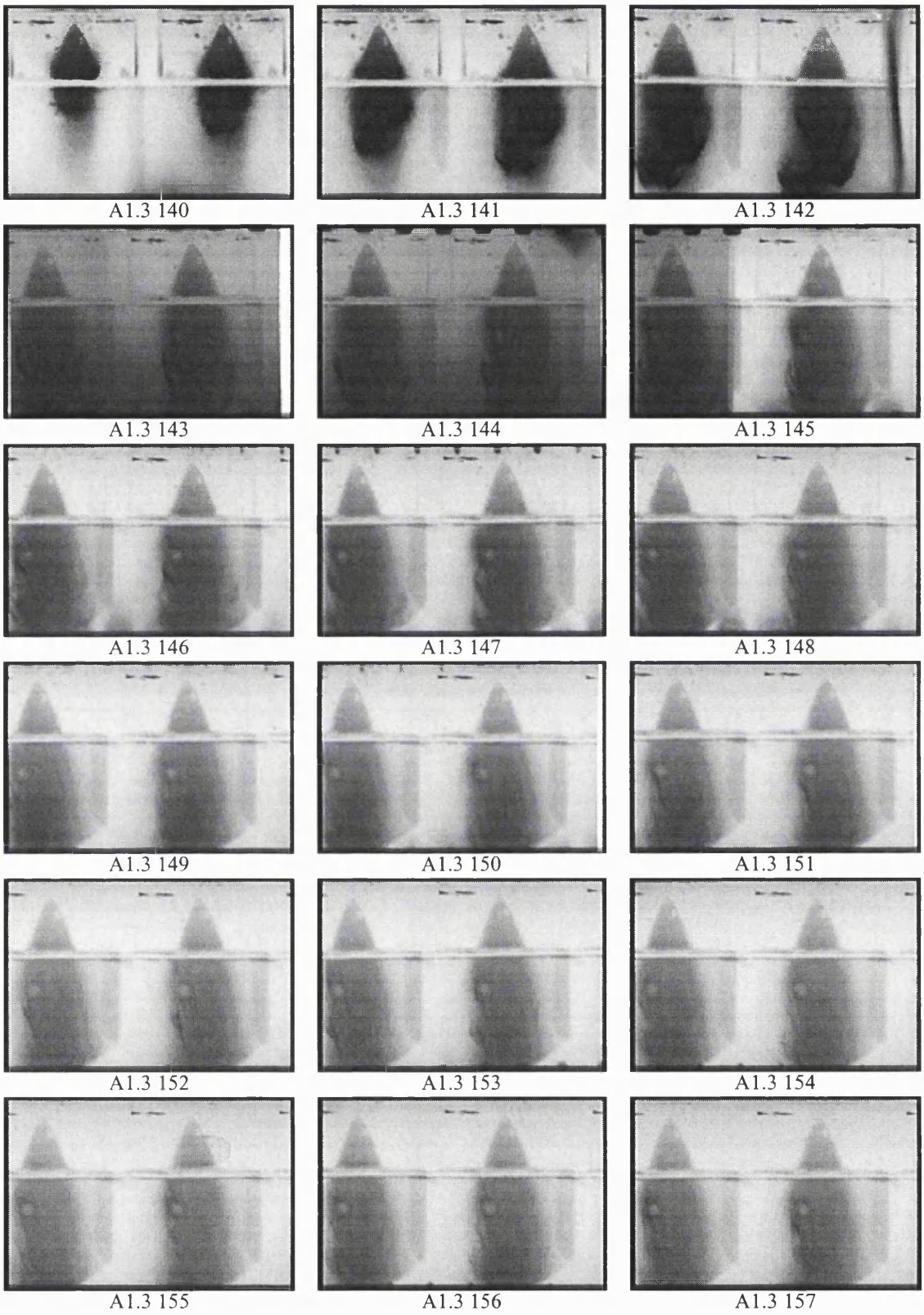

A1.3 140 A1.3 141 A1.3 142

A1.3 143 A1.3 144 A1.3 145

A1.3 146 A1.3 147 A1.3 148

A1.3 149 A1.3 150 A1.3 151

A1.3 152 A1.3 153 A1.3 154

A1.3 155 A1.3 156 A1.3 157

Variables: 0.5 bar ambient pressure, 80°C fuel temperature, 100 bar fuel pressure, gasoline, light sheet approaching spray from underneath.
Scale: width x height of frame represents 96.0 mm x 64.0 mm.
Notes: 0.1 ms between shots. 2 shots per frame. Part of spray obscured by test rig.

A1 - CATALOGUE OF FUEL SPRAY IMAGES

A1.4 - Injector D

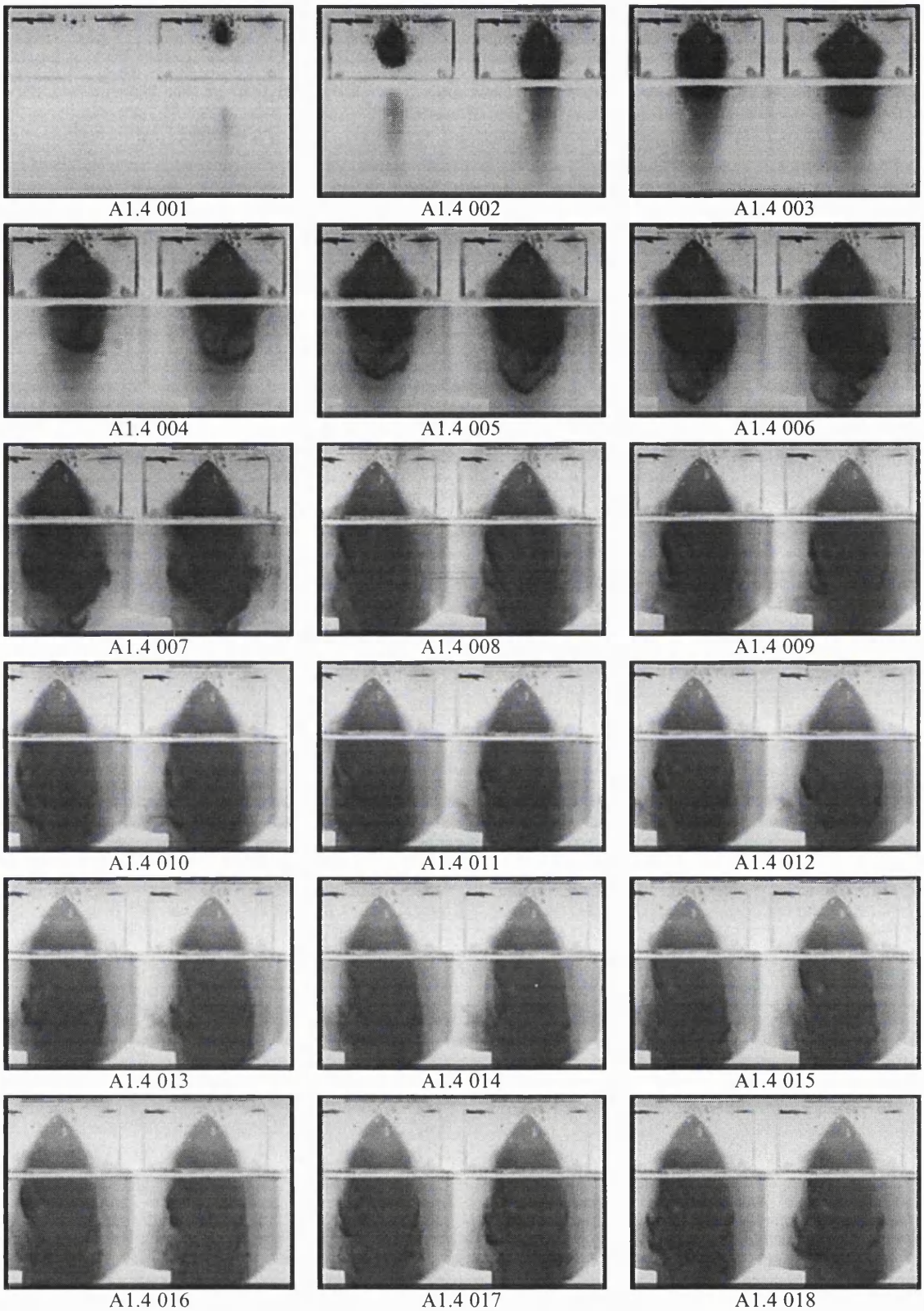

Variables: 0.5 bar ambient pressure, 80°C fuel temperature, 100 bar fuel pressure, gasoline, light sheet approaching spray from underneath.
Scale: width x height of frame represents 96.0 mm x 64.0 mm.
Notes: 0.1 ms between shots. 2 shots per frame. Part of spray obscured by test rig.

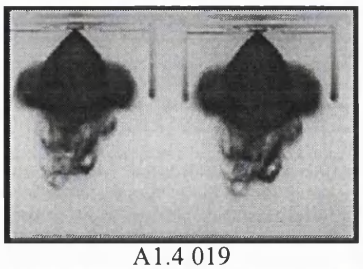
A1.4 019

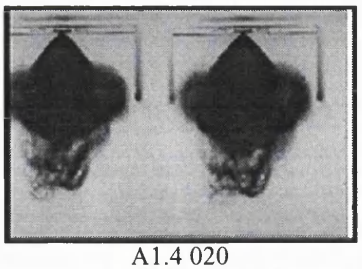
A1.4 020

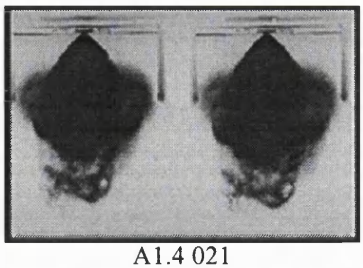
A1.4 021

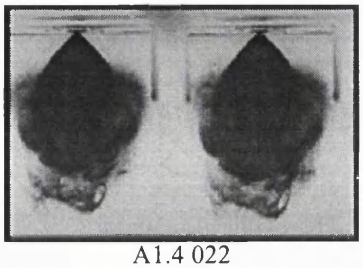
A1.4 022

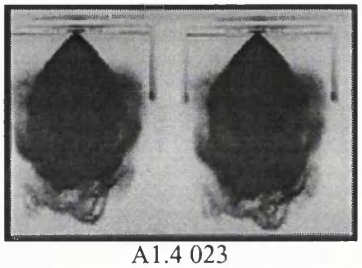
A1.4 023

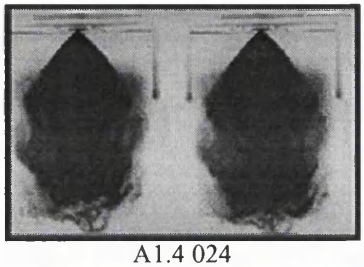
A1.4 024

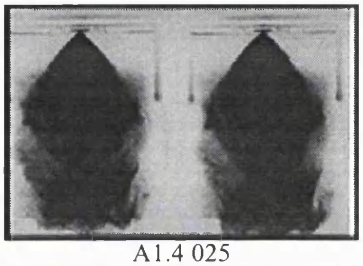
A1.4 025

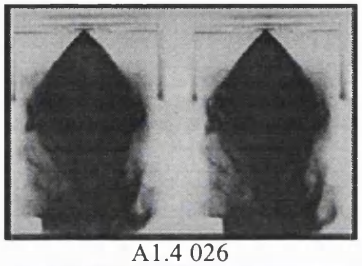
A1.4 026

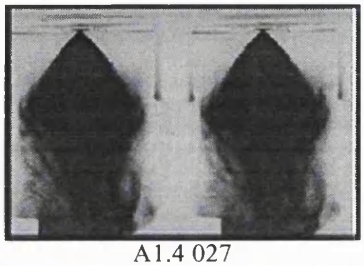
A1.4 027

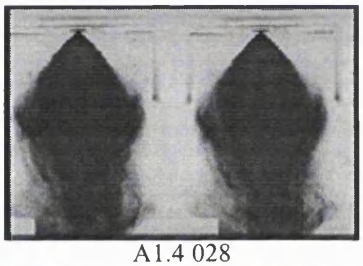
A1.4 028

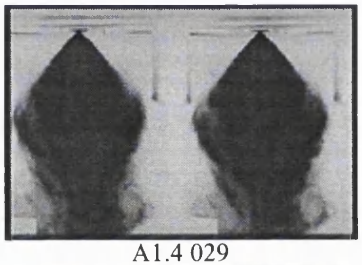
A1.4 029

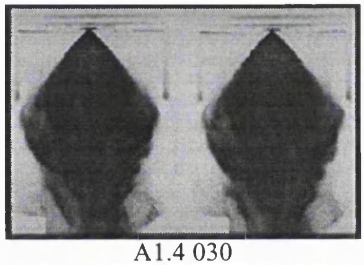
A1.4 030

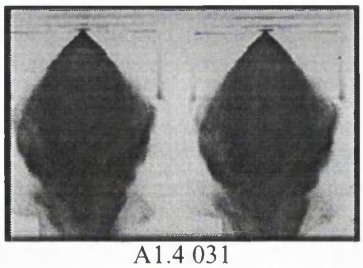
A1.4 031

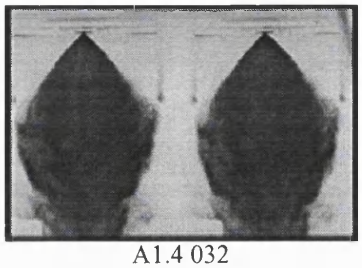
A1.4 032

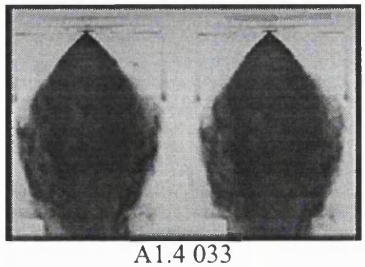
A1.4 033

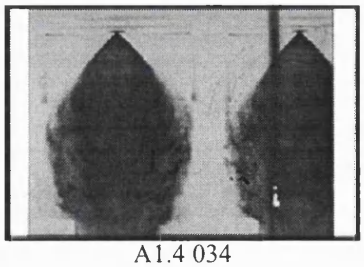
A1.4 034

Variables: atmospheric pressure, 80°C fuel temperature, 100 bar fuel pressure, iso-octane, light sheet approaching spray from underneath.
Scale: width x height of frame represents 99.0 mm x 66.0 mm.
Notes: 0.1 ms between shots. 2 shots per frame.

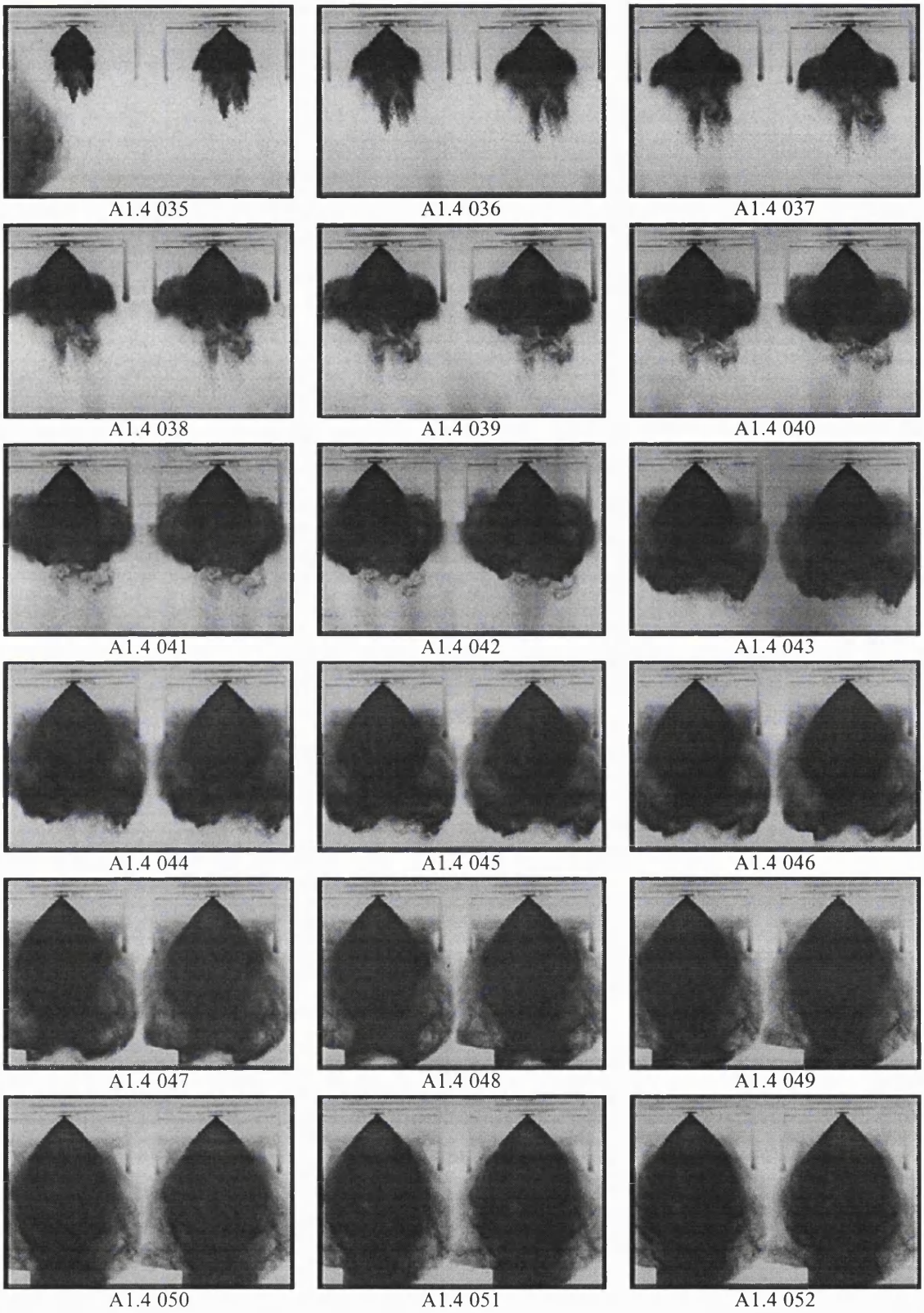

Variables: atmospheric pressure, 25°C fuel temperature, 20 bar fuel pressure, iso-octane, light sheet approaching spray from underneath.
Scale: width x height of frame represents 99.0 mm x 66.0 mm.
Notes: 0.1 ms between shots. 2 shots per frame.

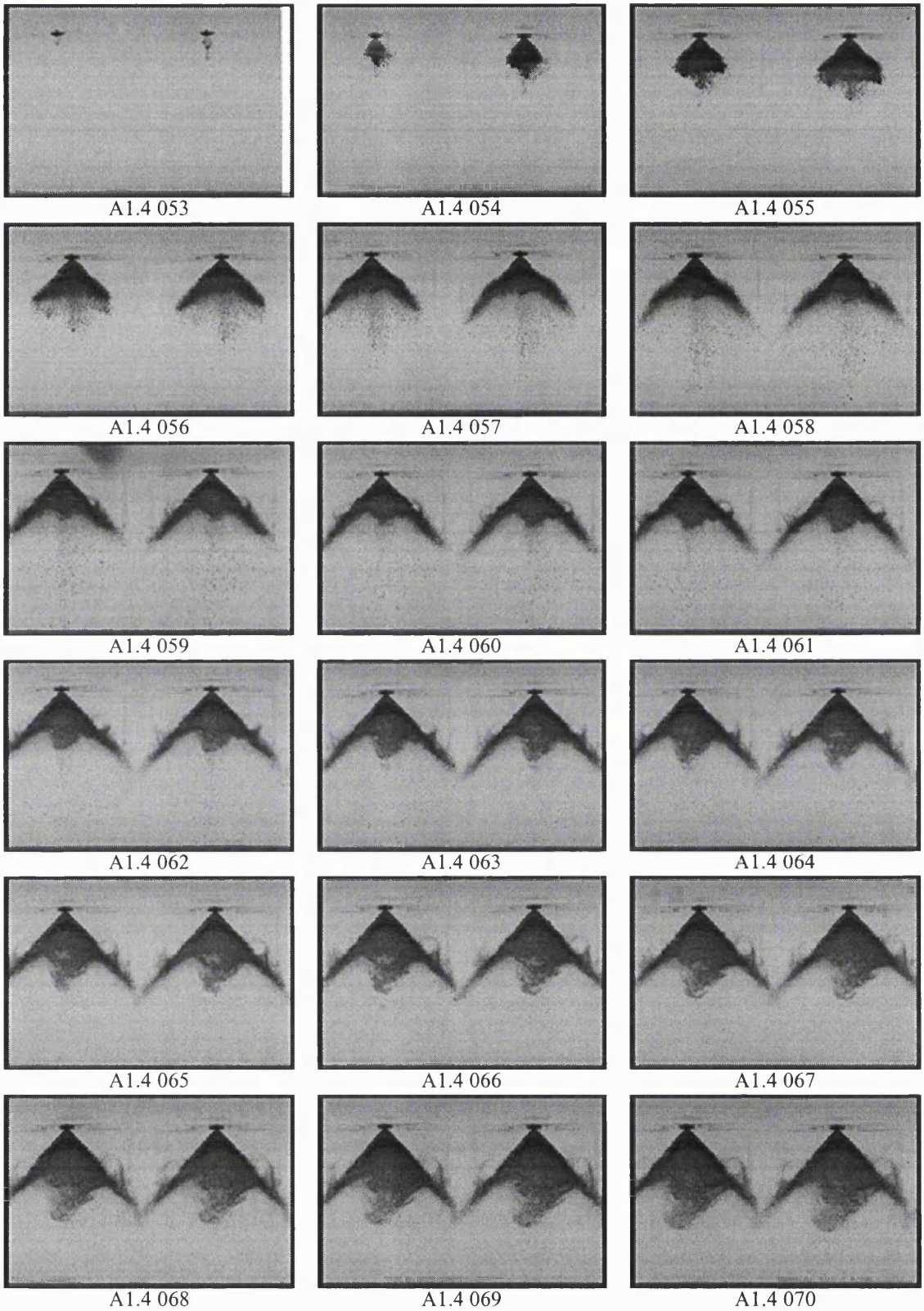

Variables: atmospheric pressure, 25°C fuel temperature, 20 bar fuel pressure, gasoline, light sheet approaching spray from underneath.
Scale: width x height of frame represents 99.0 mm x 66.0 mm.
Notes: 0.1 ms between shots. 2 shots per frame.

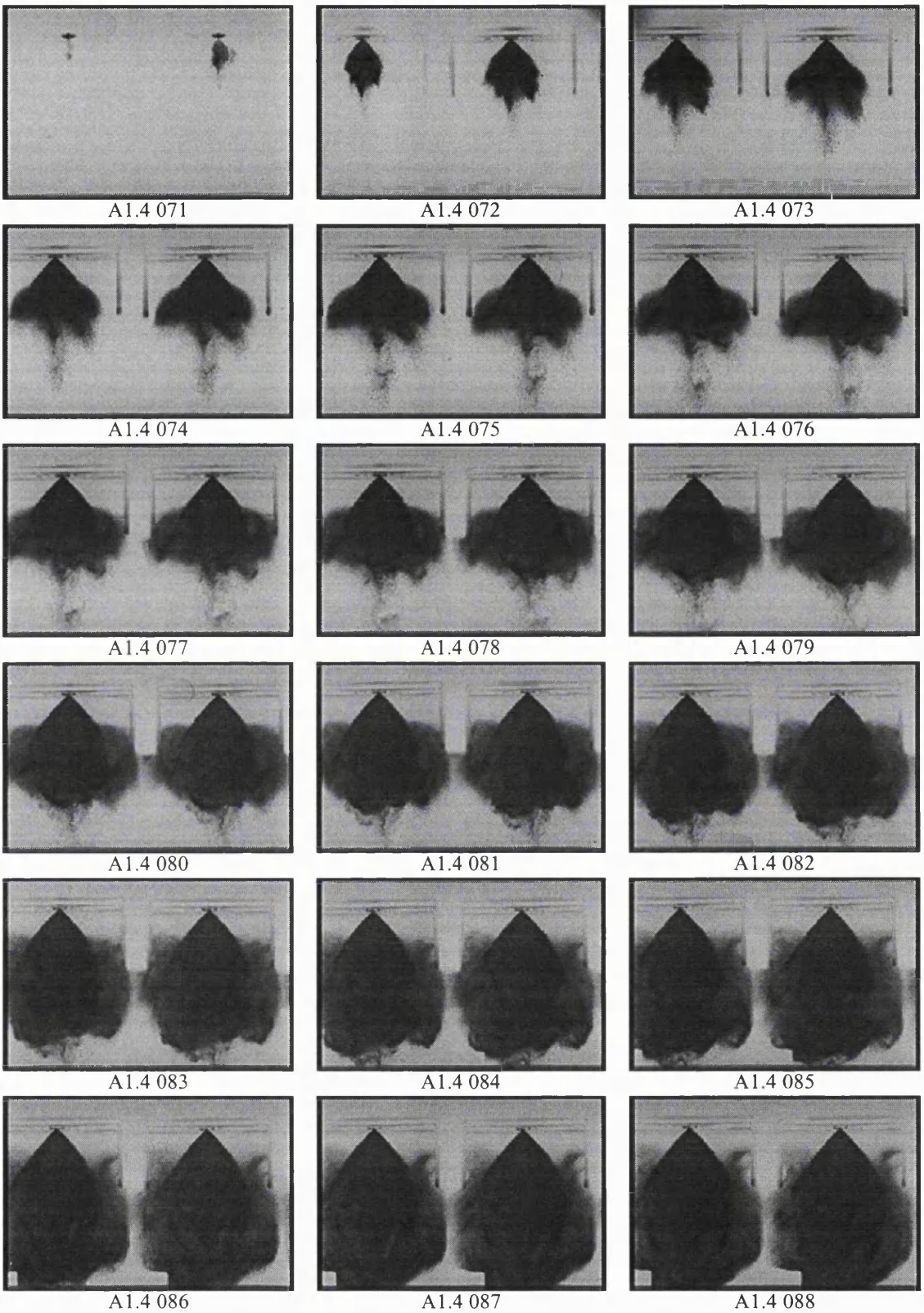

Variables: atmospheric pressure, 21°C fuel temperature, 100 bar fuel pressure, gasoline, light sheet approaching spray from underneath.
Scale: width x height of frame represents 99.0 mm x 66.0 mm.
Notes: 0.1 ms between shots. 2 shots per frame.

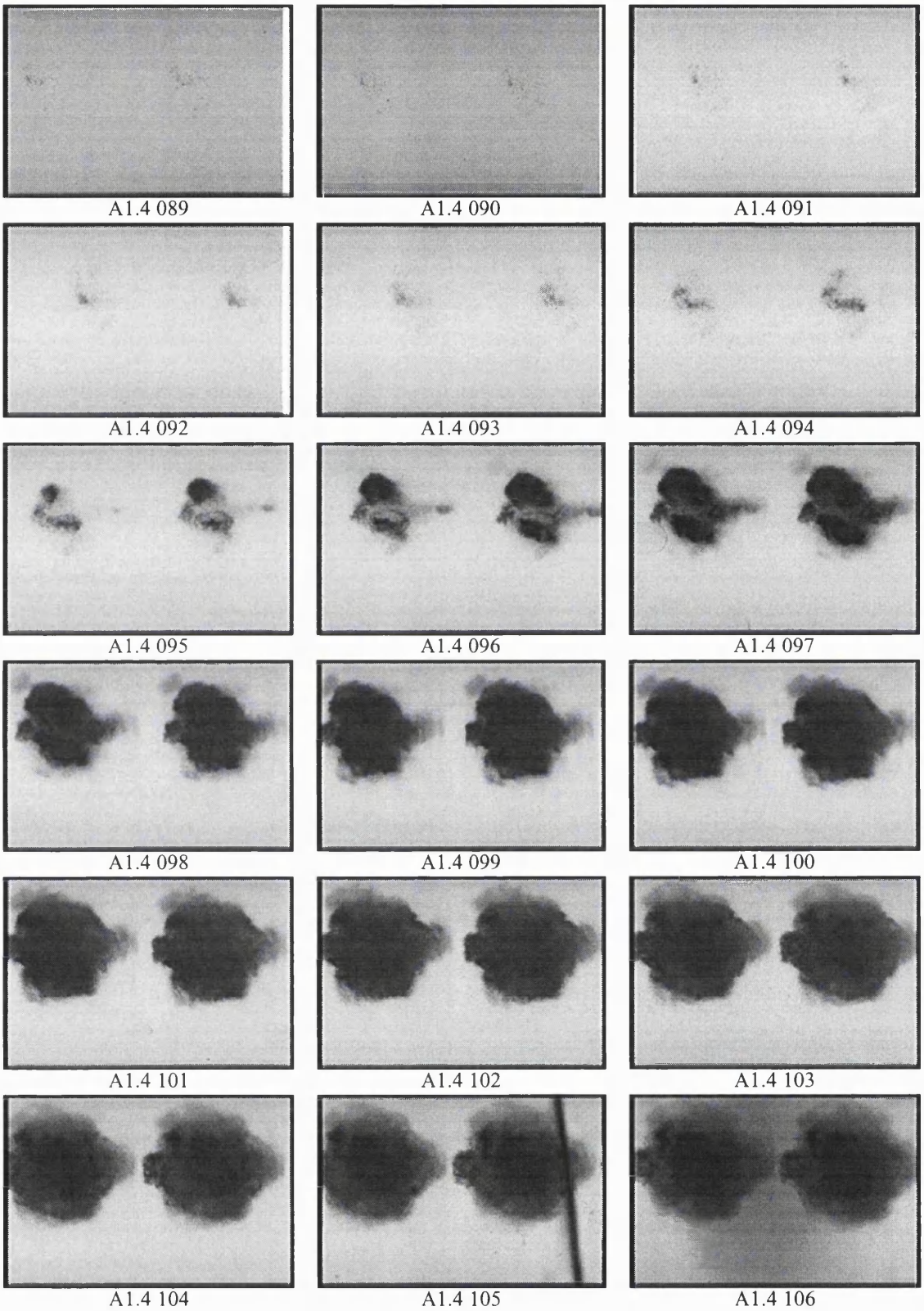

Variables: atmospheric pressure, 25°C fuel temperature, 100 bar fuel pressure, gasoline, light sheet approaching spray from left hand side.
Scale: width x height of frame represents 176.0 mm x 117.0 mm.
Notes: 0.1 ms between shots. 2 shots per frame. End-on view.

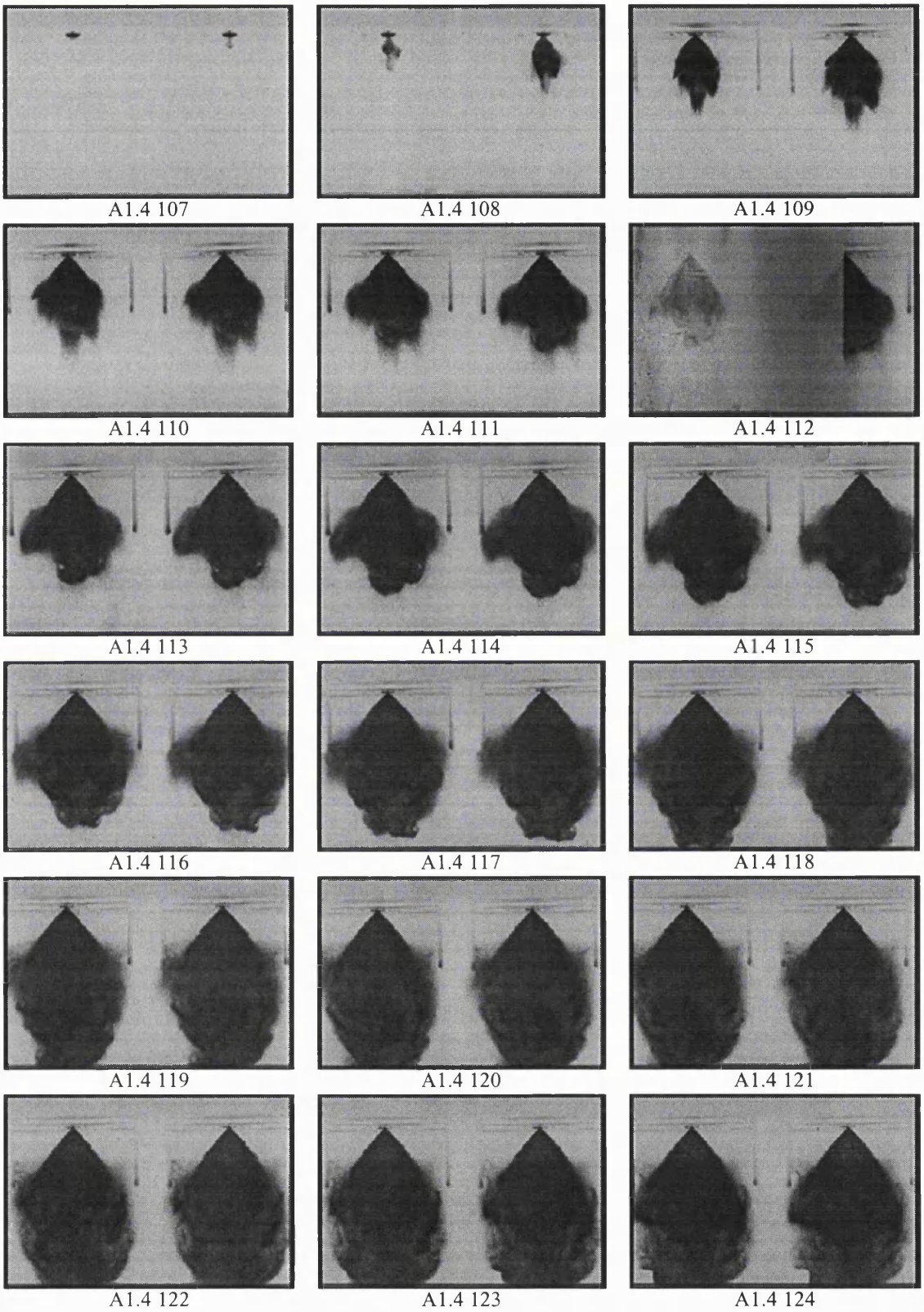

Variables: atmospheric pressure, 80°C fuel temperature, 100 bar fuel pressure, gasoline, light sheet approaching spray from underneath.
Scale: width x height of frame represents 99.0 mm x 66.0 mm.
Notes: 0.1 ms between shots. 2 shots per frame. Part of spray obscured by test rig.

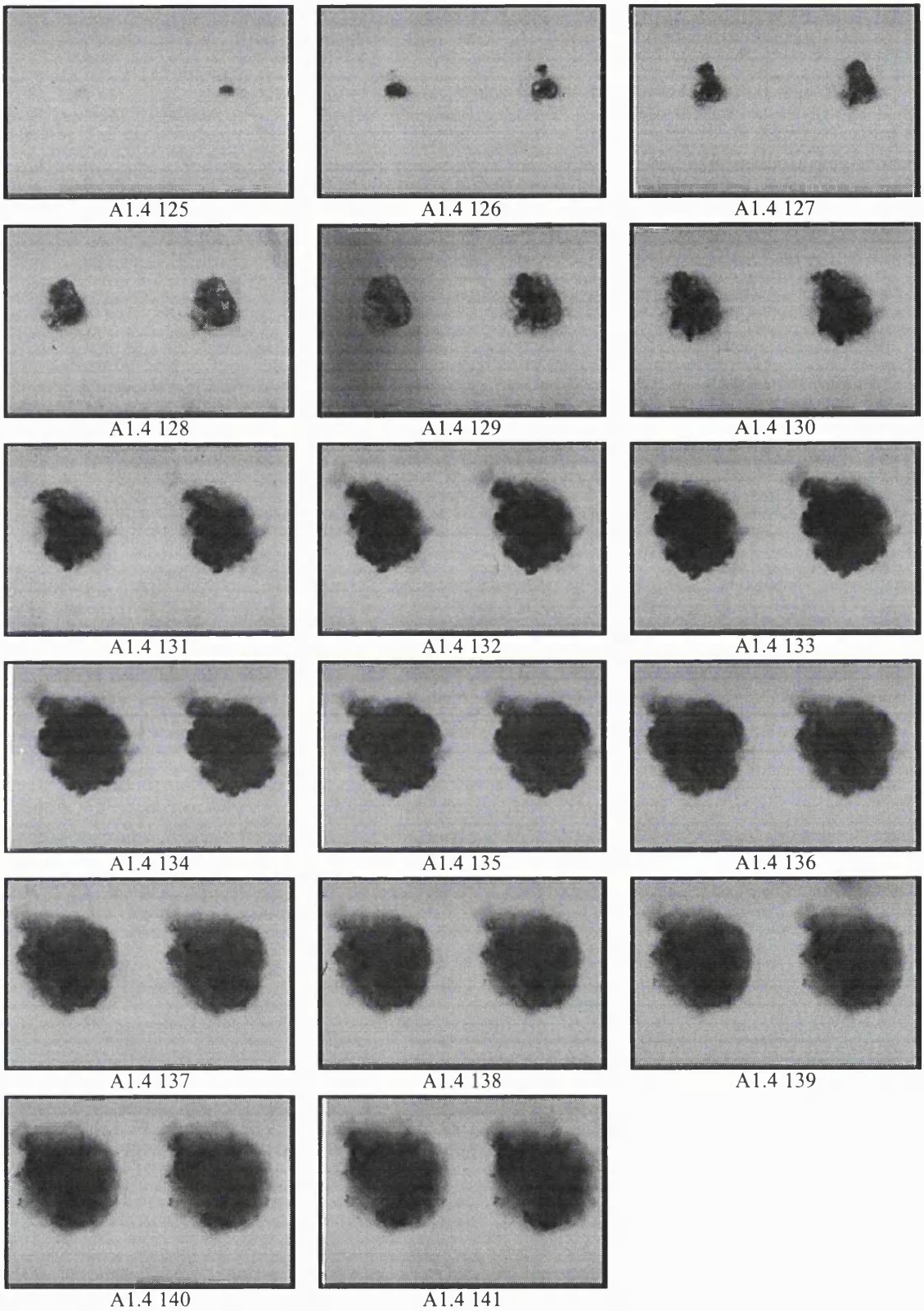

Variables: 0.5 bar ambient pressure, 80°C fuel temperature, 100 bar fuel pressure, gasoline, light sheet approaching spray from left hand side.
Scale: width x height of frame represents 232.0 mm x 155.0 mm.
Notes: 0.1 ms between shots. 2 shots per frame. End-on view.

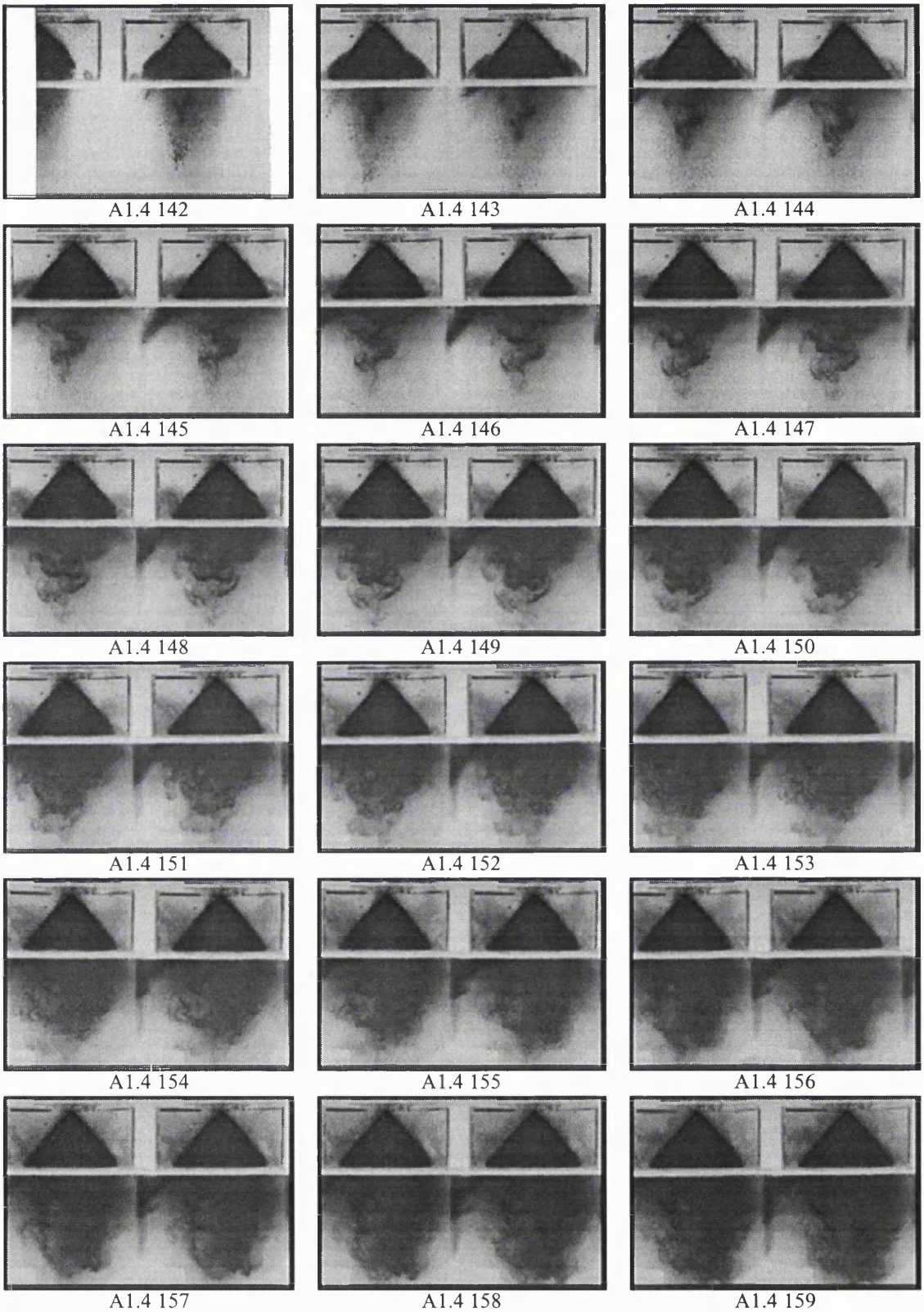

Variables: 0.5 bar ambient pressure, 22°C fuel temperature, 100 bar fuel pressure, gasoline, light sheet approaching spray from underneath.
Scale: width x height of frame represents 96.0 mm x 64.0 mm.
Notes: 0.1 ms between shots. 2 shots per frame. Part of spray obscured by test rig.

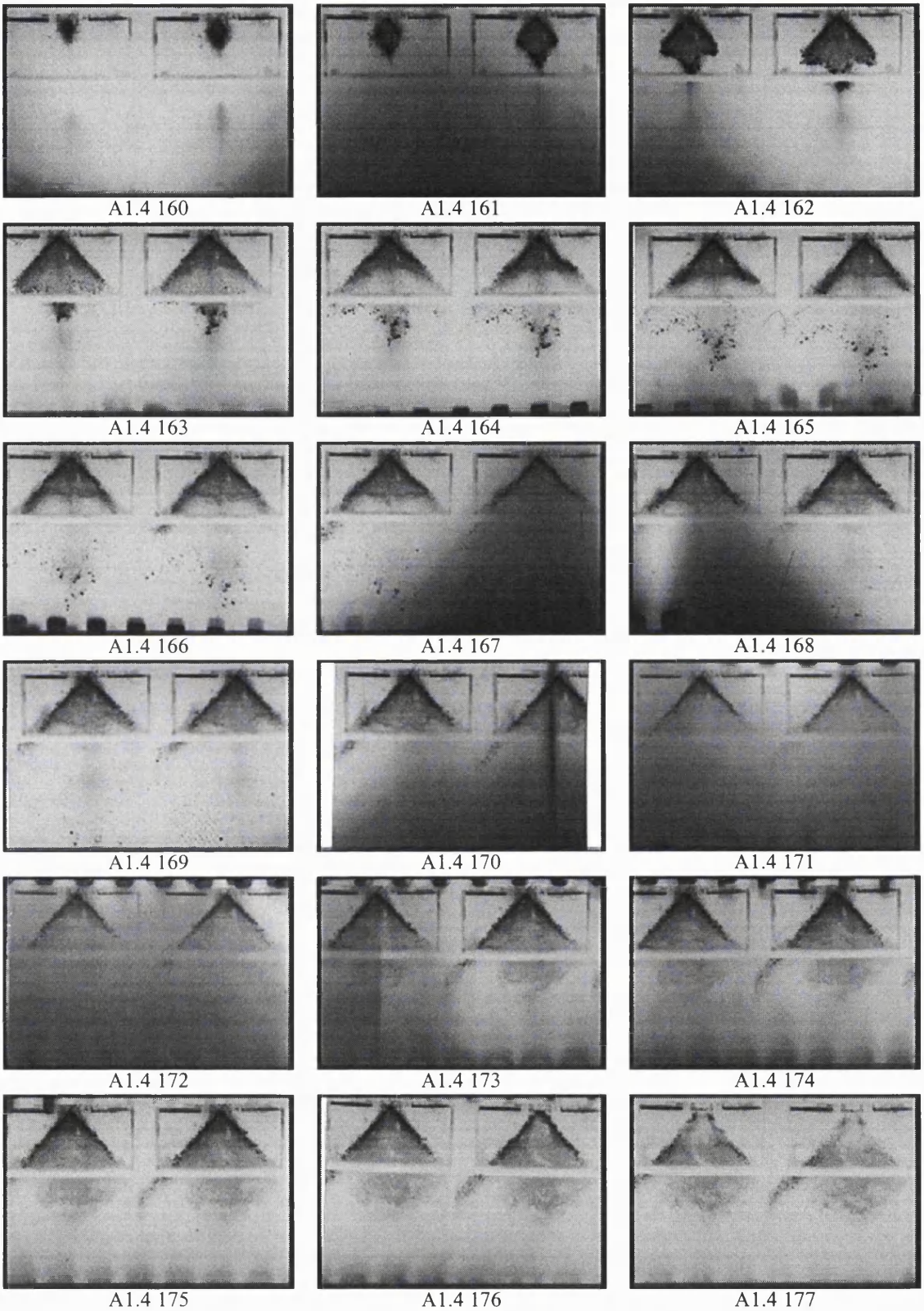

A1.4 160 A1.4 161 A1.4 162

A1.4 163 A1.4 164 A1.4 165

A1.4 166 A1.4 167 A1.4 168

A1.4 169 A1.4 170 A1.4 171

A1.4 172 A1.4 173 A1.4 174

A1.4 175 A1.4 176 A1.4 177

Variables: 0.5 bar ambient pressure, 22°C fuel temperature, 20 bar fuel pressure, gasoline, light sheet approaching spray from underneath.
Scale: width x height of frame represents 96.0 mm x 64.0 mm.
Notes: 0.1 ms between shots. 2 shots per frame. Part of spray obscured by test rig.

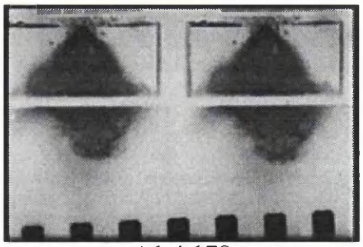
A1.4 178

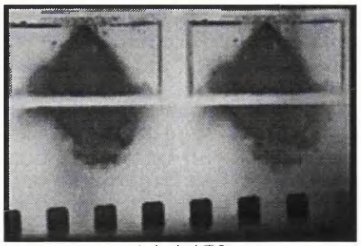
A1.4 179

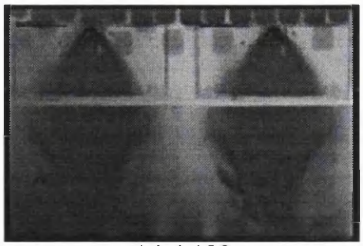
A1.4 180

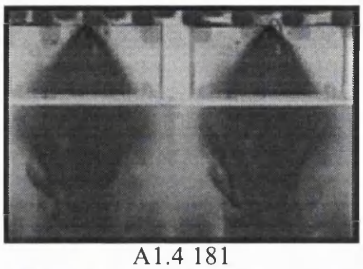
A1.4 181

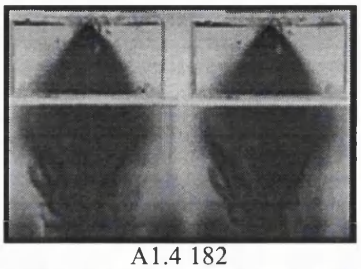
A1.4 182

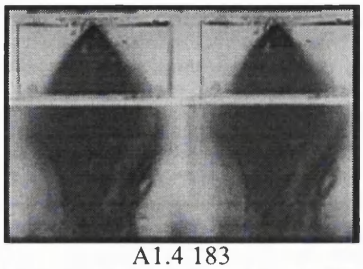
A1.4 183

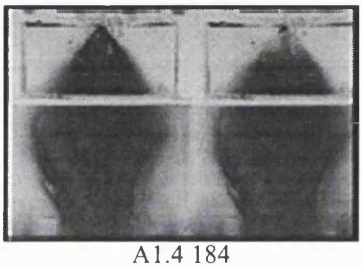
A1.4 184

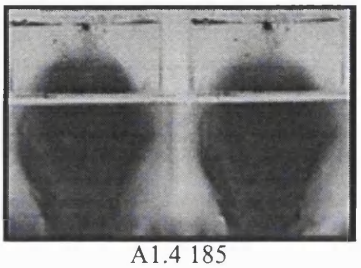
A1.4 185

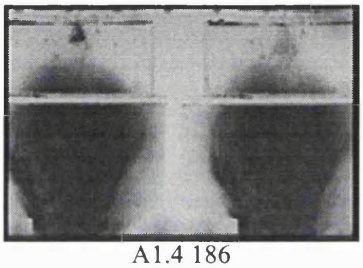
A1.4 186

Variables: 0.5 bar ambient pressure, 80°C fuel temperature, 20 bar fuel pressure, gasoline, light sheet approaching spray from underneath.
Scale: width x height of frame represents 96.0 mm x 64.0 mm.
Notes: 0.1 ms between shots. 2 shots per frame. Part of spray obscured by test rig.

A2 - ALGORITHM FOR TOMOGRAPHIC ANALYSIS

A2 - Algorithm for tomographic analysis

Figure A2.1 illustrates a cross-section of a spray taken at right angles to its axis some distance from the injector. Each 'slice' of the circle represents the section of one of the paths of the 9.0 mm diameter Malvern laser beam through the cone-shaped spray.

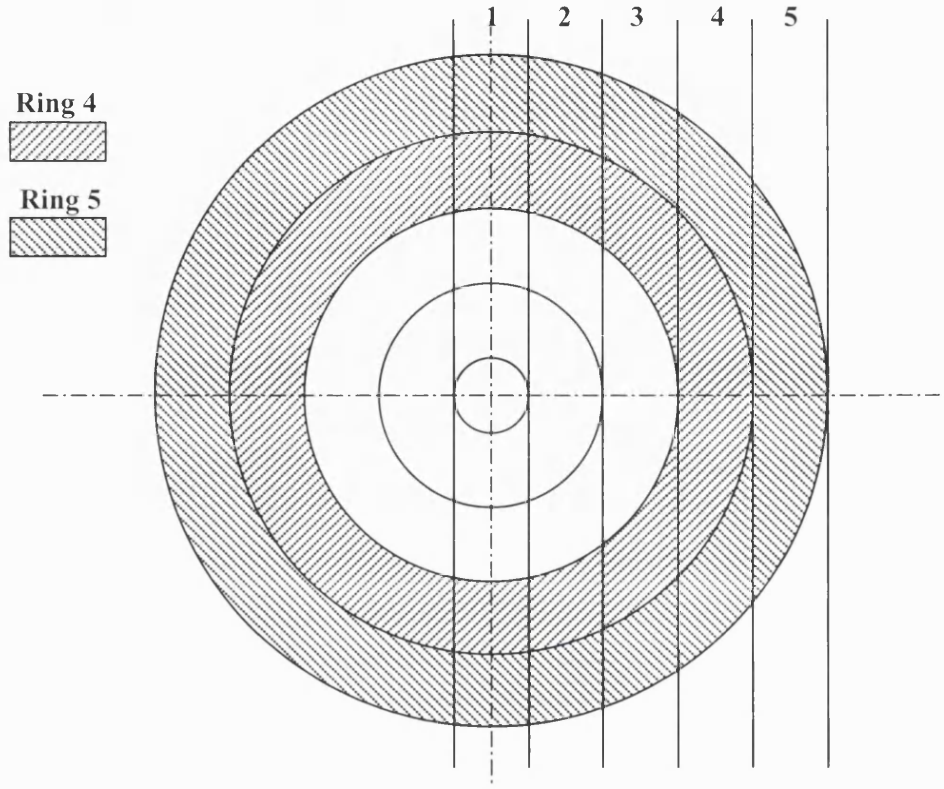

Figure A2.1 - Schematic representation of the fuel spray cross-section.

The spray has been broken up into a number of imaginary rings (five in this case, including the centre circle). It is assumed that both Sauter mean diameter and fuel concentration remain constant throughout a single ring. The thickness of the ring corresponds to the width of the laser beam, as does the width of the slice.

To begin, consider slice '5'. All droplets in this slice are in the 5th ring. Therefore, without modification, a reading of the droplet size distribution at 5 will represent the distribution throughout the 5th ring.

Next, consider slice '4'. This is made up of a part of ring 4 and two parts of ring 5. Therefore, the reading taken at 4 is not representative of the droplet size distribution in ring 4, but of a combination of the two rings. The proportion of each ring in the slice has to be calculated so that the contribution of each ring can be stated to the overall reading for the slice. The calculation becomes more complicated for the central slices, but the principle remains the same.

The volume of each section shown above was measured using a 3-dimensional model of the spray in a CAD package. The volume of the laser beam in the fuel spray was also calculated in this way. Before the calculations of the SMD can be carried out, the concentration of fuel in each ring must be calculated from the initial values given by the Malvern particle sizer.

The equation becomes:

$$c_i = \frac{(100 \times C_i) - \sum_{j=(i+1)\text{to}5} (c_j \times v_j)}{v_i}$$

Where

c_i = calculated concentration in *i*th ring (percentage)

i = ring number (1 is centre, 5 is outer in this case)

C_i = concentration value from Malvern measurement of *i*th slice (percentage)

v_i = percentage volume of the laser beam in *i*th ring (percentage)

For example, the outside ring (ring number 5) has a concentration of 0.0002% (this is the value for c_5). In the fourth slice, 2019.7 mm^3 of the laser beam is in the outer ring. This represents 47% (v_5) of the slice volume. For the fourth slice, the Malvern measurement of concentration was 0.0017%. Using the equation above:

$$c_i = \frac{(100 \times 0.0017) - (0.0002 \times 47)}{53}$$

$$\Rightarrow \qquad c_4 = 0.00303\%$$

Let:

n_5 = the number of droplets per unit volume in ring 5

d_5 = the Sauter mean diameter of droplets in ring 5

From definition of concentration:

$$c_5 = \frac{n_5 \times \frac{4}{24} \times \pi \times d_5^3 \times 100}{1}\%$$

$$n_5 = \frac{6 \times c_5}{100 \times \pi \times d_5^3}$$

Surface area per unit volume of droplets in ring 5:

$$= n_5 \times \pi \times d_5^2 = \frac{6 \times c_5}{100 \times d_5}$$

Total surface area of droplets per unit volume in slice 3 for instance:

$$= \frac{6}{100}\left\{\left(\frac{c_5 \times v_5}{d_5}\right) + \left(\frac{c_4 \times v_4}{d_4}\right) + \left(\frac{c_3 \times v_3}{d_3}\right)\right\} \times \frac{1}{100}$$

Total liquid volume per unit volume in ring 5:

$$= n_5 \times \frac{4}{24}\pi \times {d_5}^3 = \frac{6 \times c_5}{100 \times \pi \times {d_5}^3} \times \frac{4}{24} \times \pi \times {d_5}^3$$

$$= \frac{c_5}{100}$$

Total liquid volume per unit volume in slice 3:

$$= \frac{1}{100} \times \{c_5 v_5 + c_4 v_4 + c_3 v_3\} \times \frac{1}{100}$$

Surface / volume ratio:

$$= \frac{\frac{6}{100}\left\{\left(\frac{c_5 \times v_5}{d_5}\right) + \left(\frac{c_4 \times v_4}{d_4}\right) + \left(\frac{c_3 \times v_3}{d_3}\right)\right\}}{\frac{1}{100} \times \{c_5 v_5 + c_4 v_4 + c_3 v_3\}}$$

But, surface / volume ratio is also equal to:

$$= \frac{\pi \times {D_i}^2}{\frac{4}{24} \times \pi \times {D_i}^3} = \frac{6}{D_i}$$

Where D_i is the Sauter mean diameter (measured by the Malvern) of the *i*th slice.

Equating both sides and generalising for any ring:

$$d_i = \frac{c_i v_i}{\left(\frac{100 \times C_i}{D_i}\right) - \sum_{j=(i+1)\text{to}5}\left(\frac{c_j \times v_j}{d_j}\right)}$$

A3 - DRAWINGS OF ENGINE COMPONENTS

A3.1 - Cylinder block

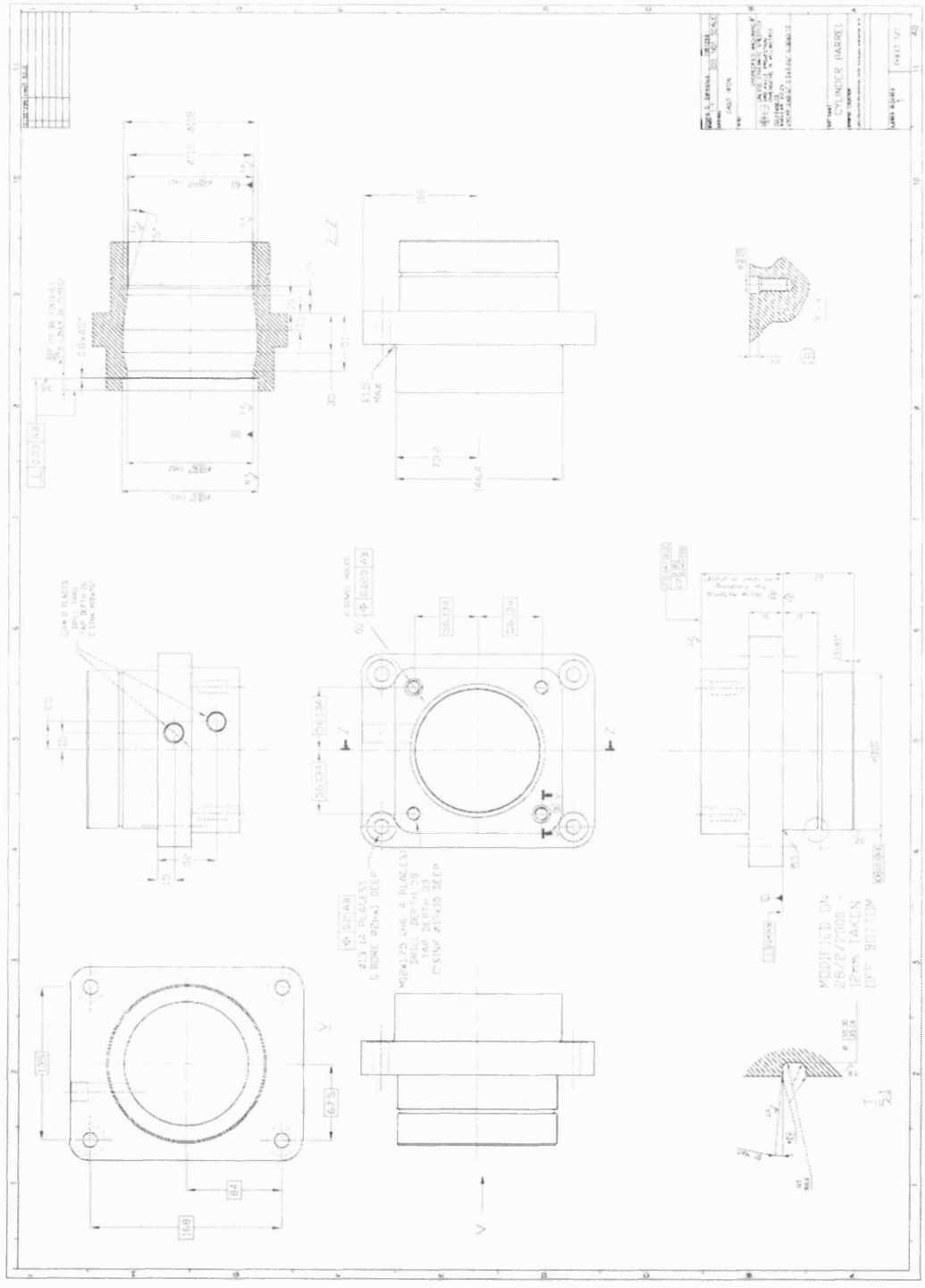

A3.2 - Cooling sleeve

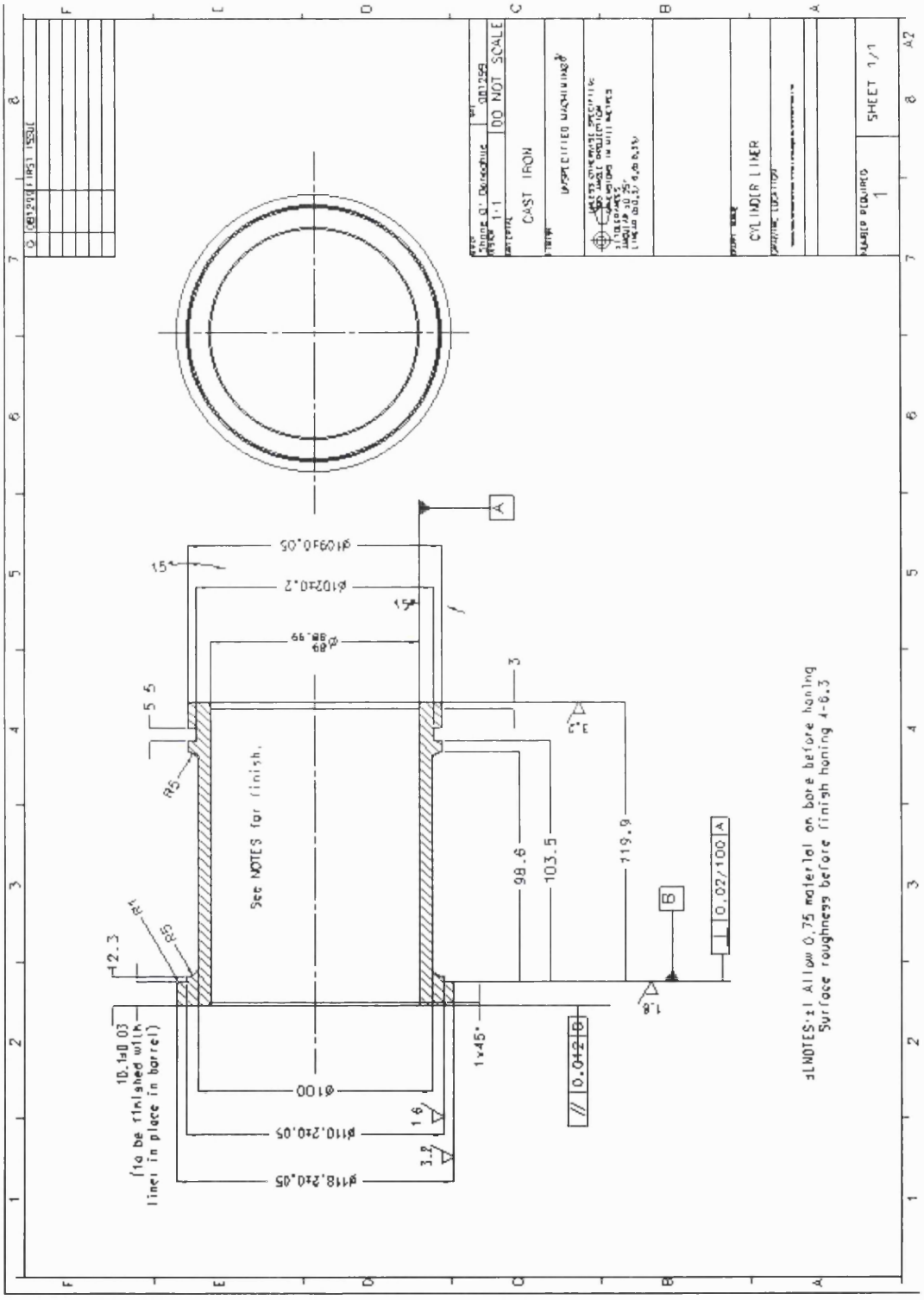

A4 - ENGINE AND INSTRUMENTATION COMPONENT SPECIFICATIONS

A4.1 - High-pressure GDI fuel pump

MICRO–HYDRAULICS HIGH PRESSURE TYPE PB36.5 ES

Fixed displacement pump for low viscosity fluids
Displacement from 0.100 to 0.360 cm^3/rev
(from 0.006 to 0.0022 cu.in.)
Max. pressure : depends on fluid used
5000 rpm
2 pistons

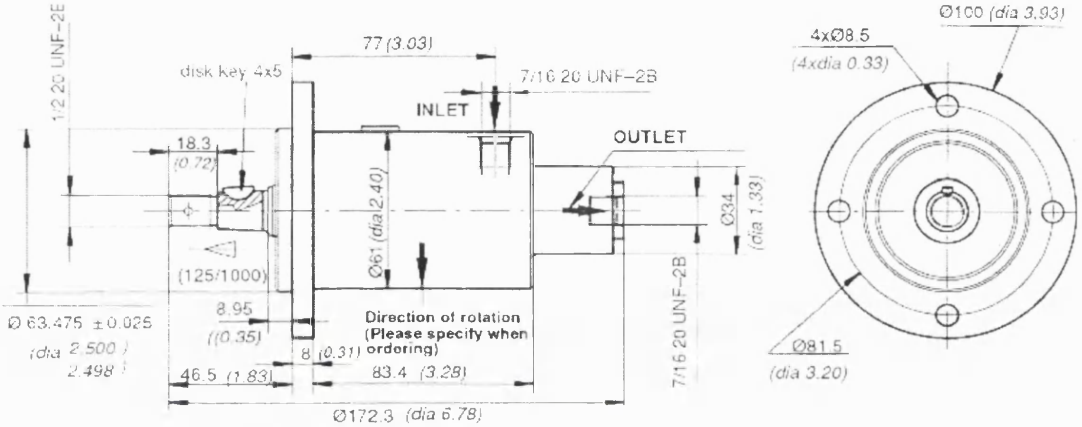

Dimensions are written in millimeters and *(inches)*

TECHNICAL CHARACTERISTICS

Pump	Displacement cm^3/rev *(cu.in./rev.)*	Max. pressure (bar) peak	Max. speed (rpm) peak
PB36.5 0510740	0.100 *(0.006)*		5000
PB36.5 0510735	0.150 *(0.009)*	Depends	5000
PB36.5 0510730	0.230 *(0.014)*	on fluid used	5000
PB36.5 0510725	0.300 *(0.018)*		5000
PB36.5 0510720	0.360 *(0.022)*		5000

Max. temperature : 200°C *(392° F)*
Weight : 2.3 kg (5.07 lbs)

TYPE PB36.5 ES

MICRO–HYDRAULICS
HIGH PRESSURE

VOLUMETRIC EFFICIENCY CURVE

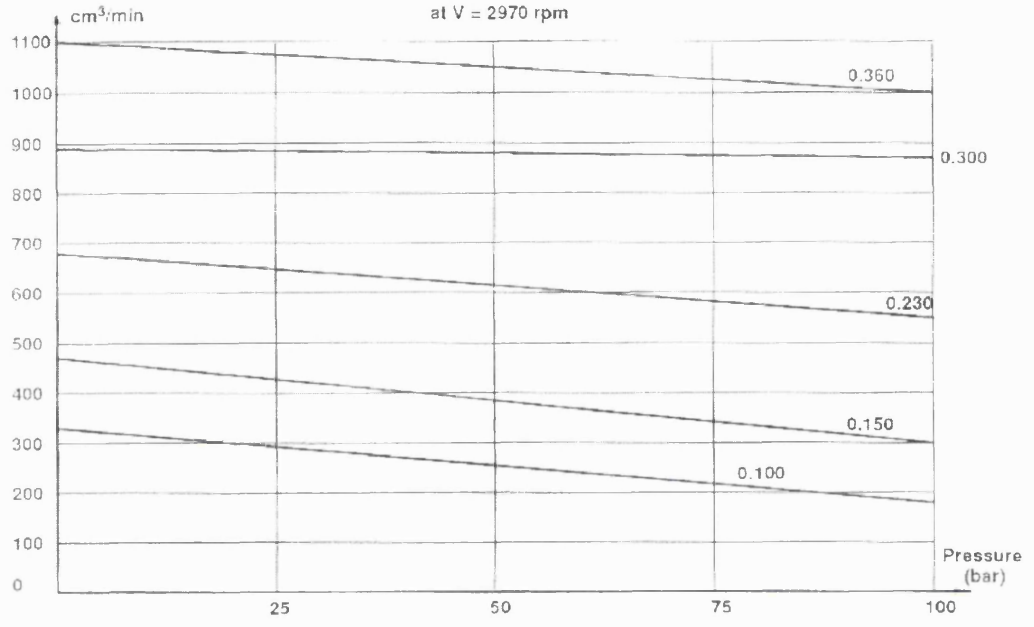

A4.2 - Calculation of plenum chamber volume

According to Plint [1999], the minimum desirable volume of airbox (plenum chamber) is given by the following equation.

$$V_b = \frac{417 \times 10^6 \times K^2 \times d^4}{N_c \times V_s \times n_{min}^2}$$

The purpose of the airbox in the work reported by Plint was to damp out the pulsations of flow into the engine so that an accurate measurement of airflow may be obtained by the use of an orifice plate. In the case of the investigation reported in this thesis, the purpose of the airbox was to provide a constant pressure at intake to the induction system. Any pulsations would not be desirable for the emissions testing as they may lead to unstable running and large cycle-to-cycle variations. The initial calculation was carried out as follows.

K = number of revolutions per cycle = 2
d = diameter of inlet to airbox = 12.5×10^{-3} m
N_c = number of cylinders = 1
n_{min} = required minimum stable speed = 500 rpm
V_s = swept volume = 4.945×10^{-4} m^3

$\Rightarrow$ $V_b = 0.329$ m^3

This volume is not practical (too large for test chamber). A volume of 0.2 m^3 was then chosen, which allows stable running as low as 650 rpm according to the equation above. The standard test point is at an engine rotational speed of 1500 rpm so this is acceptable.

A4.3 – Airflow meter calibration and description

A4.3.1 Description of airflow meter

The airflow meter was taken from the engine management system of a 4-cylinder production engine. It was modified to be more suitable for the lower air flow range of the single-cylinder test bed engine by fitting a partial blanking plate. This plate had the effect of changing the ratio of flow between the small measurement passage and the larger bypass passage. The modified flow meter was then calibrated against a rotameter, whose calibration was traceable to a national standard.

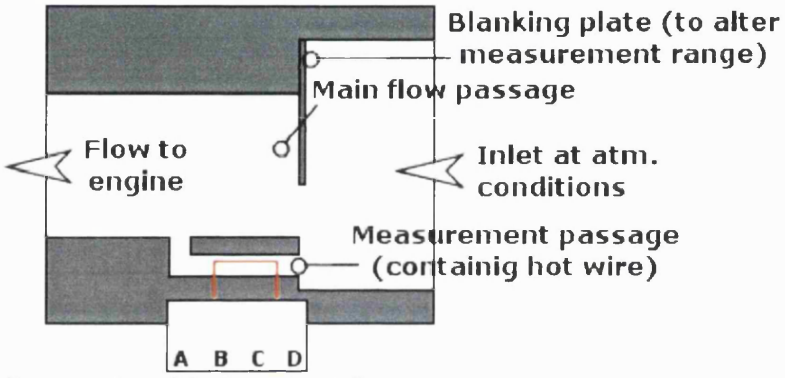

Figure A4.1 - Cross-section of the hot-wire airflow meter.

Pin A: +12V

Pin B: Ground voltmeter

Pin C: 0V

Pin D: + voltmeter

A4.3.2 Calibration of the airflow meter

A rotameter (Fisher & Porter Ltd - FP2-27-G-10/55) was employed to calibrate the airflow meter. The output from the meter was measured using a voltmeter. The calibration was performed over the range likely to be encountered during the engine testing. See figure A4.2 for the calibration.

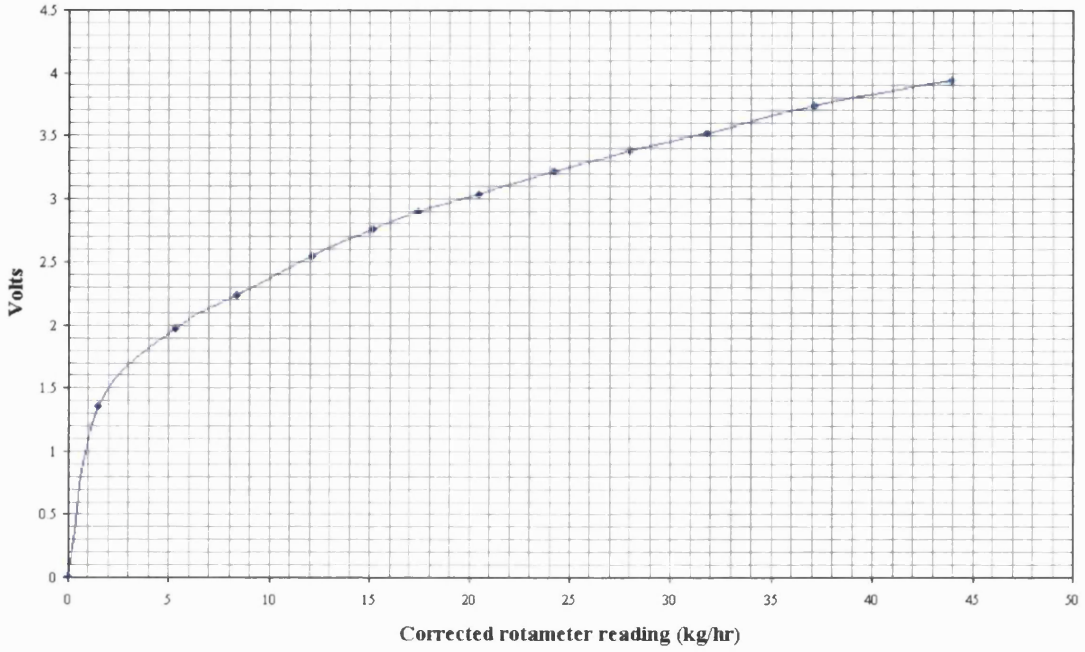

Figure A4.2 - Airflow meter calibration.

A4.3.3 Correction to rotameter readings

m = mass of float

A = area between float and glass tube

A_F = surface area of float

Δ_p = pressure drop across float

$\dot{V}$ = volumetric flow rate

$\dot{M}$ = mass flow rate

v = velocity of flow passing float

ρ = density of air

h = scale reading of rotameter

The assumption is made that, for a particular day's condition of temperature and pressure, the air density remains constant through the flowmeter.

Force balance: $mg = A_F \times \Delta_p$ (i)

Assuming that there is no downstream pressure recovery, Bernoulli's equation applied to float:

$$\Delta_p = \frac{1}{2}\rho v^2 \qquad \text{(ii)}$$

Continuity: $\dot{M} = \rho\dot{V} = \rho A v$ (iii)

Substitute (ii) into (iii): $\dot{M} = \rho\dot{V} = \rho A\sqrt{\frac{2\Delta_p}{\rho}}$

From (i): $\Delta_p = \frac{mg}{A_F}$ constant

$\Rightarrow$ $\dot{M} = A \times \text{constant} \times \sqrt{\rho}$

The flowmeter is constructed so that: A = constant x h

$\Rightarrow$ $\dot{M} = \text{constant} \times h \times \sqrt{\rho}$

On a standard day, temperature = T_0, pressure = p_0, density = ρ_0 and scale reading = h_0

$\Rightarrow$ $\dot{M}_0 = \text{constant} \times h_0 \times \sqrt{\rho_0}$

If the same reading is obtained on a day when density = ρ_1, temperature = T_1 and pressure = p_1:

$\Rightarrow$ $\dot{M}_1 = \text{constant} \times h_0 \times \sqrt{\rho_1}$

$\Rightarrow$ $\frac{\dot{M}_1}{\dot{M}_0} = \frac{\sqrt{\rho_1}}{\sqrt{\rho_0}}$

So, the actual mass flow rate is: $\dot{M}_1 = \dot{M}_0 \frac{\sqrt{\rho_1}}{\sqrt{\rho_0}}$

$\Rightarrow$ $\dot{M}_1 = \dot{V}_0 \times \rho_0 \times \sqrt{\frac{p_1 \times T_0}{p_0 \times T_1}}$

A4.4 - Engine test procedures

A4.4.1 Start-up procedure

1. Wipe up any oil left from previous testing to avoid fire risk.

2. Turn tap one turn on NO calibration gas bottle, and check that regulator is set to 0.7 bar. Turn tap one turn on oxygen gas bottle, and check that regulator is set to 0.7 bar. Turn tap one turn on nitrogen gas bottle, and check that regulator is set to 0.7 bar.

3. Turn tap one turn on hydrogen gas bottle, and check that regulator is set to 2.1 bar. Turn tap one turn on propane in air calibration gas bottle, and check that regulator is set to 0.7 bar.

4. Turn on all electrical equipment.

5. For Signal HC Analyser, press on/off key and turn on heated line controller with setting at 180°C. Check that sample tap is set to room air position.

6. For Signal NOx Analyser, press on/off key in bottom right corner. Switch on pumps.

7. Top up DI gasoline tank, taking care to minimise the loss of volatile components.

8. Turn on exhaust duct fan.

9. Select "n = constant" dynamometer control and set potentiometer to 390.

10. Set injector timing and pulse width, also ignition timing.

11. Wait until the Signal NOx Analyser indicates "STANDBY". Check that the range scale indicates "AUTO", if not change to AUTO. Press "NOx" key on bottom row of display. Press "SET" to display current value of calibration gas. Change if not correct. Press "SAMPLE" then "CAL" and check that display returns to "SAMPLE" once calibration is finished.

12. Wait until the Signal HC Analyser indicates "STANDBY". Press key immediately below "SAMPLE" (Might have to press "ESC" to get "SAMPLE"). The analyser might still need some time to warm up - once warm, it will automatically try to ignite and will indicate "SAMPLE" when successful. For calibration, first check that the value of the calibration gas

is correctly set. Press "SET" then "SPAN". Refer to manual instructions if resetting is required, otherwise press "CAL" and wait until procedure has been carried out.

13. Turn on Horiba gas analyser pump.

14. Calibrate Horiba gas analyser with aerosol calibration gas.

15. Turn on dynamometer water pump and check that there is sufficient water in tank.

16. Turn on engine water pump and check that water is circulating.

17. Turn on engine oil pump, check oil pressure and note value on engine test sheet.

18. Start engine. Check that fuel pressure is 100 bar. Run engine to 1500 rpm, no load, and set injector pulse width such that Horiba indicates 2.0% CO.

19. Check Pressure-Volume trace and adjust offset until trace is satisfactory. Transfer offset to injection controller.

20. Check that engine speed is 1500 rpm, and set dynamometer to control to this speed. Set ignition timing to 20° bTDC. Open throttle until load is 15 N, and set injector pulse width such that Horiba indicates 1.0% CO.

21. When engine coolant temperature reaches 69°C, turn on cooling water to heat exchanger, and close throttle until load is set to 10.9 N. Change injector pulse width, timing and ignition timing to appropriate values for test point.

22. Turn on exhaust gas taps in sample line so that all three analysers receive exhaust gas.

23. Record test readings whilst checking that engine coolant temperature remains between 69 and 71°C.

A4.4.2 Burn-off test

1. Adjust sample tap so that Signal Analysers are isolated from exhaust gas and take in only room air. Turn off sample line heater. Horiba should continue to measure exhaust gas constituents.

2. Adjust ignition timing to 20° bTDC and open throttle until load is set to 20 N. Adjust injector pulse width such that CO is set to 1.0 %.

3. Run engine for 10 minutes, while checking continuously that engine coolant temperature does not exceed 90°C and exhaust gas temperature does not exceed 900°C.

A4.4.3 Shut-down procedure

1. Turn off engine ignition.
2. Turn off dynamometer water pump, engine oil and water pumps.
3. Turn off electrical equipment, apart from gas analysers.
4. Turn off Horiba pump. Open drain tap in Horiba water trap and allow water to drain out. Close drain tap. Turn Horiba pump on again.
5. Put battery on charge, if needs be.
6. Turn off analyser pumps. Switch gas analysers off. Close all taps on gas bottles.
7. Turn off exhaust gas fan.
8. Check filters in Horiba analyser. Check Signal analyser filters once a week.

A4.5 - Fuel injector calibrations

It was decided to measure fuel flow rate through accurate calibration of the injectors used during the test programme. It was necessary to calibrate each injector at each fuel supply pressure so they were calibrated at 20 and 100 bar fuel pressure, with the port fuel injector calibrated at 3 bar only. The calibrations were performed with the injectors spraying into air at atmospheric pressure. Calibration of the injectors was performed at the same pulsing rate as experienced on the engine when operating at its test condition speed of 1500 rpm. The number of pulses was altered according to the pulsewidth to ensure that an accurate measurement could be obtained in the measuring cylinder. Care was taken to minimise the loss of the 'light ends' of the gasoline during calibration when the injector was spraying into a measuring cylinder.

As the GDI injectors rely on pressure from the engine-driven fuel pump, it was necessary to run the engine with PFI for these tests. The PFI calibration was carried out by use of a regular electrically driven fuel injection pump.

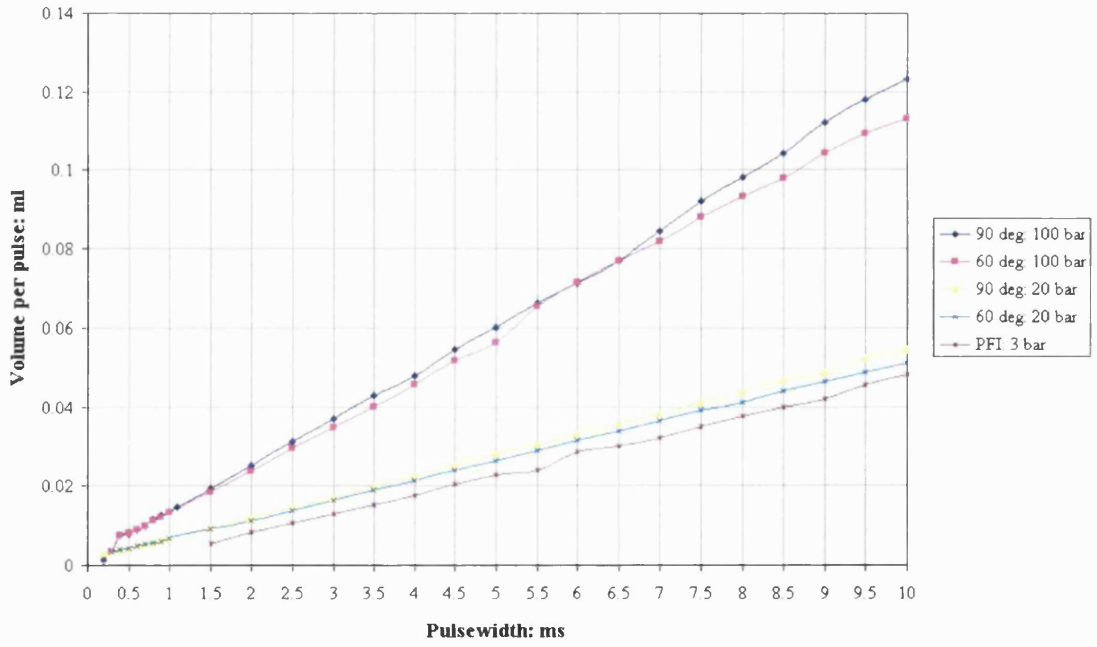

Figure A4.3 - Calibration results for injectors used in engine testing.

REFERENCES

References

Abo-Serie, E, Arcoumanis, C, Gavaises, M, Argueyrolles, B, Galzin, F (2000), "Swirl Pressure Atomizers for Direct Injection Gasoline Engines: Experiments and Modeling", SAE paper 2000-01-1044

Afzal, H, Arcoumanis, C, Gavaises, M, Kampanis, N (1999), "Internal flow in diesel injector nozzles - modelling and experiments", S492/S2/99, part of the proceedings of "Fuel Injection Systems", and IMechE seminar publication, 1999-17, 1-2 December 1999, ISBN 1 86058 247 8

Anderson, R W, Yang, J, Brehob, D D, Vallance, J K, Whiteaker, R M (1996), "Understanding the Thermodynamics of Direct Injection Spark Ignition (DISI) Combustion Systems: An Analytical and Experimental Investigation", Ford Motor Company, SAE paper 962018

Ando, H, Akishino, K, Kiyota, Y (1991), "Concept of Lean Combustion by Barrel-Stratification", No. 91207, Proceedings of the Annual Congress of JSAE

Andrews, G (1998), "The importance of A/F control with 3-way catalysts", Presentation at course entitled "Spark Ignition Engine Emissions", 23-27 November 1998, Department of Fuel and Energy, University of Leeds

Arcoumanis, C, Kashdan, J, T, Shrimpton, J, S, Gaade, J, E, Wallace, S (1999), "Spray characteristics of swirl pressure atomisers for direct-injection gasoline engines", S492/S1/99, part of the proceedings of "Fuel Injection Systems", and IMechE seminar publication, 1999-17, 1-2 December 1999, ISBN 1 86058 247 8

Banks, F, R (1950), "The Aviation Engine", James Clayton Lecture, Mechanical Engineering Proceedings, Volume 162 No. 4, 1950

Bishop, I N, Simko, A O (1968), "A New Concept of Stratified Charge Combustion - the Ford Combustion Process (FCP)", SAE paper 680041

Boheimer, A (2002), PhD thesis in progress, Department of Mechanical Engineering, University College London

Borman, G L, Ragland, K W (1998), "Combustion Engineering", WCB/McGraw-Hill, ISBN 0-07-006567-5

Bowditch, F, W (1961), "A New Tool for Combustion Research A Quartz Piston Engine", SAE transactions, Vol. 69, pp. 17-23

Box, G E P, Wilson K B (1951), "On the experimental attainment of optimal conditions", Journal of the Royal Statistical Society, Series B, Volume 13, No. 1

Brown, R, York, J, L (1962), "Sprays Formed by Flashing Liquid Jets", AIChE Journal, volume 8, p149, 1962

Burke, M W (1996), "Image Acquisition - Handbook of Machine Vision Engineering", volume one, Chapman & Hall, ISBN 0-412-47920-6

Cengal, YA, Boles, M A (1994), "Thermodynamics. An Engineering Approach", 2nd edition, McGraw-Hill, ISBN 0-07-113249-X

Cochran, W G, Cox, G M (1957), "Experimental Designs", 2nd edition, John Wiley & Sons Inc, ISBN 0-471-54567-8

Dargains, J R (1998), "A Computer Based Engine Data Logging System Using LabView", MSc dissertation, Department of Mechanical Engineering, University College London

Davy, M, Williams, P (2000), "The Effects of Flash Boiling on Mixture Formation in a Firing Direct-Injection Spark-Ignition (DISI) Engine", from Direkteinspritzung im Ottomotor 2, ISBN 3-8169-1822-0

Davy, M H (2000), "Two-Phase Fuel Visualisation in a Direct-Injection Gasoline Engine", PhD thesis, Department of Mechanical Engineering, University College London

Devore, J L (1991), "Probability and Statistics for Engineering and the Sciences", 3rd edition, Brooks/Cole Publishing Company, ISBN 0-534-14352-0

Diamond, W J (1989), "Practical experiment designs for engineers and scientists", 2nd edition, Can Nostrand Reinhold

Dodge, L G (1996), "Fuel Preparation Requirements for Direct-Injected Spark-Ignition Engines", Southwest Research Institute, SAE paper 962015

Fan, L, Li, G, Han, Z, Reitz, R D (1999), "Modelling Fuel Preparation and Stratified Combustion in a Gasoline Direct Injection Engine", SAE paper 1999-01-0175, from "Direct Injection SI Engine Technology 1999", SAE publication number SP-1416, ISBN 0-7680-0348-2

Fardad, D, Ladommatos, N (1999), "Evaporation of hydrocarbon compounds, including gasoline and diesel fuel, on heated metal surfaces", part of the proceedings of the IMechE, Volume 213, Part D, 1999

Fraidl, G K, Piock, W F, Wirth, M (1996), "Gasoline Direct Injection: Actual Trends and Future Strategies for Injection and Combustion Systems", AVL List GmbH, SAE paper 960465

Ghauri, A (1999), "An Investigation into the Effects of Variable Valve Actuation on Combustion and Emissions in an SI Engine", PhD thesis, Department of Mechanical Engineering, University College London

Han, Z, Parrish, S, Farrel, P V, Reitz, R D (1997), "Modelling Atomization Process of Pressure-Swirl Hollow-Cone Fuel Sprays", from Atomization and Sprays, 7, pp. 663.

Han, Z, Fan, L, Reitz, R D (1997), "Multidimensional Modelling of Spray Atomization and Air-Fuel Mixing in a Direct-Injection Spark-Ignition Engine", SAE paper 970884, from the proceedings of International Congress & Exposition, Detroit, Michigan, February 24-27, 1997

Harada, J, Tomita, T, Mizuno, H, Mashiki, Z, Ito, Y (1997), "Development of Direct Injection Gasoline Engine", Toyota Motor Co, SAE paper 970540

Haslett, R A, Monaghan, M L, McFadden, J J (1976), "Stratified Charge Engines", SAE paper 760755

Heywood, J B (1988), "Internal Combustion Engine Fundamentals", McGraw-Hill, ISBN 0-07-100499-8

Himes, M, Farrell, P V (1999), "Intake Air Velocity Measurements for a Motored Direct Injection Spark Ignited Engine", SAE paper 1999-01-0499

Inoue, T, Matsushita, S, Nakanishi, K, Okano, H (1993), "Toyota Lean Burn System - The Third Generation System", SAE paper 930873

Iwamoto, Y, Noma, K, Nakayama, O, Yamauchi, T, Ando, H (1997), "Development of Gasoline Direct Injection Engine", Mitsubishi Motors Corp, SAE paper 970541, from the proceedings of the International Congress & Exposition, Detroit, Michigan, February 24-27, 1997

Jackson, N S, Stokes, J, Whitaker, P A, Lake, T H (1996), "Direct Injection Stratified Charge Gasoline Combustion System for Future European Passenger Cars", Ricardo Consulting Engineers Ltd, presented at IMechE Lean Burn Combustion Engines Seminar, 3-4 December, 1996, S433

Jackson, N S, Stokes, J, Whitaker, P A, Lake, T H (1997), "Stratified and Homogeneous Charge Operation for the Direct Injection Gasoline Engine - High Power with Low Fuel Consumption and Emissions", Ricardo Consulting Engineers Ltd, SAE paper 970543

Jost, K (2000), "Direct gasoline injection from Renault", Automotive Engineering International, January 2000, volume 108, number 1

Kanda, M, Baika, T, Kato, S, Iwamuro, M, Koike, M, Saito, A (2000), "Application of a New Combustion Concept to Direct Injection Gasoline Engine", Toyota, SAE paper 00P-256

Kano, M, Saito, K, Basaki, M, Matsushita, S, Gohno, T (1998), "Analysis of Mixture Formation of Direct Injection Gasoline Engine", SAE paper 980157, from the proceedings of the International Congress & Exposition, Detroit, Michigan, February 23-26, 1998, part of "Direct Injection SI Engine Technology", SP-1314, ISBN 0-7680-0134-X

Kastner, L J (1947), "An Investigation of the Airbox Method of Measuring the Air Consumption of Internal Combustion Engines", Proc. IMechE, Vol.157, pp 387-404, 1947

Kimberley, W (1999), "Small, frugal but powerful", Automotive Engineer, November 1999, volume 24, number 10

Kiyota, Y, Akishino, K, Ando, H (1992), "Concept of Lean Combustion by Barrel-Stratification", Mitsubishi Motors Corp, SAE paper 920678

Koike, M, Saito, A, Tomoda, T, Yamamoto, Y (2000), "Research and Development of a New Direct Injection SI Gasoline Engine", Toyota, SAE paper 00P-372

Kume, T, Iwamoto, Y, Iida, K, Murakami, M, Akishino, K, Ando, H (1996), "Combustion Control Technologies for Direct Injection SI Engine", Mitsubishi Motors Corp, SAE paper 960600

Lee, C H, Chung, S H (1997), "Tomographic Reconstruction of Asymmetric Sprays From a Twin-Hole Air Shroud Injector", Department of Mechanical Engineering, Seoul National University, 1997 paper

Lienhard, J H, Day, J B (1970), "The Breakup of Superheated Liquid Jets", from the ASME Journal of Basic Engineering, September 1970

Lorusso, J A, Havstad, P H, Kaiser, E W, Rothschild, W G (1984), "Origins of Hydrocarbon Emissions From a Multifuel, Torch Ignition Assisted DI Engine", ASME paper 84-WA/HT-22

Malvern Instruments Ltd (1989), "Series 2600 Instruction Manual, IM 026, Issue 1", February 1989

Meyer, J, Kiefer, K, von Issendorff, F, Thiemann, J, Haug, M, Schreiber, M, Klein, R (1997), "Spray Visualization of Air-Assisted Fuel Injection Nozzles for Direct Injection SI-Engines", SAE paper 970623, from the proceedings of the International Congress & Exposition, Detroit, Michigan, February 24-27, 1997

Mitchell, E, Cobb, J M, Frost, R A (1968), "Design and Evaluation of a Stratified Charge Multifuel Military Engine", SAE paper 680042

Mitchell, E, Alperstein, M, Cobb, J M, Faist, C H (1972), "A Stratified-Charge Multifuel Military Engine - A Progress Report", SAE paper 720051

Mitsubishi (2000), Japanese Web site, http://www.mitsubishi.co.jp

Miyajima, A, Okamoto, Y, Kadomukai, Y, Togashi, S, Kashiwaya, M (2000), "A Study on Fuel Spray Pattern Control of Fuel Injector of Gasoline Direct Injection Engines", SAE paper 00P-78

Moriyoshi, Y, Nomura, H, Saisyu, Y (1998), "Evaluation of a Concept for DI Gasoline Combustion Using Enhanced Gas Motion", SAE paper 980152, from the proceedings of the International Congress & Exposition, Detroit, Michigan, February 23-26, 1998, SAE SP-1314, ISBN 0-7680-0134-X

Naitoh, K, Takagi, Y (1996), "Synthesized Spheroid Particle (SSP) Method for Calculating Spray Phenomena in Direct-Injection SI Engines", SAE paper 962017

Norbye, J P (1988), "Automotive Fuel Injection Systems - A Technical Guide", Haynes Publishing Group, ISBN 0-85429-755-3

Ohm, I-Y, Ahn, H-S, Lee, W-J, Kim, W-T, Park, S-S, Lee, D-U (1993), "Development of HMC Axially Stratified Lean Combustion Engine", Hyundai Motor Co, SAE paper 930879, reprinted from: "New Engine Design and Engine Component Technology", SP-972

Oza, R D, Sinnamon, J F (1983), "An Experimental and Analytical Study of Flash Boiling Fuel Injection", SAE paper 830590

Parrish, S E, Farrell, P V (1997), "Transient Spray Characteristics of a Direct-Injection Spark-Ignited Fuel Injector", University of Wisconsin-Madison, SAE paper 970629, from the proceedings of the International Congress & Exposition, Detroit, Michigan, February 24-27, 1997

Plint, M, Martyr, A (1999), "Engine Testing. Theory and practice", 2nd edition, ISBN 0 7506 4021 9

Pontoppidan, M, Gaviani, G, Bella, G, Rocco, V (1997), "Direct Fuel Injection - A Study of Injector Requirements for Different Mixture Preparation Concepts", SAE paper 970628, from the proceedings of the International Congress & Exposition, Detroit, Michigan, February 24-27, 1997

Queenan, B, Nightingale, C, Bennett, J (1997), "Charge Stratification in a 4-Valve SI Engine Through Injection Into One Intake Port with Induced Axial Swirl Within the Cylinder", SAE paper 972875, from the proceedings of the International Fall Fuels & Lubricants Meeting & Exposition, Tulsa, Oklahoma, October 13-16, 1997

Salters, D G, Greig, A R, Williams, P (1996), "Fuel Spray Characterisation within an Optically Accessed Gasoline Direct Injection Engine Using a CCD Imaging System", SAE paper 961149

Schamel, A, Limbach, S, Sweet, T, Wölfe, M, Tielkes, U (2000), "Development and Potential of a Small Direct Injection Gasoline Engine", presented in Direkteinspritzung im Ottomotor 2, ISBN 3-8169-1822-0

"Eddy current dynamometer W130 operating manual - including weighing cell and force transducer", Carl Schenck Gmbh, Darmstadt, Germany

Scherenberg, H (1955), "Ruckbliik uber 25 Jahre Benzin-Einspritzung in Deutchland", MTZ, volume 9, number 16

Scusssel, A J, Simko, A O, Wade, W R (1978), "The Ford PROCO Engine Update", SAE paper 780699

Seabrook, J F (1995), "Combustion and Emissions Optimisation in a High-Performance S.I. Engine", PhD thesis, Department of Mechanical Engineering, University College London

Senda, J, Hojyo, Y, Fujimoto, H (1994), "Modelling of Atomization Process in Flash Boiling Spray", SAE paper 941925

Senda, J, Higaki, T, Sagane, Y, Fujimoto, H, Takagi, Y, Adachi, M (2000), "Modelling and Measurement on Evaporation Process of Multicomponent Fuels", SAE paper 2000-01-0280, from the proceedings of the SAE 2000 World Congress, Detroit, Michigan, March 6-9, 2000

Selim, M, Y, E, Dent, J, C, Das, S (1997), "Application of CFD to the Matching of In-Cylinder Fuel Injection and Air Motion in a Four Stroke Gasoline Engine", SAE paper 971601, from the proceedings of the International Spring Fuels & Lubricants Meeting, Detroit, Michigan, May 5-8, 1997

Shelby, M H, VanDerWege, B A, Hochgreb, S (1998), "Early Spray Development in Gasoline Direct-Injected Spark Ignition Engines", Massachusetts Institute of Technology, SAE paper 980160, from the proceedings of the International Congress & Exposition, Detroit, Michigan, February 23-26, 1998, part of "Direct Injection SI Engine Technology", SP-1314

Simko, A, Choma, M A, Repko, L L (1972), "Exhaust Emission Control by the Ford Programmed Combustion Process-PROCO", Ford Motor Company, SAE paper 720052

Stanglmaier, R H, Hall, M J, Matthews, R D (1998), "Fuel-Spray/Charge-Motion Interaction within the Cylinder of a Direct-Injected, 4-Valve, SI Engine, SAE paper 980155, from the proceedings of the International Congress & Exposition, Detroit, Michigan, February 23-26, 1998

Stanglmaier, R H, Roberts, C E (1999), "Homogeneous Charge Compression Ignition (HCCI): Benefits, Compromises, and Future Engine Applications", SAE paper 1999-01-3682

Stone, R (1999), "Introduction to Internal Combustion Engines", 3rd edition, Macmillan Press Ltd, ISBN 0-333-74013-0

Suh, E S, Rutland, C J (1999), "Numerical Study of Fuel/Air Mixture Preparation in a GDI Engine", SAE paper 1999-01-3657, from "Gas Direct Injection Engines", SAE publication number SP-1475, ISBN 0-7680-0483-7

Takagi, Y, Itoh, T, Muranaka, S, Iiyama, A, Iwakiri, Y, Urushihara, T, Naitoh, K (1998), "Simultaneous Attainment of Low Fuel Consumption, High Output Power and Low Exhaust Emissions in Direct Injection SI Engines", Nissan Motor Co. Ltd, SAE paper 980149, from the proceedings of "Direct Injection SI Engine Technology", SP-1314, February 1998, ISBN 0-7680-0134-X

Takemura, J, Murakami, N, Kitada, T, Ando, H (1991), "Mixture preparation in the lean-burn engine employing the concept of barrel-stratification", No. 307, Proceedings of Annual Congress of JSME Kansai Branch

Tomoda, T, Sasaki, S, Sawada, D, Saito, A, Sami, H (1997), "Development of Direct Injection Gasoline Engine - Study of Stratified Mixture Formation", Toyota, SAE paper 970539

Van de Hulst, H C (1981), "Light Scattering by Small Particles", Dover Publications, ISBN 0-486-64228-3

VanDerWege, B A, Hochgreb, S (1998), "The Effect of Fuel Volatility on Sprays from High-Pressure Swirl Injectors", Twenty-Seventh Symposium (International) on Combustion, The Combustion Institute, Pittsburgh, pp. 1865-71

VanDerWege, B A, Hochgreb, S (2000), "Experimental Study of the Effects of Fuel Volatility and Operating Conditions on Fuel Sprays in DISI Engines. Part I: Planar Laser-Induced Fluorescence", SAE paper 00P-257a

VanDerWege, B A, Hochgreb, S (2000), "Experimental Study of the Effects of Fuel Volatility and Operating Conditions on Fuel Sprays in DISI Engines. Part II: Phase-Doppler Particle Analysis", SAE paper 00P-257b

Webster, D (1998), "Development of automotive catalysts- past, present and future", Presentation at course entitled "Spark Ignition Engine Emissions", 23-27 November 1998, Department of Fuel and Energy, University of Leeds

Webster, D (1998), "dNOx catalyst for lean SI engines", Presentation at course entitled "Spark Ignition Engine Emissions", 23-27 November 1998, Department of Fuel and Energy, University of Leeds

Wedd, M (1999), Malvern Instruments Ltd, telephone conversation, September 1999

Williams, P A (1994), "Characterization of Fuel Sprays in Spark Ignition Engines", PhD thesis, Department of Mechanical Engineering, University College London

Williams, P A, Davy, M H, Brehob, D D (1998), "Effects of Injection Timing on the Exhaust Emissions of a Centrally-Injected Four-Valve Direct-Injection Spark-Ignition Engine", SAE paper 982700, reprinted from "Direct Injection: Engines, Emissions, and Aftertreatment", SP-1399, October 1998

Wirth, M, Piock, W F, Fraidl, G K, Schoehhl, P, Winklhofer, E (1998), "Gasoline DI Engines: The Complete System Approach by Interaction of Advanced Development Tools", AVL List GmbH, SAE paper 980492, from the proceedings of "Direct Injection SI Engine Technology", SP-1314, February 1998, ISBN 0-7680-0134-X

Witze, P O (1980), "Influence of Air Motion Variation on the Performance of a Direct-Injection Stratified-Charge Engine", Sandia Natl Lab Rep, SAND79-8756

Wood, C D (1978), "Unthrottled Open-Chamber Stratified Charge Engines", SAE paper 780341

Yamaguchi, J (2000), "Toyota's Crowning act", Automotive Engineering International, January 2000, volume 108, number 1

Yamauchi, T, Wakisaka, T (1996), "Computation of the hollow-cone sprays from high-pressure swirl injector from a gasoline direct-injection SI engine", SAE paper 962016

Yamauchi, T, Wakisaka, T, Kaneko, T, Kaneko, M, Kato, S, Hosaka, H (1998), "Numerical Analysis of Stratified Mixture Formation in Direct-Injection Gasoline Engines", from the proceedings of Direkteinspritzung im Ottomotor, ISBN 3-8169-1685-6